

RICE UNIVERSITY

Determination of Pathways for Oxygen Binding to Human Hemoglobin A

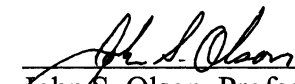
by

Ivan Birukou

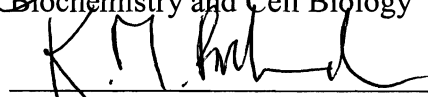
A THESIS SUBMITTED
IN PARTIAL FULLFILMENT OF THE
REQUIREMENTS FOR THE DEGREE

Doctor of Philosophy

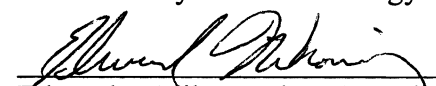
APPROVED, THESIS COMMITTEE:



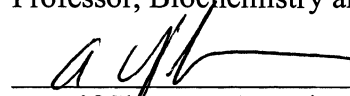
John S. Olson, Professor, Thesis Director
Biochemistry and Cell Biology



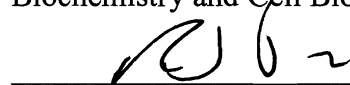
Kathleen M. Beckingham, Professor,
Biochemistry and Cell Biology



Edward P. Nikonowicz, Associate
Professor, Biochemistry and Cell Biology



Yousif Skamoo, Associate Professor,
Biochemistry and Cell Biology



Ronald J. Parry, Professor, Chemistry
and Biochemistry and Cell Biology

HOUSTON, TEXAS
MAY 2011

ABSTRACT

Determination of Pathways for Oxygen Binding to Human HbA

by

Ivan Birukou

The role of His(E7) in ligand binding to HbA was re-examined in view of discrepancies between early kinetic studies and recent structure determinations. Replacing His(E7) with Gly, Leu, Phe, and Trp causes 20- to 500-fold increases in the rates of O₂ dissociation from both subunits, and FTIR spectra reveal a shift in the C-O stretching frequency peak from 1950 cm⁻¹ to ~1970 cm⁻¹ for apolar mutations, indicating loss of a positive electrostatic field next to bound ligands. Thus, the native His(E7) side chain forms a strong hydrogen bond (~ -8 kJ/mol) with bound O₂ in both HbA subunits.

Increasing the size of the E7 residue from Gly to Trp monotonically decreases the rate constants for CO, O₂ and NO association to HbA. Substituting His(E7) with Trp also slows down opening and closing of the E7 gate. Ligand binding to the Trp(E7) subunits is markedly biphasic due to a competition between very fast recombination to an *open* conformer and relaxation of the indole side chain to *closed* or *blocked* forms. Crystal structures of Hb and Mb Trp(E7) mutants provide structural models for these *closed* and *blocked* conformers. In the *closed* state, the indole side chain fills both the E7 channel and the distal pocket, inhibiting binding to iron from any direction. In the *blocked* state, Trp(E7) is located in the solvent interface but still blocks entry into the E7 channel. The bimolecular rate constants for CO binding to the *closed* and *blocked* states are 0.08 μM⁻¹s⁻¹ and 0.7 μM⁻¹s⁻¹, respectively, which are ~100 and ~10-fold slower than average wild-type parameter (~7 μM⁻¹s⁻¹). Filling potential alternative ligand pathways with xenon

does not affect the rate or fraction of ligand escape from either HbA subunit. In contrast, reducing the volume of the distal pocket by space-filling mutations at the B10, E11 and G8 positions dramatically affects both geminate recombination and bimolecular ligand binding. Taken together, these results demonstrate that the E7 channel is the major pathway for ligand entry and escape in HbA and that previously proposed ligand migration routes involving Xe cavities are not functionally significant.

ACKNOWLEDGEMENTS

Foremost, I would like to acknowledge my scientific advisor Dr. John S. Olson, whose positive attitude and unquenchable enthusiasm replenished my energy and eagerness during all these years. His constant participation and involvement in every possible experiment make the John S. Olson Laboratory a unique place, where the professor is not some guy in a stiff suit to whom you report once a week and who gives you orders, but the core of the team, the glue which sticks all the members together. Therefore, the years spent in the graduate school will stay forever in my memory as one of the happiest times of my life.

I would like to acknowledge the members of my progress review committee, Dr. Kathleen Beckingham, Dr. Yousif Shamoo and Dr. Edward Nikonowicz for discussing the results of experiments, making valuable suggestions and providing important unbiased analysis of my work.

I am very grateful to Dr. Marian Fabian. He is the person, who suggested that I apply to Rice in the first place. Moreover, he always supported and inspired me, telling me that I have all the necessary skills to finish what I have started. But probably, the most important lesson I have learned from Dr. Fabian is that nothing can be achieved without hard work and persistence.

I want to thank Dr. Jayashree Soman for having done a great job in teaching me the basics of X-ray crystallography, for editing manuscripts and helping with this doctoral dissertation, and for always being in a good mood.

I also want to acknowledge Phillip Graves, who spent long nights teaching me how to operate the fermenter and thoroughly explaining all the steps in hemoglobin

expression and purification; our lab manager Eileen Singleton for taking care of everything in the lab so that graduate students never have delays in their research; and, of course, Dr. Neil Varnado, Dr. George Blouin, Dr. Todd Mollan, Dr. David Culbertson and Mallory Salter for being great collaborators and colleagues.

Last but not least, I want to thank my wife Anastasiya Birukova. She not only contributed to the research part of the project by creating, expressing and purifying numerous hemoglobin mutants, but she also created a warm, family atmosphere at home, where I could relax and gather energy for the next day.

TABLE OF CONTENTS

ABSTRACT	ii
ACKNOWLEDGEMENTS.....	iv
TABLE OF CONTENTS.....	vi
LIST OF TABLES.....	x
LIST OF FIGURES.....	xii
CHAPTER 1: INTRODUCTION.....	1
1.1. Primary and secondary functions of HbA.....	1
1.2. Structural factors regulating ligand binding to Hbs and Mbs.....	4
1.3. Ligand migration in globins.....	6
1.4. NO scavenging by oxyhemoglobins and the hypertensive effect of Hb-based blood substitutes.....	13
1.5. Significance and specific aims.....	19
CHAPTER 2: MATERIALS AND METHODS.....	22
2.1. Mutagenesis, expression and purification of HbA.....	22
2.2. Isolation of individual α and β subunits of HbA.....	26
2.3. Measurements of bimolecular O ₂ , CO and NO binding to hybrid Hb tetramers and isolated subunits.....	27
2.4. Measurements of NO dioxygenation by oxyHb.....	36
2.5. Measurements of geminate CO recombination to hybrid Hb tetramers and isolated subunits.....	39
2.6. Laser flash photolysis of HbA tetramers and isolated subunits in the presence of Xe.....	42

2.7. FTIR spectroscopy of HbCO tetramers and isolated subunits.....	43
2.8. Crystallization of mutant Hbs, X-ray diffraction data collection and structure determination.....	45
CHAPTER 3: HIS(E7) STABILIZES BOUND O₂ AND REGULATES LIGAND ENTRY IN α AND β SUBUNITS OF HUMAN HBA.....	
3.1. Previous ideas about the role of the distal histidine in HbA.....	49
3.2. Effects of mutagenesis at E7 position on O ₂ association.....	52
3.3. Bimolecular CO binding to E7 mutants.....	57
3.4. Crystal structures of α and β Leu(E7) mutants in CO- and deoxy-state.....	62
3.5. Direct and indirect measurements of ligand entry into α and β E7 mutants of HbA.....	66
3.6. Rate constants for O ₂ and CO dissociation from the α and β E7 mutants.....	70
3.7. Measurements of distal pocket polarity in E7 mutants of HbA by FTIR spectroscopy.....	73
3.8. O ₂ affinity of E7 mutants and hydrogen bonding.....	76
3.9. Correlation between K _{CO} and K _{O₂} and ligand discrimination.....	82
3.10. Steric hindrance of ligand binding by Phe and Trp(E7) mutations.....	84
3.11. Pathways for ligand entry into Mb and HbA subunits.....	86
CHAPTER 4: MECHANISMS FOR LIGAND BINDING TO α AND β TRP(E7) MUTANTS OF HUMAN HBA.....	
4.1. The motions of the E7 gate in Mb and Hb.....	90
4.2. CO rebinding to Trp(E7) hybrid mutant tetramers of HbA.....	92
4.3. Bimolecular CO binding to isolated α and β Trp(E7) subunits.....	94

4.4. CO recombination to Trp(E7) mutant of swMb.....	98
4.5. Crystal structures of Hb and Mb Trp(E7) mutants.....	99
4.6. Simple linear conformational relaxation mechanism.....	107
4.7. Mechanism of CO binding to α Trp(E7).....	110
4.8. Mechanism of CO binding to β Trp(E7).....	115
4.9. Comparison of the mechanisms for α and β subunits.....	122
4.10. Opening and closing of the E7 gate in wild-type and mutant Mb and Hb.....	124
4.11. Multiple pathways versus the E7 gate.....	126
CHAPTER 5: THE ROLE OF INTERNAL CAVITIES IN LIGAND BINDING	
TO HUMAN HbA.....	128
5.1. Protein cavities, Xe binding, and ligand capture in globins.....	128
5.2. Nanosecond CO recombination to α and β subunits and HbA tetramers.....	132
5.3. The effects of Phe and Trp substitutions at the B10 position on ligand binding to α and β subunits of HbA.....	136
5.4. The effects of Phe and Trp substitutions at the E11 position on ligand binding to α and β subunits of HbA.....	141
5.5. The effects of Phe and Trp substitutions at the G8 position on ligand binding to α and β subunits of HbA.....	145
5.6. Ligand binding to isolated α and β subunits and HbA tetramers at various Xe pressures.....	148
5.7. Structural interpretations of kinetic effects.....	152
5.8. Ligand trapping by noncovalent binding site.....	155
5.9. Ultra-fast phase of geminate recombination and secondary sites in HbA.....	156

5.10. Ligand migration via alternative routes in HbA.....	158
5.11. Baseball glove model and the E7 gate.....	160
CHAPTER 6: ENGINEERING HEMOGLOBINS WITH REDUCED NO SCAVENGING AND OPTIMIZED O₂ AFFINITY FOR 3RD GENERATION HB-BASED OXYGEN CARRIERS.....	
6.1. Design principles for 3 rd generation Hb-based oxygen carriers (HBOCs).....	161
6.2. Rational design of Hb distal pocket mutants with reduced NO scavenging.....	165
6.3. O ₂ and CO binding to multiple mutants.....	167
6.4. NO dioxygenation by the space-filling mutants.....	169
6.5. Improving oxygen affinity, apoglobin stability and expression yields of recombinant human HbA.....	171
6.6. Conclusions.....	175
CHAPTER 7: CONCLUSIONS.....	
7.1. Stabilization of bound oxygen in α and β subunits of human HbA.....	177
7.2. Gating of ligand entry into the subunits of HbA.....	178
7.3. Multiple <i>versus</i> single ligand migration pathways in human HbA.....	180
REFERENCES.....	182
APPENDIX 1.....	199
APPENDIX 2.....	204

LIST OF TABLES

Table 3.1. Rate and equilibrium constants for O ₂ binding to R-state native HbA, mutant hybrid tetramers and isolated mutant subunits with E7 substitutions.....	55
Table 3.2. Rate and equilibrium constants for CO binding to binding to native HbA, mutant hybrid tetramers and isolated mutant subunits with E7 substitutions.....	58
Table 3.3. Crystallization and structure determination parameters of Leu(E7) Hb mutants.....	63
Table 3.4. Rate constants for bimolecular CO and NO binding, and parameters for CO geminate recombination to isolated α and β E7 mutants.....	69
Table 3.5. Bound C-O stretching frequency peaks, ν_{C-O} , for WT and mutant α and β subunits of native and recombinant human hemoglobin.....	75
Table 3.6. Effects of small apolar E7 mutations on ΔG° for O ₂ binding to HbA and sperm whale Mb.....	79
Table 3.7. Effects of Phe(E7) and Trp(E7) mutants on O ₂ binding to HbA and sperm whale Mb.....	85
Table 4.1. Crystallization and structure determination parameters of Hb and Mb Trp(E7) mutants.....	100
Table 4.2. The parameters for ligand binding and opening and closing of the E7 gate for isolated wild-type and mutant HbA subunits and Mb.....	126
Table 5.1. Geminate parameters of CO recombination to HbA tetramers and isolated subunits.....	134

Table 5.2. Rate constants for bimolecular CO, NO binding, NO dioxygenation and parameters for the slow CO geminate recombination to isolated α and β B10 mutant subunits.....	140
Table 5.3. Rate constants for bimolecular CO, NO binding, NO dioxygenation and parameters for CO geminate recombination to isolated α and β E11 mutant subunits.....	144
Table 5.4. Rate constants for bimolecular CO, NO binding, NO dioxygenation and parameters for CO geminate recombination to isolated α and β G8 mutant subunits.....	147
Table 5.5. The effect of Xe on kinetic parameters for bimolecular CO, O ₂ binding and CO geminate recombination to isolated α and β subunits.....	149
Table 5.6. The effect of Xe on kinetic parameters for geminate CO recombination to HbA tetramers and T state parameters for bimolecular CO binding.....	151
Table 6.1. O ₂ binding parameters for space-filling mutant series.....	168
Table 6.2. CO binding parameters for space-filling mutant series.....	168
Table 6.3. Rate constants for NO dioxygenation by multiple Hb mutants and isolated chains.....	170
Table 6.4. Rate constants for NO dioxygenation by multiple low NO scavenging rHb mutants with improved apoglobin stability.....	172
Table 6.5. O ₂ and CO R-state binding parameters for multiple low NO scavenging rHb mutants with improved apoglobin stability.....	174
Table A1.1. Comparison of old and new measurements of O ₂ binding to monomeric and tetramer HbA subunits.....	200

LIST OF FIGURES

Figure 1.1. Human hemoglobin A, individual subunits and heme.....	1
Figure 1.2. Heme pocket of HbO ₂ subunit (β).....	5
Figure 1.3. Maps of ligand migration pathways in sperm whale Mb.....	8
Figure 1.4. Crystal structures of deoxy-α(B10Y/E7Q) (A) and deoxy-β(B10Y/E7Q) (B) subunits with bound Xe.....	12
Figure 1.5. Scheme for NO signaling in the endothelium, excess NO detoxification by Mb and effects of NO scavenging by extracellular Hb.....	14
Figure 1.6. Schematic representation of NO-induced oxidation reaction by MbO ₂ or HbO ₂ at neutral pH.....	15
Figure 1.7. The dependence of the hypertensive effect on (A) the rate of NO scavenging (k'_{NOD}), (B) oxygen affinity of Hb (P_{50}) and (C) the size of Hb molecules (molecular weight, MW).....	17
Figure 1.8. Hypertensive effect after administration of recombinant Hbs.....	18
Figure 2.1. rHb α(WT) β(Gly(E7)) fermentor growth profile.....	24
Figure 2.2. Chromatographic purification of recombinant HbA.....	26
Figure 2.3. Determination of the quality of isolated chains.....	27
Figure 2.4. Time courses for O ₂ binding to and displacement from isolated human Ala(E7) αCO subunits.....	30
Figure 2.5. NO binding to isolated native α and β chains.....	36
Figure 2.6. NO dioxygenation by tetrameric HbO ₂ and isolated αO ₂ and βO ₂ subunits.....	38

Figure 2.7. Schematic representation of geminate O ₂ recombination time course of Mb.....	40
Figure 2.8. CO stretching frequency (ν_{CO}) as a probe to study electrostatic environment of the distal pocket in Mb.....	44
Figure 2.9. Crystals of recombinant HbCO.....	46
Figure 3.1. His gate in deoxygenated β subunits of HbA.....	49
Figure 3.2. Bimolecular binding of O ₂ to native and E7 mutants of isolated α and β subunits of recombinant human HbA.....	54
Figure 3.3. Time courses for bimolecular CO rebinding to wild type and E7 mutants of isolated human HbA subunits after laser photolysis.....	57
Figure 3.4. Time courses for bimolecular CO rebinding to Trp(E7) mutants after laser photolysis.....	59
Figure 3.5. Structures of CO- and deoxy-forms of α and β Leu(E7) distal pockets.....	64
Figure 3.6. Stick models of deoxy (<i>green</i>) and CO-forms (<i>beige</i>) of α WT (A) and α Leu(E7) (B) distal pockets.....	65
Figure 3.7. Geminate CO recombination in wild type and E7 mutants of isolated α and β subunits of recombinant human HbA.....	67
Figure 3.8. Ligand entry and NO binding to E7 mutants of HbA subunits.....	70
Figure 3.9. Time courses for O ₂ replacement by CO in native and E7 mutant α and β subunits.....	71
Figure 3.10. FTIR spectra of wild type and E7 mutants of human HbA.....	74
Figure 3.11. Structures of the α and β active sites in HbO ₂	76

Figure 3.12. Effects of E7 mutants on K_{CO} , K_{O_2} , and their ratio, M	82
Figure 3.13. Dependence of rate constant for NO association on E7 mutations in monomeric α subunits, β subunits, and Mb.....	87
Figure 4.1. CO binding to wild-type and Trp(E7) mutants of human HbA tetramers.....	92
Figure 4.2. CO binding to α and β isolated subunits of Trp(E7) mutants.....	94
Figure 4.3. Rapid bimolecular CO rebinding to Trp(E7) α and β subunits after laser photolysis.....	96
Figure 4.4. Bimolecular CO binding to Trp(E7) sperm whale Mb.....	98
Figure 4.5. Side views of wild-type and Trp(E7) mutants of HbA.....	101
Figure 4.6. Front view of Trp(E7) α subunit in hybrid deoxyHb.....	102
Figure 4.7. Side views of wild-type and Trp(E7) mutants of Mb.....	105
Figure 4.8. Models of <i>Open</i> , <i>Closed</i> , and <i>Blocked</i> kinetic states.....	106
Figure 4.9. Fitting the dependence of α Trp(E7) slow rate on [CO] with simple linear mechanism.....	109
Figure 4.10. Dependences of the observed fast and slow rates for bimolecular CO binding and fraction of the fast phase on [CO] for both laser photolysis and rapid mixing experiments with isolated Trp(E7) α subunits.....	113
Figure 4.11. Dependences of the observed rates and the fractions of the fast and slow phases on [CO] for CO binding to isolated Trp(E7) β subunits.....	121
Figure 5.1. CO geminate rebinding to HbA and isolated chains.....	133
Figure 5.2. CO geminate rebinding to isolated Phe and Trp B10 chains.....	137
Figure 5.3. CO geminate rebinding to isolated Phe and Trp E11 chains.....	142
Figure 5.4. CO geminate rebinding to isolated Phe and Trp G8 chains.....	146

Figure 5.5. CO geminate rebinding to isolated α (A) and β (B) WT subunits in the presence/absence of Xe.....	150
Figure 5.6. Structures of the key B10, E11 and G8 mutants of HbA.....	153
Figure 5.7. Structures of the distal pockets of β subunits of oxyHbA and cyanometHb β Trp(G8), top view (A), and wild-type and Trp(G8) sperm whale Mb, side view (B).....	154
Figure 5.8. Structures of the α (A) and β (B) subunits of deoxyHb with bound Xe atoms.....	159
Figure 6.1. Reduction of k'_{NOD} using space-filling mutations at B10 and E11 positions in sperm whale Mb.....	162
Figure 6.2. Top views of the distal pockets of sperm whale MbO ₂ and α and β -subunits of human HbO ₂	165
Figure 6.3. NO dioxygenation by multiple α (A) and β (B) space-filling Hb mutants.....	169
Figure 6.4. Structure depicting candidate rHBOC features.....	176
Figure A1.1. O ₂ replacement by CO for isolated β Leu(E7) subunits.....	203

CHAPTER 1: INTRODUCTION

1.1. Primary and secondary functions of HbA.

The human body contains 20 to 30 trillion red blood cells (or erythrocytes), each of which carries approximately 280 million molecules of hemoglobin A (HbA). HbA is the major O₂-carrying protein of vertebrate animals. Nonspecific transport of gas dissolved in plasma is not efficient. Simple calculations demonstrate that at normal atmospheric pressure of air in lungs only 0.3 ml of O₂ per 100 ml of plasma may be delivered to tissues; whereas, the equivalent volume of normal blood transports ~20 ml of gaseous O₂ [1].

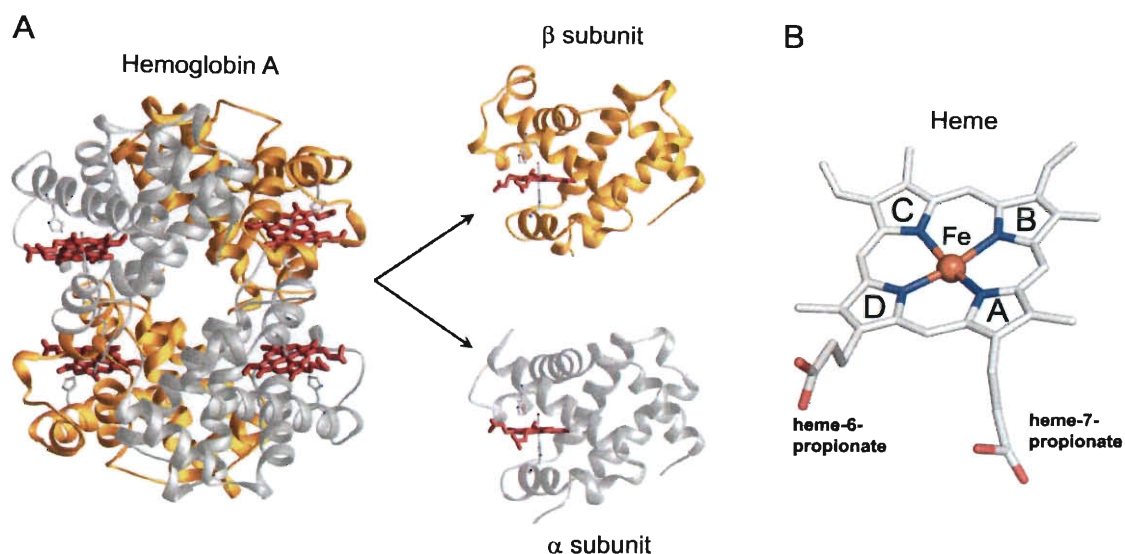


Figure 1.1. Human hemoglobin A, individual subunits and heme. (A) Protein part is shown in ribbons (silver for α , and golden for β), heme is shown as red sticks, proximal and distal histidines, and bound CO are shown as sticks. (B) Heme is shown as sticks, colored as follows: carbon, white; oxygen, red; nitrogen, blue; iron is shown as orange sphere. Pyrrole rings are labeled A-D. Created from 2DN3 [2].

Human hemoglobin A is a heterotetramer that is composed of two types of protein subunits, α and β (Fig. 1.1). Each subunit carries a prosthetic group, heme, which is capable of binding O₂ and other ligands. This binding is reversible and cooperative,

which means that each event of bond formation/disruption between Fe and O₂ in one subunit accelerates analogous interactions in adjacent subunits. When all binding sites of hemoglobin are occupied by ligand molecules, HbA tetramers stay in the high affinity R-state. When the ambient concentration of O₂ decreases, oxygen molecules dissociate from subunits and Hb switches its conformation to the low affinity T-state. In lungs, O₂ saturation of hemoglobin occurs within tenths of a second and oxyhemoglobin is then transported to respiring tissues, where O₂ is unloaded forming deoxyhemoglobin. The oxygen affinity of completely deoxygenated Hb in the T-state is ~200-fold lower than that of unliganded R-state subunits in Hb₄(O₂)₃, allowing the dissociated O₂ molecules to diffuse away from Hb tetramers without rebinding at low saturation values [3].

HbA is also capable of transporting carbon dioxide from tissues to lungs. It is accomplished by two mechanisms. First, CO₂ can directly bind to the N-termini of deoxyHb chains producing carbamates (-NHCOO⁻), which carry CO₂ to lungs where the reverse reaction occurs when O₂ is bound. The second mechanism is more complex. Dissolved CO₂ hydrates and forms carbonic acid in a reaction catalyzed by carbonic anhydrase. H₂CO₃ then dissociates to give HCO₃⁻ and H⁺. Protons bind to deoxyHb and are transported to lungs in the bound state. HCO₃⁻ is transported as the dissolved salt by plasma. Upon oxygenation in lungs, protons dissociate from HbA and recombine with HCO₃⁻ to form H₂CO₃, which dehydrates to H₂O and CO₂, and the latter gas is exhaled. This reverse reaction is also catalyzed by carbonic anhydrase [1].

Another physiologically relevant ligand, which interacts with Hb is nitric oxide. NO participates in numerous regulatory events as a secondary messenger molecule. One of its major functions is to induce the relaxation of the smooth muscle cell layer

surrounding blood vessels. NO can react with both oxy- and deoxyHb, and in both cases inactivation of nitric oxide occurs. In the first case, the products of the reaction are methemoglobin (contains Fe^{3+}) and nitrate (NO_3^-). Nitrate is an inert anion, does not possess the activity of NO, and is simply excreted from the organism. Iron-nitrosyl Hb (HbNO) results from the second reaction. The stability of this complex is extremely high and binding may be considered irreversible. Even when dissociation occurs, NO will be either consumed by oxyHb to form nitrate or rebind to deoxyHb and never be free in solution. Considering that the physiological concentration of NO is on the order of μM – nM , the proximity of Hb to the place of action of NO would represent a serious threat to the regulatory processes governed by this gas molecule. However, various barriers, including encapsulation of Hb into erythrocytes, prevent premature deactivation of NO [4-7]. NO dioxygenation by oxyHb will be discussed more thoroughly later in Section 1.4.

Two novel hypotheses for generation and transport of NO equivalents in hypoxic or acidic tissues were developed by the groups of Gladwin [8, 9] and Stamler [10, 11]. Gladwin and coworkers suggested that NO equivalents can be transported in plasma as nitrite, NO_2^- , and then reduced to NO by deoxyHb. Stamler *et al.* [11] proposed that heme-bound NO can be transferred to Cys93 residues of β chains during the T \rightarrow R quaternary state transition of HbA after re-oxygenation to form S-nitrosated Hb (SNO-Hb). They then proposed that this reaction is reversed on deoxygenation, during which some NO is transferred from βCys93 to an exchanger molecule, which transports nitric oxide outside of red blood cell. However, in both cases more experimental work is required to establish the validity of these hypotheses

1.2. Structural factors regulating ligand binding to Hbs and Mbs.

As mentioned above, HbA tetramers consist of two α and two β subunits. α chains are composed of 141 amino acid residues with a net molecular weight of 15,126 Da; β chains contain 146 amino acids, resulting in molecular weight of 15,867 Da. The prosthetic group, heme or Fe-protoporphyrin IX, is composed of a porphyrin ring with an iron atom, located in the center of the ring and coordinated to 4 pyrrole nitrogens (Fig. 1.1 B). Comparative analyses of the amino acid sequences and tertiary folds of Hb subunits reveal a high degree of homology between each other and sperm whale Mb. These proteins belong to the same single domain globin family, are composed of 6-7 α helices (labeled A-H), and share a common “3 helix on 3 helix” folding pattern, called the 3:3 globin fold. Sequence alignment of α and β -subunits of human Hb shows the presence of 57 conserved residues [1].

The most conserved region is the heme binding pocket, which is divided by the heme plane into two hemispheres, distal and proximal (Fig. 1.2). The distal ligand binding site is composed of the amino acids found in the upper part of the cavity including Leu(B10), His(E7) and Val(E11) (here the letter and number in parenthesis refer to the position of the amino acid along a particular helix starting from the N-terminus). Previous structural and functional studies on mutant Mbs, as well as molecular dynamics simulations of ligand recombination to wild-type Mb, suggested that the ligand binding process can be separated into several distinct stages.

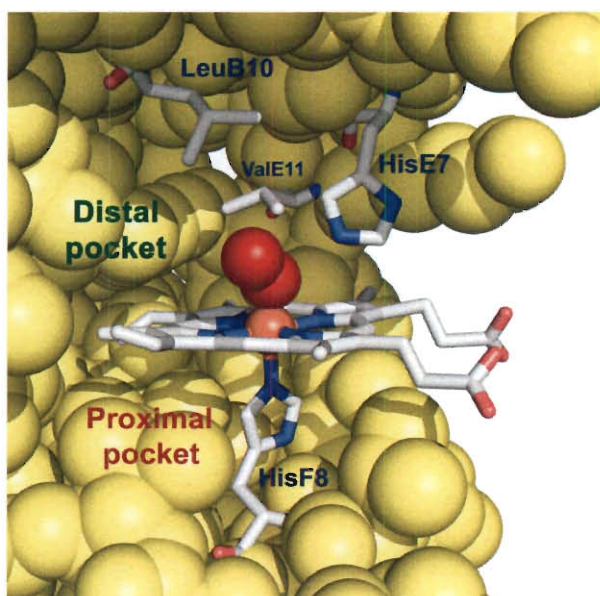


Figure 1.2. Heme pocket of HbO₂ subunit (β). The key residues and heme are shown in sticks, colored as in Fig. 1.1. Bound oxygen is shown as red spheres; Fe – as orange sphere. The atoms of other amino acids, surrounding the active site, are represented as space-filling yellow spheres. The part of the distal pocket was removed to show the internal structure. Created from 2DN1 [2].

First, the water molecule that resides in the distal pocket of unliganded Mb must dissociate before the ligand can enter the distal pocket. This stage is regulated by hydrogen bonding between the water and His(E7). The ligand association rate constant is diminished approximately 10-fold due to the energy required to break this H-bond. After the water dissociation, the ligand is thought to enter the active site through a channel, created by outward rotation of the distal His, and is captured in the apolar cavity circumscribed by Leu(B10), Val(E11), Ile(G8) and Ile(G12), which comprise a non-covalent binding site. Then, the ligand binds internally to iron of the heme. The process of bond formation is inhibited by direct steric hindrance from His(E7) and Val(E11). Finally, bound ligand is stabilized by hydrogen bonding to His(E7) [12]. Prior to this thesis, the applicability of the Mb model to α and β Hb subunits had not been verified experimentally. The biggest controversy involved the pathways for ligand migration into

the active site and electrostatic stabilization of bound oxygen by the distal His(E7) residue.

The proximal pocket is formed by the completely conserved His(F8), which coordinates directly to the heme iron atom, and the residues that surround the imidazole side chain. The functional importance of the proximal His is twofold. First, it ensures tight binding of heme cofactor to the globin part of Hb [3, 13, 14]. Second, its geometry and coordination strength regulates Fe reactivity, and its motion towards the plane of the porphyrin ring governs the T \leftrightarrow R quaternary state transitions of the Hb tetramer [3, 14-18]. After ligand dissociation, the iron atom becomes high spin, increases its diameter, and moves out of the heme plane towards the proximal pocket producing a domed heme configuration, which is much less reactive to ligands than the planar, lower spin configuration. These heme pocket rearrangements are translated through the His(F8) to the F helix and promote the formation of new inter-subunit contacts, which eventually lead to the R \rightarrow T conformational change. In the T-state, the transition of the Fe back into the plane of heme is restricted due to the strain imposed by the F-helix which pulls proximal His residue away from the heme plane, causing reduced reactivity of the deoxy-heme [1, 3, 14, 19].

1.3. Ligand migration in globins.

Pathways for ligand migration in Mb. The analyses of the first crystal structures of Mb and Hb revealed no direct tunnels connecting solvent with the heme pocket. Perutz and Matthews proposed that outward rotation of the distal His could create a channel allowing ligands to freely diffuse between the solvent and the distal pocket [13]. This

hypothesis of a His(E7) gate was confirmed in the first mutagenesis experiments on sperm whale Mb, in which His(E7) was replaced with Gly and ligand binding parameters for the mutants were measured [20]. For both O₂ and CO, the bimolecular rate constants increased dramatically upon mutation. The argument against the described experiment was that creating a hole in the distal pocket always results in accelerated ligand entry and does not find the actual port of entry.

In 1994, Boxer and Huang applied a different approach to search for ligand pathways. They created a library of random point mutants of sperm whale Mb and measured ligand recombination parameters [21]. Their results suggested that mutations at some sites located far from the heme pocket increase the bimolecular rate constants of CO and O₂ binding, supporting the idea of multiple ligand migration pathways. However, it is worth noting that they measured ligand binding parameters using laser flash photolysis of *E.coli* lysates, in which both misfolded protein and free heme could contribute to accelerated recombination. In addition, a number of the reported mutants were the replacements with Pro and Gly residues, which may also disrupt proper folding of the protein.

In 2001, Scott *et al.* reported a study of 90 sperm whale Mb point mutants with substitutions at 27 different locations [22]. The authors replaced the native amino acids with Trp or Ala and used laser flash photolysis to determine the rates of ligand entry and escape from the protein. The mutated sites, which showed the largest effects are highlighted in the diagram provided in Fig. 1.3 [22]. The main conclusion is that only residues surrounding E7 gate and the distal pocket demonstrated significant effects (i.e. residues 29, 43, 46, 64, 68, etc.), contradicting the results of Huang and Boxer. Some of

the mutants with substitutions on the periphery of the globin molecule that were reported by Huang and Boxer [21] to have marked effects on ligand migration were re-examined by Scott *et al.* [22], revealed no significant deviation from the wild-type parameters (i.e. A71F, F138A, A144V), and appear to have been false positives in the random mutagenesis screen.

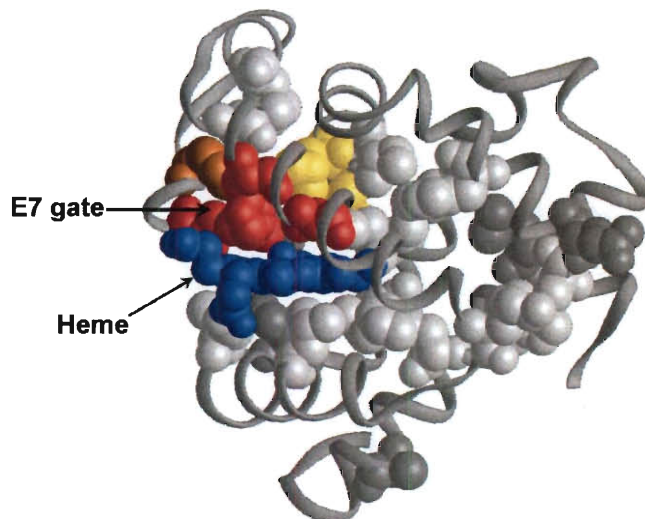


Figure 1.3. Maps of ligand migration pathways in sperm whale Mb. The effect of mutagenesis on rates of ligand entry and escape from the binding site of Mb. The protein globule is shown as grey ribbons, blue spheres represent heme, the sites of mutation are depicted as spheres of different color, which depends on the observed effect with red corresponding to the largest effect, and grey – no effect. Modified from [22].

Finding gas migration pathways is not a simple task, even with high-resolution electron density maps, because the crystal structures represent the average static protein configuration corresponding to its minimum potential energy. For ligands to bind, thermal fluctuations of the amino acid side chains must create cavities and tunnels in the structure of the protein, which are dynamic, transient, and are not visualized in the crystal structure. The gas molecules are small and apolar and may utilize these temporary channels to find their way into the protein active site. Molecular dynamic simulation

approaches allow theoretical examination of ligand migration in proteins and take into account thermal motions.

The first attempt to computationally describe ligand trajectories within Mb was published by Case and Karplus [23]. They simulated the dynamics of Mb molecule starting with the ligand placed in the heme pocket just above the Fe atom and followed its trajectory for several picoseconds. The His gate pathway was identified and seemed to involve His(E7), Thr(E10) and Val(E11) residues, as well as a secondary pathway, created by fluctuations of the side chains of Leu(E4) and Phe(B14) amino acid side chains. The main drawback of their approach was that the computations could only be done on picosecond timescales. Ligand escape to the solvent happens experimentally in hundreds of nanoseconds [22]. In the late 1970s and early 1980s, running multiple simulations for 100 ns using the computer power available at that time was not possible. Introduction of Locally Enhanced Sampling seemed to improve the situation [24]. The new idea was that multiple copies of the ligand (60 CO molecules) are placed into the active site of the protein and their simultaneous migration towards the solvent is followed during MD simulations. In addition, to shorten the time of simulation and accelerate ligand escape, the ligands were heated up to 10,000 K, whereas the protein was kept at room temperature (300 K). Again, traditional His(E7) pathway and alternative trajectories were discovered.

Another approach is called Implicit Ligand Sampling [25-27]. It is based on the idea that ligands migrate inside the protein via temporarily interconnecting channels created by thermal fluctuations of amino acid side chains. By calculating the free energy of placing the ligand molecule into the protein structure (or *potential mean force*) during

MD simulations and connecting areas with the lowest magnitudes, Cohen *et al.* [25] attempted to trace potential ligand migration trajectories. The major distinction of ILS technique from other computational methods is that only MD simulations of the protein molecule are necessary and movement of the ligand is not calculated explicitly. Again, the configuration of cavities with low potential mean force for ligand occupancies suggested multiple routes for ligand diffusion into and out of Mb. Qualitatively, each of the described computational approaches was able to predict the His(E7) gate as one of many escape pathways; however, none of these techniques provide a quantitative description of the process. First, even the longest simulations represent only ~10 ns runs, which are still an order of magnitude less than experimentally measured half-time for ligand escape. In addition, none of the systems were in equilibrium, because the ligands, which managed to escape did not return on the timescales of simulation, and thus, equilibrium approximations assumed during calculations are not completely appropriate [28].

So far, the most comprehensive investigation of gas migration in Mb was reported by Ruscio *et al.* [29]. The authors accumulated 68 trajectories, each for 90 ns. Moreover, ligand entry events into the protein from the solvent were observed, validating to a certain extent the equilibrium approximations applied to the calculations. The E7 pathway was found to be a major port of entry and escape with 5 entries and 7 escapes occurring through this gate during simulations. However, 8 alternative routes were also reported.

In general, there is a reasonable correspondence between different types of computational approaches with regard to ligand diffusion pathways. In nearly every

simulation, a very small number of ligands are observed to leave the protein through the E7 gate, and a much larger number move through internal Xe cavities. These cavities are small internal packing defects, which have been found to harbor Xe atoms when Mb is crystallized under several atmospheres of Xe gas [30, 31]. The initial diffusion pathways inside the globin molecule, especially the early events immediately after photodissociation, are consistently predicted.

The major disagreements between computational and experimental results are the actual location of the ports of ligand entry and escape. According to most structural and functional investigations of ligand binding to Mb, at least 75% of ligands enter and escape from the protein through distal His gate [22, 32]. Interestingly, in a recent paper Tetreau *et al.* [33] reported studies of O₂ and CO recombination to Mb-Xe complexes in 79% glycerol at varying temperatures. They suggested that at room temperature the escape occurs exclusively through the E7 gate, whereas at ~250K roughly 50% of CO molecules escape to the solvent directly from Xe1 cavity. This paper represents the first solid experimental confirmation of the existence of alternative ligand diffusion pathways in Mb. However, the fact that Xe1 portal was only identified at low temperatures and high glycerol concentrations suggests that non-E7 gate routes based on the results of molecular dynamics simulations may have little physiological significance.

Pathways for ligand movement in human HbA subunits. The structures of the active sites and the E7 channels in Mb and the subunits of human HbA are very similar, and thus analogous mechanisms for ligand binding are inferred. Until very recently, there were little experimental and computational data regarding the pathways for ligand migration into HbA. Mouawad *et al.* [34] observed the formation of transient cavities in

the α and β subunits of human HbA during simulations of the T to R conformational change. The authors suggested that ligands sequentially move from the existing cavity into the newly formed spaces in the protein interior and then diffuse through the globin matrix to the solvent phase. Sottini *et al.* [35] used molecular modeling approaches to find potential Xe binding cavities in human HbA and suggested that ligands could use these apolar voids as pathways to enter or escape the active site. Finally, Savino *et al.* [36] reported crystal structures of wild-type and Tyr(B10)/Gln(E7) deoxyHbAs with Xe atoms partially occupying the sites identified in molecular modeling experiments. Based on these structures, multiple routes passing through the identified Xe sites were proposed for HbA.

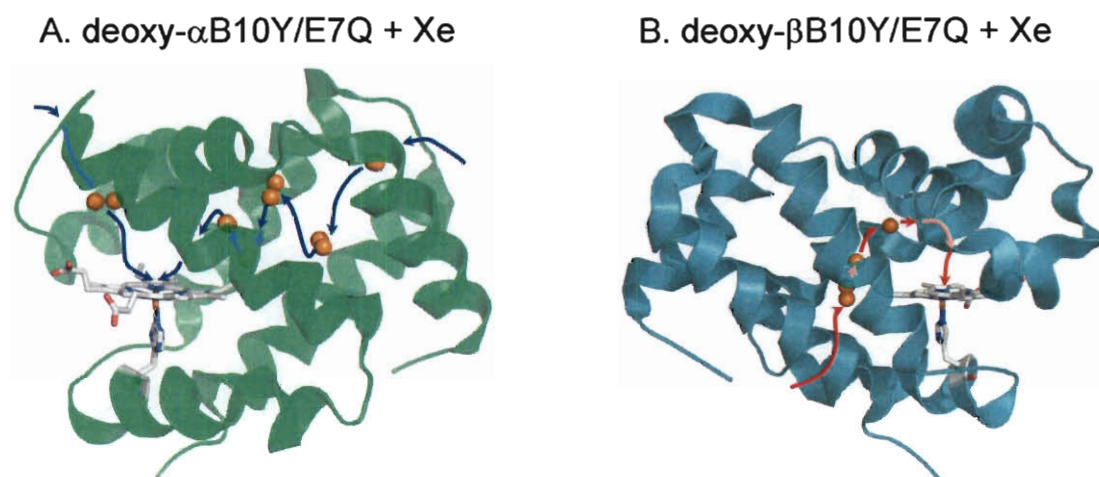


Figure 1.4. Crystal structures of deoxy- α (B10Y/E7Q) (A) and deoxy- β (B10Y/E7Q) (B) subunits with bound Xe. α helices are shown as ribbons, heme and proximal His – in sticks (color code: carbon, white; oxygen, red; nitrogen, blue; iron, orange), Xe atoms are shown as orange spheres. Blue and red arrows represent proposed ligand migration pathways. The models were created from 2W72 [36].

If only the theoretical and structural literature is examined, multiple internal pathways appear to occur for ligand entry into HbA, and the heme pocket appears to be

accessible from virtually any direction within the globin matrices. Thus, one motivation of this thesis was to determine experimentally whether the E7 pathway is the dominant route for ligand entry and escape in human HbA and whether the theoretical work was correct in suggesting multiple pathways.

1.4. NO scavenging by oxyhemoglobins and the hypertensive effect of Hb-based blood substitutes.

Nitric oxide (NO), once called endothelium derived relaxing factor (EDRF), and NO-generating compounds perform a major role in signaling relaxation of vascular and other smooth muscles. Vascular relaxation starts in the endothelial cell layer, where nitric oxide synthase (eNOS) produces NO from L-arginine. NO molecules diffuse into smooth muscle cells where they bind to the heme iron of soluble guanylyl cyclase (sGC), which catalyzes the formation of cGMP. cGMP activates cGMP-dependent protein kinase (cGK). First, cGK reduces the hydrolysis of phosphatidylinositol 4,5-bisphosphate by phospholipase C (PLC). Normally, this reaction results in the formation of inositol-1,4,5-trisphosphate (IP₃), which triggers Ca²⁺ release from intracellular stores. The inhibiting effect is achieved either via direct phosphorylation of PLC by cGK, which prevents the activation of PLC by G-protein subunits, or through the inactivation of G-protein subunits by phosphorylating the regulator of G-protein signaling-2 (RGS-2). Also, cGK diminishes Ca²⁺ release into cytoplasm by interfering with the activity of the IP₃ receptor Ca²⁺ channel of endoplasmic reticulum. Second, cGK phosphorylates BK_{Ca} ion channels, resulting in hyperpolarization of cell membrane and subsequent closure of Ca²⁺ channels, which reduces Ca²⁺ influx. Finally, phosphorylation of myosin light chain phosphatase

(MLCP) by cGK prevents inhibition of the former by other kinases (Rho-kinase, MYPT1 kinase) and promotes deactivation of myosin ATPase. As a result, the cascade of reactions that follows NO binding to sGC ultimately leads to decrease in vascular tone ([37] and references therein).

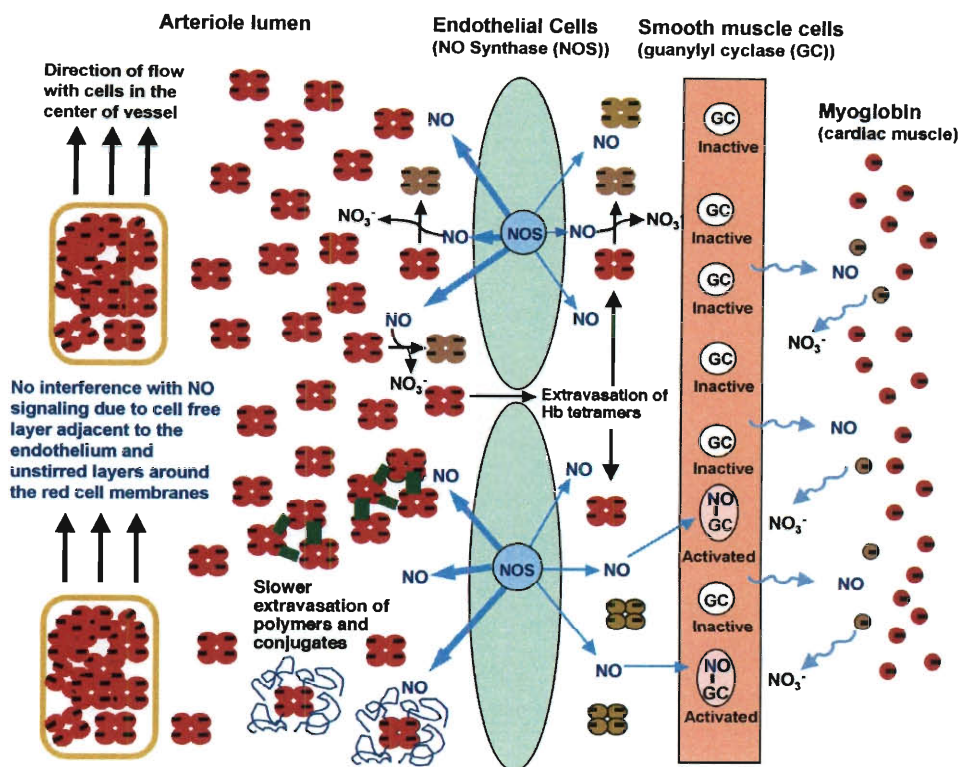


Figure 1.5. Scheme for NO signaling in the endothelium, excess NO detoxification by Mb and effects of NO scavenging by extracellular Hb. Generated by endothelial cells, NO binds to sGC in smooth muscle cells and triggers vasodilation. Acellular oxyHb scavenges NO and disrupts the signaling pathway. Extravasation of Hb tetramers into subluminal space is thought to be the major mechanism of quick NO depletion, thus, one approach to prevent pressure effect associated with infusions of acellular Hb solutions is to increase the size and/or hydrodynamic radius of Hb by polymerization and conjugation with organic polymers. NO which escapes to tissues represents a threat to enzymes involved in cellular respiration, therefore, NO dioxygenation by MbO₂ is a physiologically important mechanism of defense against NO toxicity. Modified from [5].

When hemoglobin is packed in red blood cells, there is no interference with the NO signaling system, because the large erythrocytes tend to stream in the center of the blood vessel creating cell free layers adjacent to endothelium. Additionally, unstirred

plasma layers surround the erythrocyte membrane. Thus, interaction between NO and HbA is limited by the rate of NO diffusion from endothelial cell to the erythrocyte. However, extracellular Hb molecules may approach very close the endothelial cell layer and skew the established NO gradient. Moreover, rapid penetration of HbO₂ tetramers into the lumen between endothelial cells and smooth muscle tissue completely destroys NO flux into smooth muscle cells (Fig. 1.5) [5, 7, 38].

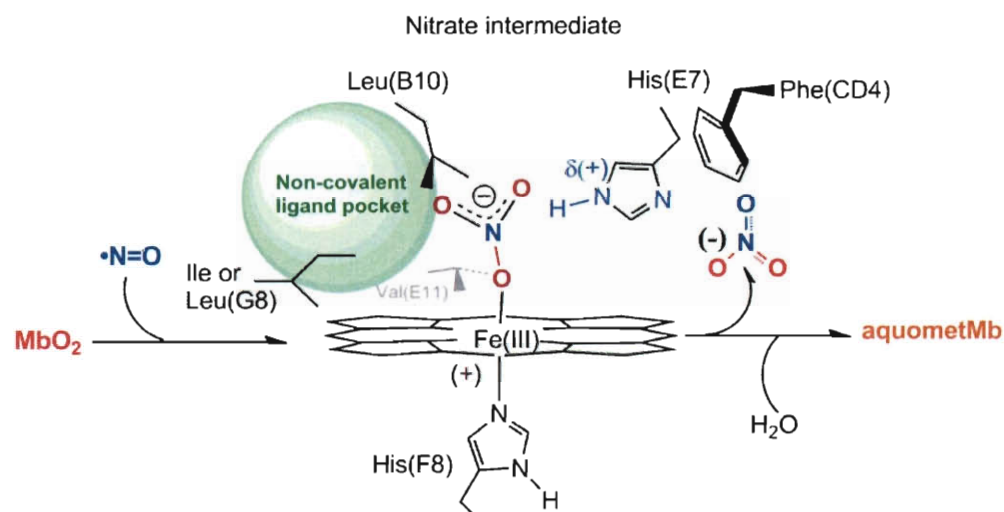


Figure 1.6. Schematic representation of NO-induced oxidation reaction by MbO₂ or HbO₂ at neutral pH. NO is captured in the back of the distal pocket (non-covalent ligand pocket), reacts with bound dioxygen to form a high spin nitrate intermediate; nitrate leaves the distal pocket and water binds to Fe(III) heme producing aquometMb.

The reaction of NO-induced oxidation by MbO₂ and HbO₂ was first observed over 100 years ago and the stoichiometry defined in 1981 [4], but little mechanistic work was done until 1996 [6]. Since then, the reaction has been studied extensively, and the following mechanism has been proposed. NO is a radical with an unpaired electron in its outermost bonding orbital and is highly reactive with other paramagnetic molecules and atoms including iron and O₂. NO enters the distal pocket of oxygenated myoglobin (or hemoglobin) and migrates to the non-covalent binding site in the distal portion of the

heme pocket. Dioxygen bound to heme iron has superoxide anion radical character. In solution, $O_2^{\bullet-}$ reacts with NO in an ultrafast, diffusion control process to form peroxynitrite. Similarly, NO in MbO₂ (HbO₂) is proposed to react immediately with bound dioxygen to generate a Fe(III)-OONO complex. This intermediate isomerizes very rapidly to generate a Fe³⁺-nitrate intermediate, which then dissociates irreversibly. The resultant oxidized heme binds a water molecule and forms aquometMb (Fig. 1.6) [5, 38]. At neutral pH, isomerization of peroxynitrite and nitrite dissociation are so fast that it is impossible to detect any intermediate, and the rate limiting step is the entry of NO into the heme pocket. Increasing pH slows down nitrate dissociation and augments the spectral differences between high spin nitrate complexes and low spin hydroxymetMb (metHb) complexes [38-40]. The utility of NO scavenging by MbO₂ is obvious and vital. NO in submicromolar concentrations can reversibly bind to cytochrome c oxidase, the terminal enzyme in the mitochondrial electron transport chain, and inhibit cellular respiration [41, 42]. Moreover, NO is extremely reactive with iron-sulfur clusters and rapidly inactivates enzymes requiring these cofactors for function. One example of such a protein is cis-aconitase, an enzyme catalyzing isomerization of citrate into isocitrate in Krebs cycle. The presence of Mb in large quantities (0.5 to 1 mM) in cells of skeletal and cardiac muscles prevents inhibition of the TCA cycle and respiration due to rapid NO detoxification by dioxygenation [41, 42].

All first generation blood substitute prototypes based on extracellular Hb cause an elevation in mean arterial blood pressure immediately after administration [43]. These extracellular hemoglobins also caused decreases in gastrointestinal motility and, in some

cases, muscle lesions adjacent to capillary beds in heart tissue [44, 45]. Three theories were proposed to explain these side effects.

Alayash and coworkers [46] initially suggested that all these effects were due to oxidative stress triggered by extracellular Hb autooxidation, H_2O_2 production and hemin loss. However, this theory is unlikely to be correct for the initial vascular effects, because the blood pressure increase is observed quickly (minutes) after infusion of the Hb solution, whereas, autooxidation and hemin loss happen on time scales measured in hours.

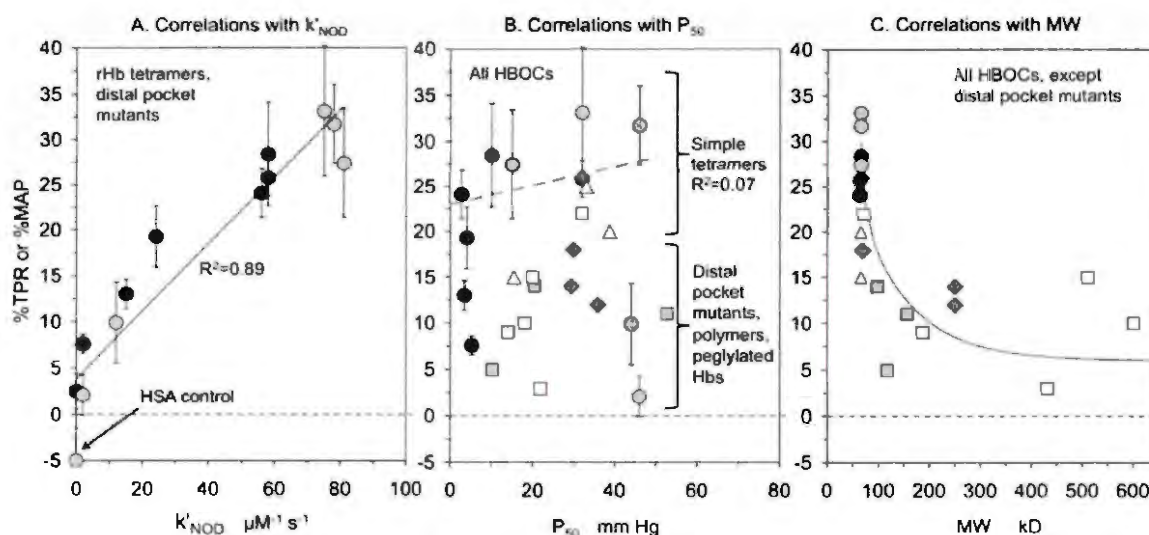


Figure 1.7. The dependence of the hypertensive effect on (A) the rate of NO scavenging (k'_{NOD}), (B) oxygen affinity of Hb (P_{50}) and (C) the size of Hb molecules (molecular weight, MW). Gray circles, %TRP (TRP = MAP/cardiac output) for 3 hemoglobins (rHb1.1, rHb1.1 Providence and rHb Providence) carrying allosteric mutations to vary P_{50} but having similar k'_{NOD} , and 2 rHbs with distal pocket mutations to reduce NO scavenging (rHb 2821, rHb 3011) [43]; black circles, %MAP for 3 rHbs with allosteric mutations to vary P_{50} (rHb 0.1, rHb 1.1, rHb Bethesda) and distal pocket mutant rHbs with low k'_{NOD} (rHb 3001, rHb 3002, rHb 3004) [7], circles for $k'_{NOD} = 0$ represent %TRP and %MAP for human serum albumin controls; open squares, %MAP for various polymerized Hb (PEG-decorated Hb, hydroxyethylstarch-conjugated XLHb, XLHb) and PEG-decorated Hb vesicles; gray squares, %MAP for hemoglobins conjugated with PEG, POE and poly-O-raffinose [47]; open triangles, chemically cross-linked Hb tetramers [47]; closed diamonds, %MAP for glutaraldehyde cross-linked Hb [48]. All experiments were conducted on rats with circles, diamonds and open squares representing 10% top load experiments, and gray squares and open triangles representing 50% isovolemic exchange.

Winslow and coworkers [47, 49, 50] attempted to explain the blood pressure effect by excessive oxygen transport by the more efficient extracellular HBOCs. They claimed that premature O₂ delivery triggers auto-regulatory responses which cause capillary constriction and the corresponding elevation of vascular resistance to blood flow. However, this idea also appears to be inconsistent with two key experimental observations. First, in many animal experiments, the amount of extracellular Hb added was only 10% and ~90% of the oxygen transport was carried out by native erythrocytes. Under these conditions, the amount of O₂ transport in the controls with serum albumin addition is approximately the same as that when the hemoglobin solution is added. Second, there is no obvious correlation between P₅₀ of the protein and blood pressure elevation after infusion of the hemoglobin solution (Fig. 1.7 B). HBOCs with high O₂ affinity do not release oxygen in capillaries, but still cause a marked increase in blood pressure even though no O₂ can be delivered.

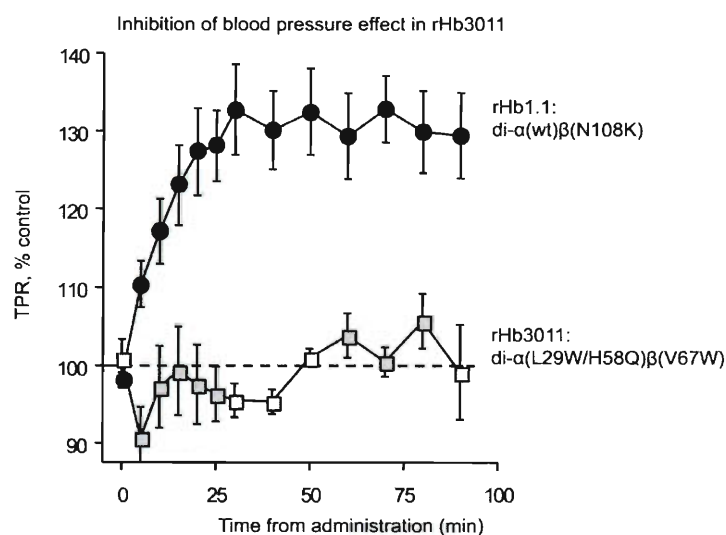


Figure 1.8. Hypertensive effect after administration of recombinant Hbs. k'_{NOD} values for rHb1.1 and rHb3011 are $70 \mu\text{M}^{-1}\text{s}^{-1}$ and $3 \mu\text{M}^{-1}\text{s}^{-1}$, respectively. Changes in Total Peripheral Resistance (TPR) are expressed as percentage above HSA control in 10% top load experiments. Presented data were taken from [43].

The most reasonable mechanistic explanation for the hypertensive effect of extracellular Hb-based blood substitutes is their high rate of NO dioxygenation, which removes free NO from the endothelial/smooth muscle signaling pathway. Proof of this concept was obtained by constructing mutants with different NO dioxygenation rate constants, k'_{NOD} , and then correlating the dependence of mean arterial pressure on k'_{NOD} (Fig. 1.7 A). The most effective Hb mutant, rHb3011, contained Trp at B10 position and Gln at E7 position in α subunits and Trp at E11 in β subunits. This combination of mutations reduced the rate of NO dioxygenation ~20-fold and inhibited the elevation of arterial blood pressure after infusion (Fig. 1.8) [5, 43]. Unfortunately, rHb3011 markedly compromises apoglobin stability and causes low expression yields, which made it difficult to use as a Hb-based blood substitute prototype.

The hypertensive effect of HBOCs was also prevented by precluding close approach of extracellular Hb molecules to the sites of NO synthesis and action, including endothelial and smooth muscle cell layers, and space between them. This effect was achieved by increasing the effective molecular size of the HBOCs (see Fig. 1.7 A, C) via polymerization of the Hb molecules and conjugation with polyethyleneglycols (PEGs). The larger polyHb complexes diffuse into the endothelium more slowly and pegylation causes the HBOC to be excluded from the endothelial surface layer. Both of these effects reduce NO scavenging and interference with signaling (see Fig. 1.5) [5, 51, 52].

1.5. Significance and specific aims.

The development of effective and safe oxygen delivery chemotherapeutics is an important world health priority. Research in the field of blood substitute production is

directed to design synthetic biomolecules capable of efficient oxygen transport without causing clinical side effects. Progress in this area would eliminate current problems in transfusion medicine caused by limited availability of donated blood and high risk of infectious disease transmission. Extracellular hemoglobin is currently the most potent oxygen carrier for use as a blood substitute prototype. Structural factors regulating ligand binding to Hb must be studied and understood thoroughly in order to optimize the O₂ transport properties of Hb-based oxygen carriers (HBOCs) and to eliminate possible side effects caused by administration of these oxygen therapeutics.

Previous investigations of the effects of distal pocket mutations on ligand binding to Mb and Hb clearly show that stereochemical hindrance and electrostatic stabilization of bound ligands by His(E7) regulate the rates and affinities of oxygen binding to both Mb and the α chain of human Hb [20]. The role of His(E7) in ligand entry and stabilization in human β -globin is still under debate.

Numerous experiments support the hypothesis that the His(E7) is the major pathway for ligand entry and escape in sperm whale Mb [22, 32, 53]. In contrast, molecular dynamic simulations always identify multiple ligand migration routes, which often involve Xe cavities as transient stations for diffusing ligands [28]. There is little experimental or theoretical data concerning ligand migration in α and β subunits of human HbA available, and thus ligand pathways in Hb are even more controversial [34-36].

Extravasation of extracellular Hb and rapid scavenging of NO interfere with NO-signaling and appear to be the main causes of the increase in mean arterial pressure by the initial HBOC products [7]. Using site-directed mutagenesis, the rate of NO scavenging

was greatly decreased by introducing space-filling Trp substitutions that reduce the size of the distal pocket in both subunits of Hb. Unfortunately, the resultant mutants express poorly and are unstable.

In the following chapters of this thesis, I have addressed each of the four issues described above. First, I will show unambiguously that His(E7) regulates the rates of ligand binding and stabilizes bound O₂ in both subunits of human HbA by measuring ligand binding parameters and FTIR spectra of Gly, Leu, Phe and Trp(E7) mutants, and by solving the crystal structures of α and β Leu(E7) mutants to support my interpretations of the kinetic results. Second, I will demonstrate that the pathway for ligand entry into HbA is created by outward rotation of E7 side chain by determining the rates of opening and closing of the E7 gate and the effects of the total blockade of the E7 channel on ligand entry into the distal pockets of α and β Trp(E7) subunits. Third, I will establish that in human HbA alternative ligand migration pathways involving Xe binding sites are not physiologically significant by measuring ligand entry and escape parameters for wild-type α and β subunit under high xenon pressures. Fourth, I have attempted to design new Hb mutants with reduced NO scavenging activity, optimized O₂ affinity and improved apoglobin stability using combinations of space-filling mutations in the active sites of α and β subunits of HbA, Gly crosslinking of the α subunits, and replacements located at the subunit interfaces to alter O₂ affinity and globin stability.

CHAPTER 2: MATERIALS AND METHODS

2.1. Mutagenesis, expression and purification of HbA.

The plasmid system and bacterial strain used for both mutagenesis and expression of recombinant Hbs were developed at Somatogen, Inc. [54, 55]. The *E. coli* strain SGE1661 represents a variant of the *E. coli* strain JM109 that allows a more rapid uptake of extracellular heme. The plasmid system pSGE1702 is composed of 1 copy of α and β globin genes positioned in tandem downstream of the inducible *tac* promoter. In each globin gene the N-terminal Val residue is replaced with Met for ease of expression in *E. coli*, producing a double mutant, $\alpha(V1M)/\beta(V1M)$, which will be referred to as wild-type rHb and is not essentially different from native human HbA with respect to R-state ligand binding characteristics and overall structure [56-58]. However, it shows slightly weaker cooperativity and sensitivity towards allosteric effectors, such as IHP and protons [54], in comparison to native human HbA.

Some of the mutants that were used in crystallization studies were expressed using the pHE2 plasmid [59, 60]. pHE2 also contains α -globin and β -globin genes placed in tandem under *tac* promoter. In addition, the gene encoding Met-aminopeptidase (MAP) was incorporated into the expression plasmid to allow posttranslational cleavage of the N-terminal Met residue of the newly synthesized globin polypeptides. Overexpression of the MAP gene results in 99% removal of N-terminal Met from α -subunits and 95% from β -subunits. The Hb fraction containing β -subunits with uncleaved N-terminal Met residues can be separated from the main fraction of HbA during the last chromatographic step of Hb isolation (see below). The *E.coli* strain JM109 was used for mutagenesis and expression of hemoglobin using the pHE2 system.

All amino acid substitutions were made using Stratagene PCR-based "QuikChange™ Side-Directed Mutagenesis" kit (Stratagene, La Jolla, CA, USA). This procedure requires the design of specific complementary mutagenic primers that span the region of substitution and have the necessary mutation. After temperature cycling, the reaction mixture was digested with Dpn I to get rid of methylated parental DNA and was transformed into competent cells. Transformed cells were placed on agar plates containing 15 µg/ml of tetracycline (for pSGE1702) or 100 µg/ml ampicillin (for pHE2) and grown overnight at 37° C. Antibiotic resistance selection was achieved due to the presence of antibiotic resistance genes in the plasmids. Distinct *E. coli* colonies were inoculated into 4 ml of LB with appropriate antibiotic and grown overnight at 37° C. After plasmids were isolated and their sequences confirmed, the corresponding cell suspensions were diluted with glycerol to achieve ~60% final concentration of cryoprotectant and stored at -80° C.

Protein was expressed in a Biostat C20 bioreactor (B Braun Biotech International, Melsungen, Germany). Cells were grown in 15 L DM media [55], initially at 37° C, pH 7. Steering speed and airflow were controlled automatically to keep the oxygen level at ~60%. The glucose (40% w/v solution) feeding profile was the following: 40 ml/h for 0-0.5 OD₆₀₀; 60 ml/h for 0.5-1 OD₆₀₀; 100 ml/h for 1-1.6 OD₆₀₀. After OD₆₀₀ reached 1.6, the temperature was decreased to 28° C and protein expression was induced by IPTG (up to final concentration 0.05 g/L). Excess heme was added throughout the expression phase at a feeding rate of ~100 ml/h (1 g/L solution), and glucose was supplied at ~50 ml/h. The expression phase was maintained for 9 to 12 hours, and then the cells were harvested.

The final suspension was bubbled with CO, pelleted by centrifugation, and frozen for storage. A typical growth profile of recombinant Hb is presented in Fig. 2.1.

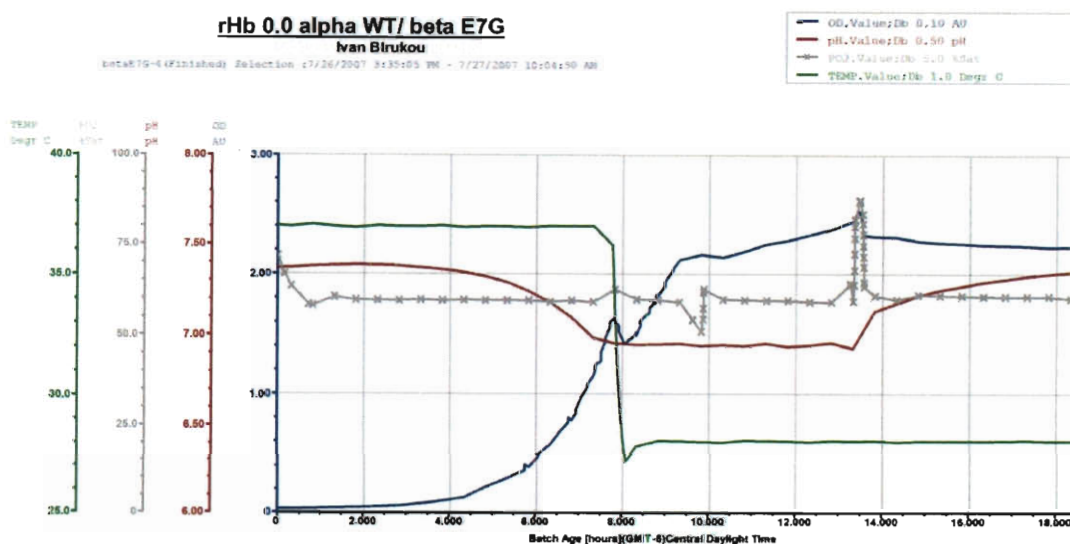


Figure 2.1. rHb α (WT) β (Gly(E7)) fermentor growth profile. Starting parameters for fermentor growth were 37° C, pO₂ ~ 60%, pH 7. Steering speed and airflow are controlled automatically to keep oxygen level at proper value. The concentration of glucose is increasing from 2% to 25%. After OD₆₀₀ reaches 1.6 the temperature is decreased to 28° C and protein synthesis is induced at this point by injecting IPTG. Excess heme is being added to maintain the concentration at 25%. Expression phase lasts 9 to 12 hours.

To isolate protein, the frozen cell paste was thawed and resuspended in buffer containing 40 mM Tris/HCl, pH 8, equilibrated with 1 atm CO, following the proportion of 1 g of cells per 3 ml of buffer. The “breaking” buffer contained 1 mM benzamidine, which serves as a protease inhibitor. Lysozyme solution was also added to lyse cell walls (1mg of enzyme per 1 g of cells). The mixture was allowed to stir for 15 min, and then deoxyribonuclease I, MgCl₂ and MnCl₂ were added to give final concentrations of 30 μ g/ml, 10 mM and 1 mM, respectively. The resultant suspension was filtered through cheesecloth and passed through a cell disruptor (Avestin, Inc., Canada) 2-3 times. Concentrated Zn acetate solution was added to the final mixture to yield 2 mM of [Zn²⁺]

and pH was adjusted to 8. To remove cell pellets, the suspension was centrifuged for up to 2 h at ~22,000 g using Beckman J-21C (Beckman Coulter, Inc., Brea, CA) centrifuge and JA-14 rotor. The clarified solution was applied to a Hi-Trap Chelating Sepharose (Pharmacia) column preloaded with Zn^{2+} . The column was washed by sequential passage of: (a) 20 mM Tris/HCl, 500 mM NaCl, pH 8.5 (3 column volumes (CV)); (b) 200 mM Tris/HCl, pH8.5 (2CV); (c) 20 mM Tris/HCl, pH8.5 (3CV). Hemoglobin was eluted with 20 mM Tris/HCl, 15 mM EDTA, pH 8.5 buffer. The eluant, representing ~ 85% recombinant CO-hemoglobin (rHbCO), was concentrated to ~2 mM in heme using an Amicon 8200 ultra-filtration unit (Millipore, Billerica, MA) with a 16,000 Da cutoff Millipore membrane. In preparation for the next chromatographic step, the protein was loaded on a Sephadex G-25 (Pharmacia) gel filtration column pre-equilibrated with 20 mM Tris/HCl, pH 8.3. Hb fractions were collected, concentrated as described above and loaded on a Q-Sepharose (Pharmacia) column equilibrated with 20 mM Tris/HCl, pH8.3. The column was washed with several column volumes of equilibration buffer and the protein was eluted using a 0-170 mM NaCl gradient (Fig. 2.2 A). A Source 15 S (Pharmacia) cation exchange column equilibrated with 10 mM NaPi, pH 6.8 was used in the last step of chromatographic isolation of Hb. The protein was loaded on the column, washed with several column volumes of equilibration buffer and eluted by a linear gradient of equilibration buffer versus 20 mM NaPi, pH 8.3 (Fig. 2.2 B). All procedures were carried out at 4° C, using ice-cold, CO-purged buffers. The protein was always kept under a CO atmosphere.

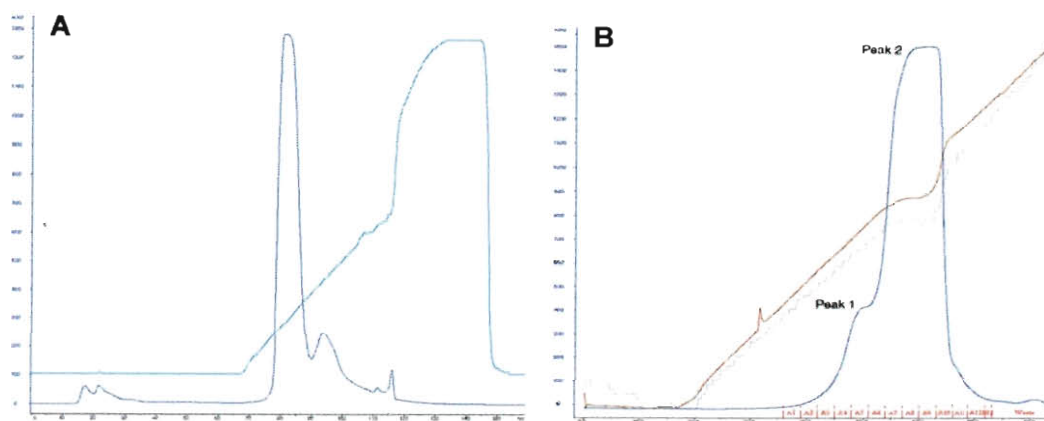


Figure 2.2. Chromatographic purification of recombinant HbA. (A) Elution profile of Hb α Leu(E7) β WT from Source 15 Q column (blue trace represents OD at 280 nm, cyan – conductivity). (B) Elution profile of Hb α Leu(E7) β WT from Source 15 S column (blue trace represents OD at 280 nm, brown – conductivity of the eluant, and gray – pH). Peak 1 represents Hb tetramers containing β -chains with uncleaved N-terminal Met residue. Peak 2 represents recombinant Hb with completely cleaved N-terminal Met's in both subunits.

2.2. Isolation of individual α and β subunits of HbA.

The procedure for chain preparation was modified from that initially developed by Parkhurst *et al.* [61]. Tetrameric Hb was buffer-exchanged against 0.1 M KPi, pH 6 and concentrated to \sim 1mM in heme. This sample was mixed with *p*-mercuribenzoate (PMB) solution in a ratio of 10 mg PMB to 220 mg Hb, adjusted to pH 6, and saturated with CO. The mixture was left at 4° C overnight. Next day, any precipitated protein was removed by centrifugation, buffer was exchanged with 10 mM NaPi, pH 8, and the PMB-bound chains were loaded on a DEAE-cellulose (Whatman) column equilibrated with 10 mM NaPi, pH 8. α subunits pass through the column without binding under these conditions; residual tetrameric rHb was washed out with 20 mM NaPi, pH 7.5, and then β chains were eluted with 0.1 M NaPi, pH 7. To remove bound PMB, the hemoglobin chains were buffer-exchanged against 0.1 M Tris/HCl, 0.1 M NaCl, 1 mM EDTA, pH

8.5, concentrated to ~ 0.4 mM, and dithiotreitol (DTT) was added to achieve 4 mM. This mixture was incubated at 4° C for 30 min.

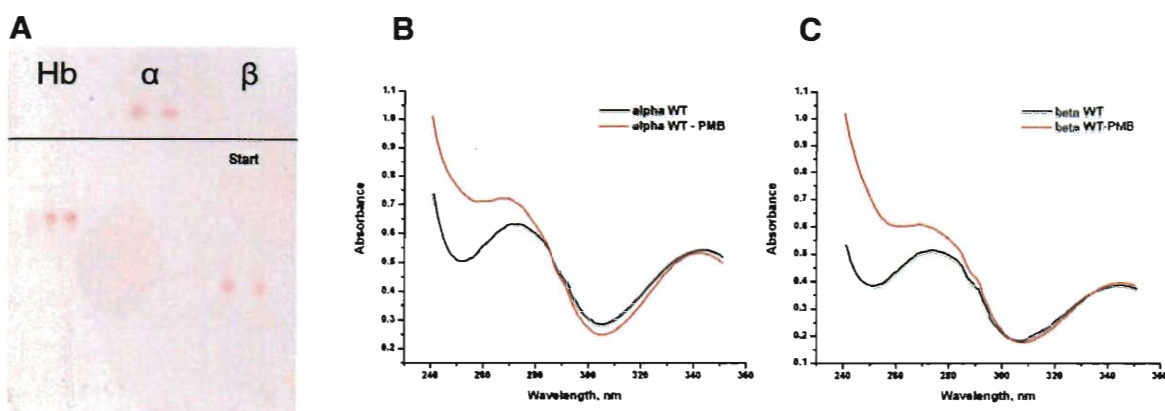


Figure 2.3. **Determination of the quality of isolated chains.** (A) Cellulose acetate electrophoregram of isolated α and β chains and Hb tetramers shows no visible contamination of Hb subunits with Hb tetramers. (B) and (C) Optical spectra of α and β subunits before and after PMB removal procedure, respectively, demonstrate the absence of bound PMB after incubation with dithiothreitol.

Regenerated chains were stripped of DTT-PMB by passage through a Sephadex G-25 column, equilibrated with 0.1 M Tris/HCl, 0.1 M NaCl, 1 mM EDTA, pH 8.5 buffer at 0.5 ml/min. Complete PMB removal often requires 3 rounds of incubation in DTT with buffer exchange after each round. The extent of removal was examined by evaluation of bound PMB extent spectroscopically (Fig. 2.3 B and C) and by PMB titration [62]. The purity of isolated Hb subunits was assessed by cellulose-acetate electrophoresis (Helena Laboratories, Beaumont, TX; Fig. 2.3 A).

2.3. Measurements of bimolecular O₂, CO and NO binding to hybrid Hb tetramers and isolated subunits.

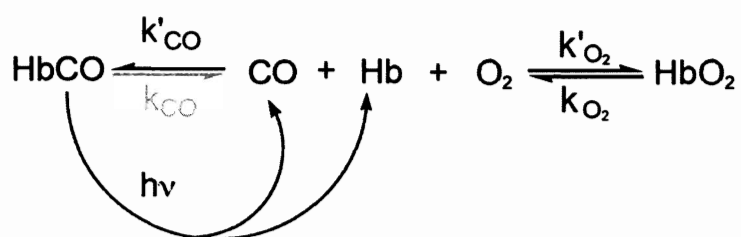
The model of cooperative binding of ligands to tetrameric hemoglobin developed by Monod, Wyman and Changeaux [63] is the most commonly accepted explanation of

cooperative O₂ binding to hemoglobin. Ligand binding to deoxyHb mediates a transition of Hb tetramers from the low affinity T-state quaternary structure to the high affinity R-state. On average, the T → R conformational switch occurs after binding of the second ligand. In practice, determination of association and dissociation rate constants for the binding of the first ligand to Hb₄ represents the kinetic parameters for ligand binding to the T-state (k'_{TX} and k_{TX}). In order to obtain rates for binding to the R-state, the kinetics of the last step of binding ($Hb_4X_3 + X \rightleftharpoons Hb_4X_4$) must be measured. In the present work mainly R-state parameters were determined.

The use of flash-photolysis technique has proved to be a very powerful method for determining the kinetic parameters for ligand binding to Mb and Hb [64, 65]. In these experiments, the energy of a laser flash disrupts the Fe-X bond and drives the ligand into solution. The bimolecular rebinding of X is observed as the decay of deoxyHb fraction with time. For Mb, this reaction is a simple, monoexponential process under pseudo first order conditions. For tetrameric HbA, the analysis of kinetic traces is complicated by the presence of different types of subunits, which have distinct binding parameters. Moreover, full photolysis of Hb results in the formation of 100% deoxyHb, but the rebinding of the first two ligands drives the T- to R-state conformational transition which competes with ligand binding to deoxyHb. Newly formed R-state tetramers bind ligands very quickly due to larger rate constants and introduce even more inhomogeneity into photolysis traces. Thus, full photolysis of tetrameric HbX cannot be used to assess k'_{RX} and k_{RX} ; however, the slowest phase in the trace allows an approximate estimate of the T-state parameters.

In the 1950s Gibson *et al.* [66, 67] showed that if the laser light intensity is decreased by placing neutral density filters in the excitation beam so that only 10% of the total absorbance change occurs, only the last step of rebinding is observed. Statistically, 10% photolysis results in the formation of only three-liganded species, Hb_4X_3 , and the T- to R-state transition does not happen.

In the current work, parameters of O_2 and CO binding to the mutant Hb subunits were measured using laser flash-photolysis of the stable HbCO complexes in O_2/CO mixtures to avoid prolonged exposure to oxygen and autooxidation [68].



Scheme 2.1

$$k_{\text{fast}} = k_{\text{O}_2}[\text{O}_2] + k_{\text{O}_2} + k'_{\text{CO}}[\text{CO}]$$

Equation 2.1

$$r_{\text{obs}} = \frac{k_{\text{O}_2}}{1 + \frac{k'_{\text{O}_2}[\text{O}_2]}{k'_{\text{CO}}[\text{CO}]}}$$

Equation 2.2

The reaction is initiated by photolyzing HbCO to generate deoxyHb species that can then react with the ligands present in solution (Scheme 2.1, Fig. 2.4). Two distinct

phases are observed after photolysis. The initial fast phase represents bimolecular ligand recombination with the transient deoxyHb species. In general, the observed rate (k_{fast} , Equation 2.1) represents the sum of association and dissociation rates for all ligands present in the cuvette. However, since the rate of CO dissociation from HbCO is extremely slow and the binding is considered irreversible, k_{CO} is not included in Equation 2.1. Moreover, the fast phase is dominated by O_2 binding, because in most cases $k'_{\text{O}_2} > k'_{\text{CO}}$ [65]. The slow replacement phase, r_{obs} , represents the displacement of transiently bound O_2 by CO. It is computed as the rate of O_2 dissociation times the fraction of deoxy-species that bind CO (Equation 2.2, Fig. 2.4 C).

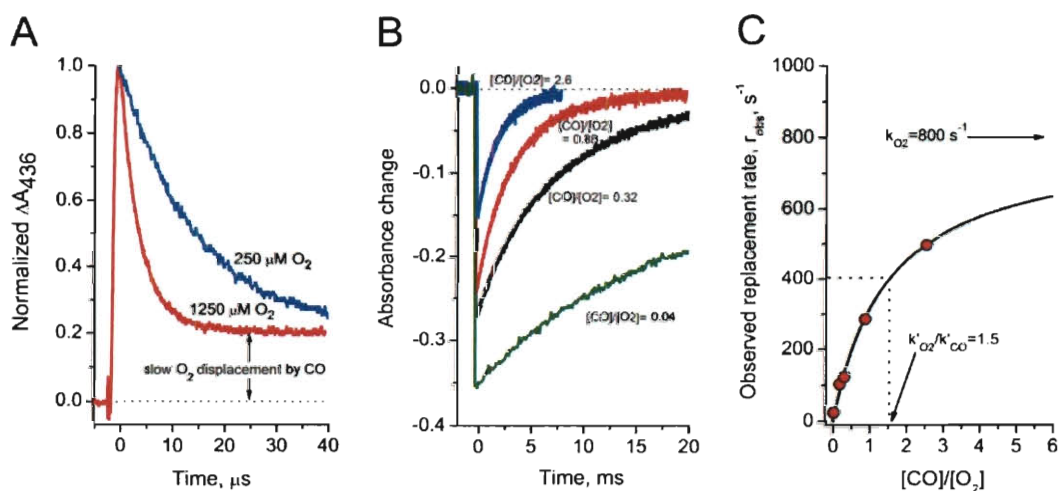


Figure 2.4. Time courses for O_2 binding to and displacement from isolated human Ala(E7) αCO subunits. (A) Reactions were carried out in buffers equilibrated with 1 atm of O_2 and air, and no free CO, until after photolysis of the αCO sample. The time courses were fitted to single exponential expressions with an offset representing the 1,000-fold slower CO replacement reaction. (B) Time courses for the slower replacement reaction measured at 425 nm at 4 different $[\text{O}_2]/[\text{CO}]$ ratios. The amplitude of the slow phase decreases as $[\text{CO}]/[\text{O}_2]$ increases because CO begins to compete with O_2 in the initial association reaction. (C) Dependence of the observed replacement rate on $[\text{CO}]/[\text{O}_2]$ and fit to Equation 2.2. The fitted curve is asymptotically approaching k_{O_2} at $r_{\text{obs}}=800 \text{ s}^{-1}$. Modified from [69].

The bimolecular binding reaction is best observed at 436 nm (Fig. 2.4 A), which is near the peak of deoxyHb, and the replacement reaction is best observed at 425 nm

(Fig. 2.4 B), near the peak for HbCO. The solutions of HbCO in O₂/CO mixtures were prepared as follows. First, 50-ml gas-tight syringes were filled with ~30 ml of buffer, and some gas space (~ 10 ml) was kept above the liquid. The syringes were capped with rubber septa, and a cannula needle was inserted through the septa into the liquid. The needle was attached to tubing connected to a gas tank through a humidifying glass chamber. The solution in the syringe was bubbled with either pure CO or O₂ for ~30 min at 20°C. In order to maintain atmospheric pressure inside the syringes during gas saturation an additional 20-gauge needle was also inserted through rubber septa. Final gas concentrations in the buffers are 1000 μM for CO and 1250 μM for O₂ at 25°C, 1 atm (at sea level). Reaction mixtures were prepared by using 1 ml gas-tight syringes to withdraw different amounts of O₂- and CO-saturated buffers to generate O₂/CO ratios equal to 100/0, 75/25, 50/50, 25/75, and 0/100 %, which correspond to 1250/~50 (from the HbCO sample after photolysis), 937.5/250, 625/500, 312.5/750, and 0/1000 μM. HbCO samples were injected into this 1 ml syringe from concentrated (~2,000 μM) stock solutions to a final concentration of ~ 50 μM (in some experiments to increase the signal amplitude ~100 μM HbCO was used). 1mm path length glass cuvettes were capped with a rubber septum and purged with pure N₂ for at least 10 minutes. Then, the sample solution was rapidly injected into the cuvettes and filled to the top without a gas space using another small needle to allow excess solution to be forced out the top along with any N₂ bubbles. In nearly every experiment the protein concentration was kept at least 5-fold smaller than ligand concentration to maintain pseudo-first order conditions.

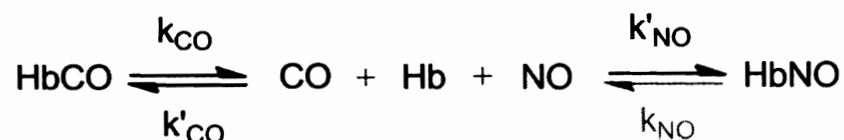
The value of k'_{CO} was determined in a separate experiment by photolyzing HbCO in the presence of only CO with a small amount of dithionite added to eliminate residual oxygen. Equation 2.1 for CO binding simplifies to $k_{\text{fast}} \approx k'_{\text{CO}}[\text{CO}]$.

Partial photolysis ($\leq 10\%$ absorbance change) was used to measure k_{fast} for mutant/wild-type hybrid HbCOs to ensure that only rebinding to the R state tetramers was being examined. Full photolysis was used for isolated subunits, which are intrinsically in R state-like conformation [65]. The slow rate for O_2 displacement by CO was measured after 100% photolysis for both tetramers and monomers because on these time scales all Hb tetramers have either 3 or 4 ligands bound and remain in the R quaternary state [65, 70, 71].

Photolysis was initiated by a $0.5 \mu\text{s}$ excitation pulse generated by a Phase-R Crop. model 2100B dye laser system (New Durham, NH, USA) using Rhodamine 575. Absorbance changes were detected using a Xe lamp (Model E7536, Hamamatsu Photonics K.K., Japan) and photomultiplier tube (Instruments SA, Inc., Metuchen, NJ, USA). Kinetic traces were recorded using a digital oscilloscope (TDS 220, Tektronix, Inc., Wilsonville, OR, USA). The observed traces for tetramers were fitted in Igor Pro 4.05A to a double-exponential expression with an offset. The observed fast (ligand rebinding) and slow (O_2 displacement by CO) pseudo first order rate constants measured at different $[\text{O}_2]$ and $[\text{CO}]$ were fitted simultaneously to the expressions in Equation 2.1 and 2.2 using the Solver routine in Microsoft Excel. In the case of mutant hybrid tetramers, observed rates assigned to wild type and to mutant subunits were fitted separately. Rate constants for the individual subunits within hybrid tetramers were assigned by comparison to previously reported results for wild type α and β subunits,

assuming that the amino acid replacements cause marked deviations of the binding parameters for mutant subunits but have little effect on the wild-type R state subunit [64]. The buffer conditions for these kinetic experiments were either 100 mM Na phosphate buffer, pH 7 (for comparison with previous Mb studies), or 50 mM HEPES, 0.1 M NaCl, 0.1 mM EDTA, pH 7.4 (for comparison with previous HbA studies). All kinetic measurements were made at 20 °C. The two different buffer conditions did not appear to influence ligand binding.

The values of CO dissociation, k_{CO} , for the mutant Hb tetramers and monomers were determined by rapidly mixing the HbCO complexes in CO (10% or 100 μM) buffer with the buffer containing an excess NO (2000 μM).



Scheme 2.2

$$r_{\text{obs}} = \frac{k_{\text{CO}}}{1 + \frac{k'_{\text{CO}}[\text{CO}]}{k'_{\text{NO}}[\text{NO}]}} \approx k_{\text{CO}}$$

Equation 2.3

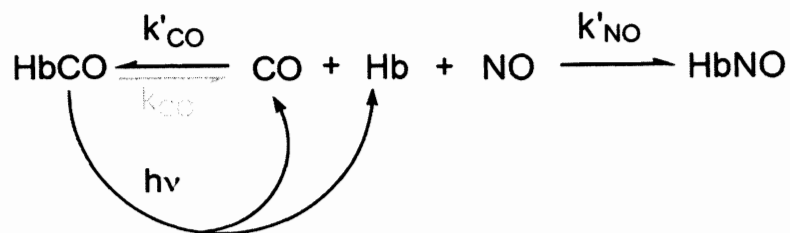
Under these conditions, NO displaces all the bound CO from Hb with an observed rate equal to k_{CO} because $k'_{\text{NO}}[\text{NO}] \gg k'_{\text{CO}}[\text{CO}]$ [65]. Experiments were conducted in a modified stopped-flow spectrophotometer D-110 (Durrum, Palo Alto, CA, USA). The absorbance changes were measured at 424 nm, and the time courses were analyzed as described for the O₂ displacement reactions [65, 70, 71].

NO binding to the wild-type and mutant HbA samples was measured using a flow-flash system to allow initiation of the reaction by photolysis of FeCO complexes, which have quantum yields for photodissociation of CO into solvent of 0.4 to 1.0. In contrast, the analogous yields for complete photodissociation of HbNO complexes are very low ≤ 0.001 , making the measurement of bimolecular NO binding very difficult by flash photolysis [17, 72, 73].

A Bio-Logic SFM-400 multi-mixer with a MPS-60 controller unit (Bio-Logic SA, Claix, France) was attached by an umbilical cord to a portable cuvette assembly in the Phase-R dye laser optical pathway, described above. A sample of HbCO was rapidly mixed with concentrated NO and then photodissociated 50 ms after flow stopped with a 0.5 μs excitation pulse. Stock syringes contained 100 μM HbCO and 2000 μM NO (100% saturated solution), respectively, in 100 mM Na phosphate, pH 7. Additional syringe contained an anaerobic buffer (*i.e.* purged with 100% N_2) to adjust the final concentration of the protein after mixing with NO buffer in stopped flow apparatus. To prepare NO stock solutions, the syringe containing air-saturated buffer was purged with N_2 for ~20-30 min, and then bubbled with 100% NO, using the approach described for preparation of O_2 and CO stock solutions. The total volume after mixing was 400 μl , and final concentrations of NO were 500 μM (25%), 1000 μM (50%) and 1500 μM (75%). The final concentration of protein was 25 μM . Occasionally, 10% and 33.3% of NO after mixing were used.

Bimolecular NO binding to the newly generated deoxyHb was followed at 436 nm. As shown in Scheme 2.3 and Equation 2.4, the observed rate, k_{obs} , is given by

$k'_{\text{NO}}[\text{NO}]$, because the concentration of CO was kept low ($\sim 50 \mu\text{M}$) and $k'_{\text{NO}} > k'_{\text{CO}}$ for all the samples examined.



Scheme 2.3

$$k_{\text{obs}} = k'_{\text{NO}}[\text{NO}] + k'_{\text{CO}}[\text{CO}] \approx k'_{\text{NO}}[\text{NO}]$$

Equation 2.4

Little difference was observed between the normalized time courses for NO binding at high and low photodissociation yield because k'_{NO} is roughly independent of quaternary state [19, 74]. The observed rates of bimolecular NO binding are linearly dependent on $[\text{NO}]$ with an intercept effectively equal to 0 and a slope equal to k'_{NO} (Fig. 2.5).

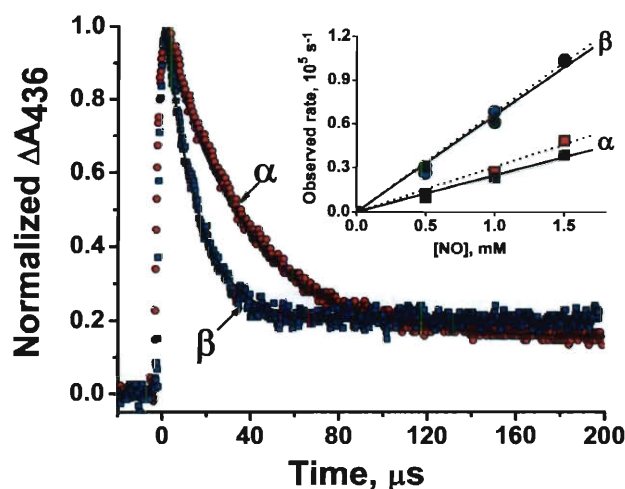


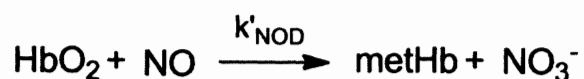
Figure 2.5. NO binding to isolated native α and β chains. HbCO samples ($25 \mu\text{M}$ after mixing) were rapidly mixed with NO ($1000 \mu\text{M}$ after mixing) and then photolyzed ~ 50 ms after flow stopped. The time courses were normalized by the absorbance change immediately before and after photolysis. The offset after the reaction is complete represents the difference in absorbance between the final product HbNO and the starting HbCO sample. The red circles and blue squares represent native α and β subunits, respectively. The black lines represent fits to single exponential expressions for the isolated α ($k_{\text{obs}} = 28,000 \text{ s}^{-1}$) and β ($k_{\text{obs}} = 68,000 \text{ s}^{-1}$) subunits. The *inset* shows the dependence of the observed pseudo-first order rate constants of native α and β subunits, and HbA tetramers on $[\text{NO}]$. The observed rates show a straight line dependence with a y-intercept equal to 0 because the NO dissociation rate constant is on the order of 10^{-4} s^{-1} [12]. The red and blue symbols in the inset correspond to the rates for isolated α and β subunits and the closed symbols represent the rates for the fast (β) and slow (α) HbA phases. The slopes represent the k'_{NO} values, which are given in Table 3.3 (Chapter 3).

2.4. Measurements of NO dioxygenation by oxyHb.

NO is a radical with an unpaired electron in its outermost bonding orbital and, thus, is highly reactive with other paramagnetic molecules and atoms including iron and O_2 . Extensive experimental work by our group and others [4-6, 39] resulted in the mechanism for NO dioxygenation by HbO₂ and MbO₂, according to which, in the distal pocket, nitric oxide reacts with the bound dioxygen to form nitrate and metHb (Scheme 2.4). At neutral pH conditions, the critical step of the reaction is NO diffusion into the distal pocket of O₂-bound globin. The following events (formation of peroxynitrite,

ONOO⁻, and subsequent isomerization into nitrate, NO₃⁻) are significantly faster and not rate-limiting.

The rates of NO dioxygenation were measured by mixing oxygenated forms of α and β subunits and HbA tetramers with solutions of NO in a modified stopped-flow spectrophotometer D-110 (Durrum, Palo Alto, CA); spectral changes were detected at 402 nm, which corresponds to metHb absorbance. Also, at this wavelength the contributions from other possible reactions, such as NO binding to deoxyHb and metHb, are minimal [6, 65]. Experiments were conducted in 100 mM NaPi, pH7, at 20 °C.



Scheme 2.4

$$k'_{\text{NOD}} = \frac{1}{t_{1/2} \times [\text{NO}]}$$

Equation 2.5

$$k_{\text{obs}} = k'_{\text{NOD}} \times [\text{NO}]$$

Equation 2.6

The reaction of NO dioxygenation is extremely fast ($\sim 60 \mu\text{M}^{-1}\text{s}^{-1}$ for HbA) and part of it can be lost in the dead time of the apparatus (1-3 ms), unless very low concentrations of HbO₂ and NO are used [6]. Mixing small equimolar amounts of oxyHb and NO (1 μM after mixing) minimizes the undetected part of the reaction. Fig. 2.6

shows the time courses for the reaction of HbA and isolated α and β chains with equimolar amounts of NO.

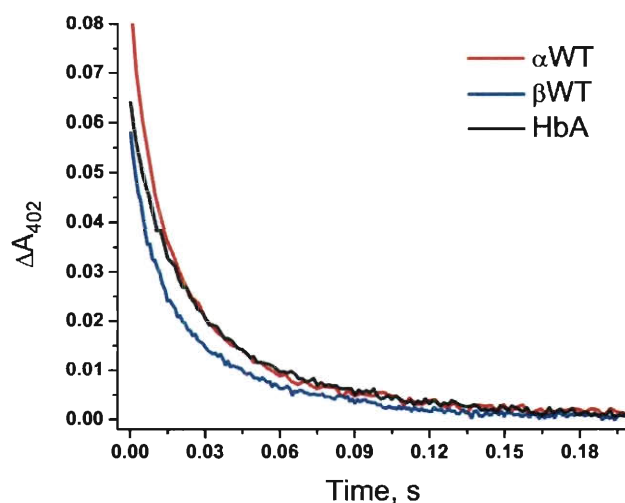


Figure 2.6. NO dioxygenation by tetrameric HbO₂ and isolated α O₂ and β O₂ subunits. 2 μ M solutions of Hb and NO were mixed (final concentration is 1 μ M) at 20°C, in 100 mM KPi buffer, pH 7; absorbance change was monitored at 402 nm. Determined rate constants were 74 μ M⁻¹s⁻¹, 90 μ M⁻¹s⁻¹ and 87 μ M⁻¹s⁻¹ for HbA, α and β subunits, respectively. The rates are slightly higher than previously reported, most likely due to the loss of the part of the time course in the dead time of the apparatus.

The rate constant, k'_{NOD} , can be estimated using Equation 2.5, where $t_{1/2}$ is the half-time of the reaction, or by fitting the observed time courses to the integrated form of an irreversible second order rate equation with equal concentrations of reactants. However, determination of rate constants from these equimolar experiments is troublesome, because it is highly dependent on the detection of the complete time course. A more accurate assessment of NO scavenging rate can be achieved by using pseudo-first order conditions with excess NO (1 μ M HbO₂ and 5 μ M NO after mixing) and calculating k'_{NOD} from observed rate of the reaction (Equation 2.6).

2.5. Measurements of geminate CO recombination to hybrid Hb tetramers and isolated subunits.

Geminate recombination represents internal rebinding of the ligand to heme Fe after photodissociation. The notable difference between bimolecular and geminate recombination is that in the latter case the same molecules of ligand and protein associate after photolysis [75]. After ligand-iron bond disruption, the ligand samples the available space inside the protein and then some of ligand molecules escape to the solvent and some geminately rebind. The speed and extent of rebinding depends on the protein and ligand reactivity. In Mb, for example, geminate NO recombination occurs on picosecond timescales and the fraction of rebinding is ~100%; in contrast, internal CO recombination is negligible, ~5%, and is observed in nanosecond range [17, 22, 73]. The shape of the rebinding curve reflects the internal architecture of the protein. Multiple phases are observed if more than one distinct docking site are present within the protein globule and the rate of ligand exchange between these sites is not faster than rebinding to heme. These speculations were confirmed by studies on geminate O₂ rebinding to Mb. As noted before, in addition to the distal pocket, the Mb molecule contains small apolar cavities, called Xe pockets [31]. Both computational and experimental techniques have demonstrated that geminate O₂ recombination to Mb is composed of fast and slow phases. The fast phase corresponds to ligand rebinding from the collective volume of the distal pocket and the adjacent Xe4 site. The slow process represents ligand rebinding from the Xe1 site, located underneath the heme [22, 24, 26, 27, 29, 30, 33, 53, 76-80]. The parameters of geminate recombination allow us to assess ligand migration inside the protein matrix.

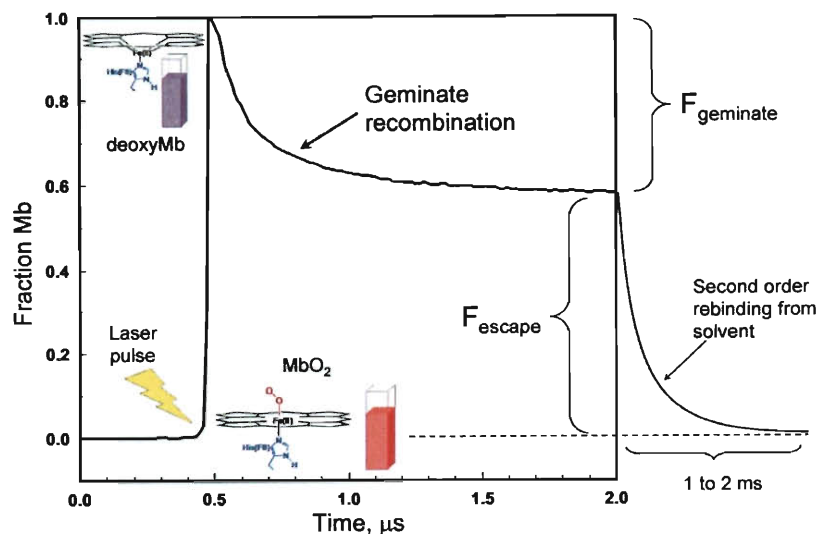
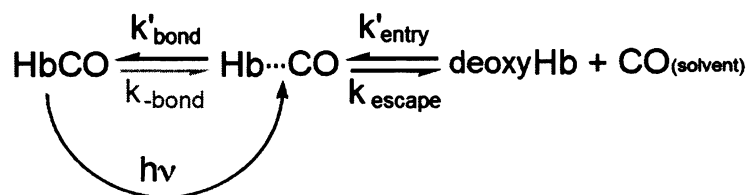


Figure 2.7. Schematic representation of geminate O_2 recombination time course of Mb. After a short nanosecond laser pulse drives O_2 photodissociation, a fraction of dissociated ligand molecules rebinds without leaving the protein (F_{geminate}); the rest escape to solvent (F_{escape}) and bimolecularly recombine with Mb on much longer timescales (ms). Spectral changes of the protein associated with transitions between liganded and unliganded states allow optical detection of the reaction (schematic representation of the cuvette with Mb sample demonstrates the color change from bright red to purple upon O_2 dissociation).

For a general case, geminate recombination is viewed as a simple first order process. It does not depend on ligand concentration. A simple two-step binding scheme is assumed for analysis (Scheme 2.5). According to this mechanism, after photodissociation the geminate state ($Hb\bullet\bullet\bullet CO$) is formed in the distal cavity, from which the ligand either rebinds to iron with the rate of internal bond formation (k_{bond}) or escapes from the protein (k_{escape}). Eventually, the ligand returns to the binding site from solvent with the bimolecular rate constant (k'_{entry}). The rate parameters for these processes define the observed rates (k_{gem} , Equation 2.8) and fractions (F_{gem} , Equation 2.7) of geminate recombination and the overall bimolecular association rate constants (k'_x , Equation 2.9)

[22]. The schematic time course for geminate O₂ recombination to Mb is shown in Fig.

2.7.



Scheme 2.5

$$F_{\text{gem}} = \frac{k_{\text{bond}}}{k_{\text{escape}} + k_{\text{bond}}}$$

Equation 2.7

$$k_{\text{gem}} = k_{\text{bond}} + k_{\text{escape}}$$

Equation 2.8

$$k'_X = \frac{k'_{\text{entry}} k_{\text{bond}}}{k_{\text{escape}} + k_{\text{bond}}} = k'_{\text{entry}} F_{\text{gem}}$$

Equation 2.9

Time courses for geminate CO recombination to 50 μM isolated wild type and mutant Hb subunits in 1mM or 100 μM CO were collected after excitation with a 7 ns pulse from a frequency-doubled YM600 Nd:YAG laser system (Lumonics, Inc., Billerica, MA). To increase the signal-to-noise of the kinetic traces, the sample was illuminated by a pulsed Xe arc lamp (model 03-102, Applied Photophysics, Inc,

Leatherhead, UK). Transmittance was measured at 436 nm using a photomultiplier tube with a 0.9 ns response time (R-1913, Hamamatsu, Japan), recorded on a digital phosphor oscilloscope (TDS 3052, Tektronix, Inc., Wilsonville, OR). A pulse/delay generator (model 555, Berkeley Nucleonics Corp., San Rafael, CA) was used to synchronize the laser firing, the Xe arc lamp pulse, and oscilloscope trigger. The data used for fitting were an average of ~16-32 time courses collected at 20-22 °C. Rates and amplitudes of geminate rebinding were obtained by fitting the time courses to the double-exponential equation $A(t) = A_{escape} + A_{gem,\alpha} \exp\{-k_{gem,\alpha} t\} + A_{gem,\beta} \exp\{-k_{gem,\beta} t\}$. For isolated subunits, the single-exponential equation $A(t) = A_{escape} + A_{gem} \exp\{-k_{gem} t\}$ was used. The fraction of geminate recombination, F_{gem} , was obtained dividing A_{gem} by the total absorbance change at 436 nm (*i.e.* $A_{gem}/(A_{escape} + A_{gem})$); k_{gem} is equal to the observed rate of the first order internal rebinding phase. Time courses were fitted in Igor Pro 4.05A. The rates of internal bond formation, escape and bimolecular entry were calculated using Equations 2.7-9.

2.6. Laser flash photolysis of HbA tetramers and isolated subunits in the presence of Xe.

Using a method adapted from Pesce *et al.* [81], bimolecular O₂ and CO binding and geminate CO recombination to HbA tetramers and isolated subunits were measured in the presence of 0, 4 and 9 atm of Xe in a home-made stainless steel pressure cell. A small amount of Hb sample (0.5-1 ml) equilibrated with 1 atm CO (1000 μM CO) or 1 atm of air (~250 μM O₂) was introduced into the sealed, CO- or air-purged pressure cell. For CO samples, several grains of Na dithionite were also added to the cell before

introducing the sample. First, time courses for the samples containing no xenon were collected. Next, Xe was introduced via a three-way valve attached to the cell and the sample was equilibrated with Xe/CO or Xe/air mixtures by vigorously shaking the cuvette for ~ 1-2 min. The final pressures of the gas mixtures in the cell were 1, 5 and 10 atm. Measurements were made as described earlier, within 10 minutes after equilibrating with Xe.

2.7. FTIR spectroscopy of HbCO tetramers and isolated subunits.

The infrared stretching frequency of bound CO ($\nu_{\text{C-O}}$) is a sensitive probe to study the structural environment of the distal pocket of hemeproteins [68, 69, 76, 82-87]. The electrostatic field surrounding the CO molecule bound to heme in Hbs and Mbs is one of the many factors affecting the magnitude of $\nu_{\text{C-O}}$. It has been proposed that the polarity of the immediate vicinity of the bound carbon monoxide alters C-O bond order, which equals 2.4-2.6 in wild type Hbs and Mbs. Changing the electrostatic field around the bound CO from "+" to "-" leads to the increase in the fraction of the $\text{Fe}^{\delta(-)}-\text{C}\equiv\text{O}^{\delta(+)}$ resonance structure with triple C-O bond character (Fig. 2.8 C). Increase in the C-O bond order is accompanied by the increase in the magnitude of ν_{CO} . This approach has been successfully verified by measuring FTIR spectra of a series of Mb mutants in which the positive electrostatic field from distal His was removed and corresponding stretching frequencies of CO shifted to the right part of the spectrum (Fig. 2.8 A; [83]). The observed shifts correlated with the increases in CO dissociation rates (Fig. 2.8 B), suggesting that the positive field of His(E7) stabilizes bound ligands by a H-bond. Here, I

have used FTIR spectroscopy to prove that His(E7) electrostatically stabilizes bound O_2 in the α and β subunits of HbA.

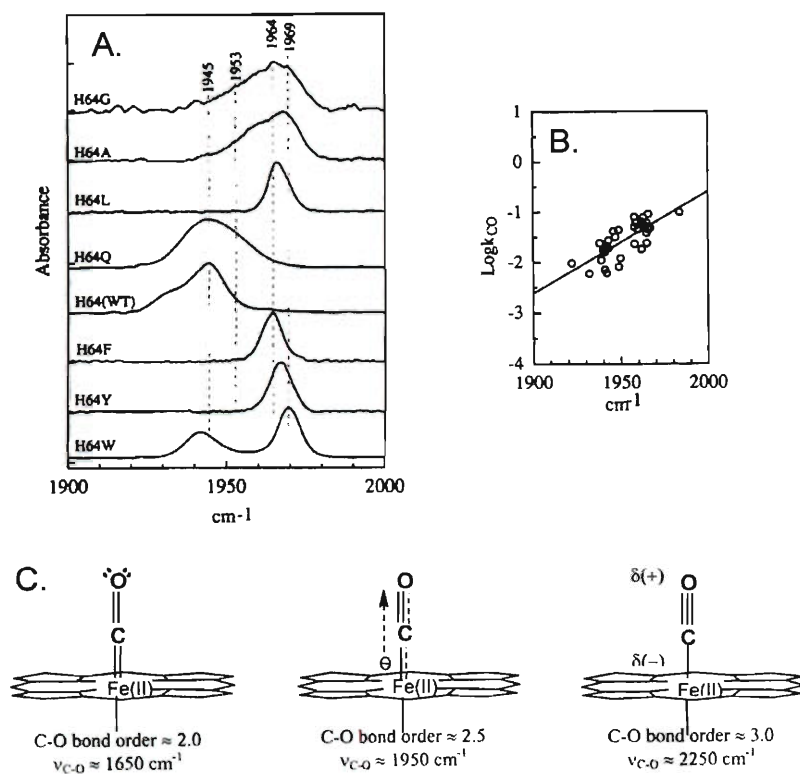


Figure 2.8. CO stretching frequency (ν_{CO}) as a probe to study electrostatic environment of the distal pocket in Mb. (A) FTIR spectra of wild-type and mutant sperm whale Mbs. Note that all apolar E7 mutations (G, A, L, F) and Tyr shift the CO stretching peak position to ~ 1965 cm^{-1} , while Gln replacement is invariant because electrostatic environment has not changed. (B) The correlation between rate of CO dissociation, k_{CO} , and ν_{CO} . Correlation coefficient is 0.8. (C) Schematic representation of the relationships between C-O bond order and ν_{CO} . The polarity changes from “+” to “-“ (left to right direction). (A) and (B) adapted from [83], (C) adapted from [69].

The samples were prepared by adding highly concentrated HbCO and a small volume of a stock 200 mM sodium dithionite solution to a nitrogen-purged 250 μ l PCR tube fitted with a rubber septum to give a final concentration of ~ 2 mM HbCO and 40 mM dithionite. The buffer conditions were the same as those used in the kinetic experiments. The solution was quickly transferred by pipet to the center of a 40 μ m well of a CaF_2 cell window and immediately sandwiched with a flat window and clamped with

the cell holder (BioTools, Inc., Canada). The cell was placed in a nitrogen purged Nicolet Nexus 470 FTIR spectrometer (Nicolet Instrument Corp., Madison, WI), equipped with an 1800 cm^{-1} to 2400 cm^{-1} band pass filter. Sixty-four interferograms were collected and averaged to produce a Fourier transformed spectrum with 1 cm^{-1} resolution. A buffer control spectrum was subtracted from the sample spectra to correct for any water vapor peaks.

2.8. Crystallization of mutant Hbs, X-ray diffraction data collection and structure determination.

Recombinant HbCOs were crystallized using the batch method initially designed by Perutz [88]. Concentrated HbCO solution (in 10 mM Na phosphate buffer, pH 7) was mixed with 3.4 M Na/K phosphate, pH 6.7 (precipitant) to yield $\sim 20\text{ mg/ml}$ HbCO in 2.3 M Na/K phosphate, pH 6.7. 100 μl of the mixture was placed in a glass vial, sealed and purged with CO, and a drop of toluene was added to the batch. A small aliquot of dilute seeding solution, prepared by finely grinding previously grown WT HbCO crystals in mother liquor, was added to the mutant HbCO mixture to initiate crystal formation. Crystals grew over 2-3 days at room temperature (Fig. 2.9). Crystals of MbCO were obtained using the batch method reported by Quillin *et al.* [89]. 10 μl of 60 mg/ml Mb solution was mixed with 3.2 M ammonium sulfate in 20 mM Tris-HCl, 1 mM EDTA, pH 9.0 to give a final $(\text{NH}_4)_2\text{SO}_4$ concentration of 2.4-2.6 M. The mixture was placed in a glass tube, seeded as above (using a small amount of a sperm whale wild-type MbCO seeding suspension), sealed and purged with CO.



Figure 2.9. Crystals of recombinant HbCO. (A) Pyramidal crystals of HbCO α WT β Leu(E7) were obtained according to the procedure reported by Perutz [88]; (B) and (C) crystals of HbCO α Trp(E7) β WT, which diffract too poorly to get any useful data.

DeoxyHbs were obtained from CO-bound proteins by successive oxidation and reduction. First, the met-form of the protein was generated by incubating concentrated HbCO with excess potassium ferricyanide in a 5 ml round bottom flask on ice under constant illumination with strong light to promote CO photodissociation. The gas space above the sample was continuously purged with N₂. After prolonged incubation, an aliquot of the protein mixture was passed through a Sephadex G-25 column to remove excess ferricyanide, and then tested for the residual HbCO in flash photolysis experiments. The whole procedure was repeated until no detectable CO photolysis and rebinding was observed. Fully oxidized protein was buffer exchanged against 10 mM ammonium phosphate, pH 7, concentrated to ~ 60 mg/ml, and degassed. The protein samples were reduced in N₂-filled anaerobic glovebox (Vacuum Atmospheres, Hawthorne, CA) by addition of a 10-fold excess of Na dithionite.

Crystallization of recombinant deoxyHb was performed according to the procedure described by Brucker *et al.* [90], which was adapted from Perutz [88]. The precipitant solution was prepared by mixing 0.5 ml 2 M monobasic ammonium phosphate, 1.5 ml 2 M dibasic ammonium phosphate and 8 ml 4 M ammonium sulfate,

and then degassed. All solutions were brought inside a glove box, and the precipitant was mixed with concentrated deoxyHb solution to give 10 mg/ml Hb and 2.26 – 2.80 M ammonium phosphate/sulfate. 120 μ l of the resultant mixture was placed in an evacuated glass vial and sealed. Large crystals were formed in 2-4 weeks.

Just before data collection, crystals were bathed in a mounting solution containing 10-15% glycerol in the appropriate mother liquor. For CO complexes, the mounting solution was saturated with 1 atm of pure carbon monoxide; for deoxyHb, the mounting solution was saturated with 1 atm of ultrapure N₂, and a few grains of Na dithionite were added to remove any residual oxygen contamination that occurred during transfer.

A cryo-cooling N₂ system was used to maintain low temperature (100 K) in the environment of the mounted crystals to reduce radiation damage. The continuous flush with ultra cold N₂ gas also sustains anaerobic conditions around crystal to prevent O₂ binding to deoxyHb and CO replacement by O₂ in HbCO and MbCO crystals. Complete X-ray diffraction data sets for each of the globins were obtained from single crystals using Cu K α radiation ($\lambda = 1.5418 \text{ \AA}$) from a Rigaku RUH3R rotating anode X-ray generator operated at 50 kV and 90 mA and a Rigaku R-AXIS IV++ image plate detector (Rigaku Americas Co., TX). Data were collected, scaled and reduced using d*TREK software [91].

The structure of Trp(E7) MbCO was solved by molecular replacement using CNS [92] and the structure of recombinant wild type sperm whale metMb (2MBW [93]) as a starting model with the solvent molecules omitted. The best solution using data from 15.0-4.0 \AA yielded a correlation coefficient of 0.65 and a R-factor of 0.35 after rigid-body refinement. This model was further refined by conjugate gradient minimization and then

simulated annealing, interspersed with manual fitting. The slow-cool protocol was also used to calculate unbiased OMIT maps to confirm the correct placement of Trp(E7). At this stage, crystallographic refinement was pursued in PHENIX [94]. After an initial round of simulated annealing refinement, several macrocycles that included bulk-solvent correction and anisotropic scaling of the data, individual coordinate refinement with minimization, and individual isotropic ADP refinement were carried out with maximum likelihood as the target. The CO ligand was modeled into the electron density maps at this point and refinement was continued with restraints imposed on the expected iron-CO geometry. Solvent molecules were then included and combined TLS and individual ADP refinements were carried out in the final stages.

The structures of HbCOs, deoxy Hbs and deoxyMb Trp(E7) were solved in CNS by direct Fourier synthesis using the structures of wild type human HbCO (2DN3 [2]), deoxyHb (2DN2 [2]), and sperm whale Trp(E7) MbCO, respectively, as starting models. The final refinements were carried out in PHENIX as described above. Map fitting and other manipulations with molecular models were performed using the graphic software COOT [95]. The accession codes for the models, crystal parameters, and statistics of X-ray data collection and refinement are provided in Tables 3.3 and 4.1. Crystallographic figures were prepared using PyMOL Molecular Graphics System, v. 1.2r3pre (Schrödinger, LLC).

CHAPTER 3: HIS(E7) STABILIZES BOUND O₂ AND REGULATES

LIGAND ENTRY IN α AND β SUBUNITS OF HUMAN HbA

3.1. Previous ideas about the role of the distal histidine in HbA.

In 1970 Perutz [14] proposed that the distal histidines located at the seventh position from N-terminus along the E-helix, α His58(E7) and β His63(E7), play crucial structural roles for regulating both the affinities and rates of O₂ binding to HbA. Several years earlier, Pauling [96] suggested that His(E7) could stabilize bound O₂ by donating a hydrogen bond to the partial negative charge on the superoxide-Fe(III)-like FeO₂ complex. Perutz and Mathews [13] had noted previously that upward rotation of the imidazole side chain would open a short and direct channel for ligand movement from the solvent into the heme pocket and that the distal histidine could be acting as a gate for entry into and exit from the active site (Fig. 3.1).

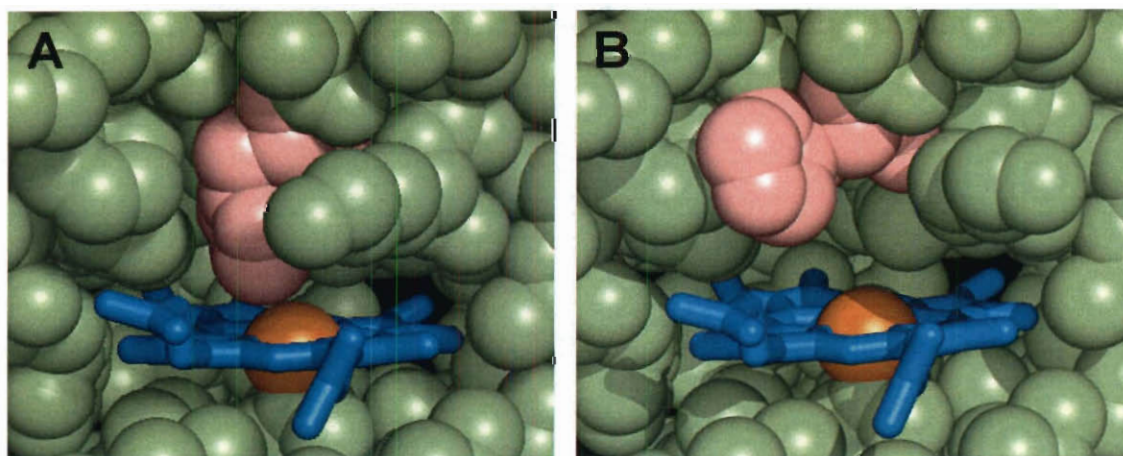


Figure 3.1. His gate in deoxygenated β subunits of HbA. (A) closed conformer; (B) hypothetical open conformer. His(E7) is depicted in pink spheres, heme – in blue sticks, iron – orange sphere, green spheres – other residues. Created from 2DN2 [2].

In the late 1970s, studies of model heme compounds and naturally occurring globins with His(E7) replacements suggested strongly that the distal histidine also plays a

key role in discrimination between O₂ and CO binding. One group suggested that the close proximity of the imidazole side chain sterically hindered the binding of CO, which requires a linear Fe-C-O geometry, whereas a "good fit" occurs for the inherently bent Fe-O-O complex [97, 98]. Another group argued that the discrimination was not against CO binding but rather in favor of O₂ binding, which is preferentially stabilized 10 to 1,000-fold by hydrogen bond donation from the imidazole N_ε-H to the polar FeO₂ complex [99-102].

The first mutagenesis studies on sperm whale Mb and human HbA reported that the His(E7) to Gly mutations in α subunits and Mb cause marked increases in the rates of O₂ dissociation and significant decreases in affinity, both of which indicate strong stabilization of the FeO₂ complex by proton donation from the wild-type His(E7) side chain [20, 100, 103]. In addition, the association rate constants for O₂ and CO binding increased 5 to 10-fold. The latter results were interpreted in terms of the distal histidine gate mechanism, with the His(E7)→Gly mutation resulting in an open E7 channel.

In contrast, neither the dissociation nor association rate constants for O₂ binding to the R state of the β Gly(E7) mutant of HbA appeared to increase significantly, implying no electrostatic stabilization of bound ligands by the native His(E7) in β-subunits and an already open gate or alternative pathway. These surprising kinetics results were explained by Shaanan's [104] published structure of human oxyhemoglobin, in which the N_εH atoms of distal histidine in β subunits seemed to be further away from the bound O₂ atoms and pointing toward the heme plane.

Between 1989 and 1999, our group and others constructed large libraries of mammalian Mb mutants as a model system for understanding the structural mechanisms

of ligand binding to vertebrate globins involved in O₂ transport and storage, and a detailed molecular mechanism for O₂ binding has emerged. Ligand entry into myoglobin occurs through the distal histidine gate; hydrogen bond donation by the neutral N_ε-H tautomer of His(E7) regulates oxygen affinity; and electrostatic stabilization of bound oxygen represents the main determinant of discrimination between O₂ and CO binding [12, 22, 32, 85, 105, 106]. During the same ten-year period, Champion, Sage, and coworkers [84, 86, 87] came to similar conclusions when examining opening of the E7 channel by protonation of His(E7) in Mb. They correlated changes in the vibrational bands of bound CO and increases in the association and dissociation rate constants for O₂ and CO binding with outward rotation of the E7 imidazole side chain as it becomes protonated at low pH. Their conclusions were verified by the low pH crystallographic studies of Yang and Phillips [107].

Similar mechanisms have been proposed to occur in the α and β subunits of HbA. However, the experimental evidence has been weak, due, in part, to the technical difficulties of generating large mutant Hb libraries, and then, assigning rate and spectral parameters to the individual subunits within mutant/wild-type hybrid tetramers in R and T quaternary structures (see [64, 71]). The measurements and interpretations are particularly difficult for distal histidine mutants, which are highly unstable with respect to autooxidation, heme loss, and denaturation.

In 2000, Chien Ho's group [108] used heteronuclear NMR spectra of chain-selectively labeled samples to show that the N_ε atoms of His(E7) imidazole rings are protonated and capable of donating hydrogen bonds to bound O₂ in both the α and β subunits of HbO₂. In 2006, Tame's group [2] reported a new ultra high-resolution crystal

structure (1.25 Å) of HbAO₂. The distances between N_ε of His(E7) and bound O₂ in this structure are 2.6 Å and 3.0 Å in the α and β subunits, respectively. These structural observations indicate significant hydrogen bonding with bound ligands in both subunits, a result which is also at odds with the lack of effect of the β His(E7) to Gly mutation reported 20 years ago [16, 103].

In order to resolve the question of hydrogen bonding in β subunits, and test the E7 gate hypothesis in HbA, I systematically studied the effects of His(E7) to Gly, Leu, Phe, and Trp mutations on the kinetics of ligand binding to wild-type/mutant hybrid HbA tetramers, and isolated individual mutant subunits to verify assignments of kinetic and spectral properties within the initial tetramers. New methods were designed to measure rate constants for O₂, CO, and NO binding under conditions that avoid autooxidation of these unstable mutants. The new kinetics results show unambiguously that bound O₂ is stabilized by hydrogen bonding in both subunits of human hemoglobin and suggest that ligands enter each Hb subunit through the distal histidine gate.

3.2. Effects of mutagenesis at E7 position on O₂ association.

In the past, O₂ binding to hemoglobin was measured after flash-photolysis of HbO₂ complexes. There are several problems with this approach when examining distal histidine mutants. First, the quantum yields for complete photodissociation of O₂ into solvent from HbO₂ complexes are inherently small, ≤ 0.1, greatly reducing the signal-to-noise ratio, and the yields often decrease even further when His(E7) is replaced with an apolar amino acid. Second, the E7 apolar mutants autooxidize rapidly and lose hemin, making the HbO₂ forms unstable with half-lives ranging from a few minutes to ≤ one

hour. Third, His(E7) mutants are prepared as reduced CO complexes, which are very stable, and because the E7 mutants have K_{CO}/K_{O_2} ratios in the range 4000 to 40000, the generation of oxy-complexes by the replacement of CO with O₂, even in the presence of strong light, is difficult and almost always leads to oxidation. In the case of the Leu(E7) mutants, CO can only be removed by oxidation with ferricyanide under an intense light, and then the oxygenated complexes have to be generated by reduction with dithionite in air and rapid removal of excess reducing agent and side products by gel filtration.

As described in Chapter 2, Fig. 2.4, Scheme 2.1 and Equations 2.1-2, I have addressed the quantum yield, autooxidation, and CO removal problems by examining O₂ binding and release starting with HbCO complexes in mixtures of O₂ and CO. Direct comparisons between my new data and older rate constant determinations are given in Appendix 1.

Time courses for O₂ rebinding to isolated subunits in photolysis experiments with HbCO in mixtures of O₂ and CO are shown in Fig. 3.2 for the complete set of E7 mutations. Similar experiments were carried out with hybrid tetramers at 10% photolysis. In the case of hybrid tetramers, the observed time courses were fitted to two exponential expressions, one for the wild-type subunit and one for the mutant subunit [70, 109].

Although physiologically more relevant, the assignments of the phases to α and β subunits within Hb tetramers can be ambiguous. The identity problem is resolved by comparisons to ligand binding time courses for isolated α and β chains. In some cases, the monomeric subunits do show slightly different ligand binding properties from those of the corresponding subunits in heterotetramers, but these differences are always small compared to those caused by the mutations (≤ 2 -fold, Table 3.1, [64]).

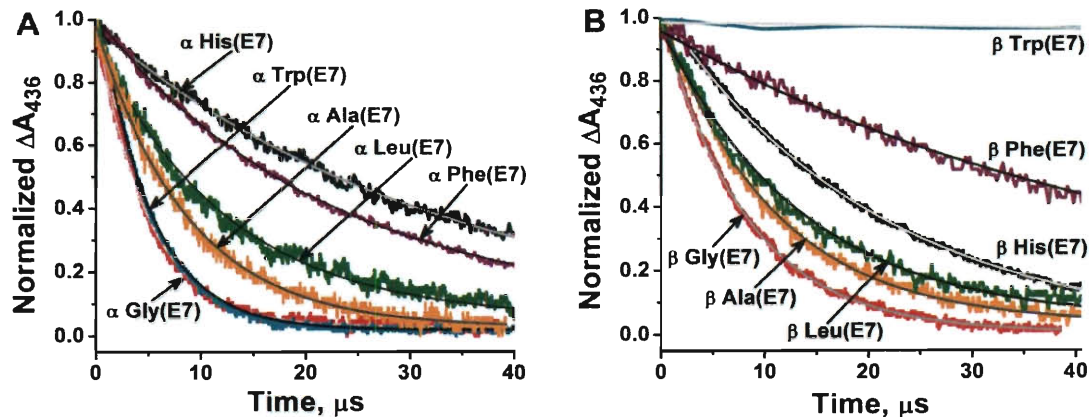


Figure 3.2. Bimolecular binding of O_2 to native and E7 mutants of isolated α and β subunits of recombinant human HbA. In these experiments, $\sim 50 \mu\text{M}$ HbCO was photolyzed with a $0.5 \mu\text{s}$ dye laser excitation pulse in a mixture of $625 \mu\text{M}$ O_2 and $500 \mu\text{M}$ CO in 0.1 M phosphate buffer, pH 7.0 or 50 mM HEPES, 0.1 M NaCl, 0.1 mM EDTA, pH 7.4, 20°C (no differences were observed between these conditions for isolated subunits and R state tetramers in partial photolysis or replacement experiments). Under these conditions the observed first order rate constant, k_{obs} , equals $k'_{\text{O}_2}[\text{O}_2] + k_{\text{O}_2} + k'_{\text{CO}}[\text{CO}]$ and, in most cases, is dominated by O_2 binding. Bimolecular rebinding was monitored at 436 nm, and the time courses were normalized from the absorbance changes for the fast bimolecular phases for ease of comparison between the mutants. (A) Time courses for O_2 rebinding to mutant α -subunits, where E7 refers to position 58; (B) Time courses for O_2 binding to mutant β -subunits, where E7 refers to position 63. Time courses for Ala(E7) were taken from [69].

A summary of the data for both isolated subunits and R-state hybrid tetramers is given in Table 3.1. In β subunits, the rate constant for bimolecular O_2 binding decreases significantly with increasing size of the E7 amino acid, from $160 \mu\text{M}^{-1}\text{s}^{-1}$ for β Gly(E7) to $1.7 \mu\text{M}^{-1}\text{s}^{-1}$ for β Trp(E7) (Fig. 3.2 B, Table 3.1). This dramatic ~ 100 -fold decrease strongly supports the idea that His(E7) is acting as a gate for ligand entry into β subunits. The His(E7) to Gln mutation has little effect on the association rate constants for O_2 binding to either Hb subunit as expected because it is similar in size and polarity to the wild-type histidine.

Table 3.1. Rate and equilibrium constants for O₂ binding to R-state native HbA, mutant hybrid tetramers and isolated mutant subunits with E7 substitutions. Equilibrium association constants were calculated as $K_{O_2} = k'_{O_2}/k_{O_2}$. The superscripts M and T refer to isolated monomers or wild-type/mutant hybrid tetramers, respectively. Data for Ala and Gln(E7) mutants were taken from [69].

Subunit	k'_{O_2} $\mu M^{-1}s^{-1}$	k_{O_2} s^{-1}	K_{O_2} μM^{-1}	Subunit	k'_{O_2} $\mu M^{-1}s^{-1}$	k_{O_2} s^{-1}	K_{O_2} μM^{-1}
α GlyE7 ^M	250	540	0.45	β GlyE7 ^M	160	680	0.24
α GlyE7 ^T	190	500	0.38	β GlyE7 ^T	95	310	0.31
α Ala(E7) ^M	160	880	0.18	β Ala(E7) ^M	120	860	0.14
α Ala(E7) ^T	170	320	0.53	β Ala(E7) ^T	120	520	0.23
α Leu(E7) ^M	91	450	0.2	β Leu(E7) ^{M,1}	110	4600(40%) 630(60%)	0.02 0.18
α Leu(E7) ^T	100±60	680±180	0.14±0.10	β Leu(E7) ^T	110±23	600±170	0.18±0.1
α Gln(E7) ^M	43	42	1.0	β Gln(E7) ^M	70	26	2.7
α Gln(E7) ^T	35	86	0.41	β Gln(E7) ^T	72	42	1.7
α Native ^M	40±2	22±6	2.5±1.2	β Native ^M	63±12	16±1.6	2.3±1.0
α WT ^T	29±11	14±8	1.9±0.5	β WT ^T	60±12	31±13	3.9±0.6
α Phe(E7) ^{M,2}	51 (63, 28)	9800 (13500, 6600)	0.0052	β Phe(E7) ^{M,2}	25 (13, 36)	2400 (1900, 3500)	0.01
α Phe(E7) ^T	47	3500	0.013	β Phe(E7) ^T	33	1700	0.02
α Trp(E7) ^M	210 ~0.5 ³	450	0.47 0.001 ³	β Trp(E7) ^M	1.7	190	0.009
α Trp(E7) ^T	260	940	0.27	β Trp(E7) ^T	4.1	200	0.02

¹ The replacement reactions for isolated Leu(E7) β subunits showed two measurably different phases, whereas the β Leu(E7)/WT mutant tetramers showed only one phase. The relative amplitudes of the two phases for the β Leu(E7) monomer O₂ dissociation traces are given in parentheses.

² Although fits to a single exponential function are satisfactory approximations, the observed time courses for O₂ binding to and dissociation from isolated α and β Phe(E7) chains are slightly biphasic, and the calculated k'_{O_2} and k_{O_2} values for each phase are presented in parentheses. Only one phase could be resolved for the same mutants in hybrid tetramers. Because the heterogeneity was not dramatic (≤ 2 -3-fold), single values for the Phe(E7) monomers were used in all remaining analyses.

³ The fast phases for O₂ binding to the α Trp(E7) monomer in the O₂/CO mixtures appeared monophasic. Slow O₂ rebinding to a closed conformer, similar to that seen for CO rebinding to this mutant (Fig. 3.3 B), is obscured in the oxygen binding experiments because the slow displacement phase (HbO₂ + CO \rightarrow HbCO + O₂) occurs on roughly the same time scale. The slow O₂ rebinding phase was observed in 100% O₂ rebinding experiments without any displacement phase. In this case, the very small slow phase suggests a bimolecular rate constant of $\sim 0.5 \mu M^{-1}s^{-1}$, which is similar in magnitude to that observed in the CO rebinding experiments.

The situation for α subunits is more complex. The value of k'_{O_2} for α Gly(E7) subunits in either R-state tetramers or isolated subunits is also very large, 200-250 $\mu\text{M}^{-1}\text{s}^{-1}$, and decreases as the amino acid is increased in size from Ala to Leu to Phe and His(E7). The average value of k'_{O_2} for α His(E7) subunits is 35 $\mu\text{M}^{-1}\text{s}^{-1}$ (Fig. 3.2 A, Table 3.1). The α Phe(E7) mutant binds O_2 slightly more rapidly than the wild-type α subunit ($\sim 50 \mu\text{M}^{-1}\text{s}^{-1}$ vs. $\sim 35 \mu\text{M}^{-1}\text{s}^{-1}$, respectively), even though the phenyl ring is bigger than the imidazole ring. This difference can be explained by the presence of a water molecule hydrogen bonded to His(E7) in wild type deoxy α subunits [2]. Distal pocket water must be displaced from the active site of wild-type α chains before ligands can enter the heme pocket and coordinate to Fe. The distal pockets of both Phe(E7) mutants are presumed to be anhydrous and the only hindrance to binding is the large aromatic side chain of the E7 residue. The smaller k'_{O_2} value for wild-type α subunits indicates that water displacement offers a larger barrier to ligand binding in this subunit than the benzyl side chain. In the case of the β Phe(E7) mutant, the value of k'_{O_2} is 2-fold smaller than that for wild type β subunits ($\sim 30 \mu\text{M}^{-1}\text{s}^{-1}$ vs. $\sim 60 \mu\text{M}^{-1}\text{s}^{-1}$, respectively). In this case, the lower rate of the mutant subunit is explained by the larger size of the Phe(E7) side chain because no water molecule is present in the distal pocket of native deoxy β subunits or it is highly disordered and easily displaced [2].

The most remarkable result in Fig. 3.2 A and Table 3.1 is the rapid rate of O_2 rebinding to the photolyzed α Trp(E7) mutant in either monomers or tetramers. The observed rate constant is 200-250 $\mu\text{M}^{-1}\text{s}^{-1}$ for α Trp(E7), which is ~ 5 times larger than k'_{O_2} for wild-type α subunits, and identical to that for the α Gly(E7) and α Ala(E7) mutants, in which the E7 gate should be completely open. This result suggests that the

indole side chain of α Trp(E7) adopts an outward pointing conformation when a ligand is bound, but, after photolysis, cannot rotate back into the E7 channel on the time scales observed for bimolecular O_2 binding shown in Fig. 3.2 A. In contrast, O_2 binding to photolyzed β Trp(E7) mutants is slow, indicating rapid relaxation of the indole ring into the E7 channel after photolysis of bound CO and blocking of ligand entry. (Note that O_2 binding was studied in the presence of O_2/CO mixtures to prevent autooxidation and to initiate the reaction by photolyzing the CO complex which has a higher quantum yield).

3.3. Bimolecular CO binding to E7 mutants.

Time courses for CO rebinding to mutant and native isolated α and β subunits are shown in Fig. 3.3, and fitted values of k'_{CO} for isolated chains and subunits within R state tetramers are given in Table 3.2.

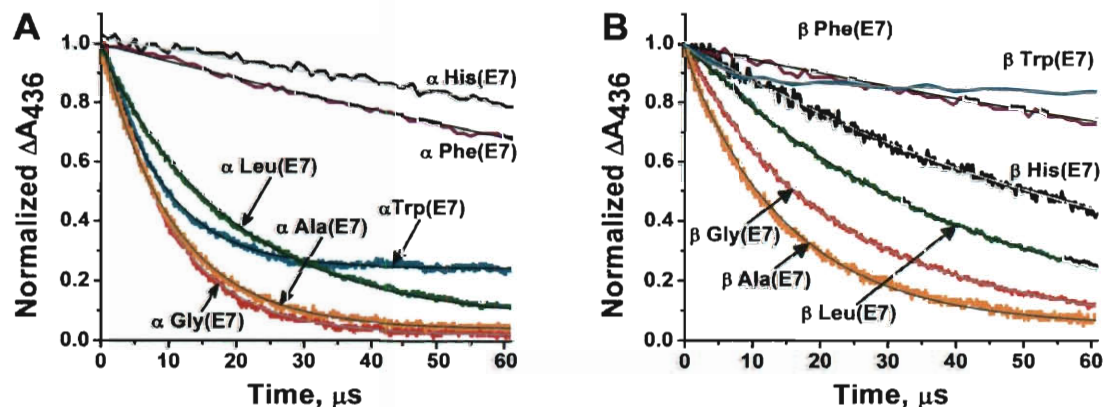


Figure 3.3. Time courses for bimolecular CO rebinding to wild type and E7 mutants of isolated human HbA subunits after laser photolysis. (A) carbon monoxide binding to mutant α -subunits, and (B) carbon monoxide binding to mutant β -subunits, both at $[CO] = 1000 \mu M$ (1 atm). Under these conditions the observed first order rate, k_{obs} , equals $k'_{CO}[CO]$. Bimolecular rebinding was monitored at 436 nm, and the time courses were normalized for ease of comparison between the mutants. Buffer conditions were the same as in Fig. 3.2. Several crystals of sodium dithionite were added into each cuvette to scavenge any residual O_2 . Time courses for Ala(E7) were taken from [69].

Table 3.2. Rate and equilibrium constants for CO binding to native HbA, mutant hybrid tetramers and isolated mutant subunits with E7 substitutions. CO equilibrium association constants for the R state, K_{CO} , were calculated from k'_{CO}/k_{CO} . The superscripts M and T refer to isolated monomers or wild-type/mutant hybrid tetramers, respectively. Data for Ala and Gln(E7) mutants were taken from [69].

Subunit	k'_{CO} $\mu M^{-1}s^{-1}$	k_{CO} s^{-1}	K_{CO} μM^{-1}	Subunit	k'_{CO} $\mu M^{-1}s^{-1}$	k_{CO} s^{-1}	K_{CO} μM^{-1}
α GlyE7 ^M	100	0.013	7700	β GlyE7 ^M	40	0.016	2500
α GlyE7 ^T	77	0.0078	9900	β GlyE7 ^T	53	0.0084	6300
α Ala(E7) ^M	93	0.014	6600	β Ala(E7) ^M	64	0.012	5300
α Ala(E7) ^T	90	0.0096	9400	β Ala(E7) ^T	48	0.01	4800
α Leu(E7) ^M	53	0.0027	20000	β Leu(E7) ^{M,1}	24	0.0056	4300
α Leu(E7) ^T	22	0.0019	12000	β Leu(E7) ^T	29	0.0014	21000
α Gln(E7) ^M	6.3	0.0071	890	β Gln(E7) ^M	10	0.0082	1200
α Gln(E7) ^T	4.8	0.011	440	β Gln(E7) ^T	13	0.0056	2300
α Native ^M	5.2±0.5	0.016±0.003	330±100	β Native ^M	11±3.3	0.010±0.001	1100±240
α WT ^T	4.0±1.1	0.011±0.004	360±200	β WT ^T	7.1±2.0	0.008±0.001	890±440
α Phe(E7) ^{M,1}	5.7 (3.5, 7.5)	0.041	140	β Phe(E7) ^{M,1}	3.9 (1.8, 6)	0.012	330
α Phe(E7) ^T	5.1	0.028	180	β Phe(E7) ^T	3.9	0.012	330
α Trp(E7) ^{M,2}	125(77%) 0.11(23%)	0.008	16000 14	β Trp(E7) ^{M,2}	150(≤20%) 0.7(60%) 0.08(~20%)	0.0037	41000 190 22
α Trp(E7) ^T	53	0.0048	11000	β Trp(E7) ^T	1.3	0.0058	220

¹ The observed time courses for CO binding to isolated α and β Phe(E7) chains were slightly biphasic and analyzed by one and two exponential expressions. I used the single exponential fits in my analyses, and the results of the two exponential analyses are given in parentheses. Note that the differences between fast and slow rate parameters were not dramatic (≤ 2 -3)

² The traces for CO rebinding to the monomeric Trp(E7) mutants contain at least two phases. For α subunits, the fraction of the fast phase is large in 1000 μM CO (77%), but the slow phase becomes dominant at low [CO] (Fig. 3.4 A). For β subunits, there is predominantly one phase (~60%), which is relatively slow ($k'_{CO} = 0.7 \mu M^{-1}s^{-1}$) and the parameter for this phase was used in further analyses. However, both a very small fast and ultraslow phases were detected.

The patterns of dependence on E7 amino acid size are similar to those observed for O₂ rebinding. As shown in Fig. 3.3, the bimolecular rate constants for CO binding to isolated α and β subunits decrease with increasing size for the Gly, Ala, Leu, and His series, from 50-100 $\mu\text{M}^{-1}\text{s}^{-1}$ to ~ 5 -10 $\mu\text{M}^{-1}\text{s}^{-1}$. CO binds slightly faster to the α Phe(E7) mutant than to the WT subunit ($\sim 5.5 \mu\text{M}^{-1}\text{s}^{-1}$ vs. $4.5 \mu\text{M}^{-1}\text{s}^{-1}$), whereas the opposite order is observed for β Phe(E7) and WT subunits. This difference in order is the same as that observed for O₂ binding and, again, is most readily explained by the presence and absence of ordered water in the α versus β deoxygenated subunits, respectively. The same trends are observed for the mutated subunits in tetramers, although assignment of parameters becomes difficult when the mutant reacts at rates similar to those of its partner wild-type subunit.

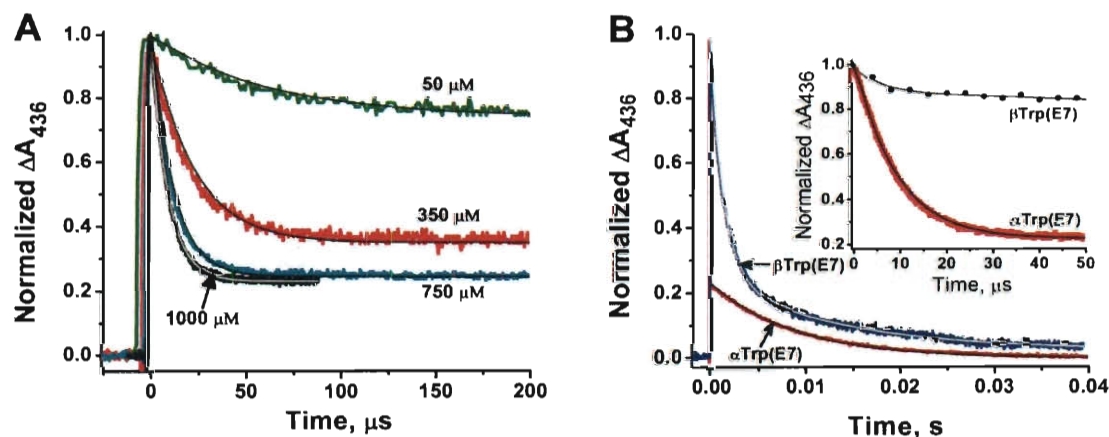


Figure 3.4. Time courses for bimolecular CO rebinding to Trp(E7) mutants after laser photolysis. (A) CO rebinding to isolated α Trp(E7) subunits at four different [CO] labeled beside each time course. The observed bimolecular rates for the fast phases of the reactions were: 16500 s^{-1} , 50 μM CO; 46000 s^{-1} , 350 μM CO; 90000 s^{-1} , 750 μM CO; and 125000 s^{-1} , 1000 μM CO. The subunit concentration was 50 μM . (B) More detailed comparison between the time courses for CO rebinding to monomeric α and β Trp(E7) mutants on both long and short time scales at [CO] = 1000 μM . Several crystals of sodium dithionite were added into each cuvette to scavenge any residual O₂. Data were normalized for the total absorbance change.

The time courses for CO binding to the α and β Trp(E7) mutants demonstrate the complexity implied in the results for O₂ binding. Rebinding to α Trp(E7) subunits at high ligand concentration (*i.e.* 1000 μ M, Fig. 3.4 A) is dominated by a rapid bimolecular phase, which defines a k'_{CO} value equal to $\sim 120 \mu\text{M}^{-1}\text{s}^{-1}$ based on the dependence of $k_{\text{obs,fast}}$ on [CO]. However, a slow phase is clearly present, even at 1000 μ M CO. When [CO] is varied from 1000 to 50 μ M in laser photolysis experiments, the fraction of the fast phase decreases from 77 to $\sim 20\%$ (Fig. 3.4 A). In the case of partial photolysis experiments with mutant hybrid tetramers, multiple phases are also seen but are almost impossible to resolve because of the presence of CO rebinding to wild-type subunits.

The slow phases in Fig. 3.4A for isolated α Trp(E7) subunits indicate a bimolecular rate constant of $0.11 \mu\text{M}^{-1}\text{s}^{-1}$ based on the dependence of the observed pseudo first order rate on [CO]. The presence of such a phase in the ligand binding experiments in O₂/CO mixtures is obscured by the O₂ replacement phase, which occurs on similar time scales. To look for this phase, a fully oxygenated sample of isolated α Trp(E7) subunits was prepared in the absence of CO and then bimolecular O₂ rebinding was measured after laser photolysis of the HbO₂ complex. Two phases of bimolecular O₂ rebinding were observed, and k'_{O_2} values for the fast and slow phases were calculated to be $230 \mu\text{M}^{-1}\text{s}^{-1}$ and $0.5 \mu\text{M}^{-1}\text{s}^{-1}$ (see Table 3.1). The latter rate constant is similar to the k'_{CO} value obtained from the slow phases shown in Fig. 3.4 A.

Together, these results suggest that the indole side chain of α Trp(E7) adopts an outward conformation when ligands are bound. This conformation persists on microsecond time scales after photodissociation. Rotation of the indole side chain into the entry channel occurs at a rate that competes with bimolecular CO binding to the “open”

conformation ($\sim 10^4$ - 10^5 s⁻¹). When the external [CO] is high, ligand binding from the solvent successfully competes with inward movement of the E7 side chain. The fast bimolecular phases after photodissociation represent O₂ and CO binding before the indole side chain has moved back into the E7 channel and over the iron atom. The slow phases represent ligand binding to the equilibrium conformational state of the α deoxyHb mutant, in which the indole side chain fills the E7 channel and blocks ligand entry.

In β subunits, Trp(E7) relaxation after complete photodissociation must be greater than $\sim 10^5$ s⁻¹ because only a small rapid phase (~ 150 $\mu\text{M}^{-1}\text{s}^{-1}$, $\sim 20\%$) is observed at the highest CO concentration and is difficult to define (Fig. 3.3 B and 3.4 B, inset). The majority of the β Trp(E7) CO rebinding phase is slow with k'_{CO} equal to ~ 0.7 $\mu\text{M}^{-1}\text{s}^{-1}$ (60%). A small third phase is seen on longer time scales with a rate similar to that for α Trp(E7) subunits, ~ 0.08 $\mu\text{M}^{-1}\text{s}^{-1}$ ($\sim 20\%$), indicating that slow relaxation to an even more blocked and hindered conformation may also occur in β subunits. This competition between Trp(E7) relaxation and ligand rebinding after photolysis in α subunits is similar to internal His(E7) coordination after photolysis of the CO complexes of non-symbiotic plant Hbs and neuroglobins [110-113]. Tian et al. [87] observed a similar competition in Mb between both geminate and bimolecular CO rebinding and inward relaxation of His(E7) at low pH values where the imidazole side chain is in the protonated open conformation when ligands are bound and in the deprotonated closed state when the heme is unliganded. A more detailed and complete analysis of these Trp(E7) movements and ligand binding to the open and closed conformers is presented in the next chapter.

3.4. Crystal structures of α and β Leu(E7) mutants in CO- and deoxy-state.

In previous sections we hypothesized that the rate of ligand binding to apolar E7 mutants partially increases due to the absence of structured water in the binding site of the protein. In order to provide a direct structural basis for this hypothesis, the structures of the α and β Leu(E7) mutants were determined by X-ray crystallography. Table 3.3 summarizes data collection and refinement statistics.

The structures of the distal pockets of Hb α (Leu(E7)) β (WT) and Hb α (WT) β (Leu(E7)) in CO- and deoxy-forms are shown in Fig. 3.5. No major deviations from wild-type structures are observed, except the differences in the E7 residues and the lack of distal pocket water in the active site of the mutant α subunit. This loss of water is expected, because substituting the polar His by the aliphatic Leu makes the whole binding site completely apolar, making the presence of internal water extremely unfavorable. In wild type α hemoglobin, an internal water molecule is weakly stabilized by electrostatic interactions with the imidazole side chain of His(E7) [2]. Displacement of this distal water represents an additional energy barrier for incoming ligand and slows down the rate of binding compared to the apolar α E7 mutants, which possess anhydrous binding sites. Surprisingly, in the deoxy- β -subunit, distal pocket water is absent even in wild type protein. This phenomenon was demonstrated by Park *et al.* in 2006 [2] and by my present structure of deoxyHb α (Leu(E7)) β (WT) (data not shown). This fact partially explains 2-3 fold higher rates of ligand binding to β WT subunits than to α WT.

Table 3.3. Crystallization and structure determination parameters of Leu(E7) Hb mutants.

Protein	DeoxyHb $\alpha(\text{Leu(E7)})\beta(\text{WT})$	HbCO $\alpha(\text{Leu(E7)})\beta(\text{WT})$	DeoxyHb $\alpha(\text{WT})\beta(\text{Leu(E7)})$	HbCO $\alpha(\text{WT})\beta(\text{Leu(E7)})$
PDB entry code	3QJD	3QJB	3QJE	3QJC
<i>Crystal data:</i>				
Resolution range (Å)	61.79-1.45	99.0-1.8	38.58-1.80	51.37-2.00
Space group	P21	P41212	P21	P41212
Unit cell parameters (Å, °)	a = 62.7, b = 82.1, c = 53.5, β = 99.5	a = b = 53.6, c = 191.2	a = 62.4, b = 81.4, c = 53.5, β = 99.6	a = b = 53.3, c = 192.7
Reflections (measured/unique)	215,542/76,521	111,460/26,524	222,287/41,952	60,659/18,799
Completeness (%)	80.9 (14.2)*	98.1 (96.9)	85.8 (81.9)	95.4 (97.4)
$\langle I \rangle / \sigma \langle I \rangle$	13.0 (1.9)	32.1 (12.5)	12.0 (2.4)	7.7 (4.3)
Redundancy	2.8 (1.5)	4.1 (4.0)	5.18 (5.43)	4.0 (4.0)
R_{merge} (%)	4.4 (16.1)	5.1 (14.8)	7.5 (30.2)	9.8 (22.9)
<i>Refinement:</i>				
Resolution range (Å)	20.60-1.56	37.18-1.80	38.58-1.80	51.37-2.00
R-factor (%)	16.9	17.0	19.9	19.4
R_{free} (%)	19.1	20.5	24.3	25.0
<i>RMS deviations from ideal values:</i>				
Bond length (Å)	0.006	0.027	0.007	0.028
Bond angles (°)	1.193	0.989	1.223	0.994
<i>Ramachandran plot:</i>				
Residues in most favorable region (%)	98.3	98.6	98.0	98.7
Residues in additional allowed region (%)	1.7	1.4	2.0	1.3

*Parameters in parentheses () are for the outer resolution shell

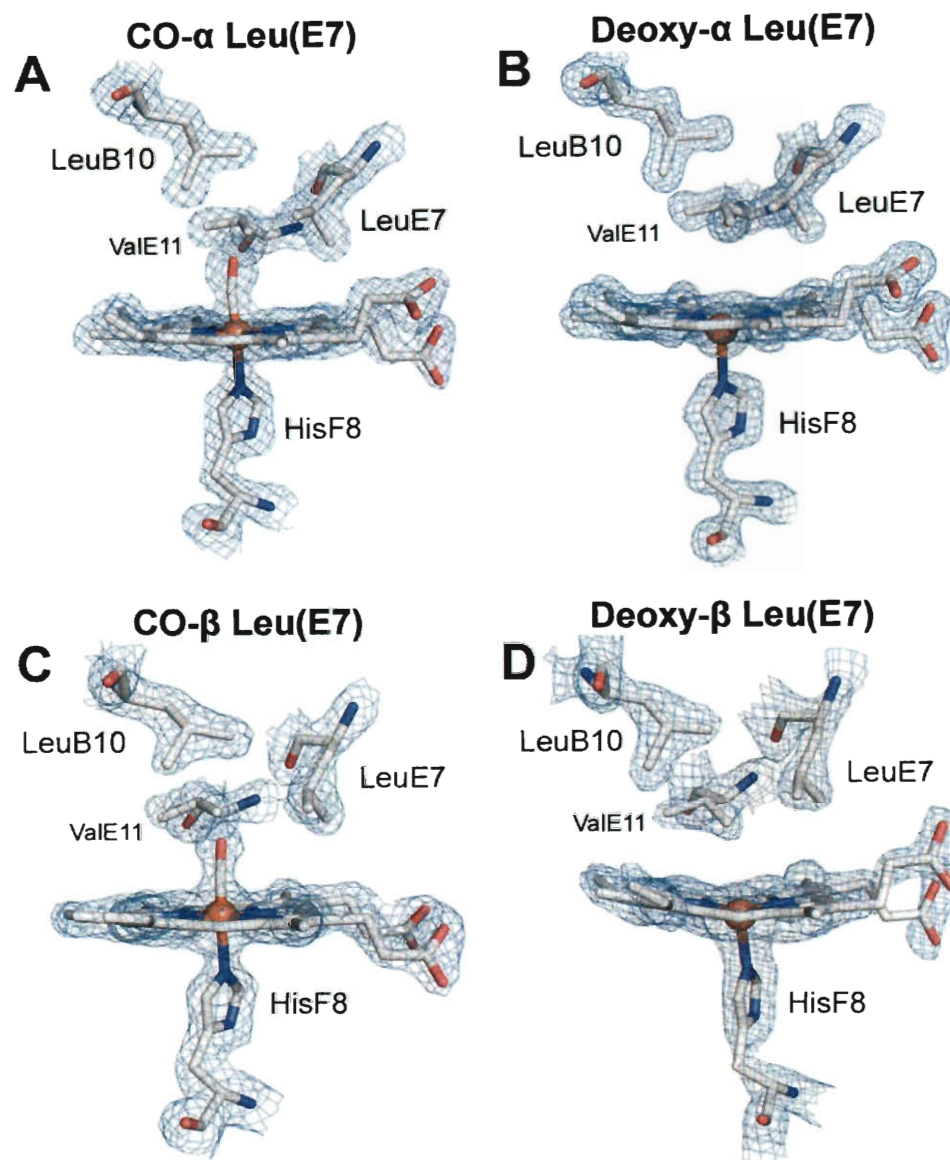


Figure 3.5. Structures of CO- and deoxy-forms of α and β Leu(E7) distal pockets. The electron density was contoured at 1.3σ and is shown as a blue net. Color code: white, carbon; red, oxygen; blue, nitrogen; orange sphere, iron.

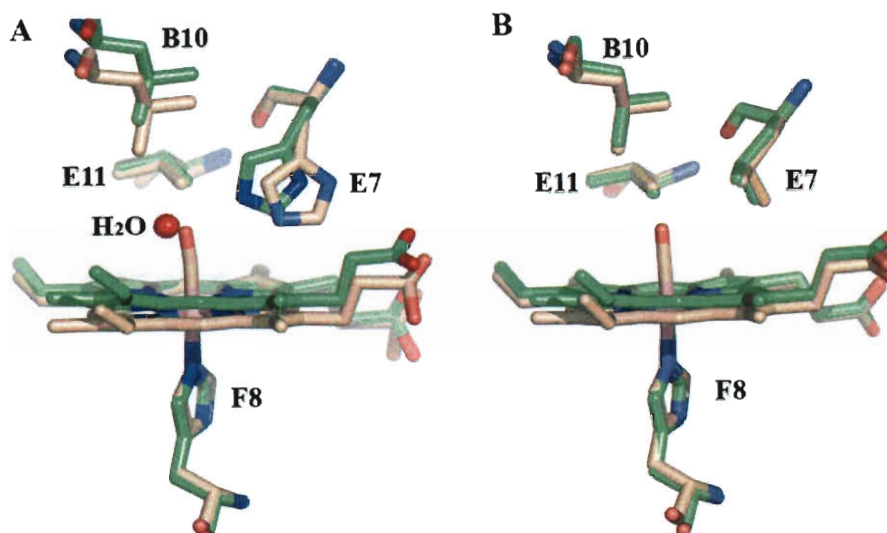


Figure 3.6. Stick models of deoxy (*green*) and CO-forms (*beige*) of α WT (A) and α Leu(E7) (B) distal pockets. The wild-type structures were created using the following PDB entries: 2DN2 for CO-form and 2DN3 for deoxy-form [2]. Color code: green or beige, carbon; red, oxygen; blue, nitrogen; pink, iron. Red sphere in (A) represents distal pocket water molecule in deoxy- α WT subunit.

In Fig. 3.6, the α Leu(E7) and α WT distal pockets in deoxy- and CO-forms are superimposed. In α WT, after photolysis, His(E7) rotates inward towards iron and occupies the "deoxy" position, which hinders ligand rebinding (Fig. 3.6A, [12]). In the mutant subunit, the immediate vicinity of iron is less crowded in both CO- and deoxy-forms of the protein, and the position of Leu(E7) does not change upon ligand dissociation (Fig. 3.6B). The greater accessibility of the iron atom explains the larger fractions of geminate recombination of photodissociated ligands in Leu(E7) mutants in comparison to HbA due to greater ease of bond formation. Moreover, the larger His side chain appears to represent a bigger barrier for the entering ligand than Leu, supporting previously proposed inverse relationship between the size of the E7 moiety and the rate of ligand recombination.

3.5. Direct and indirect measurements of ligand entry into α and β E7 mutants of HbA.

Two other sets of experiments were carried out to verify that the E7 mutations are directly affecting the rate of ligand entry into hemoglobin. Internal CO recombination after photolysis was examined on nanosecond time scales to determine the fraction of geminate recombination and estimate rates of internal ligand bond formation and escape using Equations 2.7-8 (Chapter 2). CO is the ligand of choice for hemoglobin subunits, because the quantum yield for formation of the initial CO geminate state is close to unity and the observed rate of geminate CO recombination, 2 to 70 μs^{-1} , is readily measured on nanosecond time scales. Geminate O₂ rebinding to α and β chains in the R state is too rapid to measure readily with a 7 ns YAG laser pulse, requires assumptions of a single phase for analysis of events occurring during the light pulse, and exhibits a quantum yield for formation of the geminate state of ≤ 0.2 [16]. The rates of CO entry and exit appear to be the same as those for O₂ and NO because all three diatomic gases have almost the same size and polarity [22, 32, 73, 114]. The major differences are for the iron coordination rates, k_{bond} , with $\text{NO} \gg \text{O}_2 > \text{CO}$ due to a wide range of chemical reactivities [18, 19, 73, 115, 116].

Time courses for geminate CO rebinding to isolated α and β E7 mutants are shown in Fig. 3.7. As in the case of Mb, the dependence of geminate recombination on the size of the E7 residue is complex [17, 22, 72, 89]. Replacement of His(E7) with Gly, Ala, and Leu increases the fraction of internal recombination (F_{gem}) by removal of steric hindrance for ligand return to the iron atom. As a result of these mutations, the rates of internal bond formation increase 5 to 10-fold with little change in the computed rate

constant for escape (Table 3.4). In contrast, the extents of geminate recombination in the wild type, Gln(E7), and Phe(E7) subunits are all small. As in Mb, the His(E7) and Gln(E7) side chains are close enough ($\leq 3\text{\AA}$) to donate hydrogen bonds to bound ligands, but this proximity results in steric hindrance of the initial photodissociated ligand, pushing it back into the distal pocket and inhibiting its return to the iron atom [17, 117]. As a result, k_{bond} is relatively small for CO rebinding, and the fraction of geminate recombination, F_{gem} , is ≤ 0.3 for the isolated wild type Hb subunits, and the same steric effect appears to occur for the Phe(E7) mutants.

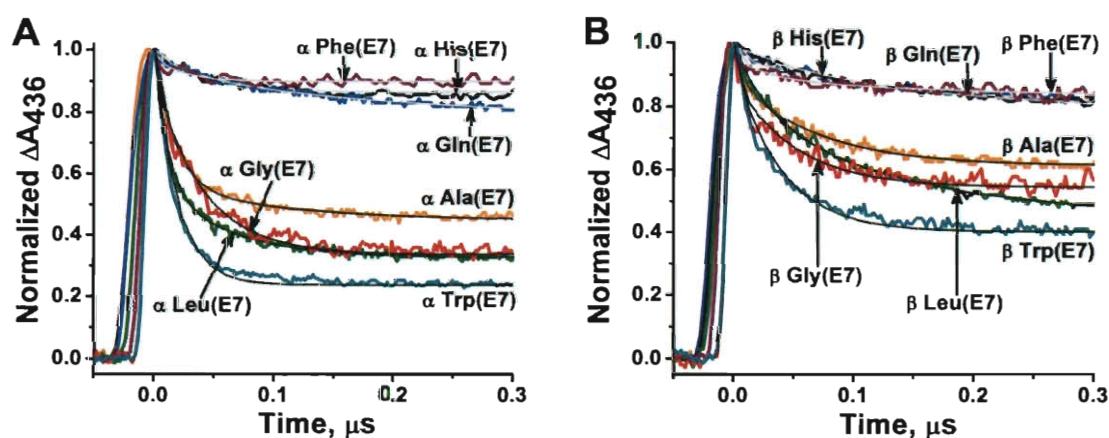


Figure 3.7. Geminate CO recombination in wild type and E7 mutants of isolated α and β subunits of recombinant human HbA. In these experiments, $\sim 50\ \mu\text{M}$ HbCO was photolyzed with a 7 ns Nd:YAG laser excitation pulse (at time 0.0) in $1000\ \mu\text{M}$ CO. Buffer conditions were the same as in Fig. 3.2. Geminate rebinding was monitored at 436 nm and the absorbance changes were normalized for comparison between the mutants. Time courses were fitted to single exponential expressions; F_{gem} is calculated as $(\text{total } \Delta A_{436} - \text{offset})/(\text{total } \Delta A_{436})$, k_{gem} is equal to the observed rate of the first order internal rebinding phase. (A) Time courses for geminate CO rebinding to mutant α -subunits, where E7 refers to position 58; (B) Time courses for geminate CO recombination to mutant β -subunits, where E7 refers to position 63.

The fractions of geminate recombination and the observed overall association rate constants for CO binding were used to estimate the bimolecular rate constants for ligand entry into the individual subunits of Hb. k'_{entry} is defined as the observed bimolecular rate constant divided by the empirically determined fraction of internal recombination, i.e.

$k'_{\text{entry}} = k'_{\text{CO}}/F_{\text{gem}}$ (see Equation 2.9, Chapter 2), regardless of the number of steps in the mechanism. Unlike the values of k_{bond} and k_{escape} , which assume only a two step mechanism, k'_{entry} is a relatively model independent parameter [22].

As shown in Table 3.4, there is a general decrease in k'_{entry} with increasing size of the E7 amino acid. Again the results for the Trp(E7) mutants warrant more careful consideration. In the case of α subunits, the large fractions of geminate rebinding and values for k_{bond} almost certainly represent CO recombination in an open conformation with the indole side chain pointing outward and with little or no steric hindrance near the iron atom. These parameters in combination with the rate for the fast bimolecular CO rebinding phase, predict that k'_{entry} for the open conformation is $\sim 160 \mu\text{M}^{-1}\text{s}^{-1}$, which is similar to that for α Gly(E7) and close to the diffusion limit, $\sim 200\text{-}500 \mu\text{M}^{-1}\text{s}^{-1}$, observed for pentacoordinate model hemes ([118, 119] and hemoglobins with unhindered active sites (i.e. leghemoglobins [120] and *Cerebratulus lacteus* mini-globin [68]). However, when α Trp(E7) relaxes to its equilibrium deoxyHb conformation, the rate of entry is markedly reduced, with a computed value of $k'_{\text{entry}} \approx 0.14 \mu\text{M}^{-1}\text{s}^{-1}$. In the case of isolated β Trp(E7) subunits, both slow phases for bimolecular CO rebinding after laser photolysis predict small values for k'_{entry} (Table 3.4).

To further verify the k'_{entry} calculations based on CO kinetics, the bimolecular association rate constants for NO binding to both mutant monomers and tetramers were measured. Many workers have shown that the fraction of geminate recombination of NO in mammalian Hbs and Mbs is ≥ 0.99 , with bond formation occurring on picosecond time scales [17, 72, 121] due to the high reactivity of the NO radical with high spin ferrous iron. In terms of Equation 2.9, Chapter 2, $F_{\text{gem}} \approx 1.0$ and $k'_{\text{entry}} = k'_{\text{NO}}$. In the case of Mb,

Scott *et al.* [22] showed that the rate constants for ligand entry computed from analysis of geminate and bimolecular O₂ binding correlate linearly with association rate constants for NO binding to ~30 different mutants.

Table 3.4. Rate constants for bimolecular CO and NO binding, and parameters for CO geminate recombination to isolated α and β E7 mutants. $k'_{\text{NO}}^{\text{tet}}$ represents NO binding to mutant subunits within Hb tetramers. All other parameters presented are for ligand binding to isolated subunits, Native α and β subunits have His(E7). Conditions were the same as in Table 3.1.

Subunit	k'_{CO} $\mu\text{M}^{-1}\text{s}^{-1}$	F_{gem}	k_{gem} μS^{-1}	k_{bond} μS^{-1}	k_{escape} μS^{-1}	k'_{entry} $\mu\text{M}^{-1}\text{s}^{-1}$	k'_{NO} $\mu\text{M}^{-1}\text{s}^{-1}$	$k'_{\text{NO}}^{\text{tet}}$ $\mu\text{M}^{-1}\text{s}^{-1}$
α GlyE7	100	0.63	25	17	8.6	150	170	140
α Ala(E7)	93	0.57	37	21	16	160	150	160
α Leu(E7)	53	0.66	45	30	16	80	82	64
α Gln(E7)	6.3	0.23	22	5.1	17	27	45	42
α Native	5.2	0.14	24	3.4	21	36	31	25
α Phe(E7)	5.7	0.13	69	8.9	60	44	94	71
α Trp(E7) ¹	125 (77%) 0.11 (23%)	0.77	67	52	15	160 0.14	150 ~0.4	n.d.
β GlyE7	40	0.45	20	9	11	89	140	120
β Ala(E7)	64	0.39	16	6.4	9.6	160	170	130
β Leu(E7)	24	0.55	14	7.7	6.3	44	91	68
β Gln(E7)	10	0.22	6	1.3	4.7	45	69	63
β Native	9.2	0.22	7.6	1.7	6	42	68	66
β Phe(E7)	3.9	0.14	37	5.2	32	28	53	44
β Trp(E7) ¹	150(~20%) 0.7(60%) 0.08(~20%)	0.61	70	43	27	(250) 1.2 (0.13)	5.4	6.4

¹The values of k'_{entry} for the Trp(E7) mutants were calculated using the single F_{gem} value listed in column 3 and the k'_{CO} values for all the observed phases.

Time courses for NO binding to native α and β subunits are shown in Fig. 2.5, Chapter 2; summaries of all the bimolecular rate constants are listed in Table 3.4; and the strong linear correlation between k'_{NO} and the k'_{entry} values calculated from CO binding data is shown Fig. 3.8.

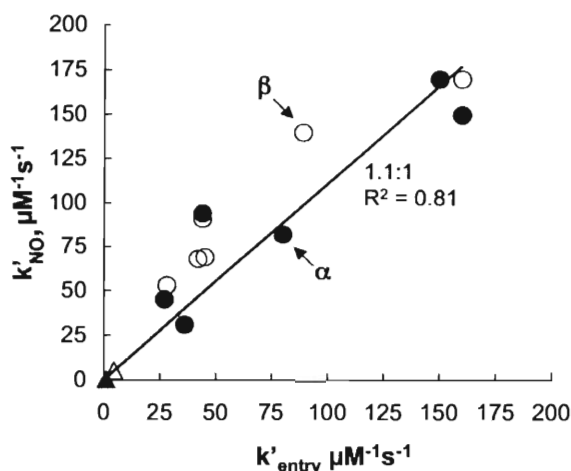


Figure 3.8. Ligand entry and NO binding to E7 mutants of HbA subunits. Comparison of calculated rates of CO entry with the bimolecular rate constants measured for NO binding to recombinant Hb. Data were taken from Table 3.4. The closed and open circles represent isolated α and β subunit rate constants, respectively, and the open and closed triangles represent values for the closed α and slowly reacting β Trp(E7) conformers.

These results confirm the ~ 2 -fold greater rate of ligand association with native β subunits than with α subunits, the ~ 200 -fold decrease in the bimolecular rate constant for ligand entry in HbA with increasing size of the E7 side chain, and the competition between α Trp(E7) relaxation to the closed conformation and ligand rebinding. In the latter case, two phases are observed for NO rebinding to isolated α Trp(E7) subunits, with the dependence on [NO] suggesting fast and slow k'_{NO} values ≈ 150 and $0.4 \mu\text{M}^{-1}\text{s}^{-1}$, respectively. The slow phase k'_{NO} value is similar to that obtained from the slow phases for O_2 and CO bimolecular rebinding to α Trp(E7) mutants (Tables 3.1 and 3.2).

3.6. Rate constants for O_2 and CO dissociation from the α and β E7 mutants.

Rate constants for O_2 dissociation were obtained by analyzing the slow phase time courses for the displacement of transiently bound O_2 by CO after laser photolysis of HbCO complexes of both isolated chains and mutant/wild-type recombinant HbA

tetramers in O₂/CO mixtures (Equations 2.1-2, Fig. 2.4, Chapter 2). Sample time courses for O₂ replacement from native and E7 mutants of isolated α and β chains are shown in Fig. 3.9, and a summary of the fitted k_{O_2} values for R state HbA are listed in Table 3.1.

It is clear that replacement of His(E7) with apolar amino acids causes marked, 20 to 500-fold increases in the rate of O₂ dissociation from both subunits. As expected, the conservative His(E7) to Gln mutations cause the least effect, 2 to 4-fold increases in k_{O_2} , whereas the Phe(E7) mutations cause the largest increases, from $\sim 20\text{ s}^{-1}$ in wild-type HbO₂ to $\sim 2,400\text{ s}^{-1}$ in β Phe(E7) chains and $9,800\text{ s}^{-1}$ in α Phe(E7) chains (Table 3.1). Similar trends were observed for the corresponding mutant subunits in hybrid tetramers, although the numerical values in these cases are almost always smaller.

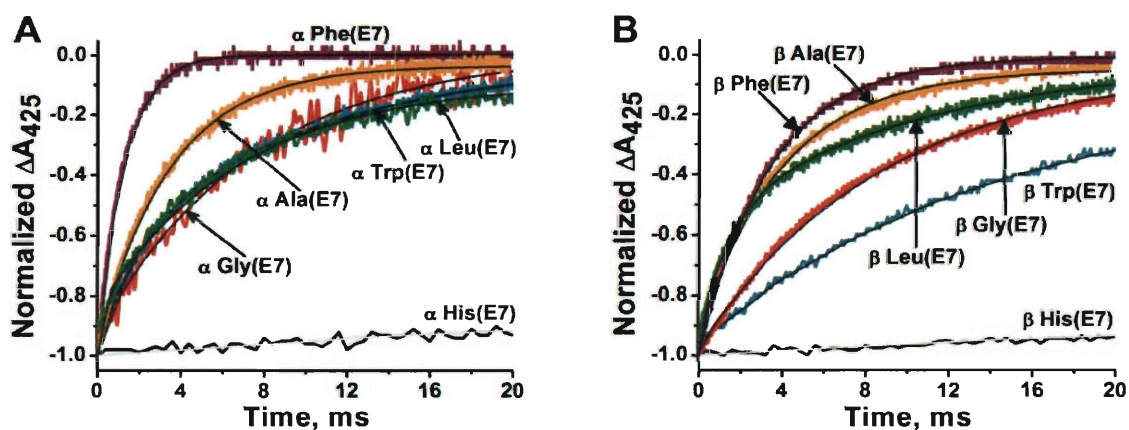


Figure 3.9. Time courses for O₂ replacement by CO in native and E7 mutant α and β subunits. The solutions contained a mixture of $625\ \mu\text{M}$ O₂ and $500\ \mu\text{M}$ CO. Buffer conditions were the same as in Fig. 3.2. Absorbance changes were detected at 425 nm and normalized for comparison between the mutants. In these experiments, HbO₂ is transiently formed after photolysis of HbCO with a $0.5\ \mu\text{s}$ dye laser pulse, and then is slowly displaced by CO present in the solution. Only the slow O₂ replacement phase of the reaction is shown, and for these time courses, the observed first order rate constant, r_{obs} , equals $k_{O_2} / (1 + k'_{O_2}[O_2]/k'_{CO}[CO])$. (A) O₂ dissociation from α -subunits, where E7 refers to position 58; (B) O₂ dissociation from β -subunits, where E7 refers to position 63.

The results for the Gly, Ala, and Leu(E7) mutations show that hydrogen bonding to the native His(E7) side chain stabilizes bound O₂ roughly 20 to 30-fold in both

subunits. In the case of β Leu(E7), heterogeneous O₂ displacement time courses were observed for isolated subunits but not for the mutant in tetramers (Fig. 3.9 B, Table 3.1). The heterogeneity for isolated Leu(E7) β subunits was verified in two completely independent preparations and does not depend on subunit concentration. The latter observation rules out differences between β monomers and tetramers and suggests conformational mobility in the active site of the isolated β chains (Appendix 1).

The much greater increase in k_{O_2} observed for the Phe(E7) mutants suggests that the larger benzyl side chain is sterically hindering the bound ligand, causing a greater rate of thermal bond disruption (k_{bond} in Scheme 2.5, Chapter 2) and sterically restricting return to the iron atom after dissociation. This interpretation is supported by the low fractions of geminate ligand rebinding to the α and β Phe(E7) mutants shown in Fig. 3.7 and Table 3.4. The rate constants for O₂ dissociation from the Trp(E7) mutants are smaller than those for the Phe(E7) mutants and more similar to those of the other apolar mutants. Presumably, the indole ring cannot be accommodated in the active site when a ligand is bound, and, therefore, does not sterically clash with the bound ligand and increase the rate of ligand-Fe bond disruption. In addition, the large indole ring may also block ligand exit from the distal pocket. Both of these effects increase geminate recombination and lower overall rates of ligand dissociation.

Rate constants for CO dissociation from isolated chains and intact tetramers are listed in Table 3.2. Unlike O₂ dissociation, there is only a small variation in k_{CO} , from ~ 0.04 to 0.002 s^{-1} for the His(E7) mutants, with the native value of k_{CO} being $\sim 0.01 \text{ s}^{-1}$ for both subunits. There is little change in the rate of CO dissociation for the Gly and Ala(E7) mutations, but a 5-fold decrease in k_{CO} is observed for both Leu(E7) mutations,

giving these mutants unusually high affinities as has been observed for Leu(E7) mutants in several different mammalian Mbs (Table 3.2, [12, 85]).

3.7. Measurements of distal pocket polarity in E7 mutants of HbA by FTIR spectroscopy.

The marked increases in the rate of O₂ dissociation due to the apolar E7 mutations in HbA indicate hydrogen bond donation from N_εH of His(E7) to bound O₂ atoms. As a final test of this idea, the C-O stretching frequencies of bound CO, $\nu_{\text{C-O}}$, for the complete series of mutant subunits were measured (Fig. 3.10 and Table 3.5). Many authors have shown that the positive electrostatic field from the N_εH atoms of His(E7) causes lower $\nu_{\text{C-O}}$ values for MbCO and HbCO complexes [82, 83, 85, 122, 123]. In sperm whale MbCO, a strong positive electrostatic field is exerted by two major His(E7) conformations and gives rise to peaks at 1932 and 1945 cm⁻¹ for the wild-type protein. Mutation of His(E7) to Ala, Val, Leu, or Phe in Mb causes shifts to single peaks in the 1962-1968 cm⁻¹ region, and similar values of $\nu_{\text{C-O}}$ are observed for model CO-heme complexes in apolar environments [83, 122]. The $\nu_{\text{C-O}}$ shifts in mutant MbCOs correlate with increases in k_{O_2} from 15 s⁻¹ to 5,000 - 10,000 s⁻¹ [85].

Representative FTIR spectra for wild-type and mutant Hb hybrid tetramers in the region of the C-O stretching frequency (1900 - 2000 cm⁻¹) are shown in Fig. 3.10 A, and spectra for isolated Hb subunits with His (native), Phe and Trp residues at the E7 position are shown in Fig. 3.10 B. The values of the corresponding peak maxima for all the distal His mutants are summarized in Table 3.5. Mutation of His(E7) to apolar amino acids in

HbA causes shifts of the $\nu_{\text{C-O}}$ peak, from 1950-1951 cm^{-1} for wild-type and native subunits to 1967-1973 cm^{-1} for the mutant subunits, both as monomers and in tetramers.

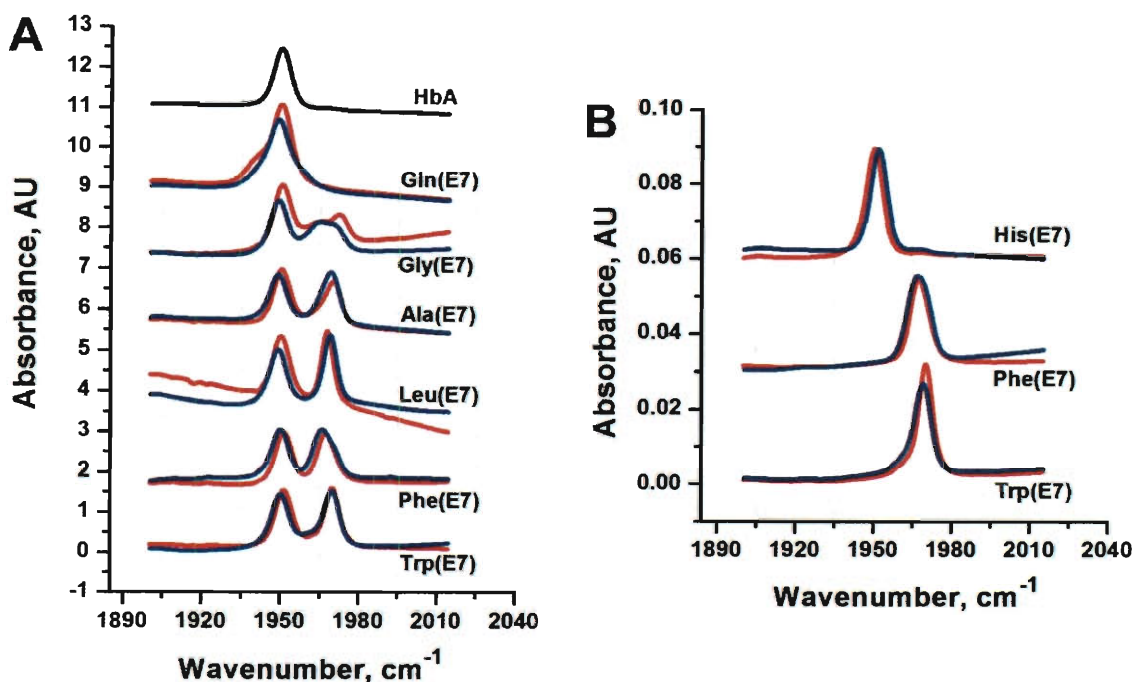


Figure 3.10. FTIR spectra of wild type and E7 mutants of human HbA. (A) Spectra for wild type HbA (black) and mutant hybrid Hb tetramers (red spectra represent Hb tetramers containing mutant α chains; blue spectra represent Hb tetramers containing mutant β chains). (B) Spectra of isolated native and mutant α (red) and β (blue) subunits. Buffer conditions were the same as in Fig. 3.2.

For all three globins, the FTIR spectra of the Gly(E7) mutants show a much broader high frequency peak, which in α subunits is clearly split into two peaks. The crystal structure of Gly(E7) metMb shows discrete water molecules in the distal pocket in positions similar to those of the N_δ and N_ϵ atoms of His(E7) in the wild-type protein [89]. Thus, multiple electrostatic fields exerted by different water conformers give rise to broadening and splitting of all the Gly(E7) mutant $\nu_{\text{C-O}}$ peaks. As expected, replacing His(E7) with Gln does not significantly change the position of the IR band. However, in

both subunits, the peak is broader than that of wild-type protein, indicating greater conformational heterogeneity of the amide side chain than that for the imidazole ring in the native subunits. In the case of the α Gln(E7) mutant subunits, a low frequency shoulder is observed at 1945 cm^{-1} , implying a small fraction of a conformer with a more positive field near bound CO than that in native α subunits containing His(E7) (Fig. 3.10, Table 3.5).

Table 3.5. Bound C-O stretching frequency peaks, $\nu_{\text{C-O}}$, for WT and mutant α and β subunits of native and recombinant human hemoglobin. Conditions were the same as in Table 3.1. The superscripts M and T refer to isolated monomers or wild-type/mutant hybrid tetramers, respectively.

Subunit	$\nu_{\text{C-O}}\text{ cm}^{-1}$	Subunit	$\nu_{\text{C-O}}\text{ cm}^{-1}$
α Native ^M	1950	β Native ^M	1950
α WT ^T	1950	β WT ^T	1951
α Gln(E7) ^M	1945,1950	β Gln(E7) ^M	1950
α Gln(E7) ^T	1945,1951	β Gln(E7) ^T	1950
α Gly(E7) ^T	1965,1973	β Gly(E7) ^T	1965,1971
α Ala(E7) ^M	1972	β Ala(E7) ^M	1971
α Ala(E7) ^T	1971	β Ala(E7) ^T	1969
α Leu(E7) ^M	1969	β Leu(E7) ^M	1970
α Leu(E7) ^T	1969	β Leu(E7) ^T	1970
α Phe(E7) ^M	1967	β Phe(E7) ^M	1967
α Phe(E7) ^T	1967	β Phe(E7) ^T	1967
α Trp(E7) ^M	1970	β Trp(E7) ^M	1969
α Trp(E7) ^T	1970	β Trp(E7) ^T	1969

Twenty years ago, Yu's group [124] obtained very similar values of $\nu_{\text{C-O}}$ for CO bound to α Gln and Gly(E7) and to β Gln, Gly, Val, and Phe E7 mutant/wild-type hybrid tetramers using resonance Raman techniques. Our new results and their old data suggest strongly that positive electrostatic fields occur near bound ligands in both native HbA subunits, and are lost when His(E7) is mutated to an apolar amino acid.

3.8. O₂ affinity of E7 mutants and hydrogen bonding.

The 1.25Å resolution crystal structures of the α and β subunits in oxygenated human HbA are shown in Fig. 3.11 [2]. Even a cursory examination shows that the imidazole side chains in both subunits have roughly the same conformation and are equidistant from the bound O₂ atoms. The reported distances between the His(E7) N_εH atoms and the ligand atoms in the α and β subunits are 2.7 and 3.0 Å, respectively [2]. These distances are similar to the values reported for MbO₂, 2.6-2.8 Å [89, 125]. The effects on oxygen affinity of the apolar E7 amino acid substitutions allow an assessment of the relative strengths of the apparent hydrogen bonds within these three globins.

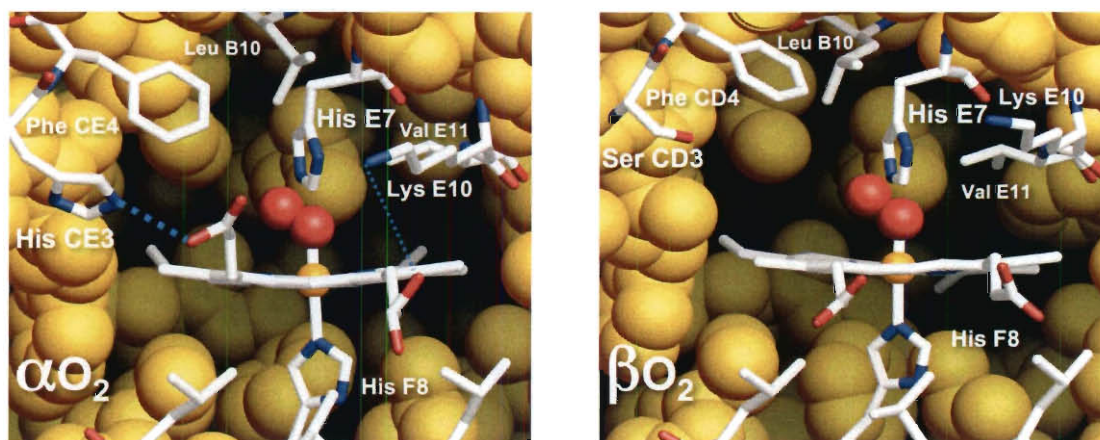


Figure 3.11. Structures of the α and β active sites in HbO₂. The structures were constructed from the PDB file 2DN1, containing the high resolution structure of human oxyhemoglobin A determined by Park *et al.* [2]. The key residues of the heme pocket are labeled and shown in sticks. The atoms of the key amino acids are colored as following: white, carbons; blue, nitrogens; red, oxygens; yellow, the atoms of other residues lining the binding site; red, O atoms of bound dioxygen; and orange, heme Fe. The blue dotted lines in the α subunits represent H-bonds between His (CE3) and the carboxylate O atoms of the heme-6-propionate, and Lys (E10) and the carboxylates of the heme-7-propionate.

The free energy released when O₂ binds to a globin can be divided into four components: (1) the intrinsic free energy change for binding to an unhindered

pentacoordinate heme in an apolar environment, $\Delta G^{\circ}_{\text{heme}}$; (2) the free energy changes associated with restricted movement of the iron into the plane of the heme, which is governed by constraints on the geometry of the Fe-His(F8) complex and back-bonding by the proximal imidazole, $\Delta G^{\circ}_{\text{prox}}$; (3) hindrance with surrounding distal pocket amino acids, excluding possible steric clashes with E7 residue, $\Delta G^{\circ}_{\text{distal}}$; and (4) both favorable and unfavorable interactions with E7 side chain, $\Delta G^{\circ}_{\text{E7}}$ (Equation 3.1).

$$\Delta G^{\circ}_{\text{O}_2} = \Delta G^{\circ}_{\text{heme}} + \Delta G^{\circ}_{\text{prox}} + \Delta G^{\circ}_{\text{distal}} + \Delta G^{\circ}_{\text{E7}}$$

Equation 3.1

Interactions with the E7 amino acid side chain can be divided into three categories: (a) stabilization of the bound ligand by hydrogen bond donation, $\Delta G^{\circ}_{\text{E7H-bond}}$; (b) inhibition of ligand binding by distal pocket water, which in the native deoxyHb subunits can be hydrogen bonded to the imidazole side chain, $\Delta G^{\circ}_{\text{E7water}}$; and (c) direct or indirect steric hindrance with the bound ligand, $\Delta G^{\circ}_{\text{E7steric}}$.

$$\Delta G^{\circ}_{\text{E7}} = \Delta G^{\circ}_{\text{E7H-bond}} + \Delta G^{\circ}_{\text{E7water}} + \Delta G^{\circ}_{\text{E7steric}}$$

Equation 3.2

When His(E7) is mutated to smaller apolar amino acids, *i.e.* Gly, Ala, and Leu, the values of $\Delta G^{\circ}_{\text{heme}}$, $\Delta G^{\circ}_{\text{prox}}$, and $\Delta G^{\circ}_{\text{distal}}$ should be unaltered. The effects of small apolar E7 substitutions on the overall free energy of O₂ binding, $\delta\Delta G^{\circ}_{\text{mutant}}$, can be

calculated from the ratio of the mutant to wild-type equilibrium constants (Equation 3.3) and should equal $\delta\Delta G^\circ_{E7}$.

$$\delta\Delta G^\circ_{\text{mutant}} = \Delta G^\circ_{O_2}(\text{mutant}) - \Delta G^\circ_{O_2}(\text{wt}) = -RT \ln \left(\frac{K_{O_2}(\text{mutant})}{K_{O_2}(\text{wt})} \right) = \delta\Delta G^\circ_{E7}$$

Equation 3.3

Because these amino acid side chains are small and apolar, they do not interact with bound ligands nor do they stabilize internal water molecules, and all three terms in Equation 3.2 should be zero for O₂ binding to these variants, *i.e.* $\Delta G^\circ_{E7}(\text{mutant}) = 0$. As a result, $\delta\Delta G^\circ_{E7} = -\Delta G^\circ_{E7}(\text{WT})$. If it is assumed that there are no unfavorable steric interactions between bound ligands and His(E7) ($\Delta G^\circ_{\text{HisE7Steric}} = 0$) and that the close proximity of the imidazole side chain to bound O₂ and CO is due to favorable hydrogen bonding interactions, according to Equation 3.2, $\delta\Delta G^\circ_{E7}$ should be approximately equal to $-(\Delta G^\circ_{\text{HisE7water}} + \Delta G^\circ_{\text{HisE7H-bond}})$, which represents the free energy difference between the loss of the unfavorable requirement to displace water non-covalently attached to His(E7) and the loss of favorable electrostatic stabilization of the bound ligand by His(E7) [12].

Values of $-\delta\Delta G^\circ_{E7}$ for isolated and tetrameric α and β subunits of HbA were calculated using the average values for the Gly, Ala, and Leu(E7) mutants for $K_{O_2}(\text{mutant})$ in Equation 3.3 and are compared in Table 3.6 with that computed for sperm whale Mb using the average K_{O_2} value for Ala, Val, and Leu(E7) mutants. Gly(E7) Mb was excluded because there are discrete water molecules in the distal pocket that clearly

Table 3.6. Effects of small apolar E7 mutations on ΔG° for O_2 binding to HbA and sperm whale Mb. $\delta\Delta G_{\text{mutant}} = \delta\Delta G_{E7} = -RT\ln(K_{O_2}(\text{mutant})_{\text{ave}}/K_{O_2}(\text{native}))$, where $K_{O_2}(\text{mutant})_{\text{ave}}$ represents the average O_2 affinity for unhindered E7 mutants containing Gly, Ala, and Leu at the E7 position (Equations 3.2 and 3.3). Oxygen affinities for these calculations were taken from Table 3.1. The K_{O_2} values for sperm whale Mb were taken from [22] as described in the text. Superscript M and T stand for monomer and tetramer, respectively. As described in the text, $-\delta\Delta G_{E7}$ for small apolar mutations defines the net electrostatic stabilization of bound O_2 His(E7) defined as the sum, $\Delta G^\circ_{\text{HisE7water}} + \Delta G^\circ_{\text{HisE7H-bond}}$. Estimates of free energy for water displacement from native deoxyHb or deoxyMb were computed from $-(-RT\ln(k'_{O_2}(\text{mutant})_{T,M,ave}/k'_{O_2}(\text{native,wild-type})_{ave}))$, where $k'_{O_2}(\text{mutant})_{T,M,ave}$ is the average O_2 association rate constant for Gly, Ala, Leu E7 mutants in monomers and tetramers of Hb subunits and Ala, Val, and Leu E7 mutants of Mb. Estimates of the free energy for H-bond donation to bound O_2 were computed from $-RT\ln(k_{O_2}(\text{mutant})_{T,M,ave}/k_{O_2}(\text{native,wild-type})_{ave})$, where $k_{O_2}(\text{mutant})_{T,M,ave}$ is the average O_2 dissociation rate constant for Gly, Ala, Leu E7 mutants in monomers and tetramers of Hb subunits and Ala, Val, and Leu E7 mutants of Mb. All rate parameters for HbA subunits were taken from Table 3.1 and those for Mb were taken from Scott *et al.* [22].

Globin	E7 Substitutions	$K_{O_2,ave}, \mu M^{-1}$	$\frac{K_{O_2}(\text{mutant})_{ave}}{K_{O_2}(\text{nat, wt})_{ave}}$	$\delta\Delta G_{E7}$ kJ/mol	$-\delta\Delta G_{E7}(\text{ave})$ kJ/mol	$\Delta G^\circ_{\text{HisE7water}}$ kJ/mol	$\Delta G^\circ_{\text{HisE7H-bond}}$ kJ/mol
α HbA	H ^M	2.5±1.2					
	G,A,L ^M	0.28±0.15	0.11±0.08	5.4±1.8	-4.7±1.2 ¹	+3.7±1.0	-8.6±1.0
	H ^T	1.9±0.5					
	G,A,L ^T	0.35±0.20	0.18±0.11	4.1±1.5			
β HbA	H ^M	2.3±1.0					
β HbA	G,A,L ^M	0.18±0.05	0.08±0.04	6.2±1.3	-6.5±0.7 ¹	+1.5±0.7	-8.0±1.2
	H ^T	3.9±0.6					
	G,A,L ^T	0.24±0.07	0.06±0.02	6.8±0.8			
	Mb SW	H	1.1±0.2				
Mb SW	A,V,L	0.020±0.008	0.018±0.008	9.8±1.0	-9.8±1.0 ¹	+4.1±1.0	-14.5±2.1

¹The value of $-\delta\Delta G_{E7}(\text{ave})$ can also be estimated from the sum of the $\Delta G^\circ_{\text{HisE7water}}$ and $\Delta G^\circ_{\text{HisE7H-bond}}$ values calculated from an analysis of the effects of mutagenesis on the O_2 association and dissociation rate constants, respectively. The correspondence between values of $-\delta\Delta G_{E7}(\text{ave})$ calculated from the sum of the entries in last two columns and that calculated from the ratio of observed equilibrium constants is quite good indicating that the analyses are self-consistent.

stabilize bound O₂, as judged by its markedly lower k_{O₂} and higher K_{O₂} values compared to those for the Ala, Val, and Leu(E7) Mb mutants [126].

The results in Table 3.6 demonstrate that the net stabilization of bound O₂ by His(E7), ($\Delta G^\circ_{\text{HisE7H-bond}} + \Delta G^\circ_{\text{HisE7water}}$), is roughly the same (average value is -5.6 kJ/mol) in both subunits of HbA, regardless of whether they are isolated or combined into R state tetramers and approximately 2-fold weaker than the net stabilization observed in mammalian Mb, $-\delta\Delta G^\circ_{\text{E7}} \approx -10$ kJ/mol at 20°C, pH 7.0.

In 1997, Olson and Phillips [12] argued that increases in O₂ association rate constants due to apolar amino acid substitutions provide a measure of the loss of distal pocket water and the free energy barrier for its displacement, as well as opening of the His(E7) gate. They estimated the value of $\Delta G^\circ_{\text{HisE7water}}$ from $-RT\ln(k'_{\text{O}_2}(\text{small apolar E7 mutant})_{\text{ave}}/k'_{\text{O}_2}(\text{wild-type, native}))$, arguing that rate of movement into an empty distal pocket would be only partially lowered by the size of the imidazole side chain and that, in Mb, a significant barrier to ligand entry is displacement of distal pocket water. Values for $\Delta G^\circ_{\text{HisE7water}}$ were estimated using average values of k'_{O₂} for the Gly, Ala, and Leu E7 mutants of Hb subunits and Ala, Val, and Leu E7 mutants of Mb and are compared in Table 3.6.

Olson and Phillips [12] also argued that the strength of His(E7) hydrogen bonding to bound O₂ could be estimated from a comparison of the apolar mutant dissociation rate constants with those for wild-type and native Mb (i.e. $\Delta G^\circ_{\text{HisE7H-bond}} \approx -RT\ln(k_{\text{O}_2}(\text{small apolar E7 mutants})/k'_{\text{O}_2}(\text{wild-type, native}))$; last column, Table 3.6). This calculation assumes that k_{O₂} reflects primarily the thermal rate of Fe-O₂ bond breakage, which will be reduced markedly by the favorable free energy of hydrogen bonding. The overall

value of k_{O_2} is reduced by geminate recombination and increased by direct steric hindrance, but these effects are small compared to the 10 to 100-fold reduction in rate due to electrostatic interaction with His(E7) (Tables 3.1 and 3.4; [12]).

The results in Table 3.6 are clear and supported by the published structures of Mb and the α and β subunits in HbA. Both α subunits and Mb contain distal pocket water [2, 89], which reduces the free energy liberated during O_2 binding by $\sim +4$ kJ/mol. In contrast, no observable water is present in the distal pocket of deoxygenated β subunits [2], and $\Delta G^\circ_{\text{HisE7water}}$ is only +1.5 kJ/mol, which is roughly zero considering the errors in the measurements. The extents of electrostatic stabilization of bound O_2 in both subunits of HbA are roughly the same, ~ -8 kJ/mol, and almost half that observed in Mb, where $\Delta G^\circ_{\text{HisE7H-bond}}$ is ~ -14.5 kJ/mol. As a result, the net stabilization of bound O_2 by His(E7) is almost 2-fold greater in Mb than in the Hb subunits (~ -10 kJ/mol vs ~ -5.6 kJ/mol)

The enhanced hydrogen bonding stabilization in myoglobin is supported by the lower ν_{C-O} value of native MbCO (~ 1941 cm^{-1}) compared to those for tetrameric and isolated αCO and βCO subunits (~ 1950 cm^{-1} , Table 3.5). In contrast, the values of ν_{C-O} for the apolar mutants of all three globins are in the 1965-1968 cm^{-1} range. Clearly there is a stronger positive electrostatic field adjacent to bound CO in Mb than in the subunits of human Hb, accounting for the greater net stabilization of bound O_2 .

3.9. Correlation between K_{CO} and K_{O_2} and ligand discrimination.

Fig. 3.12 A shows a plot of $\log K_{CO}$ versus $\log K_{O_2}$ for all the mutants listed in Tables 3.1 and 3.2.

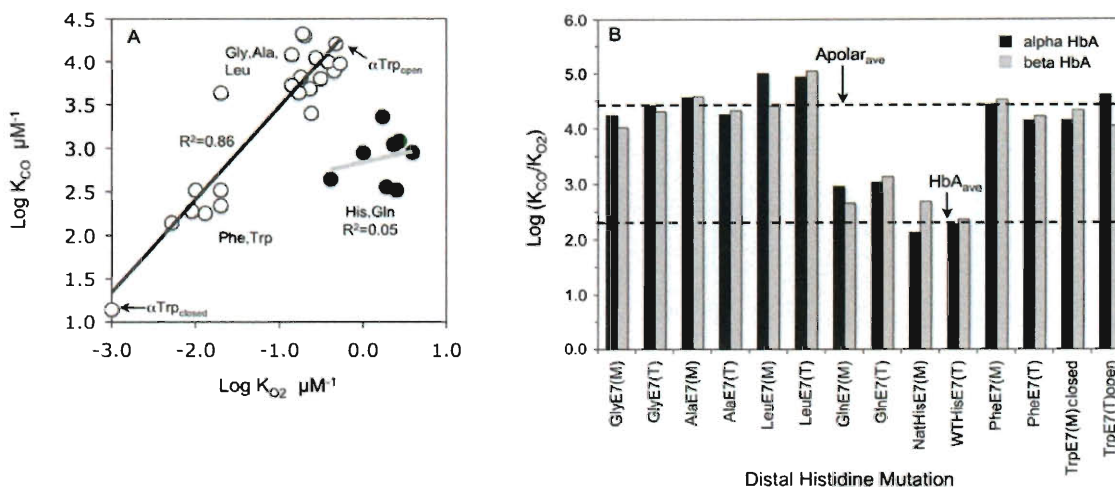


Figure 3.12. Effects of E7 mutants on K_{CO} , K_{O_2} , and their ratio M . (A) Correlation between $\log K_{CO}$ and $\log K_{O_2}$ of wild-type and E7 mutant HbA subunits and tetramers. Closed circles represent data for subunits containing polar His and Gln(E7) side chains; open circles represent data for apolar E7 mutants. There is strong linear correlation between $\log K_{CO}$ and $\log K_{O_2}$ values for the apolar mutants whereas the polar E7 variants are clearly outliers and show little correlation as a group. (B) The effects of mutagenesis on ligand discrimination expressed as $\log(K_{CO}/K_{O_2})$ or $\log(M)$ and plotted as function of the size of the E7 amino acid. Black bars represent α E7 mutants and the grey bars represent β E7 mutants. The upper dashed line represents the logarithm of the average M value for all the apolar mutants, and the lower dashed line represents the logarithm of the average M for HbA subunits. (M) and (T) in the name of the mutant specifies whether $\log(K_{CO}/K_{O_2})$ was calculated for isolated, subunit monomers or the mutant subunit in hybrid tetramers, respectively. NatHisE7 and WTHisE7 stand for native HbA (derived from red blood cells) and wild-type recombinant HbA (expressed in *E. coli*). Data for the diagrams were taken from Tables 3.1 and 3.2.

The E7 variants fall into two classes. The apolar mutant equilibrium constants define a straight line with a slope of 1. The smaller amino acid substitutions show K_{CO} and K_{O_2} values that cluster together in the upper right of Fig. 3.12 A. Increasing the size of the E7 side chain from Leu to Phe and Trp causes, with one exception, uniform decreases in both affinity constants. In the case of α Trp(E7), two sets of constants were estimated, one for the transient open conformer observed directly after laser photolysis

and one for the equilibrium closed conformation. The transient open conformer shows affinities and rate constants for CO and O₂ binding which are similar to those of the Gly(E7) and Ala(E7) mutants (upper open circles, Fig. 3.12 A), whereas the closed conformer shows the lowest affinity constants (lower open circle, Fig. 3.12 A). The polar variants (His and Gln(E7)) have much higher oxygen affinities due to preferential electrostatic stabilization of bound O₂ (solid circles, Fig. 3.12 A), and the K_{O_2} and K_{CO} values cluster significantly to the right of the line for the apolar E7 variants.

The traditional way of looking at discrimination in favor of O₂ versus CO binding is to examine the dependence of the ratio K_{CO}/K_{O_2} (M-value) on ligand size and polarity as shown in Fig. 3.12 B (K_{CO} and K_{O_2} values from Tables 3.1 and 3.2). The results are very clear. The average M value for all the apolar E7 mutants is 34,000, and, although the variation in the K_{CO}/K_{O_2} ratio appears large, $\pm 85\%$, this σ -value is small compared to the 100 to 1000-fold variation in the absolute values of K_{CO} and K_{O_2} (Fig. 3.12 A). When Gln is present at the E7 position, the average M value for the α and β subunits is $\sim 900 \pm 400$, and the average M Value for the wild-type His(E7) subunits is 260 ± 150 . The latter value is 10 times greater than that for mammalian Mb, for which $M \approx 30$. The increase in M for the α and β subunits correlates well with the less negative values of ΔG_{polar} and the higher ν_{C-O} frequencies for the CO complexes of HbA compared to the corresponding parameters for sperm whale Mb. The strength of the positive electrostatic field near bound ligands, which preferentially enhances O₂ binding, is clearly larger in Mb than in the subunits of Hb.

3.10. Steric hindrance of ligand binding by Phe and Trp(E7) mutations.

The marked decreases in K_{O_2} for β Phe(E7), β Trp(E7), α Phe(E7), and the closed α Trp(E7) mutants shown in Fig. 3.12 A and Table 3.1 imply a large increase in the $\Delta G^{\circ}_{E7\text{steric}}$ term in Equation 3.2 for these mutants. This increase is due to either direct hindrance of the bound ligand by the aromatic E7 side chains or indirect inhibition by the need to displace the side chain from the active site before incoming ligands can be captured. The extent of this "extra" hindrance by the benzyl and indole side chains can be estimated by computing $\delta\Delta G_{\text{Phe(E7) or Trp(E7)}}$ from $-RT\ln(K_{O_2, \text{mutant}}/K_{O_2, \text{native}})$ and then subtracting the $\delta\Delta G_{\text{small, apolarE7}}$ term determined from effects of the Gly, Ala, and Leu(E7) mutations, which takes into account the loss of hindrance by distal pocket water and the loss of stabilization of bound O_2 by the native His(E7) side chain (i.e. the $\Delta G^{\circ}_{E7H\text{-bond}}$ and $\Delta G^{\circ}_{E7\text{water}}$ terms in Equation 3.2). The results of these calculations for the Phe and Trp E7 mutants are summarized in Table 3.7.

For α and β subunits, the introduction of the benzyl side chain causes both the loss of net electrostatic stabilization and significant hindrance by the aromatic ring, with $\Delta G_{\text{PheE7steric}} \approx +7$ to $+9$ kJ/mol. As a result, the O_2 affinities of these Phe(E7) mutants are very small, i.e. $K_{O_2} \approx 0.01 \mu\text{M}^{-1}$ or $P_{50} \approx 100 \mu\text{M}$ in the R state. The β Trp(E7) mutation causes a similar amount of added hindrance, $\Delta G_{\text{steric}} \approx +7$ kJ/mol.

The closed deoxygenated conformer of α Trp(E7) shows a dramatic amount of steric inhibition, leading to an estimated O_2 association equilibrium constant equal to $\sim 0.001 \mu\text{M}^{-1}$ ($P_{50} \approx 1000 \mu\text{M}$) and $\Delta G_{\text{TrpE7steric}} \approx +14$ kJ/mol. In contrast, the transient open conformation of α Trp(E7) in both monomers and tetramers has an estimated K_{O_2} value of $\sim 0.4 \mu\text{M}^{-1}$, which is similar to the K_{O_2} values for the smaller Gly, Ala, and Leu(E7)

mutants, and exerts no steric resistance to ligand binding ($\Delta G_{\text{TrpE7steric}} \approx 0$ kJ/mol, Table 3.7).

Table 3.7. Effects of Phe(E7) and Trp(E7) mutants on O₂ binding to HbA and sperm whale Mb. $\delta\Delta G_{\text{PheE7 or TrpE7}}$ values were calculated as $-RT\ln(K_{\text{O}_2,\text{mutant}}/K_{\text{O}_2,\text{native}})$ and found to be significantly larger than the $\delta\Delta G_{\text{E7}}$ values computed for the smaller Gly, Ala, and Leu mutants, implying steric hindrance by the larger Phe and Trp side chains. The extent of this effect was estimated as $\Delta G_{\text{E7steric}} = \delta\Delta G_{\text{PheE7 or TrpE7}} - \delta\Delta G_{\text{small, apolar E7}}$, where $\delta\Delta G_{\text{small, apolar E7}}$ was taken from monomer and tetramer values for $\delta\Delta G_{\text{E7(ave)}}$ in Table 3.6 for each subunit. O₂ affinities for the Phe(E7) and Trp(E7) were taken from Table 3.1. K_{O₂} values for sperm whale Mb were taken from [22]. Superscripts M and T stand for monomer and tetramer, respectively. The estimated errors for $\Delta G_{\text{E7steric}}$ are assumed to be similar to those for the $\delta\Delta G_{\text{E7}}$ values in Table 3.6, i.e. $\leq \pm 2$ kJ/mol. Thus, the values of $\Delta G_{\text{E7steric}}$ for the open conformation of α TrpE7 and the PheE7 and TrpE7 mutants of Mb are very close to zero, and the decreases in K_{O₂} for these mutants are similar to those for the corresponding small apolar E7 mutants.

Globin	E7 Mutants	$\frac{K_{\text{O}_2(\text{mutant})}}{K_{\text{O}_2(\text{native})}}$	$\delta\Delta G_{\text{Phe or TrpE7}}$ kJ/mol	$\delta\Delta G_{\text{small, apolar E7}}$ kJ/mol	$\Delta G_{\text{E7steric}}$ kJ/mol
α HbA	Phe(E7) ^M	0.0021	15.0	5.4	9.6
	Phe(E7) ^T	0.0068	12.1	4.1	8.0
	Trp(E7) ^M closed	0.0004	19.1	5.4	13.7
	Trp(E7) ^M open	0.24	3.4	5.4	-2.0
	Trp(E7) ^T open	0.14	4.7	4.1	0.6
β HbA	Phe(E7) ^M	0.0043	13.2	6.2	7.0
	Phe(E7) ^T	0.0051	12.8	6.8	6.0
	Trp(E7) ^M	0.0039	13.5	6.2	7.3
	Trp(E7) ^T	0.0051	12.8	6.8	6.0
Mb SW	Phe(E7)	0.0067	12.1	9.8	2.4
	Trp(E7)	0.064	6.7	9.8	-3.1

The inhibitory effect of the Phe(E7) and the closed Trp(E7) conformers occurs roughly to the same extent for both O₂ and CO binding (Tables 3.1 and 3.2, Fig. 3.12 A). Decreases in K_{O₂} and K_{CO} for Phe(E7) mutants are caused by increased dissociation rate constants (k_{O₂} and k_{CO}, Tables 3.1 and 3.2), suggesting that negative steric effect is due to the direct hindrance of bound ligand by the benzyl side chain. The low ligand affinities for equilibrium deoxyHb Trp(E7) conformers are due to very low k'_{O₂} and k'_{CO} values.

The latter case is the example of indirect steric inhibition of ligand binding due to the requirement to displace bulky E7 side chain from the binding site.

In contrast to the HbA mutants, the Phe(E7) and Trp(E7) mutations in Mb show little or no hindrance (i.e. the small or negative $\Delta G_{E7\text{steric}}$ values for Mb mutants in Table 3.7). These results suggest that the Mb active site can either accommodate both the Trp(E7) side chain and a bound ligand or, more likely, that the Trp(E7) side chain is prevented from entering the active site and directly hindering bound ligands. These ideas are confirmed by the kinetic and structural data for the Trp(E7) HbA and Mb mutants, which are described in the next chapter.

3.11. Pathways for ligand entry into Mb and HbA subunits.

With one exception (the transient, open α Trp(E7) conformer), there are dramatic decreases in the bimolecular rates of O₂, CO, and NO binding to the subunits of Hb with increasing size of the E7 side chain (Tables 3.1-3.3). These results strongly suggest that ligands enter and exit through a channel gated by the distal histidine. Overall CO association rate constants and the fraction of geminate CO recombination were used to estimate bimolecular rate constants for ligand entry into isolated HbA subunits. Then rate constants for bimolecular NO binding to both monomers and tetramers were measured to verify experimentally these estimates of k'_{entry} (Table 3.4). The dependence of k'_{NO} on the size of the E7 side chain in monomeric α and β subunits and sperm whale Mb is shown in Fig. 3.13 using the closed conformers of the Trp(E7) mutants.

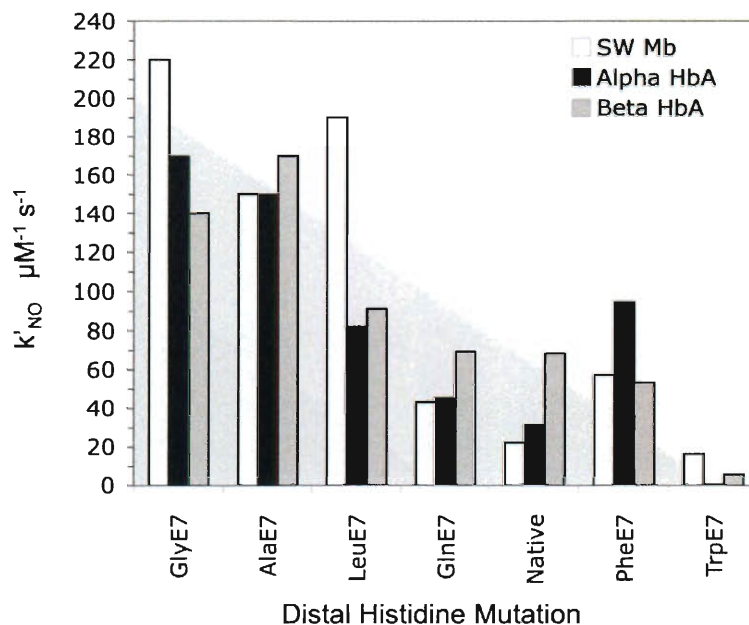


Figure 3.13. Dependence of rate constant for NO association on E7 mutations in monomeric α subunits, β subunits, and Mb. Native HbA contains His at E7 position. Only the slow phase k'_{NO} for α Trp(E7) was used since it represents NO binding to the closed, physiologically relevant equilibrium state of the mutant. Data for SW Mb mutants were taken from [22], and k'_{NO} for HbA mutants were taken from Table 3.4.

The Gly and Ala(E7) mutations open up all three proteins, giving rise, to bimolecular rate constants on the order of $200 \mu\text{M}^{-1}\text{s}^{-1}$, which is probably the diffusion limit. The highest rates of ligand binding to a globin are in the range of 200 to $500 \mu\text{M}^{-1}\text{s}^{-1}$ and have been observed for wild-type and mutant *Cerebratulus lacteus* Hbs [68], certain wild-type and mutant plant hemoglobins [110], and a few bacterial globins [127]. These values are similar to those observed for ligand binding to pentacoordinate model hemes in soap micelles or isotropic organic solvents [119]. In the closed conformation, the Trp(E7) mutations markedly decrease k'_{NO} to values $\leq 6 \mu\text{M}^{-1}\text{s}^{-1}$, effectively blocking the E7 channel, and there is a roughly monotonic decrease in the rate of NO entry with increasing size of the E7 side chain for other mutants. Scott *et al.* [22] carried out a much more extensive mutagenesis mapping study of Mb using 90 mutants at 27 different

positions, and their results confirmed quantitatively the E7 gate mechanism for ligand entry into Mb, which was originally developed using just E7 mutations [126]. By analogy with the more extensive results for Mb, it seems clear that the E7 channel is also the major route for ligand entry into both subunits of HbA.

The most striking difference between the α and β subunits is appearance of a rapidly reacting, transient intermediate after photolysis of Trp(E7) α CO subunits. It appears that relaxation of the indole side chain to its equilibrium unliganded conformation in α subunits is relatively slow compared to ligand rebinding at high CO or O₂ concentrations. Little rapidly reacting intermediate is seen after photolysis of Trp(E7) β CO subunits, which show low rates of bimolecular ligand rebinding. The cause of the slow relaxation in α subunits appears to be a narrower channel opening, due in part to the large His(CE3) side chain in α subunits (Fig. 3.11). In β subunits, the channel is larger due to a smaller Ser side chain at the CD3 position, which, presumably, facilitates inward rotation of E7 side chain after ligands leave the active site. These ideas are expanded in the next the chapter.

The larger opening in β subunits may also contribute to the two-fold larger bimolecular rate constants for O₂ and NO binding to native or wild-type β subunits, particularly, in tetrameric hemoglobin where protein fluctuations are dampened by the quaternary structure (Appendix 1). The CD3 amino acid in Mb is Arg and the rate of entry into Mb does increase up ~2-fold when this residue is decreased in size [22]. However, the differences in rate constants between the native α and β subunits are small compared to the effects of the Gly and Trp(E7) mutations which cause ~3 to 5-fold

increases and 15 to 80-fold decreases, respectively, in the rates of ligand entry into the equilibrium R-state forms of deoxygenated HbA (Fig. 3.13).

CHAPTER 4: MECHANISMS FOR LIGAND BINDING TO α AND β

TRP(E7) MUTANTS OF HUMAN HBA

4.1. The motions of the E7 gate in Mb and Hb.

Direct measurements of the rates of opening and closing of the distal histidine (E7) gate in mammalian myoglobins and hemoglobin subunits have proved to be difficult and rare. In time resolved X-ray analyses of photolyzed MbCO, the ligand is observed to move between the distal pocket and the Xe4 and Xe1 cavities on nanosecond time scales, but no rotation of the His(E7) side chain out into solvent is observed as the total ligand electron density disappears to generate transient unliganded states on nanosecond time scales. Similarly, no observable *open* conformer is observed as bound ligand electron density reappears after several hundred microseconds due to bimolecular rebinding from the mother liquor [53, 128, 129]. The imidazole side chain of His(E7) does rotate completely out into solvent in low pH wild-type and neutral pH F46V MbCO crystal structures, and these *open* conformers correlate with large bimolecular rates of ligand entry [22, 86, 87, 107, 130].

Tian *et al.* [86, 87] estimated that the rate of opening and closing of the His(E7) gate in Mb is on the order of 1 to 10 μs^{-1} , which competes with internal geminate rebinding of CO and water entry, but is much faster than bimolecular binding from solvent which is regulated by the equilibrium fraction of open states [131, 132]. Thus, CO rebinding to wild-type MbCO after laser photolysis is a simple one step process on microsecond to millisecond time scales. The unliganded intermediate generated after the 0.5 μs photolysis pulse has spectral and kinetic properties identical to the equilibrium deoxygenated state examined in rapid mixing experiments. Conformational transitions

between *open* and *closed* states of distal His were observed by Bossa *et al.* [133] in their 90 ns molecular dynamics simulation of CO photodissociation from Mb, seem to agree well with Tian's nanosecond flash photolysis results [87].

Much less is known about opening and closing of the E7 channel in the subunits of human hemoglobin. Recently, Jenkins and co-workers reported a crystal structure of a new quaternary sub-state of high affinity HbA [134], in which β His(E7) rotates into solvent creating a direct channel to the active site. However, as with Mb, only single bimolecular binding phases are observed after laser photolysis of the O₂, CO, and NO complexes of isolated wild-type and native α and β subunits (Chapter 3). Thus, any movements of the His(E7) side chain and water entry are very rapid and, like those in Mb, occur on sub-microsecond time scales [135].

However, replacing His(E7) with Trp in Hb subunits causes the appearance of complex bimolecular rebinding time courses on microsecond to millisecond time scales (Figs. 4.1 and 4.2 A). The *open* and *closed* states of the indole side chain interconvert on microsecond time scales and compete with bimolecular ligand rebinding from solvent. In contrast, water movement into the distal pocket is much faster than the rotations of the E7 side chains [135], and is in equilibrium during the observed bimolecular binding kinetics. The kinetic results for the Trp(E7) mutants also provide evidence that the E7 gate regulates bimolecular ligand binding to the α and β subunits. In effect, the large indole ring of Trp(E7) exaggerates the degree of opening and closing caused by the small, native His(E7) imidazole ring.

4.2. CO rebinding to Trp(E7) hybrid mutant tetramers of HbA.

Dramatic differences are observed for bimolecular CO rebinding to hemoglobin tetramers containing α versus β Trp(E7) mutants with wild-type partner subunits (Fig. 4.1).

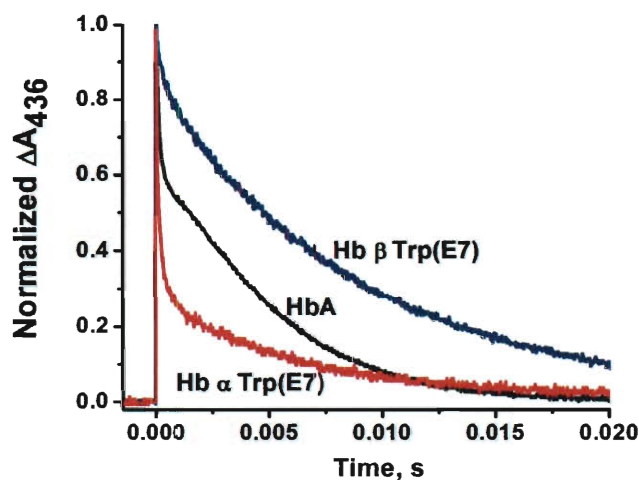


Figure 4.1. CO binding to wild-type and Trp(E7) mutants of human HbA tetramers. Bimolecular rebinding to $\sim 100 \mu\text{M}$ native HbA, $\alpha(\text{Trp}(\text{E7}))\beta(\text{WT})$, and $\alpha(\text{WT})\beta(\text{Trp}(\text{E7}))$ tetramers at $[\text{CO}] = 1000 \mu\text{M}$, after complete photolysis with a $0.5 \mu\text{s}$ excitation dye laser pulse, which "pumps" all the ligands into the solvent phase. Conditions were 100 mM Na phosphate, pH 7, 20°C .

In dye laser experiments the observed time courses represent bimolecular rebinding to the various, transiently generated conformational states of unliganded hemoglobin. In the case of wild-type HbA at $1000 \mu\text{M}$ CO, the observed time course is markedly biphasic, with a large rapid phase due to ligand binding to the R quaternary state ($\sim 40\%$) and a slow, accelerating phase due to binding to T state tetramers ($\sim 60\%$) (Fig. 4.1, black time course). After complete ligand photodissociation, the initial deoxyHb complex undergoes the $\text{R} \rightarrow \text{T}$ state transition at a rate of $\sim 10^4\text{-}10^5 \text{ s}^{-1}$ [65]. Thus, at high $[\text{CO}]$ there is competition between rapid CO binding to the deoxyHb R state

and the quaternary conformational change that leads to the slowly reacting hemoglobin T quaternary conformation.

Replacing His(E7) with Trp in one pair of subunits dramatically alters the time course for bimolecular CO binding to the resulting hybrid Hb tetramer after laser photolysis. The $\alpha(\text{Trp(E7)})\beta(\text{WT})$ HbCO mutant shows almost 80% rapid binding (Fig. 4.1, red time course), whereas the time course for CO binding to the $\alpha(\text{WT})\beta(\text{Trp(E7)})$ mutant is almost 100% slow (Fig. 4.1, blue time course). The fast phase for $\alpha(\text{Trp(E7)})\beta(\text{WT})$ is itself biphasic with apparent bimolecular R-state rate constants of $\sim 60 \mu\text{M}^{-1}\text{s}^{-1}$ ($\sim 35\%$) and $5 \mu\text{M}^{-1}\text{s}^{-1}$ ($\sim 45\%$). The latter rate constant is similar to that expected for R-state wild-type β subunits ($k'_{\text{CO}} \approx 7 \mu\text{M}^{-1}\text{s}^{-1}$, Chapter 3). The slow phase for the $\alpha(\text{Trp(E7)})\beta(\text{WT})$ mutant suggests a bimolecular rate constant of $\sim 0.2 \mu\text{M}^{-1}\text{s}^{-1}$, which is similar to CO rebinding to the T-state HbA [70, 71]. Thus, it appears that the Trp(E7) mutation in α subunits enhances rapid CO rebinding after laser photolysis by speeding up the intrinsic rate of binding to the mutated R-state subunit, which in turn generates partially liganded intermediates that prevent the R to T transition from occurring.

In contrast, the Trp(E7) mutation significantly decreases the rate of CO binding to hybrid Hb tetramers when it is in β subunits. As shown in Fig. 4.1, bimolecular CO rebinding to $\alpha(\text{WT})\beta(\text{Trp(E7)})$ is virtually all slow, with little or no rapid phase, and the apparent bimolecular rate, $\sim 0.1 \mu\text{M}^{-1}\text{s}^{-1}$ is roughly two-fold smaller than that observed for the slow phase of CO rebinding to wild-type HbA. Thus, the Trp(E7) mutation slows CO binding to R-state β subunits, which in turn allows more time for the R \rightarrow T transition to take place and results in more slowly reacting conformations.

4.3. Bimolecular CO binding to isolated α and β Trp(E7) subunits.

In order to reduce the complexity of the kinetic results and to avoid problems in partial photolysis experiments due to the significant differences in quantum yields of the native versus mutant subunits (Chapter 3), the individual α and β Trp(E7) subunits were isolated and then examined separately in both laser photolysis and stopped flow rapid mixing experiments (Figs. 4.2 A and B, Chapter 3). Under these conditions, the

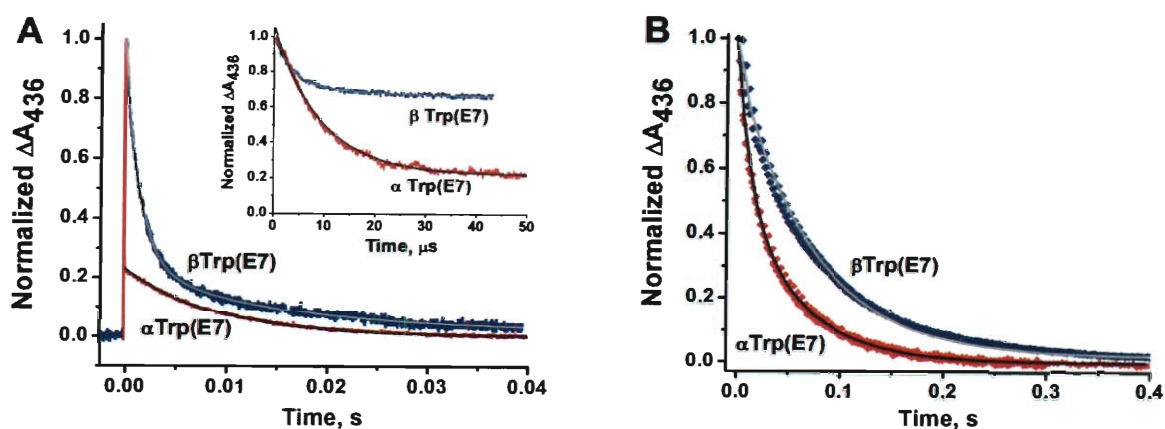


Figure 4.2. CO binding to α and β isolated subunits of Trp(E7) mutants. *A*, Slow phases for bimolecular CO rebinding to $\sim 50 \mu\text{M}$ isolated Trp(E7) α and β subunits at $1000 \mu\text{M}$ CO; *inset* shows the rapid bimolecular binding phases, which occur on μs timescale. *B*, Stopped flow, rapid-mixing experiments for CO binding to equilibrium deoxygenated forms of $\sim 5 \mu\text{M}$ isolated Trp(E7) α and β subunits at $[\text{CO}] = 200 \mu\text{M}$ after mixing. The black and gray lines in panels A and B represent fits to single or multiple exponential expressions. Conditions were 100 mM Na phosphate, pH 7, 20°C .

subunits exist in high affinity, R-state-like conformations with none of the quaternary constraints found in the tetramer. However, CO binding to isolated α Trp(E7) subunits is still biphasic, with one extremely fast phase ($\sim 90 \mu\text{M}^{-1}\text{s}^{-1}$) comprising 79% of the total absorbance change at $1000 \mu\text{M}$ CO and a small slow phase ($0.1 \mu\text{M}^{-1}\text{s}^{-1}$). Analogous experiments with β Trp(E7) subunits show a small fast phase, 33%, with an apparent rate

constant for CO binding equal to $\sim 80 \mu\text{M}^{-1}\text{s}^{-1}$, and two slow processes, with apparent rate constants equal to $0.7 \mu\text{M}^{-1}\text{s}^{-1}$ (49%) and $0.06 \mu\text{M}^{-1}\text{s}^{-1}$ (18%). As described in Chapter 3, the fast phases were attributed to bimolecular CO binding to *open* conformers of the α and β Trp(E7) mutants in which the Trp(E7) side chain has rotated out into solvent and does not obstruct the E7 channel. The bimolecular rate constants for the fast phases of both subunits approach the diffusion limit and are similar or larger than those for Gly or Ala(E7) mutants where the E7 tunnel is completely open to solvent. The slowly reacting components were assigned to species in which the pathway for ligand movement into the distal pocket is severely hindered or completely closed by the indole ring of Trp(E7). However, in the previous chapter, a detailed kinetic mechanism was not developed to describe quantitatively the competition between rapid bimolecular ligand binding to the *open* conformers and relaxation of the indole side chain to the *closed*, slowly reacting conformations.

In order to define the kinetic mechanism, the ligand concentration dependences of the observed time courses for bimolecular CO rebinding to the isolated mutant subunits after laser photolysis were measured. In the case of the α Trp(E7) mutant, the extent of rapid bimolecular rebinding diminishes from 79% at $1000 \mu\text{M}$ CO to 25% at $50 \mu\text{M}$ (Fig. 4.3 A and Chapter 3). These results demonstrate that the two phases are not due to heterogeneity in the sample, but, instead, to *open* and *closed* conformers which interconvert on the same time scale as ligand binding.

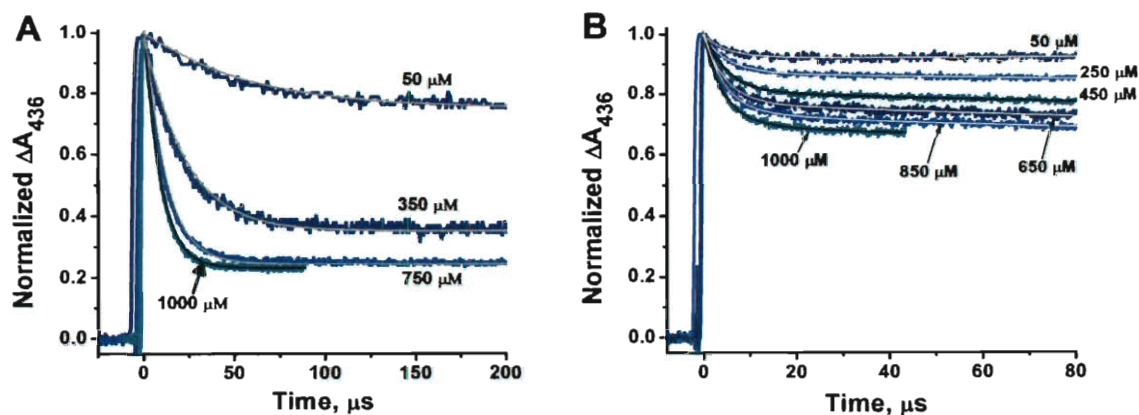


Figure 4.3. Rapid bimolecular CO rebinding to Trp(E7) α and β subunits after laser photolysis. Concentrations of CO are listed beside each curve and the lines represent fits to either a single exponential process with an offset or to a two exponential process with a second very slow phase. Experiments were conducted in 100 mM Na phosphate, pH 7, 20 °C. A, time courses for $\sim 50 \mu\text{M}$ isolated Trp(E7) α CO. B, time courses for $\sim 50 \mu\text{M}$ isolated Trp(E7) β CO. Complete photolysis was achieved with a $0.5 \mu\text{s}$ excitation pulse from dye laser.

In contrast to the α mutant, bimolecular CO rebinding to isolated Trp(E7) β subunits is mostly a slow process, and only at very high $[\text{CO}]$ is there a significant fraction of the fast phase, 33% at 1000 μM (Fig. 4.3 B). In addition, the rate of the fast phase does not show a large dependence on $[\text{CO}]$, increasing from $\sim 190,000 \text{ s}^{-1}$ to $260,000 \text{ s}^{-1}$ over a 20-fold increase in ligand concentration. The observed rate of the fast phase at $[\text{CO}] \rightarrow 0$ represents the rate of interconversion between *open* and *closed*, slowly reacting conformations and equals $\sim 175,000 \text{ s}^{-1}$, which is roughly 10-fold greater than the estimated rate for the same conformational relaxation in Trp(E7) α subunits.

To prove that the *closed*, slowly reacting forms represent the equilibrium, deoxygenated conformation, deoxygenated solutions of α and β Trp(E7) subunits were rapidly mixed with various $[\text{CO}]$ in stopped-flow experiments. As shown in Fig. 4.2B, only slow phases are seen in these mixing experiments, even at very low ligand concentrations where fast bimolecular binding could be detected. Thus, the slowly

reacting *closed* conformations are completely favored at equilibrium. The *open*, rapidly reacting unliganded conformers are transient and only observed immediately after laser photolysis.

In the rapid mixing experiments with isolated α Trp(E7) subunits, two slow phases are observed (Fig. 4.2 B). The initial slow phase corresponds to the slow bimolecular phase for CO rebinding observed after photolysis. The second, smaller phase is 5-fold slower. This second slow phase represents a conformer of deoxy- α Trp(E7), which is even more restricted to ligand binding than the initial *closed* state, is formed much more slowly, and is not observed in the laser experiments. Trent *et al.* [112] observed similar discrepancies between the slow phases observed in laser-photolysis *versus* rapid-mixing experiments with the nonsymbiotic hexacoordinate hemoglobin from rice, nsHb1. They proposed that, at equilibrium, deoxygenated rice nsHb1 also exists in two structurally distinct, slowly interconverting, closed deoxyHb forms [112, 136].

In the case of β Trp(E7), two significantly different slow CO binding phases are observed after laser photolysis suggesting transitions to at least two distinct slowly reacting conformers (Fig. 4.2 A). In rapid mixing experiments with isolated β Trp(E7) subunits, only the very slow phase seen in the laser experiments is observed (Fig. 4.2 B). The dominant middle phase from the flash photolysis time courses is absent in the stopped flow experiments, implying that at equilibrium there is primarily just one *closed* Trp(E7) β conformer that reacts very slowly with CO.

4.4. CO recombination to Trp(E7) mutant of swMb.

As a control, ligand binding to Trp(E7) sperm whale Mb was examined to look more carefully for slow interconversions between *open* and *closed* states. Both O₂ and CO association time courses show no heterogeneity after laser photolysis at either low or high ligand concentrations (Fig. 4.4A), and the observed bimolecular rate constants are identical to those observed in stopped flow experiments at low [CO] (Fig. 4.4 B) and to those reported previously [83].

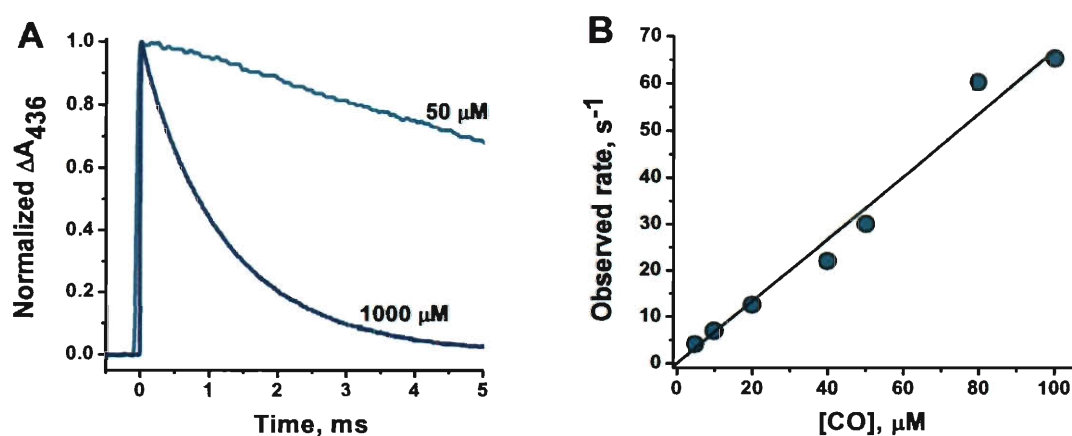


Figure 4.4. Bimolecular CO binding to Trp(E7) sperm whale Mb. *A*, time courses for bimolecular CO rebinding to $\sim 50 \mu\text{M}$ Trp(E7) Mb after complete photolysis by the $0.5 \mu\text{s}$ dye laser at $[\text{CO}] = 1000$ and $\sim 50 \mu\text{M}$. The fitted and estimated observed pseudo first order rate constants were $\sim 700 \text{ s}^{-1}$ and $\sim 35 \text{ s}^{-1}$, respectively. *B*, Dependence of the pseudo first order rate constant on $[\text{CO}]$ for CO binding to the equilibrium deoxygenated form of Trp(E7) Mb measured in stopped-flow, rapid mixing experiments at low ligand concentrations. The slope of the fitted line gives an association rate constant equal to $0.69 \mu\text{M}^{-1}\text{s}^{-1}$, which is identical to the value computed from the laser photolysis data in *panel A*.

The absolute value of k'_{CO} for Trp(E7) Mb is roughly the same as that observed for wild type Mb, $\sim 0.7 \mu\text{M}^{-1}\text{s}^{-1}$ and 10 to 20-fold smaller than that observed for Gly(E7) and Ala(E7) mutants (Chapter 3). Thus, either the Trp(E7) side chain cannot enter and completely close the E7 gate in myoglobin, or, if multiple conformations exist, they

interconvert very rapidly, resulting in population averaging, with the observed rate of ligand binding being proportional to the equilibrium fraction of *open* conformers.

4.5. Crystal structures of Hb and Mb Trp(E7) mutants.

To examine the structures of the *open* and *closed* conformations of the Trp(E7) side chains, I attempted to crystallize the deoxygenated and CO forms of Hb $\alpha(\text{WT})\beta(\text{Trp(E7)})$, Hb $\alpha(\text{Trp(E7)})\beta(\text{WT})$ and sperm whale Mb Trp(E7). Despite extensive efforts, high quality crystals of the deoxy form of $\alpha(\text{WT})\beta(\text{Trp(E7)})$ and the CO form of $\alpha(\text{Trp(E7)})\beta(\text{WT})$ were not obtained. Fortunately, the high resolution crystal structures of deoxyHb $\alpha(\text{Trp(E7)})\beta(\text{WT})$ (pdb code **3NMM**), HbCO $\alpha(\text{WT})\beta(\text{Trp(E7)})$ (pdb code **3NL7**), MbCO Trp(E7) (pdb code **3NML**), and deoxyMb Trp(E7) (pdb code **3OGB**) were obtained and provide plausible structural models for the *closed*, *blocked*, and *open* conformers of the mutants defined in the kinetic mechanisms proposed in the end of this Chapter. The crystal properties and statistical parameters for X-ray diffraction data collection and model refinement of all four proteins are given in Table 4.1, and electron density maps of the active sites are shown in Figs. 4.5 and 4.7.

Remarkably, the Trp(E7) mutations do not cause any significant global perturbations of the structures of either HbA or Mb. Alignment of deoxy- $\alpha(\text{Trp(E7)})\beta(\text{WT})$ with native deoxy-HbA gave average *rmsd* values of 0.26 Å for the C_α atoms in α chains, and 0.17 Å for the C_α atoms in β subunits. In case of the CO forms of $\alpha(\text{WT})\beta(\text{Trp(E7)})$ and HbA, the rms deviation of the C_α atoms of the β subunits is 0.18 Å, whereas the value for the native *versus* wild-type α chains is 0.10 Å.

Table 4.1. Crystallization and structure determination parameters of Hb and Mb Trp(E7) mutants.

Protein	DeoxyHb $\alpha(\text{Trp58(E7)})\beta(\text{WT})$	HbCO $\alpha(\text{WT})\beta(\text{Trp63(E7)})$	MbCO Trp64(E7)	DeoxyMb Trp64(E7)
PDB entry code	3NMM	3NL7	3NML	3OGB
<i>Crystal data:</i>				
Resolution range (Å)	52.67-1.60	51.27-1.80	41.59-1.68	23.57-1.60
Space group	P 2 ₁	P 4 ₁ 2 ₁ 2	P 2 ₁ 2 ₁ 2 ₁	P 2 ₁ 2 ₁ 2 ₁
Unit cell parameters (Å, °)	a = 62.6, b = 81.8, c = 53.4, β = 99.8	a = b = 53.2, c = 191.8	a = 38.9, b = 47.0, c = 89.5	a = 38.8, b = 47.1, c = 88.9
Reflections (measured/unique)	176,967/62,570	94,990/25,409	71,043/19,145	78,267/21,466
Completeness (%)	89.5 (72.3)*	95.5 (98.8)	98.9 (94.7)	96.6 (91.0)
$\langle I \rangle / \sigma \langle I \rangle$	15.9 (4.2)	8.8 (3.5)	19.7 (7.0)	15.5 (4.1)
Redundancy	2.83 (2.64)	3.74 (3.46)	3.71 (3.20)	3.65 (3.66)
R _{merge} (%)	3.8 (18.7)	7.4 (26.0)	4.1 (13.4)	4.3 (26.3)
<i>Refinement:</i>				
Resolution range (Å)	28.82-1.60	31.11-1.80	22.71-1.68	23.57-1.60
R-factor (%)	17.3	18.6	16.6	18.0
R _{free} (%)	19.8	23.3	19.6	20.3
<i>RMS deviations from ideal values:</i>				
Bond length (Å)	0.013	0.028	0.019	0.006
Bond angles (°)	1.571	1.281	1.242	1.088
<i>Ramachandran plot:</i>				
Residues in most favorable region (%)	94.4	93.2	92.8	92.0
Residues in additional allowed region (%)	5.6	6.8	7.2	8.0

*Parameters in parentheses () are for the outer resolution shell

Thus, the functional changes resulting from the large indole side chain appear to be localized to the E7 channel and active site, including greater blocking of ligand entry into the active site and less accessibility of the iron atom.

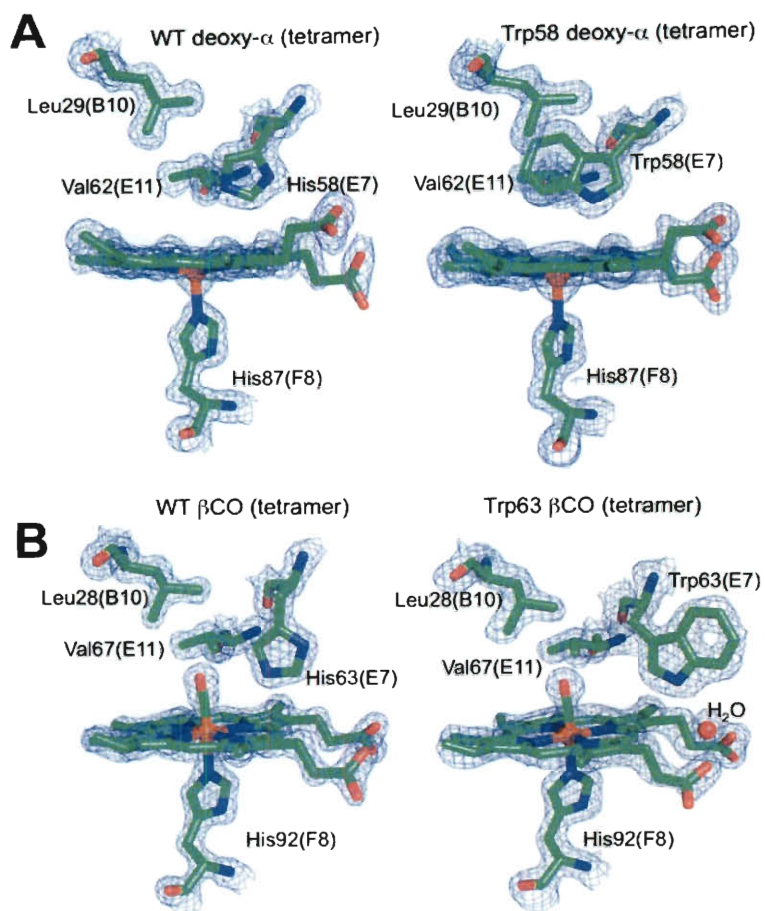


Figure 4.5. Side views of wild-type and Trp(E7) mutants of HbA. The electron density was contoured at 1.3σ and is shown as a blue net. The color code for atoms is: green, carbon; blue, nitrogen; red, oxygen; orange, iron. The key residues are shown clockwise: Trp(E7) or His(E7), His(F8), Val(E11) and Leu(B10). The hemoglobin subunits are part of a tetrameric structure with wild-type or native subunit partners. *A*, native deoxy- α ([2], 2DN2) with the distal pocket water removed and Trp(E7) deoxy- α (3NMM); *B*, native CO- β ([2], 2DN3) and Trp(E7) β CO (3NL7).

Fig. 4.5A compares the structures of the ligand binding sites in native *versus* Trp(E7) α subunits in deoxyHbA tetramers. As described by Park *et al.* [2], the distal histidine side chain moves inward in deoxy α and β subunits compared to its position in

the O₂ or CO complexes (compare to native β CO subunit in Fig. 4.5B). In the native deoxy- α structure, an internal water molecule is also present directly above the iron atom and hydrogen bonded to the N ϵ atom of the E7 imidazole side chain (not shown in Fig. 4.5A). In the structure of the deoxygenated Trp(E7) α subunit, the large indole ring has rotated into the distal pocket, completely closing the E7 channel for ligand entry, and hindering access to the iron atom from any direction. CO binding to this conformation is impossible without outward rotation of the Trp(E7) side chain, and as a result, this structure is assigned as a model for the *closed*, very slowly reacting states observed in the kinetic mechanisms.

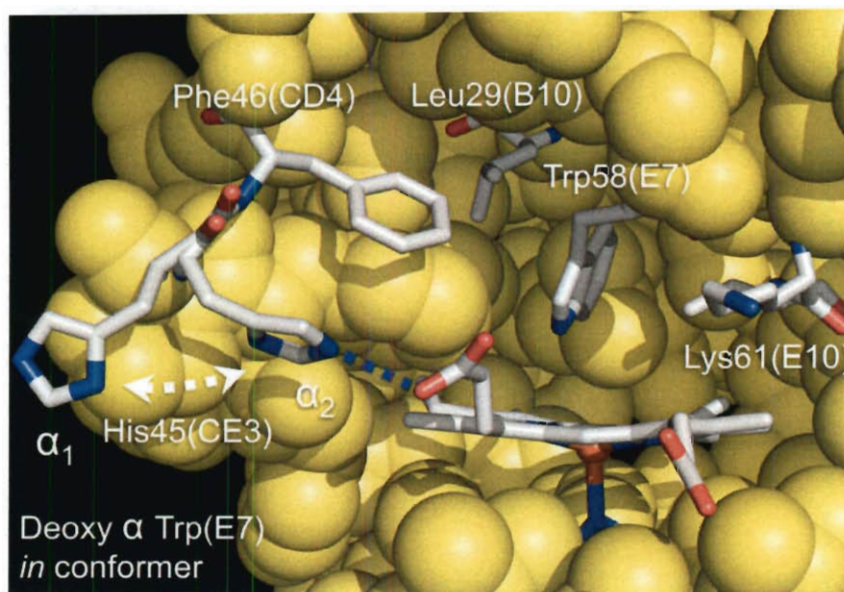


Figure 4.6. Front view of Trp(E7) α subunit in hybrid deoxyHb. Different conformers of α His45(CE3) are observed in the α_1 and α_2 subunits of deoxygenated α (Trp(E7)) β (WT) tetramers (3NMM). The stick models of the key amino acids are colored as: white, carbon; blue, nitrogen; red, oxygen. The atoms of the other amino acids are represented as space-filling yellow spheres. The orange sphere represents the heme iron. The blue dotted line in the α_2 subunit represents a H-bond between His45(CE3) and the heme-6-propionate with an inter-atomic distance of 3.0 Å.

There are two other major changes in the structure of the distal pocket of Trp(E7) deoxy- α compared to that of the native subunit. First, the side chain of Leu(B10) has

rotated clockwise, $\sim 90^\circ$ around $C\alpha-C\beta$ bond, causing an expansion of the distal pocket to make room for the large indole side chain. Second, multiple conformations are observed for the α His45(CE3) side chain (Fig. 4.6). In α subunits of native deoxyHbA, the CE3 imidazole is pointing towards the carboxyl O atoms of the heme-6-propionate, forming a strong electrostatic interaction that stabilizes bound heme [2, 137]. In the α_1 subunit of the $\alpha(\text{Trp(E7)})\beta(\text{WT})$ deoxy-tetramer, the CE3 imidazole has rotated out into solvent and is far away from the heme propionate (Fig. 4.6, α_1 conformer). The space between His(CE3) and the heme propionate is filled with several high occupancy water molecules (positions not shown). However, in the α_2 subunit of the mutant tetramer, the position of the His(CE3) is the same as in the native subunit (Fig. 4.6, α_2 conformer). These results imply that the His45(CE3) interaction with the heme-6-propionate must be disrupted before the Trp(E7) side chain can enter the distal pocket.

In contrast, there is no interaction between the heme-6-propionate and the spatially equivalent but much smaller Ser44(CD3) side chain in β subunits [2]. This lack of stabilization of the heme-6-propionate in β subunits explains the higher rates of hemin dissociation from β subunits in native HbA [137]. The lack of electrostatic interaction between the CD3 side chain and the heme-6-propionate may also facilitate inward rotation of the large Trp(E7), accounting in part for the more rapid conformational transitions between the *open* and *closed* states in β subunits.

The distal histidine remains in the distal pocket of the α and β subunits of native HbA and sperm whale Mb when ligands are bound. The $N\epsilon$ atom of His(E7) donates a hydrogen bond to bound ligands in all three globins, which is manifested as decreased rates of ligand dissociation and shifts of the ligand stretching frequencies ([85], and Fig

3.10). When His(E7) is replaced by Trp in α CO and β CO subunits, the stretching frequency of the bound ligand, $\nu_{\text{C-O}}$, increases from ~ 1950 to ~ 1970 cm^{-1} indicating the loss of the positive electrostatic field donated by the native distal histidine (Fig. 3.10). This result suggests that there is no interaction with either the edge of the aromatic indole ring or the pyrrole N-H atoms and that the side chain is not in the distal pocket near bound CO. This prediction is verified by the structure of the Trp(E7) β CO subunit in which the large indole ring is precluded from the active site by the bound ligand (Fig. 4.5B).

The indole side chain of Trp(E7) β CO is located outside of the distal pocket with most of the indole ring exposed to solvent. The nitrogen atom of the indole ring is hydrogen bonded to a water molecule, which, in turn, is donating hydrogen atoms to the O atoms of both heme propionates (Fig. 4.5B). These electrostatic interactions appear to be quite strong and cause a downward displacement of the $\text{C}\alpha$ atom of Trp(E7) by 0.67 Å with respect to the position of the $\text{C}\alpha$ of His(E7) in native β CO subunits. Although not in the distal pocket and interacting with the bound ligand, the β Trp(E7) side chain does physically block the entrance to the E7 channel in the crystal structure, and ligand entry through the E7 pathway requires outward rotation of the indole ring.

A comparison of the crystal structures of wild-type and Trp(E7) MbCO and deoxyMb are shown in Fig. 4.7. In both Trp(E7) Mb structures, the indole ring has moved further away from the heme ring by additional rotation about the $\text{C}\alpha$ - $\text{C}\beta$ bond than in Trp(E7) β CO subunits. The entire side chain is in the solvent phase. The aromatic ring has rotated 180° about the $\text{C}\beta$ - $\text{C}\delta$ bond, causing the phenyl portion of the indole ring to be closer to the heme than the pyrrole portion. This indole ring orientation is similar to

that seen in the *closed* Trp(E7) deoxy- α structure but is the opposite of that seen for Trp(E7) β CO. The E7 channel is significantly but not completely blocked in the Trp(E7) Mb structures and small rotations about the C β -C δ bond would open up the channel completely.

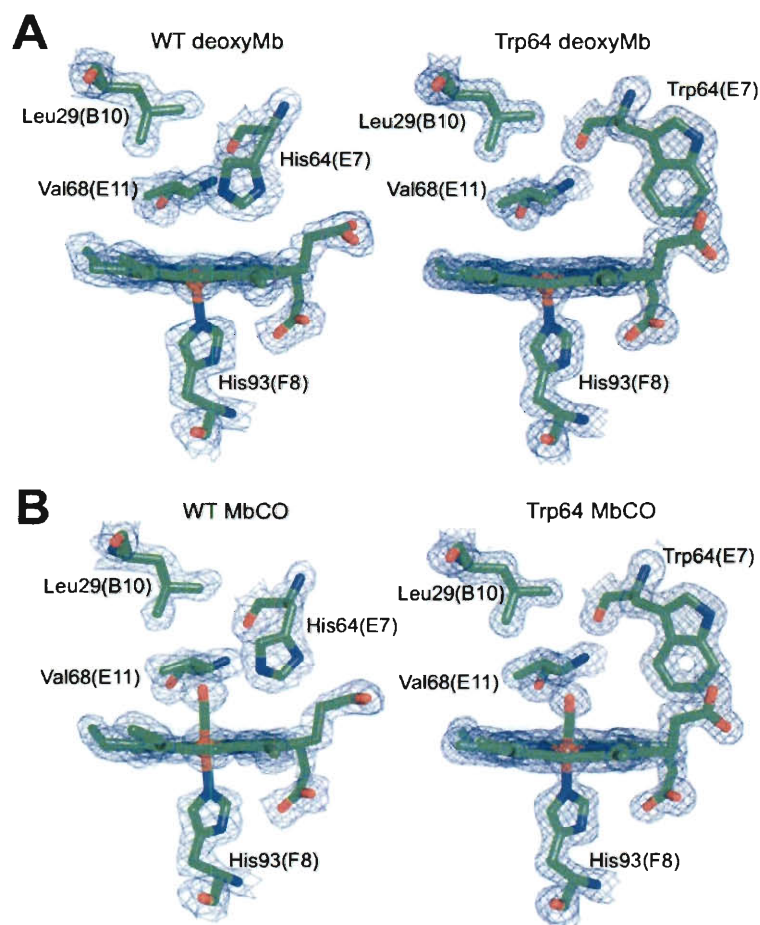


Figure 4.7. Side views of wild-type and Trp(E7) mutants of Mb. The electron density was contoured at 1.3σ and is shown as a blue net. The color code for atoms is: green, carbon; blue, nitrogen; red, oxygen; orange, iron. The key residues are shown clockwise: Trp(E7) or His(E7), His(F8), Val(E11) and Leu(B10). A, wild-type deoxyMb ([89], 2MGL) with the distal pocket water removed and Trp(E7) deoxyMb (3OGB); B, wild-type MbCO ([89], 2MGK) and Trp(E7) MbCO (3NML).

The solution FTIR spectrum for Trp(E7) MbCO shows two ν_{C-O} bands, one at 1969 cm^{-1} (60%) and another at 1942 cm^{-1} (40%) [83]. The high frequency band probably

reflects the properties of the conformers shown in Fig. 4.7, whereas the low frequency band implies hydrogen bonding from internal water molecules that may have penetrated into distal pocket and interacted with the bound CO when the Trp(E7) side chain populates an *open* conformation. However, the spectrum of Trp(E7) metMb(FeIII) has a broad Soret peak at 395 nm, which is indicative of a five-coordinate heme complex and no coordinated water [89]. Thus the active site of Trp(E7) Mb appears to be primarily apolar with ligand entry partially blocked by the indole ring.

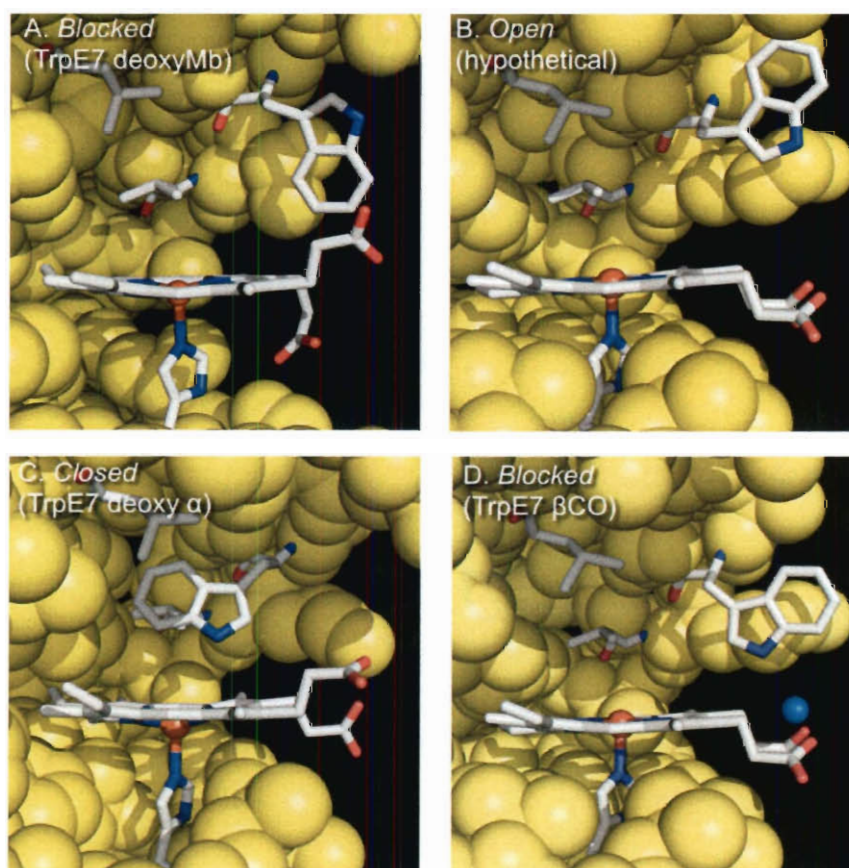
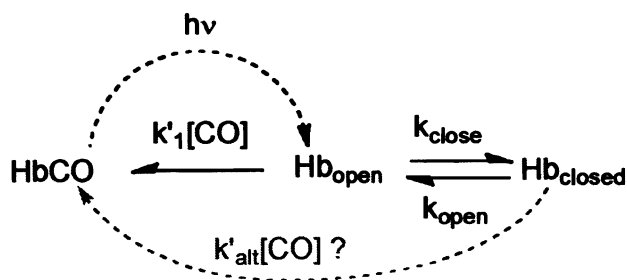


Figure 4.8. Models of *Open*, *Closed*, and *Blocked* kinetic states. *A*, model for one of the *blocked* states based on the crystal structure of Trp(E7) deoxyMb (3OGB). *B*, hypothetical model of an *open* state based on the Trp(E7) β CO structure shown in *panel D*, in which the E7 indole side chain has moved further away from the porphyrin ring by rotation about the C α -C β bond to an angle similar to that for the indole side chain in Trp(E7) deoxyMb (*panel A*). *C*, *closed* conformation observed in the structure of deoxy- α (Trp (E7)) β (WT) HbA (3NMM). *D*, *blocked* conformer based on the observed structure of α (WT) β (Trp(E7)) HbCO with the ligand removed (3NL7) and blue sphere representing the water molecule interconnecting the indole N atom with the heme propionates. The color scheme is identical to that in Fig. 4.6.

The crystal structures of the Trp(E7) mutants of Mb, α - and β Hb subunits described above provide the models for the *open*, *blocked* and *closed* states responsible for the appearance of fast, middle and slow phases, respectively, in the kinetics of ligand binding to α - and β Trp(E7) mutants (Fig. 4.8). Here, the *closed* and *blocked* states correspond to existing structures of deoxy- α Trp(E7), β CO Trp(E7) and the deoxy- and CO-forms of Mb Trp(E7). The open conformer was not observed in any of the crystal structures, and was generated by rotating the Trp(E7) side chain in the β CO structure (Fig. 4.8D) by $\sim 60^\circ$ about C α -C β bond to create an open channel connecting solvent and distal pocket.

4.6. Simple linear conformational relaxation mechanism.

The simplest mechanism for explaining the rapid and slow bimolecular binding phases observed after laser photolysis of Trp(E7) α CO is shown in Scheme 4.1. It is analogous to the mechanism proposed 14 years ago for ligand binding to non-symbiotic, plant hemoglobins [110, 138-140], in which the fast process represents competition between His(E7) coordination and ligand binding to an *open* conformation, whereas the slow phase reflects the displacement of the coordinated distal histidine by ligands incoming from solvent. In Trp(E7) α subunits, bound CO displaces the large indole side chain, pushing it out into solvent. Thus, after photodissociation the initial conformer is *open* (Hb_{open} in Scheme 4.1, modeled in Fig. 4.8 B), and there is a competition between rapid bimolecular binding and conformational relaxation of the indole side chain back into the distal pocket to form the *closed*, slowly reacting deoxy- α conformer (Hb_{closed} in Scheme 4.1, modeled in Fig. 4.8 C).



Scheme 4.1

$$k_{fast} \approx k'_1[CO] + k_{close}$$

Equation 4.1

$$f_{fast} \approx \frac{k'_1[CO]}{k'_1[CO] + k_{close}}$$

Equation 4.2

$$k_{slow} \approx k_{open} \frac{k'_1[CO]}{k'_1[CO] + k_{close}}$$

Equation 4.3

Scheme 4.1 successfully describes the dependence of the observed fast rate and the fraction of the fast phase on [CO] for isolated Trp(E7) α subunits but cannot reproduce the almost linear dependence of k_{slow} on [CO] (Fig. 4.9) without allowing binding to Hb_{closed} by alternative routes (gray dashed line and k'_{alt}). The hyperbolic dependence of the slow phase rate, k_{slow} , on [CO] was obtained by simultaneously fitting the dependences of k_{fast} , f_{fast} , and k_{slow} on [CO] to the expressions in Equations 4.1-3. The

best fit values of k'_I , k_{close} , and k_{open} are $\sim 95 \mu\text{M}^{-1}\text{s}^{-1}$, $\sim 15,000 \text{ s}^{-1}$ and $\sim 120 \text{ s}^{-1}$, respectively. In Scheme 4.1, a linear dependence of k_{slow} on $[\text{CO}]$ can only be obtained when $k_{close} \gg k'_I[\text{CO}]$, but then f_{fast} would be ≈ 0.0 and the time courses would show completely slow bimolecular rebinding. Thus, this simple mechanism cannot quantitatively describe bimolecular CO rebinding to Hb α Trp(E7) subunits even though the basic idea of a competition between closing of the E7 gate and ligand binding to an *open* state is qualitatively correct.

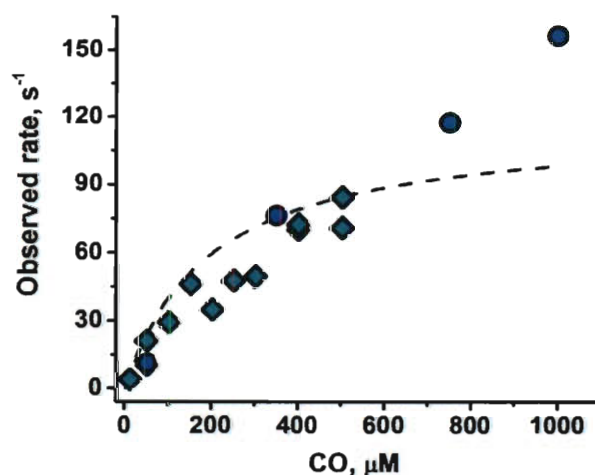


Figure 4.9. Fitting the dependence of α Trp(E7) slow rate on $[\text{CO}]$ with simple linear mechanism. The dark cyan diamonds represent rates determined in stopped flow, rapid mixing experiments with the equilibrium deoxy forms of the Trp(E7) α subunits. The blue circles represent slow rates obtained in laser photolysis experiments. The *dashed line* represents a fit to Scheme 4.1. The experimental conditions were 100 mM Na phosphate, pH 7, 20 °C.

The linear dependence of k_{slow} on $[\text{CO}]$ can be explained by direct ligand binding to the *closed* α Trp(E7) subunits as indicated in Scheme 4.1 by the *gray dashed arrow* and question mark. In this interpretation ligand binding does not require a transition to an *open* E7 channel state, and the *closed* conformer can bind ligands that migrate to the active site via alternative pathways. If the rate of outward movement of Trp(E7) were

very small, the observed slow bimolecular rate for CO binding would reflect the speed of bimolecular binding via non-E7 gate routes.

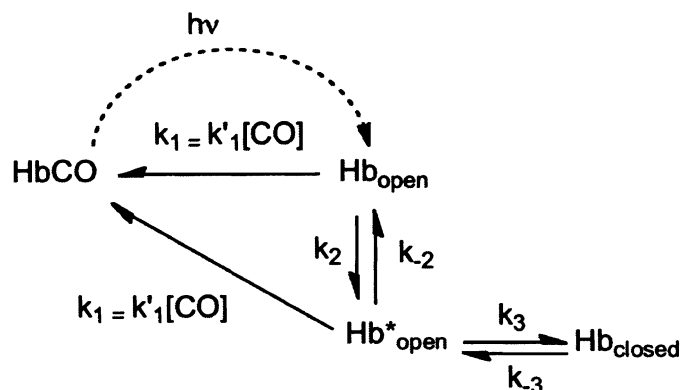
A major argument against using Scheme 4.1 with alternative binding to the Hb_{closed} state is the structure of the deoxy- α Trp(E7) distal pocket (Figs. 4.8 C). Access to the iron atom is inhibited directly by the bulky indole side chain, which not only blocks the E7 channel, but also is located directly above the iron atom. Thus, any binding event, regardless of the direction of ligand migration, requires outward rotation of the α Trp(E7) side chain to allow access to the iron atom.

4.7. Mechanism of CO binding to α Trp(E7).

Analysis of the molecular models of *open* and *closed* states of α Trp(E7) subunits (Figs. 4.8 B and C) demonstrate that it is impossible to position the Trp side chain into the E7 channel and the distal pocket by simple rotation about C α -C β or C β -C γ bonds. Severe steric clashes between the edge of the indole ring and the surface of the heme group occur, regardless of whether the pyrrole or phenyl portion of the indole ring is pointing toward the protein interior. Thus, there must be transient expansion of the heme pocket in the *open* state (conformer Hb*_{open}) to increase the size of the E7 channel and allow inward movement of the large Trp side chain.

A mechanism, which can quantitatively describe the kinetics of CO binding to mutant α subunits and take into account transient expansion of the distal pocket, is shown in Scheme 4.2. Here, both *open* conformers (Hb_{open} and Hb*_{open}) react rapidly with CO at pseudo first order rates, $k_f = k'_f[\text{CO}]$, but only the expanded Hb*_{open} conformation allows the Trp side chain to move rapidly into the distal pocket, close the E7 channel, and form

the slowly reacting Hb_{closed} conformer. The linear dependence of the slow phase rate on [CO] requires that the rate of closing of the E7 gate in the Hb*_{open} is very rapid compared to the interconversion of *open* states (i.e. $k_3 \gg k_2$ and k_{-2}).



The observation of only slow phases in rapid mixing experiments demonstrates that closing is highly favored and almost complete at equilibrium ($k_3 \gg k_{-3}$). For these conditions, a steady state assumption can be made for [Hb*_{open}] during both the fast and slow phases after laser photolysis, and k_{-3} can be neglected during the fast phase. An analytical solution for the formation of HbCO as function of time during the fast phase can be derived (Appendix 2, Equations S1-S9) and provides the following expressions for k_{fast} and f_{fast} after laser photolysis of Trp(E7) α CO:

$$k_{fast} = \frac{(k'_1[CO])^2 + k'_1[CO](k_{-2} + k_3 + k_2) + k_2k_3}{k'_1[CO] + k_{-2} + k_3}$$

Equation 4.4

$$f_{fast} = \frac{(k'_1[CO])^2 + k'_1[CO](k_{-2} + k_3 + k_2)}{(k'_1[CO])^2 + k'_1[CO](k_{-2} + k_3 + k_2) + k_2k_3}$$

Equation 4.5

Both expressions show a complex quadratic dependence on [CO]. However, if $k_3 \gg (k'_1[CO], k_2, \text{ and } k_{-2})$, then only the k_3 terms in the numerators and denominators need to be considered. Under these conditions, $k_{fast} \approx k'_1[CO] + k_2$, and $f_{fast} \approx k'_1[CO]/(k'_1[CO] + k_2)$, which are analogous to the simple expressions for Scheme 4.1 in Equations 4.1-3.

The binding of CO to the Hb_{closed} state, which occurs during the slow phase after laser photolysis and in rapid mixing experiments, can be analyzed by assuming a steady-state for both *open* conformers and taking into account the rate of the Hb_{closed} to Hb^*_{open} transition, k_{-3} . A complete derivation for k_{slow} is given in Appendix 2, Equations S11-S21, and the final expression is:

$$k_{slow} = \frac{k_{-3}k'_1[CO]}{(k'_1[CO] + k_{-3}) + \frac{k_3(k'_1[CO] + k_2)}{(k'_1[CO] + k_2 + k_{-2})}}$$

Equation 4.6

This expression also implies a complex quadratic dependence on [CO], but if $k_3 \gg (k'_1[CO], k_{-3}, k_2, \text{ and } k_{-2})$, it simplifies to $k_{slow} \approx k'_1[CO]k_{-3}/k_3 = k'_1[CO]/K_3$ at high [CO], which prescribes a linear dependence on [CO] and an inverse dependence on the equilibrium constant for the Hb^*_{open} to Hb_{closed} transition, K_3 (Appendix 2, Equations S20 and S21). Thus, the apparent bimolecular rate constant for the slow phase (*i.e.* the slope

of k_{slow} versus [CO] shown in Fig. 4.10 B) can be interpreted as the rate constant for binding to the *open* form times the equilibrium fraction of Hb^*_{open} , $I/(I+K_3)$, which equals I/K_3 when K_3 is large.

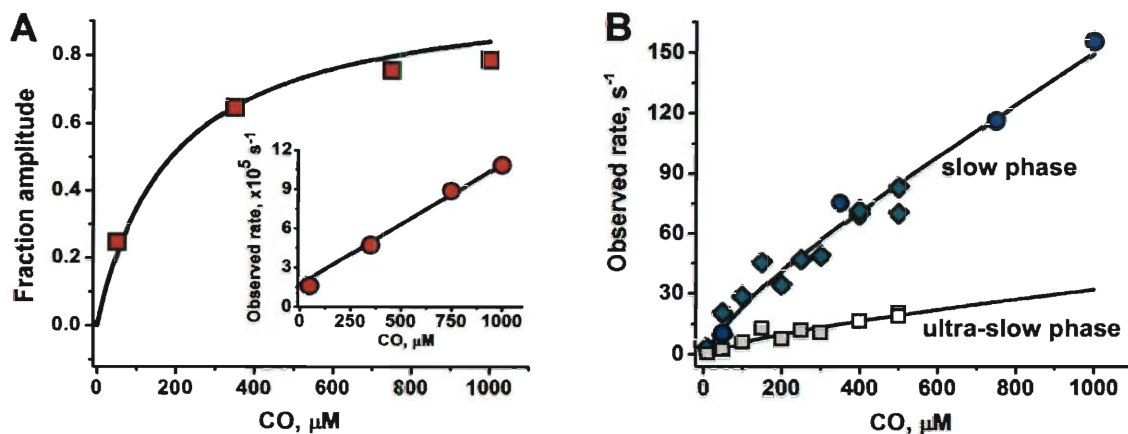


Figure 4.10. Dependences of the observed fast and slow rates for bimolecular CO binding and fraction of the fast phase on [CO] for both laser photolysis and rapid mixing experiments with isolated Trp(E7) α subunits. A, dependence of k_{fast} (red circles) and f_{fast} (red squares) on [CO]. B, dependence of k_{slow} (circles and diamonds) and $k_{ultra-slow}$ (gray squares) on [CO]. The dark cyan diamonds represent rates determined in stopped flow, rapid mixing experiments with the equilibrium deoxy forms of the Trp(E7) α subunits. The blue circles represent data from laser photolysis experiments. Black lines represent fits to the model described in Scheme 4.2, and the fitted parameters are listed in the text. The rates for the ultra slow phase were fit using the previous parameters and the model described in Appendix 2, Equations S22-S28. The fitted rate constants for the interconversion of the slow α subunits forms are $k_s = 610 \text{ s}^{-1}$, $k_{-s} = 200 \text{ s}^{-1}$. The experimental conditions were 100 mM Na phosphate, pH 7, 20 °C.

The full expressions in Equations 4.4-4.6 were used to successfully fit plots of k_{fast} , k_{slow} , and f_{fast} values vs. [CO] for bimolecular CO rebinding to Trp(E7) α subunits after laser photolysis (Fig. 4.10). The fitted value of k'_1 for bimolecular CO binding to the *open* α forms is $92 \mu\text{M}^{-1}\text{s}^{-1}$. The fitted values of k_2 and k_{-2} for the interconversion of *open* conformers are $\sim 18,000 \text{ s}^{-1}$ and $\sim 21,000 \text{ s}^{-1}$ and on the same order as the pseudo first rates of CO binding to Hb_{open} . The fitted rate of the Hb^*_{open} to Hb_{closed} transition was 100 times larger, $k_3 = 2,010,000 \text{ s}^{-1}$, whereas k_{-3} , the rate for opening the closed E7 channel is much smaller $2,900 \text{ s}^{-1}$. As result, K_3 is equal to 690, and the equilibrium fraction of deoxy- α

subunits in the *open* state is $1/(1+K_3) \approx 1/K_3 = 0.0015$, which accounts for the 1000-fold smaller bimolecular rate constant for CO binding to the *closed* conformer, $k'_{slow} \approx 0.1 \mu\text{M}^{-1}\text{s}^{-1}$.

The fitting analysis indicates that the absolute values of k_3 and k_{-3} are poorly defined, but k_3 must be $\geq \sim 1,000,000 \text{ s}^{-1}$. Thus, the expansion of the distal pocket and inward movement of the indole side chain are concerted processes, with the rate limiting step being the increase in size of the active site (i.e. $k_2 \leq k_3$ in Scheme 4.2). In contrast, the ratio of k_3/k_{-3} (i.e. K_3) is well determined by the observed dependence of the slow phase rate on [CO] and must be ~ 700 . In addition, the detailed shape of the plot of k_{slow} versus [CO] (Fig. 4.10 B) does exhibit curvature at low [CO] reflecting the quadratic expressions for [CO] in Equation 4.6.

In this interpretation, the slow bimolecular rates observed in rapid mixing and flash photolysis experiments reflect the very small fraction (≤ 0.001) of *open* states at equilibrium in the unliganded form instead of the rate of binding through alternative routes with very high kinetic barriers. Unfortunately, distinguishing between ligand binding by alternative pathways and the E7 gate cannot be achieved unambiguously by kinetic data alone. We favor scheme 4.2 because the crystal structure suggests that outward rotation of Trp(E7) is needed for any ligand to bind and the more complex quadratic expression in Equation 4.6 does emulate the observed curvature in plots of k_{slow} versus [CO].

The rate of the first slow phase observed for CO binding to equilibrium deoxy $\alpha\text{Trp(E7)}$ subunits in stopped flow experiments matches exactly that for the slow phase observed in the laser photolysis experiments (see dark cyan diamonds in the upper curve,

Fig. 4.10 B). The second ultra slow phase is unique to the mixing experiments. Similar ultra-slowly reacting deoxy forms are seen in stopped flow rapid mixing experiments for CO binding to non-symbiotic, hexacoordinate plant hemoglobins [112] and the heme protein transcription factor *CooA* [141]. These slowly reacting forms can be modeled by an additional linear transition to an even more hindered, less accessible form of $\text{Hb}_{\text{closed}}$ (Appendix 2, Scheme 4.2c). Thus it appears that, after the initial *closed* state is formed, the Trp side chain induces further expansion of the distal pocket to bury itself even deeper in the protein interior, giving rise to the observed ultra-slow phase (a more detailed mechanistic description is provided in Appendix 2, Equations S22-S28).

4.8. Mechanism of CO binding to β Trp(E7).

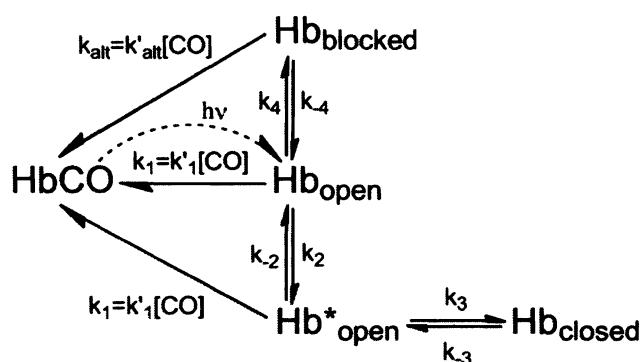
As shown in Fig. 4.2A, three phases are observed for CO rebinding to Trp(E7) β subunits after laser photolysis. A small, very fast phase is followed by a dominant, moderately slow middle phase and then a smaller phase with a rate similar to that of the slow phase observed after laser photolysis of Trp(E7) α CO subunits. The rate of the fast phase, k_{fast} , shows a linear dependence on [CO] with a large y-intercept reflecting the rate of conformational relaxation to the slowly reacting species (*blocked* and *closed*) (Fig. 4.11B). The competition between conformational relaxation and rapid ligand rebinding to the *open* conformer of β Trp(E7) is demonstrated by the increases in f_{fast} and the decreases in the fractions of the middle, f_{middle} , and slow, f_{slow} , phases with increasing [CO] (Fig. 4.11A). The middle and slow phase rates, k_{middle} and k_{slow} , both show a linear dependence on [CO]. Thus, in the case of β subunits, two slowly reacting conformers are formed from the unliganded *open* state immediately after photolysis.

I have assigned the slowest process to a *closed* conformation of Trp(E7), similar to Hb_{closed} for α subunits, in which the indole ring fills both the E7 channel and the distal pocket, restricting ligand access to the iron from any direction (see Fig. 4.8C). The middle phase is assigned to bimolecular ligand rebinding to Hb_{blocked}, a deoxygenated *blocked* conformer resembling the structure shown in Fig. 4.8D for the mutant subunit in $\alpha(\text{WT})\beta(\text{Trp}(\text{E7})) \text{HbCO}$. In this case, the indole side chain is located outside the distal pocket, being held in place by a water molecule that interconnects the indole N atom and two heme propionates. In contrast to the *closed* state, the Trp side chain in the Hb_{blocked} conformer blocks only the entrance to the E7 gate but not access to the iron from within the heme pocket. Thus, the *blocked* conformer could bind ligands migrating via alternative routes.

The *blocked-to-closed* transition cannot be achieved by a simple one step rotation of the indole side chain about C α -C β bond due to severe clashes with the heme and other residues lining the inner surface of the distal pocket. Instead, the indole side chain in the *blocked* state shown in Fig. 4.8D must first rotate outward about the C α -C β bond forming a transient *open* state similar to that proposed in Fig. 4.8B, "flip" its orientation about the C β -C γ bond to generate a conformer analogous to that in Fig. 4.8A, and finally swings back into the distal pocket by rotation about the C α -C β bond to form a *closed* state similar to that seen for Trp(E7) deoxy α subunits in Fig. 4.8C. Thus, Hb_{closed} cannot be formed directly from the *blocked* β conformer without first returning to an *open* conformation (i.e. from Fig. 4.8D to 4.8B to 4.8A to 4.8C).

A mechanism for ligand binding to β Trp(E7), which accommodates the structural interpretations described above, is shown in Scheme 4.3. The *open* conformation of the

protein is generated immediately after CO photodissociation, and then, either CO rebinds rapidly to Hb_{open} or Hb_{open} interconverts to $\text{Hb}_{\text{blocked}}$ and $\text{Hb}_{\text{closed}}$. As in case of α Trp(E7) subunit, the transition from Hb_{open} to $\text{Hb}_{\text{closed}}$ involves the expansion of the initial *open* state ($\text{Hb}_{\text{open}} \rightarrow \text{Hb}^*_{\text{open}}$) to accommodate the indole side chain orientation shown in Fig. 4.8 C. In contrast, relaxation of Hb_{open} to the *blocked* state (Fig. 4.8 D) does not require any significant structural perturbations at the active site because the E7 indole side chain only blocks the channel and can be described as a one-step process.



Scheme 4.3

In this mechanism, direct CO binding to the *blocked* state was modeled as due to ligand movement into the active site by alternative routes without requiring opening of the *blocked* state, and thus, the middle phase rates in Fig 4.11 C are postulated to represent $k'_{\text{alt}}[\text{CO}]$. Alternatively, these rates could represent the fraction of open states derived from $\text{Hb}_{\text{blocked}}$ (i.e. $1/(1+K_4)$ where $K_4 = k_4/k_{-4}$). It is not possible to discriminate between these interpretations of the middle phase, and we have chosen to use Scheme 4.3 as a compromise that allows an alternative route interpretation for analyzing ligand binding to Trp(E7) β subunits.

A steady-state approximation was assumed for $\text{Hb}^*_{\text{open}}$ to derive expressions for the dependencies of k_{fast} , f_{fast} , f_{middle} and f_{slow} on $[\text{CO}]$, and the rates $k'_{alt}[\text{CO}]$, k_3 and k_4 , were neglected when analyzing the initial phase, because CO binding to the *blocked* and *closed* species is significantly slower than binding to the open states (Appendix 2, Equations S29-S44). When $k_3 \gg k'_1[\text{CO}]$, k_2 and k_4 , simple expressions for the observed photolysis parameters can be obtained (Equations 4.7-10), which are analogous to the expressions for the simple linear mechanism in Scheme 4.1 and simplified equations for Scheme 4.2.

$$k_{fast} \approx k'_1[\text{CO}] + k_2 + k_4$$

Equation 4.7

$$f_{fast} \approx \frac{k'_1[\text{CO}]}{k'_1[\text{CO}] + k_2 + k_4}$$

Equation 4.8

$$f_{middle} \approx \frac{k_4}{k'_1[\text{CO}] + k_2 + k_4}$$

Equation 4.9

$$f_{slow} \approx \frac{k_2}{k'_1[\text{CO}] + k_2 + k_4}$$

Equation 4.10

An expression for the rate of CO binding to the Hb_{blocked} state was derived by applying steady-state approximations for both *open* intermediates (Hb_{open} and Hb*_{open}) and ignoring CO binding to Hb_{closed} because k_{middle} is observed to be ≥ 10 -fold faster than k_{slow} . The detailed derivation can be found in Appendix 2, Equations S45-S50.

$$k_{middle} = k'_{alt}[CO] + k_{-4}(1 - f_{middle})$$

Equation 4.11

Thus, the middle phase is a sum of two binding processes: (1) ligand binding via alternative routes directly to Hb_{blocked} (expressed as $k'_{alt}[CO]$) and (2) CO recombination to *open* conformers originating from Hb_{blocked} (expressed as the $k_{-4}(1 - f_{middle})$ term). Although, Equation 4.11 predicts a complex dependence on [CO], since f_{middle} is inversely proportional to [CO]; k_{middle} is effectively equal to $k'_{alt}[CO]$ when the ligand concentration is high and k_{-4} is small.

An analytical solution for the slow phase after laser photolysis of Trp(E7) β CO subunits was derived assuming a steady-state for Hb_{open}, Hb*_{open} and Hb_{blocked} in Scheme 4.3 (Appendix 2, Equations S51-S58). When $k_3 \gg k_1, k_{-2}, k_2$ and k_{-3} , the expression for k_{slow} can be simplified to:

$$k_{slow} \approx \frac{1}{K_3} \left(k'_1[CO] + k_{-2} \frac{k'_1[CO] + \frac{k'_{alt}[CO]k_4}{k'_{alt}[CO] + k_{-4}}}{k'_1[CO] + k_2 + \frac{k'_{alt}[CO]k_4}{k'_{alt}[CO] + k_{-4}}} \right)$$

Equation 4.12

The $1/K_3$ term represents the fraction of $\text{Hb}^*_{\text{open}}$ formed from $\text{Hb}_{\text{closed}}$ when $K_3 \gg 1$. If $k_{-4} \ll k'_{\text{alt}}[\text{CO}]$ so that $k_{-4} + k'_{\text{alt}}[\text{CO}] \approx k'_{\text{alt}}[\text{CO}]$, the ratio in parentheses reduces to $(k'_1[\text{CO}] + k_4)/(k'_1[\text{CO}] + k_2 + k_4)$, which is $\sim(1-f_{\text{slow}})$. As a result, the final form of the Equation 4.12 becomes:

$$k_{\text{slow}} \approx \frac{1}{K_3} (k'_1[\text{CO}] + k_{-2}(1 - f_{\text{slow}}))$$

Equation 4.13

and is analogous to the rate expression for the middle phase (Equation 4.11). Thus, the rate for slow CO recombination to $\text{Hb}_{\text{closed}}$ is the sum of all possible binding processes:

(1) CO binding to $\text{Hb}^*_{\text{open}}$ ($\text{Hb}_{\text{closed}} \rightarrow \text{Hb}^*_{\text{open}} \rightarrow \text{HbCO}$); (2) CO binding to Hb_{open} ($\text{Hb}_{\text{closed}} \rightarrow \text{Hb}^*_{\text{open}} \rightarrow \text{Hb}_{\text{open}} \rightarrow \text{HbCO}$); and (3) CO binding to $\text{Hb}_{\text{blocked}}$ ($\text{Hb}_{\text{closed}} \rightarrow \text{Hb}^*_{\text{open}} \rightarrow \text{Hb}_{\text{open}} \rightarrow \text{Hb}_{\text{blocked}} \rightarrow \text{HbCO}$).

The dependences of fractions and rates of fast, middle and slow phases on $[\text{CO}]$ were fitted to full expressions for f_{fast} , f_{middle} , f_{slow} , k_{fast} , k_{middle} and k_{slow} . The solid lines in Fig. 4.11 represent best fits with parameter values $k'_1 = 81 \mu\text{M}^{-1}\text{s}^{-1}$, $k_2 = 51,000 \text{ s}^{-1}$, $k_{-2} = 14,000 \text{ s}^{-1}$, $k_3 = 3,500,000 \text{ s}^{-1}$, $k_{-3} = 2150 \text{ s}^{-1}$, $k_4 = 125,000 \text{ s}^{-1}$, $k_{-4} = 100 \text{ s}^{-1}$, $k'_{\text{alt}} = 0.61 \mu\text{M}^{-1}\text{s}^{-1}$.

Generally, most of these values are similar to the analogous parameters for α Trp(E7) subunit (except for k_4 , k_{-4} and k'_{alt} , which are unique to β Trp (E7) subunits). The values of k_3 and k_{-3} are undetermined; however, k_3 must be at least 10-fold larger

than k_4 . At the same time, the equilibrium constant for the *closed* conformer, $K_3 = k_3/k_{-3}$, is defined and equals ~ 1600 . This large value of K_3 determines the very small fraction of *open* conformers compared to $\text{Hb}_{\text{closed}}$ and explains the markedly slow bimolecular rate of CO binding to the *closed* species.

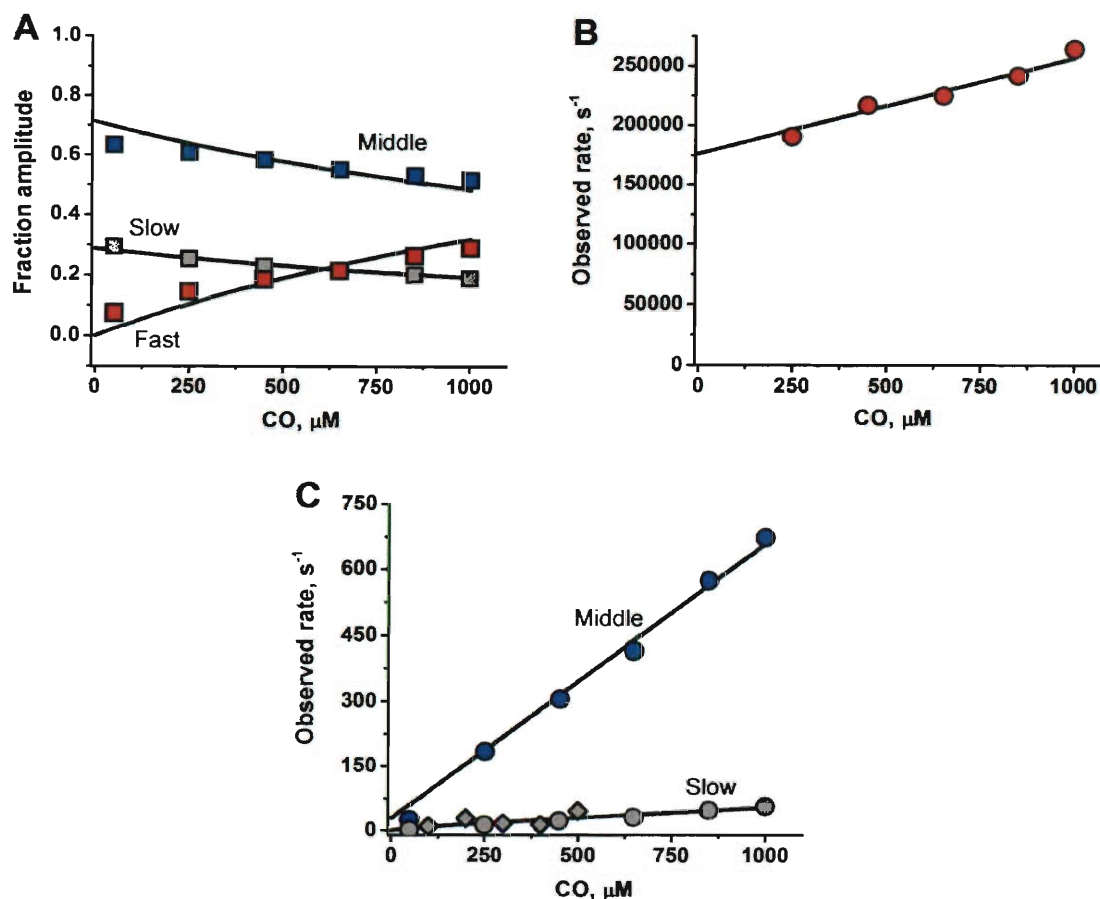


Figure 4.11. Dependences of the observed rates and the fractions of the fast and slow phases on [CO] for CO binding to isolated Trp(E7) β subunits. A, squares represent the observed fractions of the fast (red), middle (blue), and slow (gray) phases (f_{fast} , f_{middle} , f_{slow} , respectively) observed after laser photolysis of Trp(E7) βCO subunits (see Figs. 4.2 and 4.3) B, red circles represent the observed rates for the fast phase, k_{fast} . C, circles represent the rates for the middle (blue), k_{middle} , and slow (gray), k_{slow} , phases, respectively, measured after laser photolysis. The gray diamonds represent the slow phase measured in stopped flow rapid mixing experiments with the equilibrium forms of Trp(E7) deoxy β subunits. The black lines represent fits to the model described in Scheme 4.3 for the *blocked* and *closed* states, and the fitted parameters are listed in the text. The experiments were conducted in 100 mM Na phosphate, pH 7, 20 $^{\circ}\text{C}$.

Only slow phases are seen when isolated deoxy- β Trp(E7) subunits are rapidly mixed with CO in stopped-flow experiments (Figs. 4.2B and 4.11C). Thus, at equilibrium the *closed* Trp(E7) conformer is also favored in β subunits, whereas the *blocked* conformer is a transient state, which is primarily seen after photolysis. This conclusion is supported quantitatively by equilibrium analysis of Scheme 4.3 (Appendix 2, Equations S59-S62), which indicates that the fraction of *closed* state for deoxy Trp(E7) β subunits is ≥ 0.9 .

4.9. Comparison of the mechanisms for α and β subunits.

In both subunits, ligand binding to the *open* state is fast ($\sim 90\text{-}80 \mu\text{M}^{-1}\text{s}^{-1}$) and comparable to that for Gly and Ala(E7) mutants ($\sim 90\text{-}50 \mu\text{M}^{-1}\text{s}^{-1}$) (Chapter 3). The rate of the decay of the initial *open* state (Hb_{open}) to the *closed* or *blocked* states is 10 times faster in β subunits than in α subunits ($175,000 \text{ s}^{-1}$ vs. $18,000 \text{ s}^{-1}$, respectively). The multiple orientations of His45(CE3) in the crystal structure of deoxy- α (Trp(E7)) β (WT) (Fig. 4.6) provide a possible explanation for these differences. In the wild-type structures of either deoxy- α or α CO subunits, His(CE3) forms a salt bridge with the heme-6-propionate, which would have to be disrupted for either outward or inward movement of the distal E7 tryptophan. In β subunits, the equivalent CD3 amino acid is Ser44. This Ser residue is located too far to interact strongly with the heme-6-propionate, which could explain the more rapid formation of the expanded *open* state ($\text{Hb}^*_{\text{open}}$) in β subunits and account for the higher rates of inward movement of the β Trp(E7) side chain.

This idea is supported by the lack of a *closed* conformation in Trp(E7) Mb. In wild type Mb, Arg(CD3) forms strong hydrogen bonds with the heme-6-propionate and

water molecules at the entrance to the E7 channel, and the heme-7-propionate is fixed in position by strong electrostatic interactions with His97(FG3), both of which would inhibit expansion of the E7 channel. These interactions reduce the rate of heme loss markedly in ferric Mb (0.01 hr^{-1}) compared to Hb subunits in R state ferric hemoglobin [137], and will also inhibit expansion of the E7 channel, preventing inward movement of the Trp(E7) side chain in Mb.

The lifetime of Hb_{open} in β subunits is also shortened by the appearance of the unique *blocked* conformer of β Trp(E7). The formation of the *blocked* conformer in β subunits appears to depend on the orientation of the heme propionates, with the carboxyl atoms lying below the heme plane, and the presence of a water molecule between them (Figs. 4.5 B and 4.8 D). In α subunits and Mb the existence of this *blocked* conformer is unlikely, because the heme-6-propionate is involved in strong electrostatic interactions with either His45(CD3) (α subunits) or Arg45(CD3) (Mb), both of which keep the 6-propionate “arm” above the heme plane (Fig. 4.5 A and 4.7). In the *blocked* conformer of Trp(E7) Mb (Figs. 4.8 A), the indole ring has rotated 180° about the $\text{C}\beta\text{-C}\gamma$ bond causing the pyrrole N atom to be far away from the heme propionates.

In general, there appears to be more conformational flexibility in the β subunits. This idea is supported by the observations that β subunits bind and release all the diatomic gases ~ 2 times more rapidly and react much more rapidly with larger ligands than the α subunits [142]. Larger rates of formation of the *blocked* and *closed* states in β subunits add further support to this conclusion.

4.10. Opening and closing of the E7 gate in wild-type and mutant Mb and Hb.

Roughly 15 years ago Champion and coworkers examined the interconversion of the *open* and *closed* states of the His(E7) side chain in sperm whale MbCO [86, 87]. Using double-pulse flash photolysis methods, they were able to kinetically select and then measure the fraction of *open* Mb molecules after the initial excitation pulse. The interconversion rate between *open* and *closed* forms was estimated to be $1,400,000 \text{ s}^{-1}$ in aqueous solutions of Mb at neutral pH. A similar and probably, greater rate occurs between the *open* and *closed* forms of His(E7) in hemoglobin subunits, which are, in general, less rigid with fewer electrostatic interactions between His(E7), surrounding amino acid side chains, and the heme propionates. Thus, the smaller, naturally occurring His(E7) side chain can move rapidly between *open* and *closed* conformational states on sub-microsecond time scales, probably without significant expansion of the distal portion of the heme pocket. In contrast, inward movement of the larger Trp(E7) side chain requires expansion of the distal pocket, which occurs at rates equal to $\sim 18,000 \text{ s}^{-1}$ and $\sim 51,000 \text{ s}^{-1}$ in the α and β subunits, respectively, and competes with bimolecular ligand rebinding after laser photolysis.

Morikis *et al.* [84] and Tian *et al.* [86, 87] estimated that in Mb, the His gate is open 3-5% of the time at neutral pH. In HbA, similar fractions of *open* His(E7) states (~ 0.07) are obtained from comparisons of CO binding to the wild type Hb subunits ($k'_{CO} \approx 6 \mu\text{M}^{-1}\text{s}^{-1}$) and to the *open* forms ($\sim 80\text{-}90 \mu\text{M}^{-1}\text{s}^{-1}$). The slow phase rate constants, $k'_{CO} \approx 0.1 \mu\text{M}^{-1}\text{s}^{-1}$, observed in rapid mixing experiments, indicate that the equilibrium fraction of *open* Trp(E7) conformers is 50-fold smaller (~ 0.001) than that observed for His(E7).

The larger more apolar Trp side chain prefers the interior, *closed* position and can be accommodated at equilibrium in the distal pockets of both the α and β subunits.

In contrast to the Hb subunits, the indole side chain in Trp(E7) Mb does not appear to form a *closed* conformer but remains in a *blocked* conformation in both the liganded and unliganded states (Fig. 4.7). Rotation about the C α -C β Trp(E7) bond to bring the indole ring into a *closed*, internal conformation is restricted by close contacts with the heme ring and by significant steric clashes with Val68(E11). In addition, the cluster of charged amino acids (Arg 45, Asp 60 and Lys 66) and ordered water molecules located in vicinity of the pyrrole portion of the indole ring (data not shown) may electrostatically stabilize the conformation seen in Fig. 4.7. This structural interpretation is supported by the observation of simple kinetics after laser photolysis of Trp(E7) MbCO (Fig. 4.4 A). The observed bimolecular rate for CO binding to the Mb mutant is close to that for the wild-type protein (Table 4.2), indicating that there is no dramatic increase in hindrance at the iron atom due to filling of the distal pocket with the indole side chain.

The bimolecular rate of CO binding to Mb is limited by internal Fe-ligand bond formation, and is not affected significantly by the bimolecular rate of ligand entry [73, 143]. Because the Trp(E7) side chain can only block the entrance to the E7 channel and does not influence iron reactivity, it has little effect on the overall association rate constant for CO binding. In contrast, the bimolecular rate constant for O₂ binding to Mb is governed more strongly by the rate of ligand entry. As a result, k'_{O_2} for Trp(E7) Mb is ~3-fold less than for wild-type Mb due to blocking of the entrance to the E7 channel (Table 4.2).

Table 4.2. The parameters for ligand binding and opening and closing of the E7 gate for isolated wild-type and mutant HbA subunits and Mb

Globin and conformer	k'_{CO} $\mu\text{M}^{-1}\text{s}^{-1}$	<i>Open</i> \rightarrow <i>Closed</i> , <i>Blocked</i> (s^{-1})	k'_{O_2} $\mu\text{M}^{-1}\text{s}^{-1}$	k'_{entry} $\mu\text{M}^{-1}\text{s}^{-1}$
His(E7) α	5.5 ^a	$\geq 1,400,000^{\text{d}}$	40 ^a	36 ^a
Gly(E7) α	100 ^a	N.A.	250 ^a	150 ^a
Trp(E7) α				
<i>Open</i>	92		210 ^{a,c}	160 ^a
<i>Closed</i>	0.12	18,000	$\sim 0.5^{\text{a}}$	0.14 ^a
His(E7) β	7.2 ^a	$\geq 1,400,000^{\text{d}}$	52 ^a	42 ^a
Gly(E7) β	40 ^a	N.A.	160 ^a	89 ^a
Trp(E7) β				
<i>Open</i>	80		130 ^c	250 ^a
<i>Blocked</i>	0.7	130,000	1.7 ^a	1.2 ^a
<i>Closed</i>	0.06	50,000		0.13 ^a
His(E7) Mb	0.51 ^b	1,400,000 ^d	17 ^b	34 ^c
Gly(E7) Mb	5.8 ^b	N.A.	140 ^b	540 ^c
Trp(E7) Mb	0.70	N.A.	6.2 ^b	8.6 ^c

Rate parameters taken from: ^a Chapter 3; ^b Springer *et al.* [100]; ^c Scott *et al.* [22]; ^d The interconversion rate for Mb was taken from Tian *et al.* [86, 87]; corresponding parameters for Hb subunits were assumed to be equal or larger than that for Mb (see section 4.1); ^e Computed as the slope of the linear dependence of the observed rate on [ligand].

Scott *et al.* [22] estimated that the specific bimolecular rate constants for ligand entry into the distal pockets of wild-type and Trp(E7) Mb are $34 \mu\text{M}^{-1}\text{s}^{-1}$ and $8.7 \mu\text{M}^{-1}\text{s}^{-1}$, respectively. In contrast, the slow phases for O₂ binding to the Trp(E7) Hb subunits exhibit bimolecular rate constants on the order of $2\text{-}5 \mu\text{M}^{-1}\text{s}^{-1}$, which is significantly smaller than for Trp(E7) Mb (Table 4.2), and suggests that the side chain of Trp(E7) can enter the distal pockets of the α and β subunits of human hemoglobin but not in Mb.

4.11. Multiple pathways versus the E7 gate.

In both Hb subunits, the large indole side chain can enter the distal pocket and form a *closed* conformer, which obstructs the E7 channel, restricts access to the iron atom, and lowers the bimolecular rate of ligand binding 50-100-fold compared to wild-

type human HbA. In β subunit, an additional conformation is formed in which Trp side chain only blocks the entrance to E7 channel, but not access to the iron atom within the distal pocket. Bimolecular ligand binding to this *blocked* conformer is still 10-fold slower than to wild-type protein, suggesting that, if alternative ligand migration pathways occur, those routes are taken $\leq 10\%$ of the time in β subunits containing His(E7). Much smaller effects are observed for sperm whale Trp(E7) Mb where k'_{entry} is only ~ 3 to 4-fold less than the value for the wild type protein, implying that more ligands could take alternative routes in Mb. Alternatively, this smaller effect can be explained by a more flexible orientation of the indole ring in the *blocked* conformer of Trp(E7) Mb in comparison to that for the *blocked* β Trp(E7) state (see Figs. 4.8 A and D). In Mb, the Trp(E7) side chain appears to have more rotational freedom about the C α -C β and C β -C γ bonds.

These structural and kinetic data for the Trp(E7) mutants argue strongly that the E7 channel is the major route for ligand entry and escape, particularly for β subunits of human hemoglobin. If the alternative pathways based on Xe binding and computational predictions [36] were major routes for ligand migration in Hb, it would be hard to understand how the *blocked* conformer of the β Trp(E7) mutant subunit (Fig. 4.8 D) could have such large effects on the time courses for bimolecular ligand rebinding after laser photolysis. These ideas are explored further in the next chapter where the effects of Xe binding to and changes in internal volume in the Hb subunits are examined.

CHAPTER 5: THE ROLE OF INTERNAL CAVITIES IN LIGAND BINDING TO HUMAN HBA

5.1. Protein cavities, Xe binding, and ligand capture in globins.

Internal voids and pockets are common features of protein structure [144, 145]. Often, these cavities play obvious crucial roles in the function of the particular protein, i.e. fatty acid binding in serum albumin [146] and oxygen access to the active site in heme oxygenase [147]. In other proteins, internal cavities are referred to as simple packing defects and their functional significance is not entirely clear, including myoglobin [30, 31], hen egg-white lysozyme [148], IL-1 β [149], Scapharca Hb [150], cytoglobin [151], neuroglobin [152]. However, the conservation of some of these cavities during the course of evolution implies their importance because the presence of these packing defects appears to have a high energetic cost during protein folding and reduces protein thermostability [145, 153-157].

Mb was the first globin molecule in which the existence of internal cavities was discovered. In 1965, the Kendrew group [30] and then, in 1985, Petsko and coworkers [31] reported crystal structures of Xe-bound Mb. Xe-harboring sites were found in the proximal part of the heme pocket just below pyrrole ring B (called Xe1), behind the heme next to the vinyl group of pyrrole B (Xe2), in the back of the distal pocket (Xe4), and between EF corner and H helix (Xe3). Later, it was demonstrated by our group and others that these Xe cavities are involved in kinetics of internal ligand movements after photolysis of Mb-ligand complexes [22, 33, 80, 158-160]. Most authors suggested that Xe cavities, particularly Xe4 and Xe1, serve to capture and retain entering ligands before they bind to the heme iron, thereby, increasing the efficiency of ligand capture [158,

160]. Molecular modeling and dynamic simulations went further and predicted that apolar cavities may function as transient stations for ligands migrating from the solvent to the active site of Mb and may be part of the pathways for ligand entry and exit [23, 24, 26, 27, 29, 77]. However, most experimental data do not support these theoretical conclusions.

Filling these cavities with Xe or space-filling mutations (Trp, Phe) does not affect significantly the rates of ligand entry and escape in Mb [22, 32, 80]. Time-resolved crystallography demonstrated that the lifetime of CO in the Xe1 pocket strongly depends on the size of the B10 residue, which is located on the opposite side of the heme, suggesting that ligands can not diffuse into the solvent directly from the Xe1 cavity and must first return to the distal pocket [53]. Replacing Leu(F4), which shields the Xe1 pocket from solvent, with Gly did not increase the rate of ligand entry, indicating strongly that the Xe1 cavity is not a part of the major ligand migration pathway [161]. In contrast, analogous mutations at the E7 position resulted in ~10-fold increase in the association rate constants for O₂ binding [20, 126]. Thus, functional studies almost uniformly indicate that ligands enter the distal pocket via the channel created by outward rotation of His(E7) [22, 32, 80, 84, 86, 87, 107, 126, 130].

Apart from harboring and helping to capture gaseous ligands, the Xe cavities in Mb were also reported to bind fatty acids at very high concentrations, suggesting that Mb may participate in transporting it to mitochondria. However, there is little or no *in vivo* experimental evidence to support this hypothesis [162].

Hemoglobin I from blood clam *Scapharca inequivalvis* (HbI) is another representative of the globin family revealing a system of apolar, internal cavities similar

to those in Mb. Time resolved X-ray crystallography and FTIR spectroscopy associated with temperature-derivative spectroscopy demonstrated that these cavities can trap photodissociated CO molecules. However, again blocking these docking sites with Xe atoms and organic halides (dichlorethane), as well as space-filling mutations, caused no appreciable effect on ligand escape from protein [150, 163]. Thus, as in the case of Mb, the distal His in the clam Hb was also proposed to be the major entry/exit pathway for ligands.

However, the His(E7) gate is not a universal pathway for ligand diffusion in globins. In some bacterial truncated 2/2 hemoglobins and the neuronal mini-globin from the Nemertean seaworm *Cerebratulus lacteus*, ligands enter the protein between the C-terminal ends of the E and H helices through an apolar tunnel [164]. Our group has shown that, in *Cerebratulus lacteus* Hb (CerHb), either blocking the apolar tunnel with Trp mutations or filling the tunnel with Xe results in markedly diminished fractions of ligand escape to solvent and slower rates of ligand entry into the distal pocket [68, 81].

As described in the previous chapters, detailed information regarding ligand migration in human HbA is scarcer than for the monomeric globins due to the complexity of four subunits, at least two quaternary structure transitions, and experimental difficulties associated with the differences between α and β subunits. Adachi and coworkers [165] used time-resolved crystallography of Fe-Ni hybrid hemoglobins to study ligand recombination in T-state Hb. After CO photodissociation, the electron density corresponding to ligand in α subunits was observed in the primary docking site, located 3.5 Å away from Fe above the pyrrole C ring. In β chains, an additional ligand

electron density sphere was found in the back of the distal pocket, ~ 8.5 Å from Fe, in a cavity circumscribed by B10, E11, E12 and G8 amino acid side chains.

Sottini *et al.* [35, 166] measured CO rebinding kinetics for R-state HbCO encapsulated in silicon hydrogels in the presence of 80% glycerol at 10 °C and resolved two different geminate rebinding phases with characteristic rebinding times of $\sim 10^{-8}$ and 10^{-6} s. They concluded, that these phases did not reflect subunit heterogeneity but rather corresponded to ligand rebinding from two discrete sites. Using molecular modeling, the authors suggested potential ligand docking sites in the α and β distal pockets located in the regions similar to the Xe4 binding site in Mb, and proposed that these cavities are responsible for slower geminate process as was observed in Mb at physiological conditions [22].

In an attempt to experimentally locate these internal, apolar cavities in α and β subunits of HbA and to determine their potential involvement into ligand migration, Savino *et al.* [36] crystallized Xe-bound deoxyHbA. In α chains, three Xe sites were found, one in the distal pocket close to Phe(CD4) and two others roughly 14 Å away from heme iron in the protein matrix. In β chains, four Xe binding sites were identified, two of which corresponded to the Xe4 and Xe2 cavities of Mb. An additional Xe atom was found between these two cavities, and one atom was external, located between A and H helices. Savino *et al.* [36] proposed that these Xe binding sites map multiple ligand migration pathways from the active site to the solvent in both Hb subunits.

In the preceding chapters, the E7 gate in HbA was blocked and closed by replacing the distal His with a larger Trp residue. The rate of bimolecular CO and O₂ binding to the blocked β Trp(E7) conformer decreased 10-fold in comparison to wild-

type, His(E7) species, suggesting that at least in β subunit ~ 90% of ligands bind to heme via the His(E7) gate. In this chapter, the contribution of the apolar distal pocket and small internal cavities on ligand migration within the α and β subunits of HbA were investigated by measuring the effects of high xenon pressures and Phe and Trp substitutions at the internal B10, E11 and G8 positions on ligand binding to isolated chains.

5.2. Nanosecond CO recombination to α and β subunits and HbA tetramers.

Monitoring geminate rebinding after laser photolysis provides indirect evidence for the extent of ligand migration inside globins immediately after the bond between the ligand and Fe has been disrupted. Depending on the reactivity of the ligand and iron, the length of the laser pulse, and the experimental conditions, rebinding from the initial docking site of the ligand and/or from more distant locations within the protein can be observed. In case of myoglobin, geminate O_2 recombination with the heme iron is moderately slow ($\sim 10 \mu s^{-1}$), which allows ligand molecules to migrate from the distal pocket and rebind from more remote sites, presumably the Xe cavities. In human hemoglobin A, due to the staggered orientation of the proximal His, the rate of in-plane movement of heme iron increases, and, hence, the reactivity of the iron with ligands is much greater [167]. As a result, O_2 geminate recombination in HbA is very fast ($>100 \mu s^{-1}$) and reflects primarily ligand rebinding from the vicinity of Fe [16]. More information about ligand migration in hemoglobin subunits can be obtained by measuring geminate CO recombination. The rate of internal CO rebinding to Fe is 10-fold lower than that for O_2 , which allows the ligand to escape to more distant sites. In addition, HbCO complexes

are much more stable than HbO_2 , which tends to autooxidize, particularly in the case of unstable mutants.

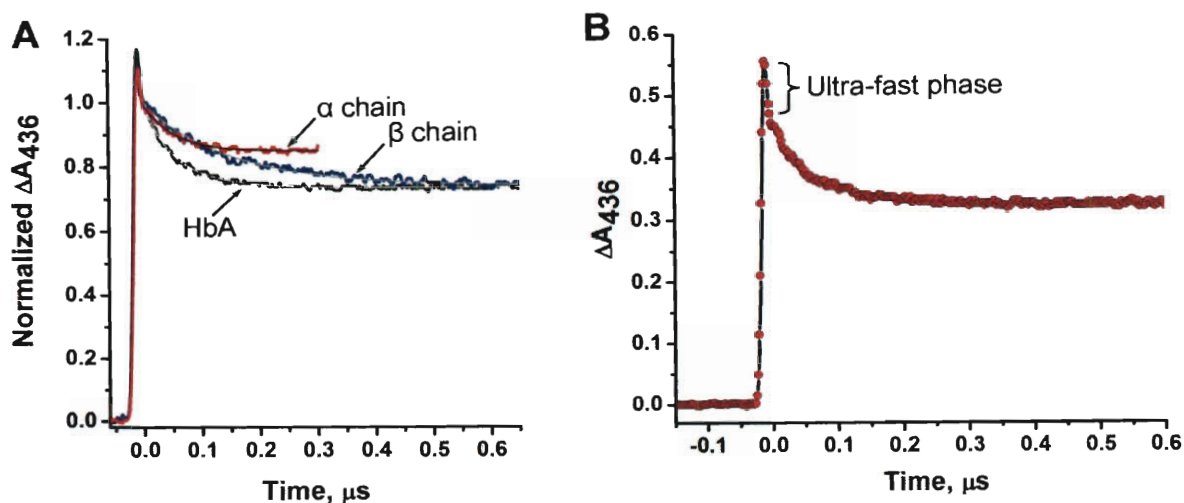


Figure 5.1. CO geminate rebinding to HbA and isolated chains. (A) Geminate CO recombination to HbA tetramers and isolated native α and β subunits. Smooth lines represent best fits to single or double exponential equations. The signal was normalized (excluding the ultra-fast phase). (B) Geminate CO recombination to HbA tetramers emphasizing the ultra-fast phase. Samples, containing $\sim 100 \mu\text{M}$ HbA(CO) in $1000 \mu\text{M}$ CO, were photolyzed with a 7 ns Nd:YAG laser excitation pulse (at time 0.0). Geminate recombination was monitored at 436 nm. The ultra-fast phase is not well-resolved, because it decays simultaneously or even faster than the laser pulse, and varies between experiments. The slow phase represents rebinding from within the distal pocket. Measurements were conducted in 100 mM NaPi, pH 7, 20°C .

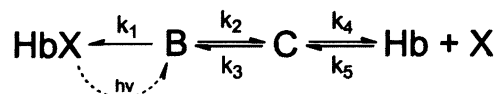
Fig. 5.1A shows typical time courses for CO geminate recombination to tetrameric HbA and isolated α and β subunits. Calculated kinetic parameters are presented in Table 5.1. In both subunits and tetramers, the kinetic traces are markedly biphasic with one small ultra-fast phase in addition to a nanosecond geminate rebinding process (Fig. 5.1). The ultra-fast phase represents ligand rebinding from the initial photodissociated state adjacent to the heme iron atom and can not be measured reliably using our 7 ns YAG laser, because this state decays simultaneously or even faster than

the laser pulse ($\geq 100 \mu\text{s}^{-1}$). In this work the ultra-fast phase was excluded from the analysis.

Table 5.1. Geminate parameters of CO recombination to HbA tetramers and isolated subunits. Geminate parameters were computed using Scheme 5.2 and Equations 5.1-3. To compare F_{gem} of isolated subunits to those of subunits within HbA tetramers, the latter were multiplied by 2 to normalize for heme concentration (*i.e.* in HbA one half of heme groups is α , and the other half is β).

Subunit	Parameter	Monomer	Tetramer
α WT	k_{gem}	19.7	33.7
	F_{gem}	0.157	0.284
	k_{bond}	3.09	9.51
	k_{escape}	16.61	24.13
β WT	k_{gem}	7.1	10.4
	F_{gem}	0.262	0.33
	k_{bond}	1.86	3.43
	k_{escape}	5.24	6.97

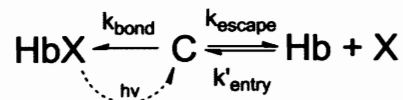
One possible schematic representation of the multiple events occurring after laser flash is provided in Scheme 5.1. In this mechanism, the ultra-fast phase corresponds to



Scheme 5.1

ligand recombination from the initial B state (the first geminate state), presumably the area in the distal pocket just above the iron atom. The existence of this state was previously identified in Mb [17] and suggested for hemoglobin subunits [16]. State C represents ligands in rapid equilibrium between the B state and locations more distant from the iron. The slower phase corresponds to ligand recombination from this C state. When the rebinding and escape from the B state (k_1 and k_2) are significantly faster than

geminate rebinding from the C state, the mechanism can be simplified (Scheme 5.2), and the rate of ligand-iron bond formation can be expressed as $k_{\text{bond}} = k_3k_1/(k_1 + k_2)$.



Scheme 5.2

Scheme 5.2 allows the rates of ligand entry and escape and ligand-iron bond formation to be calculated using the following relationships, where k'_{CO} represents the overall bimolecular rate constants for ligand binding from the solvent phase.

$$k_{\text{bond}} = k_{\text{gem}} F_{\text{gem}}$$

Equation 5.1

$$k_{\text{escape}} = k_{\text{gem}} (1 - F_{\text{gem}})$$

Equation 5.2

$$k'_{\text{entry}} = \frac{k'_{\text{CO}}}{F_{\text{gem}}}$$

Equation 5.3

Similar biphasic geminate CO recombination to gel-immobilized HbA in 80% glycerol was reported by Sottini *et al.* in 2005 [35]. They reported the characteristic half-times for the fast and slow phases to be on the order of 10^{-8} and 10^{-6} s, respectively, and

suggested that slow phase reflects rebinding from distant cavities within protein matrix, equivalent to the Xe sites in Mb.

The measured parameters for the major slow phases for the α and β subunits agree well with previous estimates. Geminate rebinding is faster in α than in β subunits ($20 \mu\text{s}^{-1}$ vs. $7 \mu\text{s}^{-1}$, respectively), whereas the fraction of recombination is larger in β than in α (26% vs. 16%, respectively) (see Table 5.1). When the subunits are in tetramers, the parameters change slightly. The fractions become $\sim 30\%$ for both subunits, mostly due to an ~ 2 -fold increase of F_{gem} for the α subunits. k_{gem} increases in both subunits $\sim 50\%$, due to an increase in the rate of bond formation between ligand and Fe (Table 5.1). The escape rates did not alter significantly (≤ 30 -40% increases). These increases in the rate and extent of geminate rebinding are most likely associated with increasing compactness and decreased flexibility of the distal pocket upon formation of subunit interfaces in the HbA tetramer. α subunits demonstrated larger changes, in part, because at high concentrations (50-100 μM), isolated β subunits exist in the tetrameric β_4 form, and thus, conformational mobility of the β distal pocket does not change significantly after the formation of $\alpha_2\beta_2$ tetramers. α subunits, on the other hand, are mostly monomers at the protein concentrations used, and aggregation into HbA appears to dampen the fluctuations of its tertiary structure.

5.3. The effects of Phe and Trp substitutions at the B10 position on ligand binding to α and β subunits of HbA.

Representative time courses for geminate CO recombination to α and β Phe(B10) and β Trp(B10) isolated subunits are shown in Fig. 5.2. The ultra-fast phase, reflecting

ligand rebinding from the initial photodissociated B state, was observed in the time courses for each mutant subunit. The corresponding fitted parameters for the slow phases are provided in Table 5.2. I used hybrid tetramers rHb $\alpha(\text{Trp}(\text{B10}))\beta(\text{WT})$ to measure ligand binding to $\alpha\text{Trp}(\text{B10})$ subunits, which are not stable enough to be prepared as isolated chains.

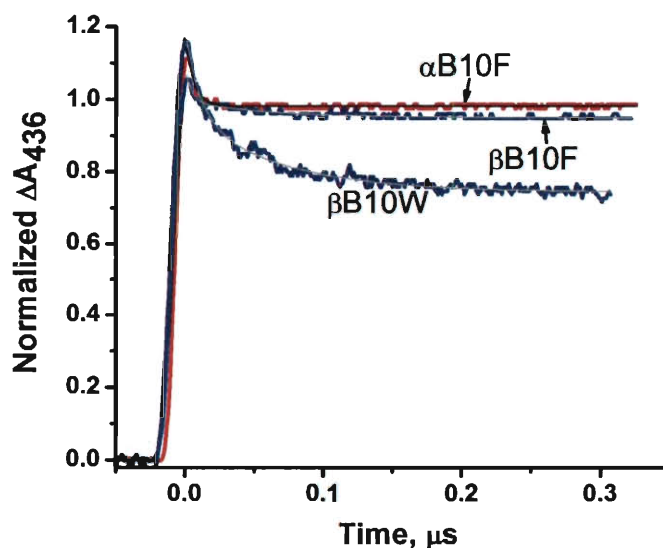


Figure 5.2. CO geminate rebinding to isolated Phe and Trp B10 chains. Smooth lines represent best fits to single or double exponential equations. In $\alpha\text{Phe}(\text{B10})$, only the ultra-fast phase was observed. Geminate rebinding to $\alpha\text{Trp}(\text{B10})$ was not analyzed, because isolated chains were not possible to prepare, probably, due to instability of the protein in monomeric state. Geminate parameters for $\alpha\text{Trp}(\text{B10})$ were obtained using hybrid tetramers Hb $\alpha\text{Trp}(\text{B10})\beta\text{WT}$ (data not shown). The signal was normalized (excluding the ultra-fast phase). Conditions were the same as in Fig. 5.1. B10 corresponds to position 29 in α subunits, and 28 – in β .

In α subunits, both Phe(B10) and Trp(B10) mutations cause complete inhibition of slow geminate rebinding. In $\beta\text{Phe}(\text{B10})$ subunits, the fraction of slow geminate recombination is reduced to 4%. These results are consistent with the effects of similar replacements in sperm whale Mb on geminate O_2 rebinding, where the extent of total recombination was reduced from 0.5 for wild-type Mb to 0.3 and 0.05 for Phe and

Trp(B10) mutants, respectively [22]. Dramatic reductions of slow geminate CO rebinding were also reported for Hb mutants containing Tyr(B10) and Gln(E7) in both subunits [168], and hybrid Hb tetramers containing α Phe(B10) or α Trp(B10) in addition to inter-subunit interfacial mutations [109]. These results demonstrate that bulky aromatic side chains at the B10 position severely hinder the access to the iron for photodissociated ligands that have moved to the back of the distal pocket and markedly decrease k_{bond} . These mutations also dramatically reduce the size of the distal pocket, which entropically reduces the barrier to ligand escape. This conclusion is supported by the calculated geminate parameters for the β Phe(B10) subunits (Table 5.2), in which k_{bond} decreased 2-3-fold and k_{escape} increased almost 4-fold. Similar conclusions explain the behavior of Phe(B10) Mb mutants [80].

Surprisingly, in β Trp(B10), the fraction of rebinding is only slightly lower than that for β WT, and moderate increase in both ligand escape and bond formation are observed (see Table 5.2). In this case, the more flexible β distal pocket can, probably, accommodate both the large Trp(B10) side chain and the bound ligand, and because the indole side chain is pushed away from the iron, it does not severely interfere with the rebinding from the C geminate state. However, the volume of the distal pocket is reduced and, hence, the values of k_{bond} and k_{escape} increase.

Space-filling mutations at the B10 position markedly affected bimolecular ligand binding as well. The CO association rate constant, k'_{CO} , decreases 160 and 1600-fold for the Phe and Trp α B10 mutants, respectively, compared to the wild-type subunit. Similar trends are observed for O₂ and NO binding. The large differences between the rate constants for the three ligands are due to intrinsic differences in their reactivities with

iron. For CO, the formation of the bond between ligand and heme iron represents the rate limiting step of reaction. NO binding is governed solely by the rate of ligand entry into the distal pocket, because nitric oxide is highly reactive toward iron due to its radical nature [73, 143]. O₂ association is regulated by a combination of these processes. The most dramatic inhibition of the rate of ligand binding to Phe and Trp α B10 mutants is observed for CO (Table 5.2). This effect is caused by severe hindrance of the access to the iron atom by the large aromatic rings at the B10 position. NO association rate constants for α Phe(B10) and α Trp(B10) are only 6- and 30-fold smaller than the wild-type parameters, respectively, and reflect the effects of these mutations on ligand entry into the distal pocket. In case of O₂ binding, the decreases in k'_{O_2} are intermediate between those for CO and NO, supporting the idea that both ligand entry and ligand-iron bond formation limit O₂ association.

The presence of the ordered water molecule in the distal pocket of the α WT deoxy-subunit confers resistance to bimolecular ligand binding (Chapter 3). The distal pockets of the B10 mutants are, most likely, anhydrous, because the bulky B10 side chains should displace water from the vicinity of the distal histidine. Displacing water from the distal pocket partially compensates for the loss of volume in the active site and the decrease of the access to the iron atom by the phenyl ring. Bimolecular binding to β B10 mutants is more complex due to the appearance of the second, faster phase for all three ligands. It is likely, that faster phase reflects an alternative, less hindered conformation of the B10 side chains. The presence of distal pocket heterogeneity in Phe and Trp B10 mutants of Hb was previously noticed by Wiltrout *et al.* [169] based on

Table 5.2. Rate constants for bimolecular CO, NO binding, NO dioxygenation and parameters for the slow CO geminate recombination to isolated α and β B10 mutant subunits. Wild-type α and β subunits have Leu(B10). In cases, where numerous rebinding phases were observed, numbers in parentheses provide relative contributions of each phase. Parameter values after calculations were rounded to two significant digits. K_{entry} was calculated using formula $K_{\text{entry}}=k'_{\text{entry}}/k_{\text{escape}}$. Conditions were the same as in Fig. 5.1.

Subunit	F_{gem}	$k_{\text{gem}}^{\text{gem}}$ μs^{-1}	$k_{\text{bond}}^{\text{bond}}$ μs^{-1}	$k_{\text{escape}}^{\text{escape}}$ μs^{-1}	k'_{CO} $\mu\text{M}^{-1}\text{s}^{-1}$	k'_{entry} $\mu\text{M}^{-1}\text{s}^{-1}$	K_{entry} M^{-1}	k'_{NO} $\mu\text{M}^{-1}\text{s}^{-1}$	k'_{NOD} $\mu\text{M}^{-1}\text{s}^{-1}$	k'_{O_2} $\mu\text{M}^{-1}\text{s}^{-1}$
α WT	0.16	20	3.1	17	5.2	33	2.0	31	50 ³	40
α Phe(B10)	~0	n.d.	n.d.	n.d.	0.032	n.d.	0.27 ⁵	4.5	8.0	0.87
α Trp(B10) ¹	~0	n.d.	n.d.	n.d.	0.0033	n.d.	0.048 ⁵	0.81 ²	1.6 ²	0.033
β WT	0.26	7.1	1.9	5.2	9.2	35	6.7	68	50 ³	60
β Phe(B10)	0.04	19	0.81	18	1.6(48%) 0.27(52%)	37 6.3	2.1 0.35	57	$\geq 100^4$	26(56%) 5.8(44%)
β Trp(B10)	0.22	15	3.4	12	5.1(62%) 0.0029(38%)	23 0.013	2.0 0.0011	22(56%) 0.34(44%)	50(72%) 3.7(28%)	23(58%) 0.013(42%)

¹ Geminate and bimolecular binding parameters for α Trp(B10) mutant were determined using hybrid mutant tetramer Hb α Trp(B10) β WT. To analyze geminate parameters for mutant subunit within tetramer, the fraction of recombination was calculated from the expression $2F_{\text{gem}}=F_{\alpha}+F_{\beta}$, where F_{gem} is the fraction of recombination for a tetramer, and F_{α} and F_{β} - fractions of recombination for isolated subunits; the wild-type value for β subunit was taken from Table 5.1. The calculated fraction for α Trp(B10) subunit appeared as small negative number, therefore, I assigned it the value of 0. ² The amplitude of the slow phase in both NO dioxygenation and bimolecular NO binding was less than 0.5 of the total absorbance change. The fast phase parameters agreed well and were assigned to the wild-type β subunits. ³ k'_{NOD} for α and β WT subunits within HbA tetramer. ⁴ The rate of reaction was too fast to be reliably measured. ⁵ k'_{NO} was used as the rate of ligand entry, and wild-type parameters of the rates of ligand escape.

NMR studies. The slow phases for β Trp(B10) subunits are identical to those for α Trp(B10), suggesting that the conformation of the Trp side chain in the slow form of β Trp(B10) is similar to that in α Trp(B10). The observed “wild-type-like” geminate rebinding of β Trp(B10) most likely corresponds to the species reacting faster in bimolecular experiments, in which the indole ring is originally located further away from the bound ligand in the ground state and stays there immediately after photolysis. For β Phe(B10), the rate constants also monotonically decrease for the series NO, O₂, CO; however, k'_{NO} is little affected by the mutation, suggesting the absence of any influence on the ligand entry.

Ligand migration into distal pocket is also a rate limiting step in case of NO dioxygenation by oxyHb. Thus, k'_{NOD} can be used to assess k'_{entry} for liganded distal pocket. NO scavenging is significantly inhibited in α Phe(B10), α Trp(B10), and β Trp(B10) (Table 5.2). Surprisingly, in β Phe(B10) k'_{NOD} increased 2-fold in comparison to β WT, suggesting, surprisingly, that in the O₂-bound form the mutated distal pocket is even more accessible to NO than in the wild-type subunit.

5.4. The effects of Phe and Trp substitutions at the E11 position on ligand binding to α and β subunits of HbA.

Time courses for geminate CO recombination to Phe and Trp(E11) mutants of the α and β subunits are shown in Fig. 5.3. Fitted geminate parameters as well as calculated rates of bond formation and escape are provided in Table 5.3. Like position B10, space-filling substitutions at E11 demonstrate markedly different geminate CO recombination from those of wild-type subunits. However, in contrast to B10 mutants, dramatic

increases in the extent of internal rebinding are observed for these mutations at the E11 position. On average, 70% of ligands recombine in α mutants, and 90% in β mutants containing Phe or Trp(E11). Analogous effects were reported for Phe and Trp(E11) mutants of sperm whale Mb, where geminate O_2 recombination increased from 50% in wild-type protein to 90-100% in aromatic E11 variants.

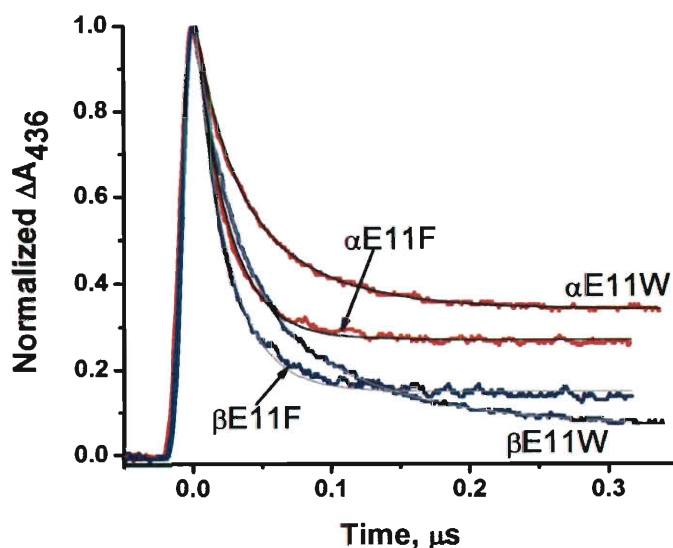


Figure 5.3. CO geminate rebinding to isolated Phe and Trp E11 chains. Smooth lines represent best fits to single or double exponential equations. No ultra-fast phase was detected. The signal was normalized. Conditions were the same as in Fig. 5.1. E11 corresponds to position 62 in α subunits, and 67 in β .

The increases in F_{gem} for the Phe(E11) mutants are primarily due to 10- and 20-fold increases in k_{bond} for the α and β subunits, respectively. The analysis of the Trp mutants is complicated by the presence of two slow geminate phases; but it is clear that almost complete recombination is achieved by much faster iron-ligand bond formation. To simplify the analysis we assumed that the two phases represented distinct non-interconverting conformations and fitted the time courses to two independent exponential expressions and analyzed each phase in terms of Equations 5.1-3. In α Trp(E11), k_{bond}

increases 2- to 5-fold. In β Trp(E11), 10-fold increases in k_{bond} are observed only for the larger phase, whereas the parameters for smaller phase are identical to those for the wild-type β subunit. Variations in k_{escape} are smaller for the E11 mutants, ranging from \sim 2-fold increases to 50% decreases (Table 5.3).

The effects of the E11 mutations can be readily interpreted in terms of structural alterations of the distal pocket. First, the removal of steric hindrance by C γ of Val(E11) in both the Trp and Phe mutants should facilitate the access to the iron atom and increase the rate of ligand-iron bond formation. Second, reduced distal pocket volume increases both the probability of bond formation and ligand escape into solvent. The crystal structures of Trp [32] and Phe [143] E11 Mb mutants demonstrate less crowding in the immediate vicinity of Fe compared to wild-type Mb with the naturally occurring Val(E11). Steric relief is also observed as an \sim 3-fold increase of k_{bond} in Mb Ala(E11). The \sim 10-fold acceleration of the ligand-iron bond formation in Phe and Trp E11 Mb mutants is achieved due to both the loss of hindrance and sequestering the ligand closer to the iron [22]. These volume considerations are also consistent with the fact that the geminate parameters for α WT are larger than those for β WT subunit, in which the distal pocket is less crowded.

The rate constants for bimolecular ligand binding to the Phe(E11) mutants are not markedly different from the wild-type parameters. CO binding is essentially unchanged, and only 2-4-fold decreases in k'_{NO} and k'_{O_2} are observed. As mentioned above, the release of steric hindrance by Val(E11) \rightarrow Phe substitution increases the reactivity of heme iron. On the other hand, the ability of the distal pocket to capture and retain the

Table 5.3. Rate constants for bimolecular CO, NO binding, NO dioxygenation and parameters for CO geminate recombination to isolated α and β E11 mutant subunits. Wild-type α and β subunits have Val(E11). In cases, where numerous rebinding phases were observed, numbers in parentheses provide relative contributions of each phase. Parameter values after calculations were rounded to two significant digits. K_{entry} was calculated using formula $K_{\text{entry}}=k'_{\text{entry}}/k_{\text{escape}}$. Conditions were the same as in Fig. 5.1.

Subunit	F_{gem}	$k_{\text{gem}}^{\text{gem}}$ μS^{-1}	$k_{\text{bond}}^{\text{bond}}$ μS^{-1}	$k_{\text{escape}}^{\text{escape}}$ μS^{-1}	k'_{CO} $\mu\text{M}^{-1}\text{s}^{-1}$	k'_{entry} $\mu\text{M}^{-1}\text{s}^{-1}$	K_{entry} M^{-1}	k'_{NO} $\mu\text{M}^{-1}\text{s}^{-1}$	k'_{NOD} $\mu\text{M}^{-1}\text{s}^{-1}$	k'_{O_2} $\mu\text{M}^{-1}\text{s}^{-1}$
α WT	0.16	20	3.1	17	5.2	33	2.0	31	50 ¹	40
α Phe(E11)	0.73	43	31	12	4.0	5.5	0.47	18	42	10
α Trp(E11)	0.37	17	6.2	11	4.6(50%)	13	1.2	23(67%)	43	11(61%)
	0.29	48	14	34	0.85(50%)	2.9	0.086	3.1(33%)		
β WT	0.26	7.1	1.9	5.2	9.2	35	6.7	68	50 ¹	60
β Phe(E11)	0.85	43	37	6.5	7.8	9.2	1.4	21	23	19
β Trp(E11)	0.30	8.2	2.4	5.8	4.5(30%)	15	2.6	8.3(46%)	9.4	8.8(38%)
	0.65	36	23	13	1.0(70%)	1.6	0.13	2.3(54%)		

¹ k'_{NOD} for α and β WT subunits within HbA tetramer

ligand efficiently is compromised by reducing the accessible volume of the distal cavity. Roughly equal contributions of these two structural factors determine the absence of dramatic changes in the overall kinetic parameters of bimolecular ligand binding to the Phe(E11) mutants, despite the dramatic increases in geminate recombination.

Both Trp(E11) mutants reveal biphasic bimolecular ligand binding. In α Trp(E11), the fast phase parameters for CO, O₂ and NO recombination are identical to those of α Phe(E11) mutant, suggesting that Trp residue acquired the conformation exhibiting structural effects equivalent to α Phe(E11). The slow phase, most likely, reflects α Trp(E11) conformer in which the inhibition of ligand entry many times exceeds the favorable relief of steric hindrance at the iron atom. Similar conclusions can be drawn for ligand binding to β Trp(E11). Rates of NO dioxygenation for α Phe(E11), α Trp(E11) and β Phe(E11) mutants are not markedly decreased, compared to the wild-type, except in the case of β Trp(E11) subunits, where a large decrease is observed.

5.5. The effects of Phe and Trp substitutions at the G8 position on ligand binding to α and β subunits of HbA.

In contrast to the results for positions B10 and E11, Phe and Trp substitutions at G8 did not produce marked changes in the slow geminate CO recombination phases compared to wild-type Hb subunits (Fig. 5.4, Table 5.4). In α subunits, k_{bond} decreased only marginally for Phe and Trp(G8) mutants, and similar 30% decreases were observed for the escape rates. The largest change in fraction of rebinding was observed for β Phe(G8), where F_{gem} dropped 2-fold mostly due to a decrease in k_{bond} from 1.9 to 0.6 μs^{-1} , for the wild-type and mutant proteins, respectively. In β Trp(G8), both k_{bond} and k_{escape}

decreased ~ 2 -fold, leaving F_{gem} intact. Generally, such changes in geminate parameters would suggest that the distal pockets of α and β subunits are slightly expanded by the Trp and not decreased in volume, a somewhat puzzling result.

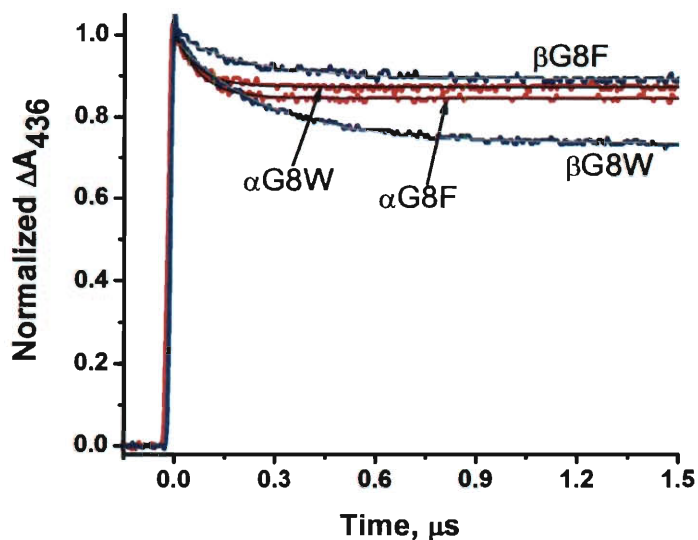


Figure 5.4. CO geminate rebinding to isolated Phe and Trp G8 chains. Smooth lines represent best fits to single exponential equations. The signal was normalized (excluding the ultra-fast phase). Conditions were the same as in Fig. 5.1. G8 corresponds to position 101 in α subunits, and 106 – in β .

In Mb, the Phe or Trp(G8) substitutions speed up both the ligand-iron bond formation and escape processes, which is consistent with a decreased distal pocket volume. Generating additional space in the Mb distal pocket by the Ile(G8) to Ala mutation results in the opposite changes, decreases in k_{gem} and F_{gem} [22].

The G8 mutants cause more pronounced alterations of the overall bimolecular kinetic parameters (Table 5.4). Gradual decrease of association rates with increasing the size of G8 residue from Leu to Phe and Trp are observed for CO and O₂ binding to α mutants. However, NO binding remains unaffected, implying that the mutations decrease

Table 5.4. Rate constants for bimolecular CO, NO binding, NO dioxygenation and parameters for CO geminate recombination to isolated α and β G8 mutant subunits. Wild-type α and β subunits have Leu(G8). Parameter values after calculations were rounded to two significant digits. K_{entry} was calculated using formula $K_{\text{entry}}=k'_{\text{entry}}/k_{\text{escape}}$. Conditions were the same as in Fig. 5.1.

Subunit	F_{gem}	$k_{\text{gem}}^{\text{gem}}$ μS^{-1}	$k_{\text{bond}}^{\text{bond}}$ μS^{-1}	$k_{\text{escape}}^{\text{escape}}$ μS^{-1}	k'_{CO} $\mu\text{M}^{-1}\text{s}^{-1}$	k'_{entry} $\mu\text{M}^{-1}\text{s}^{-1}$	K'_{entry} M^{-1}	k'_{NO} $\mu\text{M}^{-1}\text{s}^{-1}$	k'_{NOD} $\mu\text{M}^{-1}\text{s}^{-1}$	k'_{O_2} $\mu\text{M}^{-1}\text{s}^{-1}$
α WT	0.16	20	3.1	17	5.2	33	2.0	31	50 ¹	40
α Phe(G8)	0.15	13	2.0	11	3.6	24	2.1	40	55	30
α Trp(G8)	0.12	14	1.7	12	2.0	16	1.3	30	74	19
β WT	0.26	7.1	1.9	5.2	9.2	35	6.7	68	50 ¹	60
β Phe(G8)	0.12	5.2	0.6	4.6	2.2	19	4.2	41	75	31
β Trp(G8)	0.26	3.8	0.97	2.8	1.1	4.3	1.5	10	15	9.6

¹ k'_{NOD} for α and β WT subunits within HbA tetramer

the rate of ligand-iron bond formation, but not the rate of entry, which agrees well with the geminate data. All three gaseous ligands bind slower to the aromatic β G8 mutants. It is particularly noticeable in β Trp(G8), where the rates of bimolecular ligand binding are reduced ~10-, 6- and 7-fold for CO, O₂ and NO, respectively. Similar trends are observed for NO dioxygenation. Again, only β Trp(G8) shows a marked decrease in k'_{NOD} compared to wild-type β subunits.

The small effects of G8 substitutions on the geminate CO parameters suggest that the immediate vicinity of the G8 position is not extensively involved in the stabilization of the geminate state C (see Scheme 5.2). However, the strong effect of the β Trp(G8) on bimolecular ligand binding does indicate a role of this position for ligand capture in β subunits.

5.6. Ligand binding to isolated α and β subunits and HbA tetramers at various Xe pressures.

Representative time courses for CO geminate recombination to isolated α WT chains at 0, 4 and 9 atm of Xe are shown in Fig. 5.5 A. Calculated kinetic parameters are listed in Table 5.5. Only slight increases in F_{gem} and no changes in k_{gem} were detected with increases in Xe partial pressure from 0 to 9 atm. The very small observed effects are due primarily to a ~50% increase of k_{bond} from 3.1 to 4.8 μs^{-1} . The average escape rate showed only very small, statistically insignificant decreases. No effect of Xe pressure was observed for bimolecular CO and O₂ binding. Kinetic traces for geminate CO rebinding to β subunits at 0, 4 and 9 atm of Xe are shown in Fig. 5.5 B, fractions and

Table 5.5. The effect of Xe on kinetic parameters for bimolecular CO, O₂ binding and CO geminate recombination to isolated α and β subunits. Data, when possible, were presented as mean value \pm standard deviation. Parameter values after calculations were rounded to two significant digits. K_{entry} was calculated using formula $K_{\text{entry}}=k'_{\text{entry}}/k_{\text{escape}}$. Conditions were the same as in Fig. 5.1.

Subunit	F_{gem}	$k_{\text{gem}}^{\text{gem}}$ μS^{-1}	$k_{\text{bond}}^{\text{bond}}$ μS^{-1}	$k_{\text{escape}}^{\text{escape}}$ μS^{-1}	k'_{CO} $\mu\text{M}^{-1}\text{s}^{-1}$	k'_{entry} $\mu\text{M}^{-1}\text{s}^{-1}$	K_{entry} M^{-1}	k'_{O_2} $\mu\text{M}^{-1}\text{s}^{-1}$
$\alpha^{\text{M}} + 0 \text{ atm Xe}$	0.16 ± 0.01	20 ± 1	3.1 ± 0.4	17 ± 2	5.8 ± 0.2	37 ± 3	2.2 ± 0.3	45 ± 3
$\alpha^{\text{M}} + 4 \text{ atm Xe}$	0.19 ± 0.01	19 ± 1	3.7 ± 0.5	16 ± 2	6.1 ± 0.2	31 ± 2	2.0 ± 0.3	42 ± 3
$\alpha^{\text{M}} + 9 \text{ atm Xe}$	0.24 ± 0.01	20 ± 1	4.8 ± 0.5	15 ± 1	6.0 ± 0.1	25 ± 2	1.7 ± 0.1	41
$\beta^{\text{M}} + 0 \text{ atm Xe}$	0.26 ± 0.02	7.1 ± 0.6	1.9 ± 0.3	5.3 ± 0.4	14.7 ± 0.2	56 ± 5	11 ± 1	74 ± 2
$\beta^{\text{M}} + 4 \text{ atm Xe}$	0.29 ± 0.02	8.8 ± 1.2	2.5 ± 0.6	6.3 ± 1.8	12.8 ± 0.2	45 ± 4	7.1 ± 2.1	65 ± 1
$\beta^{\text{M}} + 9 \text{ atm Xe}$	0.30 ± 0.02	11 ± 1	3.2 ± 0.6	7.4 ± 2.1	11.0 ± 0.3	36 ± 3	4.9 ± 1.4	59

rates are provided in Table 5.5. Again, F_{gem} increases only marginally upon addition of Xe, from 0.26 to 0.30, whereas, there is an increase in k_{gem} , from $7.1 \mu\text{s}^{-1}$ to $11 \mu\text{s}^{-1}$.

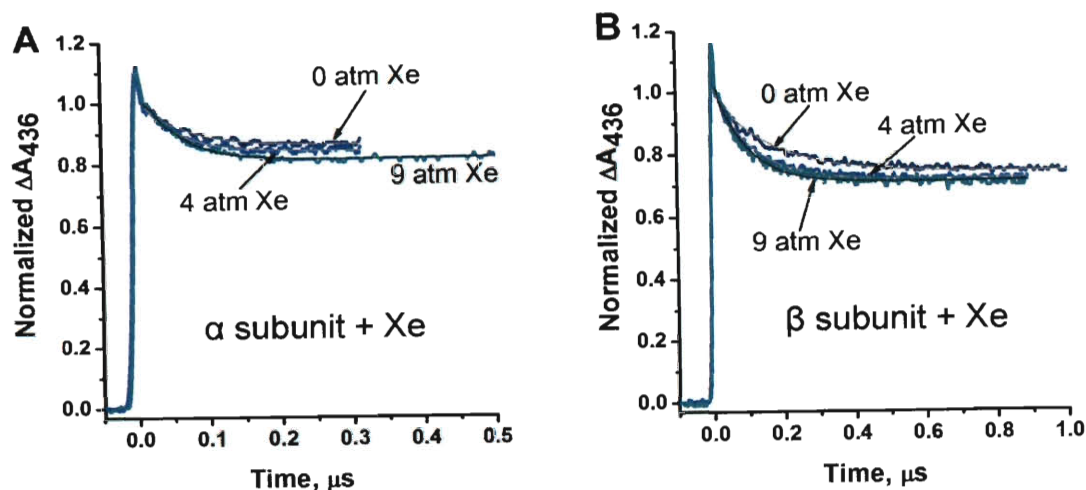


Figure 5.5. CO geminate rebinding to isolated α (A) and β (B) WT subunits in the presence/absence of Xe. Kinetic measurements were conducted in specially constructed high-pressure cuvette (see Chapter 2 and [81]) in 1 atm CO plus 0, 4 and 9 atm of Xe. The signal was normalized for comparison. Smooth lines represent best fits to single-exponential equation. Experimental conditions were the same as in Fig. 5.1.

Both ligand-iron bond formation and ligand escape processes speed up upon addition of the Xe, suggesting that Xe atoms may occupy space inside the distal pocket reducing its accessible volume, and thus, increasing the probabilities of either collision of the ligand with Fe or encounter with the exit route. Non-specific pressure effect for Hb and other globins have been ruled out previously by others [33, 80, 81]. The distal pocket Xe binding hypothesis is also supported by the small decreases in the rates of bimolecular CO and O₂ binding to β subunits at increasing Xe pressures (Table 5.5). A more crowded distal pocket reduces the probability of the ligand being captured in the active site. In general, this effect is analogous to E11 space-filling mutations discussed in the previous sections. However, the changes due to Xe addition are much smaller, presumably, because the extent of Xe binding in the distal pocket is small.

The parameters for geminate CO recombination to HbA tetramers shown in Table 5.6 are also little affected by Xe pressure, as expected from the results for isolated subunits. To assess the influence of Xe atoms on ligand binding to T-state HbA, I measured CO rebinding to Hb tetramers after full photolysis. Time courses at varying Xe pressures are virtually indistinguishable from those in the absence of the noble gas (not shown). To estimate the rate constants (k'_{TCO}) of CO binding to T-state HbA, I fitted the slow phase of each trace. Again, no changes were detected upon addition of Xe (Table 5.6).

Table 5.6. The effect of Xe on kinetic parameters for geminate CO recombination to HbA tetramers and T state parameters for bimolecular CO binding. Data, when possible, were presented as mean value \pm standard deviation. Parameter values after calculations were rounded to two significant digits. $F(\alpha + \beta)$ represents the sum of F_{gem} for α and β subunits. Conditions were the same as in Fig. 5.1.

Subunit	F_{gem}	$F(\alpha + \beta)$	k_{gem}^{-1} μs^{-1}	k_{bond}^{-1} μs^{-1}	k_{escape}^{-1} μs^{-1}	k'_{TCO} $\mu\text{M}^{-1}\text{s}^{-1}$
Hb α + 0 atm Xe	0.14 ± 0.03	0.31 ± 0.03	34 ± 3	4.7 ± 0.6	29 ± 4	0.24 ± 0.01
Hb β + 0 atm Xe	0.17 ± 0.02		10 ± 2	1.7 ± 0.4	8.7 ± 1.5	
Hb α + 4 atm Xe	0.22 ± 0.03	0.37 ± 0.04	30 ± 3	6.4 ± 1.1	23 ± 2	0.22 ± 0.01
Hb β + 4 atm Xe	0.16 ± 0.03		9.9 ± 2.6	1.6 ± 0.5	8.3 ± 2.1	
Hb α + 9 atm Xe	0.23 ± 0.03	0.42 ± 0.02	33 ± 3	7.4 ± 0.7	26 ± 3	0.24
Hb β + 9 atm Xe	0.19 ± 0.02		11 ± 1	2.0 ± 0.4	8.5 ± 1.1	

The absence of effects of Xe on ligand recombination in HbA was not a surprise. In Mb, increasing Xe partial pressure did not change the fraction of CO recombination, which is inherently very small (~ 0.05) [81]. In the case of geminate O_2 rebinding to Mb, the total amount of recombination also stayed unchanged upon addition of 15 atm of Xe; however, the slow phase of the reaction disappeared [22, 80], suggesting that even though ligands do visit the Xe binding sites in protein matrix, these cavities do not serve as ports

of entry or escape. In *Scapharca* dimeric HbI, Xe binding did not affect ligand escape either; even though, MD simulations suggested that the route of escape should continue through Xe binding cavities [150]. Only in CerHb did addition of Xe significantly increase the fraction of geminate recombination (from 0.05 to ~0.30), confirming the role of the apolar tunnel as part of the major route for ligand entry and escape [81].

5.7. Structural interpretations of kinetic effects.

The structures of the distal pockets of deoxy- α Trp(B10) (pdb code: 1O1N), deoxy- α Phe(B10)/Gln(E7) (pdb code: 1O1J), deoxy- β Trp(E11) (pdb code: 1O1M) and cyanomet- β Trp(G8) (pdb code: 1O1I) are presented in Fig. 5.6. These structures were solved by Dr. E. Brucker, who was part of the Phillips/Olson group at Rice University in the middle 1990s and a senior scientist at Somatogen, Inc. I was unable to obtain crystals of the rest of space-filling mutants, used in these experiments.

From Figs. 5.6A and 5.6B, it is clear that the immediate vicinity of the iron atom is restricted by B10, E11 and E7 side chains. The distances from iron to α Phe(B10) and α Trp(B10) are 5.5 Å and 4.8 Å, respectively. In native α subunits, the distance from iron to C δ 2 methyl of Leu(B10) is 7.4 Å. In wild-type subunits, the Leu(B10) and His(E7) side chains are flexible allowing up to 30% geminate CO recombination. Phe or Trp at the B10 site are less prone to large fluctuation due to their bulky side chains, and sterically hinder the formation of the first geminate state (state B in Scheme 5.1), which almost completely abolishes geminate rebinding. In addition, the negative center of the B10 benzyl ring multipole may interact with the partially positive N ϵ -H of His(E7) imidazole (Fig. 5.6 A), reducing its flexibility and pulling it over the iron atom. Two

significant structural alterations occur in β Trp(E11) (Fig. 5.6 C). First, the indole side chain fills the accessible space in the back of the distal pocket markedly reducing its volume; and second, replacing Val with Trp removes the unfavorable steric hindrance imposed by the second valine γ methyl group.

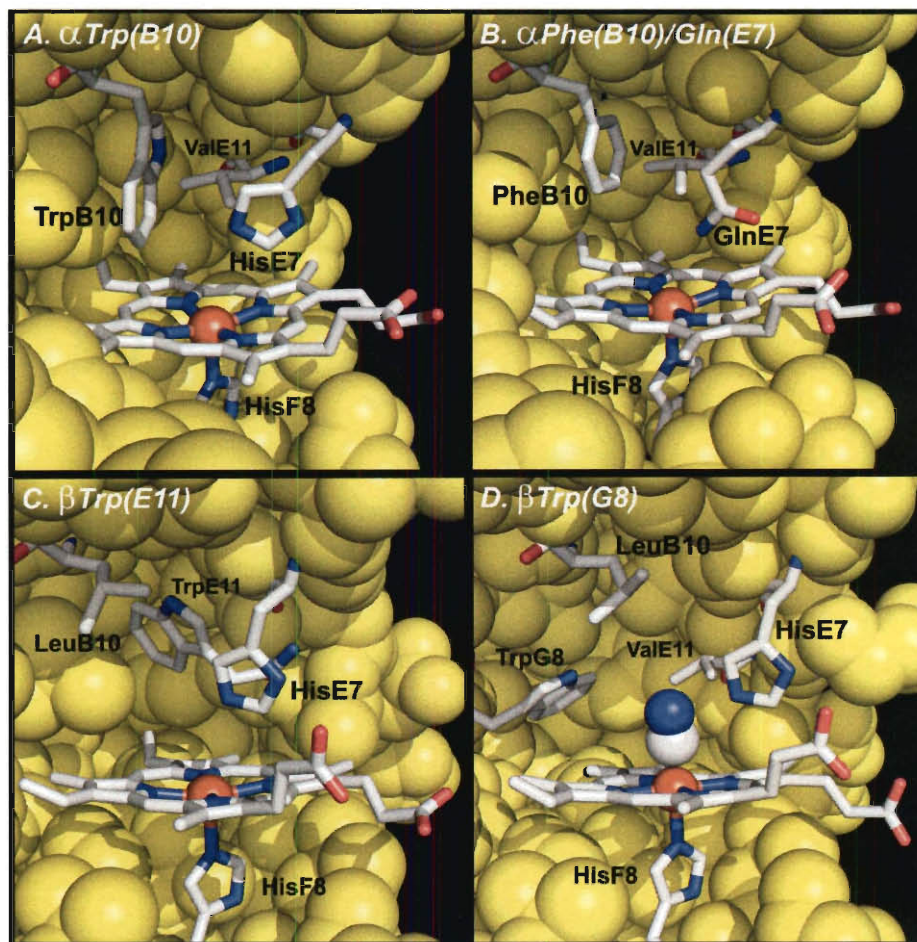


Figure 5.6. Structures of the key B10, E11 and G8 mutants of HbA. The models of the mutant distal pockets were constructed from the following structures: (A) deoxyHb α Trp(B10) β (WT) (pdb code: **1O1N**); (B) deoxyHb α Phe(B10)/Gln(E7) β Trp(G8) (pdb code: **1O1J**); (C) deoxyHb α Phe(B10)/Gln(E7) β Trp(E11) (pdb code: **1O1M**); and (D) cyanometHb α Phe(B10)/Gln(E7) β Trp(G8) (pdb code: **1O1I**) determined by Dr. Eric A. Brucker (in addition to listed mutations each structure contains Gly links between α subunits and VIM replacements in both α and β subunits). The key residues of the heme pocket are labeled and shown in sticks. The atoms are colored as following: white, carbon; blue, nitrogen; red, oxygen; yellow, the atoms of other amino acids lining the binding site; and orange, heme Fe. In (D), white and blue spheres represent CN group bound to Fe^{3+} . In each panel, the part of the distal pocket was removed to show the internal structure.

These structural features explain the dramatic increases in the fractions and rates of CO geminate recombination in the Phe and Trp(E11) mutants. The conformations of the Phe(B10), Trp(B10), and Trp(E11) residues in the mutant Hb crystal structures are almost identical to those of Phe(B10), Trp(B10), and Trp(E11) side chains in the corresponding Mb mutants [32, 143], and, in general, the effects of these substitutions on ligand recombination kinetics are also similar. β Trp(G8) does not demonstrate any dramatic effects on CO geminate recombination, suggesting that the changes associated with this mutation do not significantly influence ligand migration pathways.

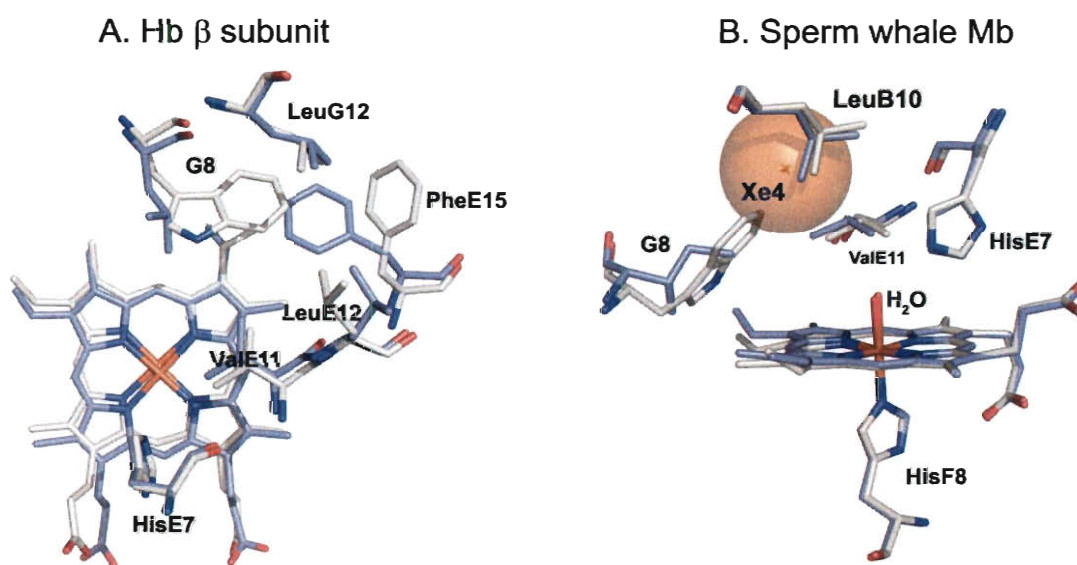


Figure 5.7. Structures of the distal pockets of β subunits of oxyHbA and cyanometHb β Trp(G8), top view (A), and wild-type and Trp(G8) sperm whale Mb, side view (B). The structures were constructed from the PDB files: 2DN1 (oxyHbA); 1O1I (cyanometHb α Phe(B10)/Gln(E7) β Trp(G8)); 2MBW (aquometMb); 2OHB (aquometMb Trp(G8)). The atoms are colored as in Fig. 5.6, except, carbons are white in mutant structures, and purple in wild-type structures. Large brown sphere represents Xe4 cavity in Mb. Coordinated water molecules in aquometMb structures are shown as sticks.

In Fig. 5.7A, the model of the wild-type β O₂ distal pocket is superimposed on the model of cyanomet- β Trp(G8) distal pocket. In addition to the change in the size of the

G8 side chain there are other structural alterations in the heme pocket. In wild-type β subunits, the side chain of Phe(E15) points toward the B pyrrole ring and is parallel to the heme plane. In the Trp(G8) mutant, the phenyl ring of Phe(E15) has rotated $\sim 90^\circ$ away from the heme to accommodate the bulky G8 indole group. The additional empty space in the distal pocket created by rotation of Phe(E15) appears to compensate for the loss of volume occupied by the indole ring of Trp(G8). In Mb, the Trp(G8) side chain assumes a different conformation (Fig. 5.7 B) and does not displace any amino acid side chains.

Thus, in Mb, Trp(G8) does accelerate the bond formation and escape and inhibits ligand diffusion into the remote docking Xe1 and Xe4 binding sites, which markedly diminishes the secondary, slow O₂ geminate recombination phase [22, 32]. In the deoxy- β Trp(G8) distal pocket (pdb code 1O1J, E. Brucker, not shown), the conformation of the G8 indole is similar to that in cyanomet form, however, a water molecule is coordinated to the pyrrole nitrogen of the Trp(G8), and the carbonyl O atoms of Gly(B6) and Gly(E8). The distances between the water and Trp(G8), Gly(B6) and Gly(E8) residues (3.2 Å, 2.8 Å and 3.1 Å, correspondingly) allow the formation of strong hydrogen bonds. This additional filling of space in the distal cavity significantly reduces the bimolecular rates for ligand binding to β Trp(G8) in comparison to wild-type β subunits (Table 5.4).

5.8. Ligand trapping by noncovalent binding site.

The equilibrium constant for non-covalent ligand entry can be computed as $K_{\text{entry}} = k'_{\text{entry}}/k_{\text{escape}}$ to quantify the ligand capture efficiency of the distal pocket. This constant depends on the volume and steric hindrance in the non-covalent binding site, which is in or near the active site and serves to retain the captured ligand until it binds to

the heme iron. For α and β native subunits these values are 2 and 6.7 M^{-1} , respectively (Table 5.2-4), which is consistent with previous data suggesting a more spacious distal pocket in β chains (Chapter 3, [103]). The presence of distal pocket water molecule in wild-type α subunits is part of the cause of its smaller K_{entry} value. Significant decreases in K_{entry} were found for aromatic B10 and E11 mutants, with the Trp replacements showing the most dramatic effects (Table 5.2-3). As expected, the G8 replacements in HbA subunits did not appreciably affect K_{entry} (Table 5.4). The largest effect was ~4-fold decrease of equilibrium constant for ligand entry in $\beta\text{Trp(G8)}$ due to both the bulky indole ring of Trp and a water molecule connected to it. Together, these results support “baseball glove” mechanism for ligand binding to Hb subunits, previously developed for sperm whale Mb, which predicts a decrease in the rate and extent of entry when the back of the distal pocket is filled with aromatic side chains [22]. The addition of Xe to the HbCO solution has little effect on the accessibility of the non-covalent binding sites in the α and β subunits of HbA. The only significant effect is found in β subunits, where K_{entry} decreased ~2-fold (Table 5.5). In α subunits, this parameter is diminished ~20% in the presence of Xe. These results support the idea that Xe atoms may penetrate into the β distal pocket and reduce the volume of the non-covalent binding site, which diminishes K_{entry} . The α distal pocket appears inaccessible to xenon. However, the effects are small in either case due, probably, to very weak binding of the noble gas.

5.9. Ultra-fast phase of geminate recombination and secondary sites in HbA.

The mechanism of geminate ligand recombination in myoglobin assumes that the geminate O_2 rebinding is biexponential, with a fast phase reflecting ligand association

from the distal pocket and adjacent Xe4 cavity and a slower phase, comprising ~25% of the total geminate recombination, representing ligand rebinding from the more distant Xe1 site [22, 32, 53, 80]. Recently, Sottini and coworkers reported the first evidence of multiple geminate phases in human HbA [35, 166]. Based on the mechanism for O₂ internal recombination to Mb, these authors linked the slower phase to ligand rebinding from remote sites, distinct from the distal pocket, and identified the potential locations of those cavities as Xe binding sites using molecular modeling. Later, these Xe cavities were visualized in crystals of deoxyHbA [36].

In contrast, my results suggest that there are no remote secondary sites in HbA, which are analogous to those in Mb. The slower phase for CO geminate recombination in HbA was assigned to ligand rebinding from within the distal pocket or sites closely adjacent to it. The ultra-fast phase was assigned to the rapid rebinding from the first geminate state, where the ligand is still at or very near the iron atom (Scheme 5.1, state B). My arguments are as follows. First, the slow phase for CO geminate recombination does not disappear in the presence of Xe for either isolated HbA subunit (Fig. 5.5) as was observed for Mb. In the latter protein, the geminate O₂ rebinding process becomes fast and a single-phase in the presence of 2-5 atm of Xe due to occupation of secondary Xe4 and Xe1 sites. Second, the pathways leading to the proposed distant ligand docking sites [35, 36, 166] would be sterically hindered by the E11 mutations, especially by the Trp replacements, which would inevitably result in a decrease of the fraction of the slow phase of recombination and a corresponding increase of the ultra-fast phase. In my experiments, however, the slow phase does not disappear and the ultra-fast phase is not observed at all in the geminate time courses for α and β E11 mutants (Fig. 5.3).

Additionally, the absence of the ultra-fast phase for the internal CO rebinding in E11 mutants of HbA suggests that the naturally occurring Val(E11) is the structural barrier between the kinetic states B and C (Scheme 5.1) that is responsible for the appearance of the ultra-fast and slow CO recombination phases observed in the wild-type subunits.

5.10. Ligand migration via alternative routes in HbA.

Fig. 5.8 shows the crystal structures of the α and β Hb subunits with bound Xe atoms as determined by Savino *et al.* [36]. These authors proposed that the cavities occupied by Xe atoms comprise transiently open channel within protein matrix that guides the diffusion of ligands between solvent and distal pocket. From Fig. 5.8 it is clear that this tunnel is more pronounced in the β subunit and contains the string of well ordered waters and xenon atoms, which visualize a potential migratory pathway very similar to the apolar tunnel in *Cerebratulus lacteus* miniHb (CerHb) [68, 81]. Interestingly, the proposed tunnel in β subunit can be blocked by mutating Val(E11) to Trp (see Fig. 5.6 C). In β Trp(E11), the indole ring of the Trp is located in the space above the B ring of the porphyrin. The same area is occupied by Xe2 in the structure of xenon-bound β WT subunit. My geminate recombination experiments seem to partially support the role of the Xe cavities in ligand entry and escape mechanism. In α and β Trp(E11) mutants the fraction of recombination increases dramatically (Table 5.3, Fig. 5.3). However, the calculated rates of escape do not decrease in the Trp(E11) mutants, but instead increase 2-fold and the observed increases in the fractions of recombination are due almost exclusively to a markedly larger rate of ligand-iron bond formation. In addition, Xe binding did not show any significant inhibition of ligand entry or escape

(Table 5.5 and 5.6). In contrast, when the E7 gate in β subunits is blocked by replacing His(E7) with Trp, a dramatic 10-fold reduction in the rate of ligand entry was observed (see Chapter 4).

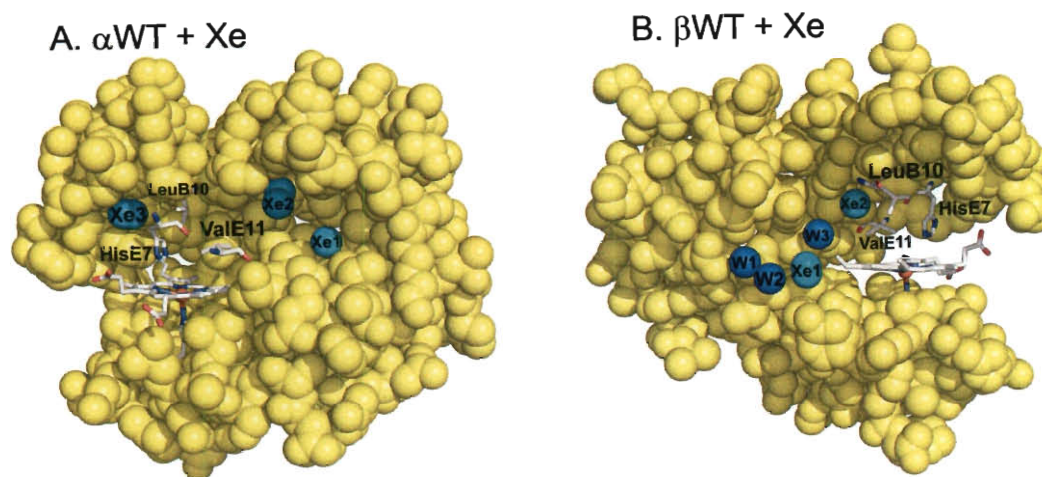


Figure 5.8. Structures of the α (A) and β (B) subunits of deoxyHb with bound Xe atoms. The structures were constructed from the PDB file 2W6V (deoxyHbA with Xe) [36]. The key residues of the heme pocket are labeled and shown in sticks. The atoms of the key amino acids are colored as in Fig. 5.6, except, cyan spheres represent Xe, and blue spheres – water molecules. Xe atoms identified in both α_1 , α_2 and β_1 , β_2 chains are shown. In β subunit, water molecules are shown to emphasize possible ligand migration pathway. In (B), the W1 and W2 are external waters, while W3 and Xe atoms are buried inside the protein. In both (A) and (B), part of the protein was removed to show the internal structure.

In CerHb, replacing one of the apolar tunnel residues, Ala(E18), with Trp leads to ~13-fold drop in the rate of escape [68]. Mutating CerHb Leu(G12), another tunnel residue, to Trp also dramatically increases the extent of internal ligand rebinding. However, this time the effect is due to 10-fold increase of k_{bond} [81]. The difference between two residues is their position relative to the distal pocket. E18 is located at the solvent entrance to the apolar channel and truly blocks the entry pathway. Trp(G12) is closer to the heme and effects of reduced distal pocket volume prevail. Thus, Trp(G12) mutant cannot be used as a major argument in favor of the apolar tunnel being the main

pathway for ligand migration in CerHb. However, a complete set of E7 mutants and other substitutions in the apolar tunnel of CerHb strongly suggest that the latter passageway regulates ligand entry and escape. Similarly, large increases in F_{gem} for the α and β Trp(E11) mutants of HbA solely are not sufficient to prove the existence of the alternative, non-E7 gate pathway proposed by Savino *et al.* [36]. When all the data are taken into consideration, it seems clear that ligands primarily enter and exit the distal pockets in subunits of HbA via the His(E7) route.

5.11. Baseball glove model and the E7 gate.

The work presented in this chapter suggests that the “baseball glove” model of ligand binding, proposed originally for sperm whale Mb [22], is applicable to the α and β subunits of HbA, because reducing the volume of the noncovalent binding site in both subunits decreases the ability of the distal pockets to retain captured ligands until the bond between ligand and iron is formed. The small internal cavities, analogous to the Xe pockets in Mb, do not appear to transiently host ligands during nanosecond laser flash photolysis experiments. In both subunits of HbA, the slow phase of geminate recombination appears to correspond to ligand rebinding from within or very near the distal pocket, and the ultra-fast process reflects rebinding from the initial geminate state formed immediately after ligand photodissociation. Finally, the system of Xe-binding sites observed in crystal structures does not appear to be part of the major pathway for ligand migration between solvent and active site, because filling these cavities with Xe gas does not affect significantly either ligand escape or bimolecular entry.

CHAPTER 6: ENGINEERING HEMOGLOBINS WITH REDUCED NO SCAVENGING AND OPTIMIZED O₂ AFFINITY FOR 3RD GENERATION HB-BASED OXYGEN CARRIERS

6.1. Design principles for 3rd generation Hb-based oxygen carriers (HBOCs).

The first attempts to use the solution of hemoglobin A as an artificial oxygen carrier demonstrated that acellular Hb quickly clears from the bloodstream because Hb tetramers dissociate into dimers, which are small enough to penetrate endothelial barrier of the glomerular filters in kidneys and are excreted in urine [51]. One approach to prevent tetramer dissociation was by genetically fusing α subunits of Hb via a single Gly linker. The sequences encoding for α subunits were put in tandem in a vector with the C-terminus of the α_1 subunit connected to the N-terminus of the α_2 subunit by a Gly residue [170]. The circulation half-life of expressed cross-linked recombinant Hb tetramers increased up to 4-5 hours [51]. However, negative side effects were still observed.

Almost all Hb-based blood substitute prototypes cause an elevation in mean arterial blood pressure immediately after administration. These extracellular hemoglobins also cause decreases in gastrointestinal motility and small numbers of muscle lesions adjacent to capillary beds in heart tissue [43-45, 171]. Acellular Hb appears to extravasate into the space between endothelial and smooth muscle cell layers, scavenge NO molecules by dioxygenation, and prevent NO signaling of smooth muscle relaxation. In the scavenging reaction, oxyHb acts as a pseudoenzyme by oxidizing NO to nitrate and then being re-reduced to oxyHb by reductases, glutathione, and/or ascorbate [5, 6, 172].

One strategy to reduce the rate of NO dioxygenation is to decrease the rate of ligand entry into binding site of HbO₂ by decreasing the size of the distal cavity. As discussed in the previous chapter, this reduction in ligand capture rate can be achieved by replacing residues lining the interior of distal pocket with amino acids possessing bulky aromatic side chains. Filling the distal pocket by introducing Trp and Phe residues at the B10 position in sperm whale Mb led to 10- and 4-fold decreases in the bimolecular rate constants for NO dioxygenation (k'_{NOD}), respectively. Similar decreases in k'_{NOD} were observed for Trp and Phe substitutions at positions E11 and, to a lesser extent, G8 (Fig. 6.1) [5, 7, 38].

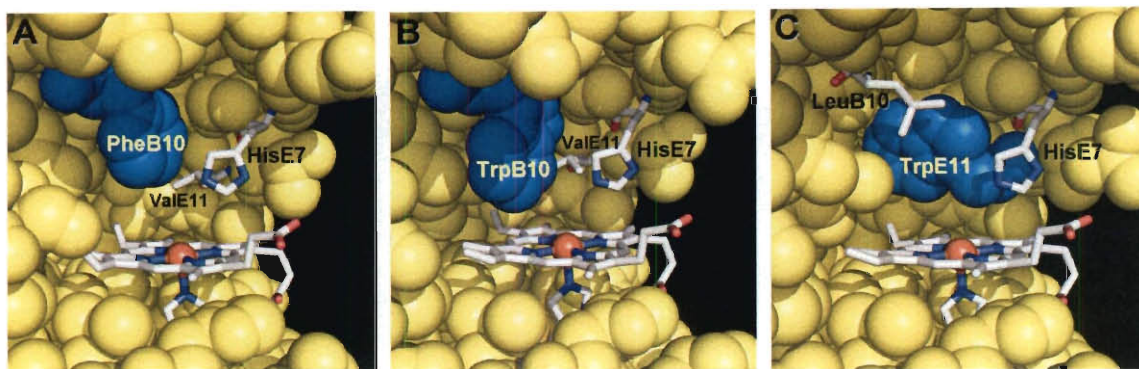


Figure 6.1. Reduction of k'_{NOD} using space-filling mutations at B10 and E11 positions in sperm whale Mb. The models were constructed using the following PDB files: (A) Mb Phe(B10), 2G0R; (B) Mb Trp(B10), 1LTW; (C) Mb Trp(E11), 2OH9. The k'_{NOD} parameters for depicted mutants were 8.1, 3.2 and 4.1 $\mu\text{M}^{-1}\text{s}^{-1}$ for Phe(B10), Trp(B10) and Trp(E11), respectively (wild-type value is 34 $\mu\text{M}^{-1}\text{s}^{-1}$). Heme and key residues are shown in sticks (color code: white, carbon; blue, nitrogen; red, oxygen), space-filling replacements are shown in blue spheres, surrounding residues are shown in yellow spheres; iron is shown as orange sphere. Some residues were removed to demonstrate the inner structure of distal cavity.

The same approach was successfully used to reduce k'_{NOD} in recombinant Hb blood substitute prototypes [38, 43]. Insertion of Phe at the B10 position caused large decreases in the rate of NO dioxygenation reaction in α subunits but only modest decreases in β subunits. On the other hand, a significant reduction of k'_{NOD} was observed

for the Phe(E11) mutation in β subunits but not in α subunits [6]. Trp replacements at B10 and E11 positions were even more effective [43]. Unfortunately, recent work in the Olson laboratory has shown that the Trp(B10) mutation dramatically decreases apoglobin stability and the production of holoprotein during expression in *E. coli*.

Decreasing the volume of the distal pocket slows down the rate of NO entry and hinders to almost the same extent the binding of other ligands, including oxygen. This decrease in k'_{O_2} has been demonstrated for Mb mutants containing Phe and Trp substitutions at E11 and B10 positions [5]. In addition, these Mb variants often show large decreases in the rate constant for O_2 dissociation. Based on these initial results, some research groups have argued that NO dioxygenation and O_2 transport are tightly linked and that side-directed mutagenesis would fail to design an efficient oxygen carrier with a low rate of NO scavenging [47, 50].

In 2002, Dou and coworkers [5] studied O_2 uptake and release by recombinant Mb prototypes in a 25 μm capillary system and demonstrated that for physiologically relevant residence times (0.5 s), even an 100-fold decrease in the O_2 association rate constant (*i.e.* mutation of Leu(B10) to Trp) will still allow ~90% uptake of O_2 in a situation resembling lung alveolar capillaries. In contrast, ligand dissociation rates are critical for efficient O_2 delivery. In the Phe(B10) Mb O_2 mutant, which has markedly reduced P_{50} (0.067 μM) and rate of O_2 dissociation (1.4 s^{-1}), the extent of oxygen release decreased 10-fold in comparison to O_2 release value for the wild-type oxyMb, which has a "normal" P_{50} (0.91 μM) and k_{O_2} (15 s^{-1}).

Because O_2 dissociation is governed primarily by electrostatic stabilization by His(E7) in both Hb and Mb, P_{50} and NO scavenging can be manipulated independently

by site-directed mutagenesis [5, 12, 103]. First, weakening the strength of hydrogen bonding between bound ligand and distal His increases the rate of O₂ dissociation. This weakening can be achieved by replacing His(E7) with Gln. In Mb, introducing a Gln(E7) substitution into the Phe(B10) mutant leads to a ~30-fold increase in P₅₀ (from 0.067 μM to 2.2 μM), while k'_{NOD} increased only 2-fold (from 8.1 μM⁻¹s⁻¹ to 17 μM⁻¹s⁻¹) [5, 38]. Additionally, the Val(E11) to Ile substitution preferentially reduces O₂ affinity (P₅₀ increased from 0.91 μM to 4.35 μM) due to restricted access to Fe atom in deoxy-state and steric clash between Cδ of Ile side chain and bound oxygen in the liganded form, but has little or no effect on NO binding or dioxygenation [143].

In the case of tetrameric HbA, the introduction of allosteric mutations represents another approach to improve the O₂ transport characteristics of potential Hb-based O₂ carriers (HBOCs). This strategy allows modification of O₂ affinity without changing the amino acid content and architecture of the active site and involves perturbing the R to T quaternary state equilibrium with mutations that are usually located at the inter-subunit contacts. For example, the β Asn108(G10) → Lys substitution (Hb Presbyterian) was used in rHbs containing genetically fused α subunits to raise P₅₀ from 10 to 32 mm Hg [43]. The β Lys82(EF6) → Asp mutation (Hb Providence) increases P₅₀ to a lesser extent but has the added advantage of increasing the expression yields and stability of the mutant HbA [173]. When introduced together, these mutations exhibit additive effects and can cause P₅₀ to rise to 46 mm Hg [38]. The effects of these replacements are caused by stabilization of low affinity T-quaternary state. In contrast, the replacement of Tyr at position 145 with His in β-chains locks tetrameric Hb in the R-state and P₅₀ drops from

10 to 2.7 mm Hg [43]. These substitutions allow adjustments of O_2 to either higher or lower values.

6.2. Rational design of Hb distal pocket mutants with reduced NO scavenging.

As stated above, the reduction of NO dioxygenation can be achieved by using space-filling mutations in the distal pockets of α and β subunits. Unfortunately, the most effective Hb mutant, rHb 3011, containing Trp replacements at α B10 and β E11 positions, shows reduced globin stability and expression yields, most likely caused by introducing large, partially polar indole side chains into the distal pockets of the Hb subunits. Thus, my first approach was to try to decrease the ligand capture volume in the distal pocket using new space-filling mutations of HbA, avoiding Trp substitutions.

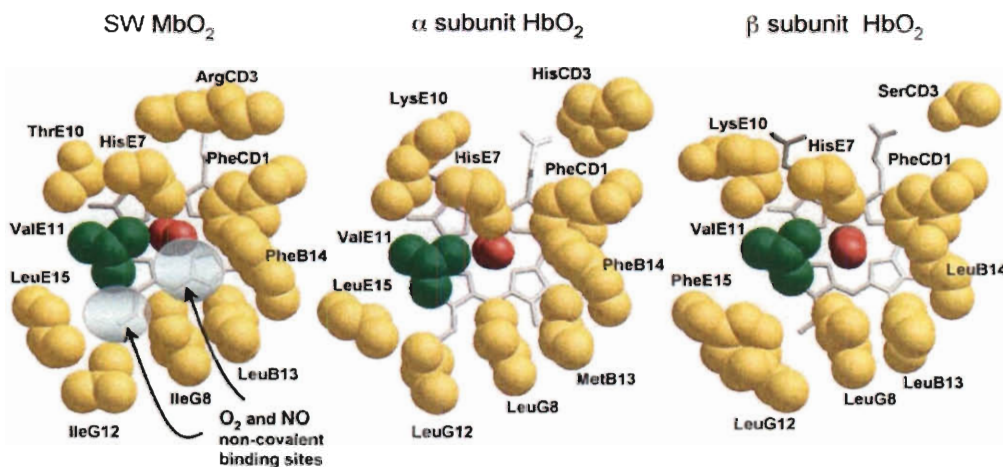


Figure 6.2. Top views of the distal pockets of sperm whale MbO₂ and α and β subunits of human HbO₂. In Mb, the size of non-covalent binding sites was successfully reduced by Trp and Phe replacements at B10 and E11 positions (see Fig. 6.1). In Hb, similar approach is proposed to lower NO scavenging. Heme is shown in white sticks, amino acid residues are labeled and shown in yellow spheres (except, Val(E11) is shown in green), B10 residue is not shown to visualize non-covalent binding sites; O₂ is shown in red spheres. PDB codes for Mb and Hb are 1A6M and 1HHO, respectively.

Previously, large decreases in k'_{entry} , and k'_{NOD} were observed for the single Phe(E11) mutation in β chains, in part because the phenyl ring of β Phe(E15) keeps the large Phe(E11) side chain in position to decrease the distal pocket volume and inhibit non-covalent ligand capture (Fig. 6.2, β subunit) [6]. In α -subunits, the E15 position is occupied by Leu, which appears to allow the α Phe(E11) side chain to rotate away from the capture cavity, leaving its volume relatively unchanged (Fig. 6.2, α subunit). My first mutagenesis attempt was to introduce Phe at E15 position in α -subunits to see if the double mutant α Phe(E11)/Phe(E15) would have a reduced k'_{NOD} value similar to those seen for the single β Phe(E11) mutant.

Insertion of Phe at the α B10 position demonstrated large decreases in the rate of NO dioxygenation reaction. Surprisingly, in β -subunits, the Leu(B10) \rightarrow Phe mutation caused only small effects, and Eich *et al.* [6] hypothesized that large Phe(B10) side chain in β chain may rotate into the empty space next to the β Leu(B13) and β Leu(B14) side chains. In α chains, the B13 and B14 positions are occupied by Met and Phe side chains, respectively, which prevent Phe(B10) rotation. As a result, the α Phe(B10) mutation markedly decreases the rate of NO entry into the mutant α subunit. A second mutagenesis experiment was to try to “lock down” the Phe(B10) side chain in β subunits by introducing an additional Phe residue at the β B13 position, imitating the situation in α chains.

Dou *et al.* [5] reported three Mb mutants containing Phe(B10), Gln(E7) and Ile, Leu, or Phe at the E11 position. These three triple Mb mutants exhibited 3-20-fold decreases in NO dioxygenation in MbO₂ and high levels of expression. Thus, my third mutagenesis experiment was to introduce these same triple combinations into the α and β

chains of Hb. Based on these ideas and previous work, I constructed and purified the following mutant combinations: Phe(B10)/Gln(E7)/Leu(E11), Phe(B10)/Gln(E7)/Phe(E11), and Phe(B10)/Gln(E7)/Ile(E11) in both α and β subunits in the form of mutant hybrid tetramers, which contain one wild-type subunit pair and one mutant subunit pair, and multiple mutant Hb tetramers with Phe(E11)/Phe(E15) in α chains and Phe(B10)/Phe(B13) in β subunit.

Our goals in this work were to screen for new rHbs with low k'_{NOD} values that express well and have O_2 affinities equal or less than that of wild-type HbA (*i.e.* $P_{50} \geq 10$ mmHg). All of the proteins demonstrated robust expression yields, resistance to autooxidation and stability even after numerous freeze-thaw cycles. The expressed multiple mutant combinations possess a variety of interesting O_2 and CO binding properties related to increases or decreases in direct steric hindrance and in electrostatic interactions with the bound ligands. However, the focus of this chapter is on reduction of k'_{NOD} and enhanced expression and stability. More detailed discussions of how the individual mutations affect O_2 and CO binding are given in Dou *et al.* [5], Mathews *et al.* [103], and theses of Drs. Rachel Schweers [69] and David Maillett [58].

6.3. O_2 and CO binding to multiple mutants.

Tables 6.1 and 6.2 provide parameters for O_2 and CO binding to the space-filling, double and triple mutant subunits within hybrid tetramers. The key conclusions from these data are as follows. (1) The His(E7) to Gln mutation increases the rate of O_2 dissociation from α subunits containing Phe(B10) substitution and decreases their O_2 affinities making them viable O_2 transporters. (2) The Phe(B10) and Gln(E7) mutations

in β subunits uniformly increase k_{O_2} and decrease K_{O_2} , again making the mutants better for oxygen delivery. (3) The double mutants α Phe(E11)/Phe(E15) and β Phe(B10)/Phe(B13) cause smaller effects on O_2 and CO binding. (4) In α subunit, replacing Val(E11) with Ile dramatically increases O_2 dissociation and decreases O_2 affinity.

Table 6.1. O_2 binding parameters for space-filling mutant series. The parameters shown are for the subunits within hybrid mutant tetramers (i.e. Hb α (mutant)/ β (wild-type)). Assignment of the observed phases was done based on comparison to wild-type parameters. Data for wild-type subunits were taken from Table 3.1 (Chapter 3). Values were rounded to two significant digits. To identify the mutations, the conventional polypeptide nomenclature was used, according to which amino acids are enumerated starting from the N-terminus of the protein. In α subunits, position 29 corresponds to B10 position in helical nomenclature, 58 – E7, 62 – E11, 66 – E15; in β subunits, position 28 corresponds to B10, 31 – B13, 63 – E7, 67 – E11.

Globin	k'_{O_2} , $\mu M^{-1}s^{-1}$	k_{O_2} , s^{-1}	K_{O_2} , μM^{-1}	Globin	k'_{O_2} , $\mu M^{-1}s^{-1}$	k_{O_2} , s^{-1}	K_{O_2} , μM^{-1}
α WT	29 \pm 11	14 \pm 8	1.9 \pm 0.5	β WT	60 \pm 12	31 \pm 13	3.9 \pm 0.6
α L29F/H58Q/V62I	48	130	0.37	β L28F/ H63Q/V67I	10	140	0.075
α L29F/H58Q/V62L	9.8	6.4	1.5	β L28F/ H63Q/V67L	13	110	0.11
α L29F/H58Q/V62F	5.7	9.9	0.58	β L28F/ H63Q/V67F	13	51	0.26
α V62F/L66F	38	34	1.1	β L28F/L31F	18	21	0.85

Table 6.2. CO binding parameters for space-filling mutant series. The parameters shown are for the subunits within hybrid mutant tetramers (i.e. Hb α (mutant)/ β (wild-type)). Assignment of the observed phases was done based on comparison to wild-type parameters. Data for wild-type subunits were taken from Table 3.1 (Chapter 3). Values were rounded to two significant digits. Here, the same nomenclature was used to specify the mutation as in Table 6.1.

Globin	k'_{CO} , $\mu M^{-1}s^{-1}$	k_{CO} , s^{-1}	K_{CO} , μM^{-1}	Globin	k'_{CO} , $\mu M^{-1}s^{-1}$	k_{CO} , s^{-1}	K_{CO} , μM^{-1}
α WT	4.0 \pm 1.1	0.011 \pm 0.004	360 \pm 200	β WT	7.1 \pm 2.0	0.008 \pm 0.001	890 \pm 440
α L29F/H58Q/V62I	2.4	0.0075	320	β L28F/ H63Q/V67I	0.26	0.0076	34
α L29F/H58Q/V62L	1.6	0.0072	220	β L28F/ H63Q/V67L	0.57	0.0049	116
α L29F/H58Q/V62F	0.26	0.0068	38	β L28F/ H63Q/V67F	1.2	0.0050	244
α V62F/L66F	5.5	0.0063	870	β L28F/L31F	1.5	0.0063	237

6.4. NO dioxygenation by the space-filling mutants.

As discussed in Chapters 2 and 3, nitric oxide is a free radical and extremely reactive with other molecules with unpaired electrons (i.e. superoxide) and high spin ferrous iron (Fe^{2+}). As a result, NO binding and NO dioxygenation are limited only by the rates of ligand entry into the distal pocket, and not steric restrictions at the iron atom [6].

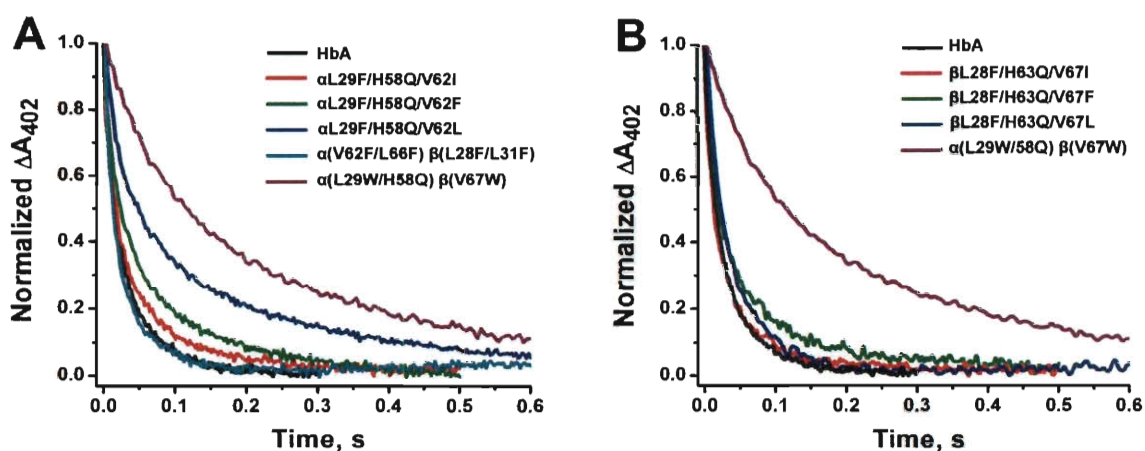


Figure 6.3. NO dioxygenation by multiple α (A) and β (B) space-filling Hb mutants. $2 \mu\text{M}$ solutions of Hb and NO were mixed in stopped flow, rapid mixing apparatus (final concentration is $1 \mu\text{M}$) at 20°C , in 100 mM KPi buffer, pH 7. Absorbance changes were monitored at 402 nm and normalized for comparison. rHb3011 (purple), containing $\alpha\text{L29W}/\text{H58Q}$ and βV67W mutations, and HbA (black) were used as controls for slow and fast NO scavenging, respectively. Here, the same nomenclature was used to specify the mutation as in Table 6.1.

Fig. 6.3 shows time courses for NO dioxygenation after mixing equimolar amounts of the space-filling oxyHb mutants with nitric oxide in a stopped-flow spectrophotometer. HbA and rHb3011 ($\alpha\text{L29W}/\text{H58Q}$ and βV67W) served as controls for fast and slow NO scavenging, respectively. In order to compute k'_{NOD} for these proteins the same reactions were carried out under pseudo-first order conditions (≥ 5 -fold excess NO). The measured k'_{NOD} values are presented in Table 6.3. The association rates

for NO binding were determined using flow-flash technique (see Chapter 2). Both k'_{NO} and k'_{NOD} follow the trends observed for k'_{O_2} and k'_{CO} in Tables 6.1 and 6.2. In α mutants, the lowest rate constants for NO binding and dioxygenation were observed for the $\alpha\text{Phe(B10)/Gln(E7)/Leu(E11)}$ and $\alpha\text{Phe(B10)/Gln(E7)/Phe(E11)}$ combinations. No reduction and, in some cases, even slight increases in rates were seen for rHb tetramers containing $\alpha\text{Phe(B10)/Gln(E7)/Ile(E11)}$ and $\alpha\text{Phe(E11)/Phe(E15)}$. In β subunits, the NO association rate constants diminished only ~2-fold for all the multiple mutants in comparison to wild-type parameters; the best combination, $\beta\text{Phe(B10)/Gln(E7)/Phe(E11)}$, demonstrated only a 3-fold reduction of k'_{NOD} .

Table 6.3. Rate constants for NO dioxygenation by multiple Hb mutants and isolated chains. The parameters shown are for the subunits within hybrid mutant tetramers (i.e. Hb $\alpha(\text{mutant})/\beta(\text{wild-type})$). Subunit assignments of the observed phases were done based on comparison to wild-type parameters. In mutant tetramer Hb $\alpha(\text{V62F/L66F})\beta(\text{L28F/L31F})$, subunit assignments were based on comparison to the hybrid tetramer Hb $\alpha(\text{V62F/L66F})\beta(\text{WT})$. NO association rate constants for wild-type subunits were taken from Table 3.4 (Chapter 3). k'_{NOD} parameters for αWT , βWT and rHb3011 were obtained from single-exponential fits of NO dioxygenation time courses. Values were rounded to two significant digits. The same nomenclature was used to specify the mutation as in Table 6.1.

Globin	$k'_{\text{NO}}, \mu\text{M}^{-1}\text{s}^{-1}$	$k'_{\text{NOD}}, \mu\text{M}^{-1}\text{s}^{-1}$	Globin	$k'_{\text{NO}}, \mu\text{M}^{-1}\text{s}^{-1}$	$k'_{\text{NOD}}, \mu\text{M}^{-1}\text{s}^{-1}$
αWT	31	74	βWT	68	74
rHb3011 ¹	4.8	5.6	rHb3011 ¹	4.8	5.6
$\alpha\text{L29F/H58Q/V62I}$	53	84	$\beta\text{L28F/H63Q/V67I}$	34	47
$\alpha\text{L29F/H58Q/V62L}$	15	17	$\beta\text{L28F/H63Q/V67L}$	39	32
$\alpha\text{L29F/H58Q/V62F}$	8.9	19	$\beta\text{L28F/H63Q/V67F}$	26	23
$\alpha\text{V62F/L66F}$	55	62	$\beta\text{L28F/L31F}$	35	100
$\alpha\text{L29F/H58Q/V62L}^2$	n. d.	18			
$\alpha\text{L29F/V62L}$	35	≥ 120			

¹ k'_{NO} parameters were measured for rHb3011 analog, containing di- α crosslink and stability mutations, described later in the Section 6.5. These modifications did not show any effects on NO dioxygenation (see Table 6.4). ²NO dioxygenation was measured for the isolated subunit.

Unfortunately, none of the new multiple mutants show k'_{NOD} values equal to or less than that of rHb3011 ($\leq 6 \mu\text{M}^{-1}\text{s}^{-1}$). The best candidate, rHb $\alpha\text{Phe(B10)/Gln(E7)/Leu(E11)}$, was characterized more thoroughly. The mutant α subunit was isolated and NO dioxygenation measured under pseudo-first order conditions with excess [Hb]. Again the corresponding rate constant was 2-3-fold larger than that of the previous best mutant, rHb3011. In attempt to further reduce NO scavenging in rHb containing $\alpha\text{Phe(B10)/Gln(E7)/Leu(E11)}$, I increased the size of the E7 gate by the reverse mutation $\text{Gln(E7)} \rightarrow \text{His}$. However, this substitution caused an increase in k'_{NOD} (Table 6.3) to a value almost 10 times larger than the original Gln(E7) containing mutant. Thus, it is clear that the side chains at positions B10, E7 and E11 can interact in non-additive ways making the design of a more compact active site difficult.

In general, the effects of space-filling mutations were disappointingly smaller than expected (Table 6.3). Some of the multiple mutants even increased rates of NO binding and scavenging (i.e. $\alpha\text{Phe(B10)/Gln(E7)/Ile(E11)}$, $\alpha\text{Phe(B10)/Leu(E11)}$, $\beta\text{Phe(B10)/Phe(B13)}$) suggesting that combinations of large residues in the distal pocket may cause expansion of the active site and greater access to the iron atom and bound O_2 .

6.5. Improving oxygen affinity, apoglobin stability and expression yields of recombinant human HbA.

Our experiments and observations suggested that the $\alpha\text{Trp(B10)}$ substitution is the main cause of the lower expression and reduced apoglobin stability of rHb3011, which was the most effective 2rd generation rHb-based blood substitute prototype with low NO scavenging developed by Somatogen, Inc [43]. To test this idea Trp at the αB10

position was replaced with Phe. The Phe(B10) mutation also significantly decreases the rate of NO dioxygenation in α subunits [6]. The negative feature of the α Phe(B10) mutation is that it increases O_2 affinity in both the R and T states [58, 109]. Unfortunately, when the Gln(E7) mutation is added to increase P_{50} , it also raises k'_{NOD} several fold. To address the O_2 affinity issue for the single α Phe(B10) mutant, two allosteric mutations, α Val96(G3) \rightarrow Trp and β Lys82(EF6) \rightarrow Asp were added to the recombinant Hb containing the α Phe(B10) replacement. Both these substitutions stabilize the low affinity T state formation and markedly decrease O_2 affinity [109, 173]. In addition, β His(E7) was replaced with Gln to increase O_2 dissociation from the β subunit containing the Val67(E11)Trp mutation. The final combination included α Phe(B10)/Trp(G3) and β Gln(E7)/Trp(E11)/Asp(EF6). The NO dioxygenation rate constant for this mutant was measured and is presented in Table 6.4 along with parameters for other low NO scavenging Hb mutants, discussed in the following sections.

Table 6.4. Rate constants for NO dioxygenation by multiple low NO scavenging rHb mutants with improved apoglobin stability. The same nomenclature was used to specify the mutation as in Table 6.1. The positions of allosteric and stability mutations are converted to helical nomenclature as follows: $\alpha 15 - \alpha(A13)$, $\alpha 96 - \alpha(G3)$, $\beta 16 - \beta(A13)$, $\beta 82 - \beta(EF6)$, $\beta 116 - \beta(G18)$.

Mutant	k'_{NOD} $\mu\text{M}^{-1}\text{s}^{-1}$
HbA	50.0
rHb $\alpha(L29W/H58Q)$ $\beta(V67W)$	3.8
rHb $\alpha(L29W/H58Q) + \alpha_1\text{-G-}\alpha_2 \beta(V67W)$	3.5
rHb $\alpha(G15A/L29W/H58Q) + \alpha_1\text{-G-}\alpha_2 \beta(G16A/V67W/H116I)$	4.2
rHb $\alpha(L29F/V96W)$ $\beta(H63Q/V67W/K82D)$	6.8

The expression yields of the new mutant improved markedly. The total amount of the rHb $\alpha(\text{Phe(B10)/Trp(G3)})\beta(\text{His(E7)/Trp(E11)/Asp(EF6)})$ after final stages of purification was ~ 2.5 g (20 L fermenter/ ~ 300 g packed cells), while the expression of

wild type HbA usually results in ~ 1.5 g. The oxygenated form of this mutant revealed no signs of rapid autooxidation. The increase in the yield was attributed not only to the removal of the destabilizing α Trp(B10) mutation, but also to the introduction of β Asp(EF6) mutation [173].

Previously, our lab had shown [174] that both rHb expression and apoglobin stability can be increased by incorporating replacements obtained from sequence comparisons of α and β chains of human HbA with the corresponding subunits of the more stable sperm whale and human fetal hemoglobins. The final combination, which demonstrated strong additive increases in the stability of the Hb tetramer contained Gly(A13) to Ala replacement in α subunits and Gly(A13) to Ala and His(G18) to Ile mutations in β subunits. The Gly \rightarrow Ala mutations appear to strengthen A helices in the α and β subunits, and the β Ile(G18) replacement strengthens the $\alpha_1\beta_1$ interface.

Looker *et al.* [170] showed that di- α crosslinking not only increases the retention of rHbA in the bloodstream but also appears to enhance resistance to denaturation. One Gly residue can be used to genetically connect the C-terminus of α_1 with the N-terminus of α_2 , and the resultant di- α gene can be co-expressed with the β gene to produce crosslinked HbA tetramers, which are structurally and functionally very similar to wild-type HbA.

In collaboration with Dr. Cornelius Varnado, we constructed, expressed and purified Hb mutants containing the di- α genes and stability mutations. The rate constants for NO dioxygenation were measured for these proteins and are provided in Table 6.4. All the mutants exhibited low k'_{NOD} values. Neither di- α crosslinking, nor the stability replacements reversed the effects of distal pocket mutations on NO dioxygenation.

Substituting Phe for Trp at α B10 position slightly increased k'_{NOD} , but not significantly ($6.8 \mu\text{M}^{-1}\text{s}^{-1}$ vs. $4 \mu\text{M}^{-1}\text{s}^{-1}$). The allosteric mutations Trp(G3) and Asp(EF6) did not modify the reactivity towards NO, but did greatly improve expression and stability. The R-state parameters of O_2 binding for the multiple rHb mutant containing α Phe(B10)/Trp(G3) and β His(E7)/Trp(E11)/Asp(EF6) and the rHb3011 mutants containing di- α crosslinking and stability mutations were measured and are listed in Table 6.5. In all three low NO scavenging mutants, the association rate constants for O_2 and CO binding decreased dramatically in comparison to wild-type parameters, whereas oxygen dissociation rates are equal or higher than those for native HbA subunits. As a result, O_2 affinity in these multiple rHb mutants diminished ≥ 100 -fold.

Table 6.5. O_2 and CO R-state binding parameters for multiple low NO scavenging rHb mutants with improved apoglobin stability. The same nomenclature was used to specify the mutation as in Table 6.4.

Globin	k'_{O_2} , $\mu\text{M}^{-1}\text{s}^{-1}$	k_{O_2} , s^{-1}	K_{O_2} , μM^{-1}	k'_{CO} , $\mu\text{M}^{-1}\text{s}^{-1}$
α WT	29 \pm 11	14 \pm 8	1.9 \pm 0.5	4.0 \pm 1.1
β WT	60 \pm 12	31 \pm 13	3.9 \pm 0.6	7.1 \pm 2.0
rHb α (L29F/V96W) β (H63Q/V67W/K82D)	4.1 0.93	520 43	0.022 0.0079	0.013 0.043
rHb α (L29W/H58Q) + α_1 -G- α_2 β (V67W)	0.66	30	0.023	0.038
rHb α (G15A/L29W/H58Q) + α_1 -G- α_2 β (G16A/V67W/H116I)	0.73	30	0.024	0.041

Table 6.4 and 6.5 demonstrate that the rHb3011 analogs with improved stability and newly designed multiple rHb mutant containing α Phe(B10) substitution are viable 3rd generation rHBOC candidates. These proteins have relatively high O_2 dissociation rates and low O_2 affinities, which, in the case of α Phe(B10)-containing mutant, is due to the effects of allosteric mutations α Trp(G3) and β Asp(EF6). Further optimization of the

stability and expression yields for multiple rHb mutant containing α Phe(B10) can be achieved by the insertion of di- α crosslink and α Ala(A13), β Ala(A13), and β Ile(G18) stability mutations. At the same time, P_{50} of rHb3011 analogs can be decreased by introducing the allosteric substitutions α Trp(G3) and β Asp(EF6).

6.6. Conclusions.

Even though no new mutant with a k'_{NOD} value equal or less than that of rHb3011 was found, the new rHbs in Tables 6.4 and 6.5 do possess greater stability and show higher expression yields, which are important improvements. In addition, the principle for lowering NO scavenging by reducing the size of the distal cavity via space-filling mutations was confirmed. An almost 4-fold decrease in the rate of NO dioxygenation compared to HbA was achieved by introducing Phe(B10)/Gln(E7)/Leu(E11) or Phe(B10)/Gln(E7)/Phe(E11) combinations into α subunits without compromising globin stability and oxygen transport properties. Finally, these results also show that di- α subunit cross-linking and insertion of stability mutations do not affect the NO scavenging properties of the multiple rHb mutants (Table 6.4).

A summary of our current strategy for developing improved Hb-based artificial oxygen carriers is shown in Fig. 6.4. The ultimate combination will include all of the engineering principles, discovered by Olson group and others: (1) tetramer crosslinking by creating a di- α gene with a glycine linker (di- α Gly) to prevent dissociation into dimers; (2) inhibition of the rate of NO dioxygenation by reducing the capture volume in the distal portion of the heme pocket (α Phe(B10) or α Trp(B10) and β Trp(E11)); (3) raising the P_{50} (i.e., lower the O_2 affinity) directly by weakening stabilization of the

bound ligand (α Gln(E7)) or allosterically by stabilizing the low affinity T quaternary state of the tetramer (α Trp(G3) and β Asp(EF6)); and (4) enhancing apoHb stability by strengthening the $\alpha_1\beta_1$ interface and monomer stability (α Ala(A13), β Ala(A13), and β Ile(G18)).

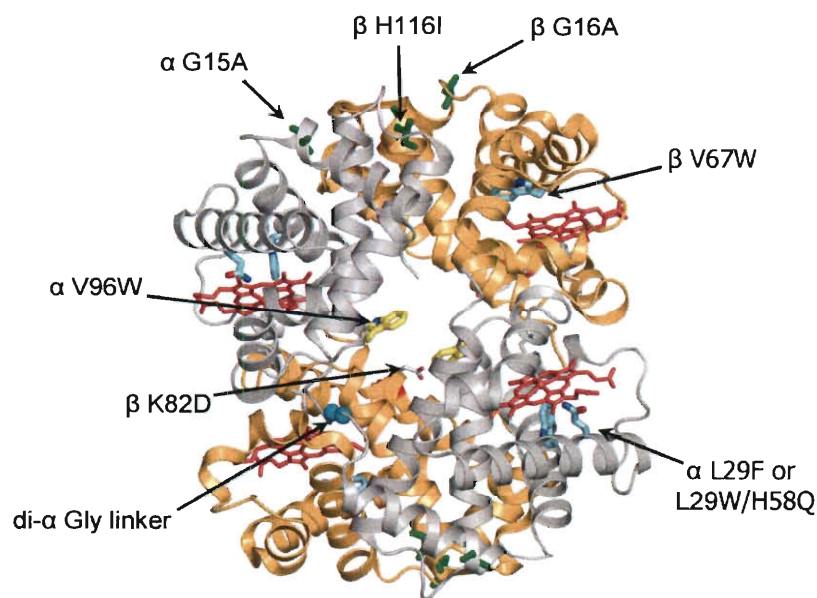


Figure 6.4. Structure depicting candidate rHBOC features. This structure is based on PDBs 101L (rHb α (L29F) + α_1 -G- α_2 β (WT)), 101M (rHb α (WT) + α_1 -G- α_2 β (V67W)) and 1VWT (rHb α (V96W) β (WT)), with the remaining mutations modeled into the composite. α chains are depicted in grey; β chains are depicted in gold; heme groups are depicted in red; and residues of interest are depicted using stick structures. The same nomenclature was used to specify the mutations as in Table 6.4.

CHAPTER 7: CONCLUSIONS

7.1. Stabilization of bound oxygen in α and β subunits of human HbA.

In the late 1980s, Olson and coworkers reported the first mutagenesis studies on globins [20], where they investigated the functional role of His(E7) in sperm whale Mb and the subunits of human HbA. Unexpectedly, β Gly(E7) and β Phe(E7) mutants appeared to have little effect on O₂ binding parameters. These unexpected data seemed to support the conclusions of Shaanan that β His(E7) is not involved in electrostatic interactions with bound dioxygen [104]. However, the more recent NMR and X-ray data cast doubt on the validity of the earlier conclusions [2, 108]. In 2003, a previous member of our lab, Dr. Rachel Schweers, re-examined the effects of E7 mutations on O₂ binding to HbA by studying Gln, Ala and Leu(E7) mutants of α and β Hb chains [69], and these studies were extended to include Gly, Phe and Trp(E7) mutants and more detailed experiments with isolated α and β subunits.

Our new results provide unequivocal proof that His(E7) stabilizes bound O₂ in both the α and β subunits. The replacement of the distal His residue with small apolar amino acids (Gly, Ala or Leu) leads to ~30-fold increases in the rates of O₂ dissociation in both Hb subunits. FTIR spectra of the apolar E7 mutant subunits and hybrid mutant tetramers demonstrate the loss of positive electrostatic field adjacent to bound ligands and confirm the electrostatic nature of O₂ stabilization in the wild-type protein. The calculated free energy of the hydrogen bond between O₂ and His(E7) appears to be roughly the same in both subunits (~ -8.3 kJ/mol). In Mb, the hydrogen bond between His(E7) and O₂ is approximately two-fold stronger than that in Hb subunits and equals ~ -14.5 kJ/mol. The ~100-fold increases in M-values of the apolar E7 mutants of HbA,

compared to wild-type or the Gln(E7) variants, demonstrate that ligand discrimination in human HbA is due to preferential electrostatic stabilization of O₂ and not due to unfavorable steric hindrance of CO. Unfavorable steric effects do occur in the Phe(E7) and Trp(E7) variants caused by inward movements of the large aromatic side chains. In Phe(E7) mutants, direct interaction of phenyl side chain with bound ligand dramatically increases dissociation rate of both O₂ and CO. In the closed conformation of the Trp(E7) mutants, the indole ring of the distal Trp fills the distal pocket and prevents ligand entry and bond formation with iron. Regardless of the mechanism, in both Phe(E7) and Trp(E7) mutants, ligand affinity decreases markedly.

7.2. Gating of ligand entry into the subunits of HbA.

The very first crystal structures of Hb demonstrated the absence of a direct channel between solvent and active site of the globin [13]. Ligands were proposed to enter the distal pocket via a transiently open E7 channel, created by outward/inward motions of the distal His. Mutagenesis studies in sperm whale Mb revealed the dependence of ligand entry and escape rates on the size of the E7 residue [20, 22, 100]. Laser flash photolysis of MbCO complexes allowed monitoring the competition between opening of the distal His gate and ligand geminate rebinding [87]. However, little direct evidence for the applicability of the His gate hypothesis in human HbA existed.

This thesis work has demonstrated that in both subunits of HbA the size of E7 residue appears to regulate the bimolecular rate constants for ligand binding. Association rate constants for O₂ and CO binding markedly decrease with the increasing size of the E7 side chain. The calculated rates of ligand entry obtained from geminate CO

recombination kinetics and directly measured k'_{entry} determined in bimolecular NO binding experiments reveal the same correlation. This situation is analogous to sperm whale Mb and argues strongly that distal His acts as a gate for ligand entry and escape in α and β subunits of human HbA.

Ligand recombination to α and β Trp(E7) mutant subunits in laser photolysis experiments showed a highly complex kinetics for bimolecular binding. In both Hb chains, the time course consists of one extremely fast phase, similar to that for the Gly and Ala(E7) mutants, and one or more slow phases with apparent rate constants ~ 100 - 1000 -fold smaller. The fast phase results from ligand binding to an open conformation, in which the Trp(E7) side chain is located in the solvent phase and the E7 channel is unhindered. The slow phases represent ligand binding to a closed conformer, in which the indole ring of Trp(E7) is obstructing access into the distal pocket. Crystal structures of α and β Trp(E7) mutants in CO- and deoxy-forms provide structural models for the slowly reacting conformers observed in the kinetic experiments. In the *closed* form, the large indole side chain of Trp(E7) enters the distal pocket, fills the E7 channel and restricts access to the iron atom. In both mutant subunits, this *closed* conformer lowers the bimolecular rate of ligand binding ~ 50 - 100 -fold, compared to wild-type HbA subunits. A distinct *blocked* state is formed in β subunit, in which the Trp side chain obstructs the E7 channel and prevents ligand entry through the E7 gate, but does not enter the distal pocket and does not sterically hinder the access to the iron atom. Bimolecular ligand binding to the *blocked* β Trp(E7) subunits is 10-fold slower than to the wild-type human HbA, suggesting that in β subunits $\geq 90\%$ of ligands enter the distal pocket via the E7 gate.

The *blocked* conformation of Trp(E7) also exists in sperm whale Mb but is not as effective in shielding ligand entry into the distal pocket as in the β Trp(E7) subunits of human HbA. The Trp(E7) mutation causes smaller effects on k'_{entry} in Mb (~3-4-fold decrease compared to that for wild-type Mb), implying that either more ligands take alternative routes in native sperm whale Mb or the Trp(E7) side chain is more flexible in the *blocked* Mb conformer.

7.3. Multiple *versus* single ligand migration pathways in human HbA.

The discovery of Xe binding sites in the structure of Mb [31] provided the basis of an alternative hypothesis for ligand migration in globins. In this multiple pathway mechanism, the E7 gate is not the major pathway, and, instead, ligands can enter and exit the binding site by a variety of transient channels appearing in the protein matrix with the Xe cavities playing the role of transient stations for diffusing ligands. Most computational analyses support this theory [28]. Laser photolysis experiments and time-resolved crystallography demonstrate that ligands visit the Xe sites, which accounts for the biphasicity of geminate O₂ recombination to Mb. However, all experimental data indicate that ligands enter and exit Mb by the E7 channel [22, 32, 53]. Recently, Xe binding sites were identified in Hb subunits and analogous hypotheses for multiple pathways for ligand migration in HbA have been proposed [35, 36].

In this thesis, the functional significance of the accessible volume of the Xe cavities and the distal pockets of both Hb subunits was examined by mutagenesis and exposure to high pressures of Xe gas. First, decreasing the size of the distal pocket in both α and β subunits of HbA by Trp and Phe mutations at B10, E11 and G8 positions

does have dramatic effects on geminate and bimolecular ligand binding parameters. The bimolecular association rate constants diminished significantly for some of these mutations, which agrees well with the “baseball glove” model of ligand binding, proposed earlier for sperm whale Mb [22]. The rates of ligand-iron bond formation and escape increase in the mutants with clearly reduced distal pocket volumes.

Second, there is little effect of adding high pressures of Xe gas on either geminate or bimolecular ligand recombination after photolysis of intact tetrameric Hb and its isolated subunits. Thus, in contrast to Mb, ligands do not migrate to remote Xe cavities in the α and β subunits of HbA, but instead recombine geminately from within the distal pocket. Ligand escape is not slowed down by filling the Xe binding sites. Similarly, the rates of bimolecular ligand entry are little affected by high pressures of Xe gas. The small effect that is observed appears to be due to a small reduction of the distal pocket volume and not direct blocking of the pathway for ligand entry. Again, all these data add further support to the conclusion that ligands enter and leave the distal pocket through the His(E7) gate in animal Mbs and Hbs.

REFERENCES

1. Dickerson, R.E. and I. Geis, *Hemoglobin: structure, function, evolution, and pathology.*, ed. P. Hagopian. 1983: The Benjamin/Cummings Publishing Company, Inc. 176.
2. Park, S.Y., et al., *1.25 Å resolution crystal structures of human haemoglobin in the oxy, deoxy and carbonmonoxy forms.* J Mol Biol, 2006. **360**(3): p. 690-701.
3. Antonini, E. and M. Brunori, *Hemoglobin and Myoglobin in Their Reactions with Ligands.* 1971, London, England: North-Holland Publishing Company.
4. Doyle, M.P. and J.W. Hoekstra, *Oxidation of nitrogen oxides by bound dioxygen in hemoproteins.* J Inorg Biochem, 1981. **14**(4): p. 351-8.
5. Dou, Y., et al., *Myoglobin as a model system for designing heme protein based blood substitutes.* Biophys Chem, 2002. **98**(1-2): p. 127-48.
6. Eich, R.F., et al., *Mechanism of NO-induced oxidation of myoglobin and hemoglobin.* Biochemistry, 1996. **35**(22): p. 6976-83.
7. Olson, J.S. and D.H. Maillett, *Designing recombinant hemoglobin for use as a blood substitute.*, in *Blood Substitutes*, R.M. Winslow, Editor. 2006, Academic Press. p. 354-374.
8. Gladwin, M.T., J.H. Crawford, and R.P. Patel, *The biochemistry of nitric oxide, nitrite, and hemoglobin: role in blood flow regulation.* Free Radic Biol Med, 2004. **36**(6): p. 707-17.
9. Kim-Shapiro, D.B., A.N. Schechter, and M.T. Gladwin, *Unraveling the reactions of nitric oxide, nitrite, and hemoglobin in physiology and therapeutics.* Arterioscler Thromb Vasc Biol, 2006. **26**(4): p. 697-705.
10. Gow, A.J. and J.S. Stamler, *Reactions between nitric oxide and haemoglobin under physiological conditions.* Nature, 1998. **391**(6663): p. 169-73.
11. Angelo, M., D.J. Singel, and J.S. Stamler, *An S-nitrosothiol (SNO) synthase function of hemoglobin that utilizes nitrite as a substrate.* Proc Natl Acad Sci U S A, 2006. **103**(22): p. 8366-71.

12. Olson, J.S. and G.N. Phillips, *Myoglobin discriminates between O₂, NO, and CO by electrostatic interactions with the bound ligand*. Journal of Biological Inorganic Chemistry, 1997. **2**(4): p. 544-552.
13. Perutz, M.F. and F.S. Mathews, *An x-ray study of azide methaemoglobin*. J Mol Biol, 1966. **21**(1): p. 199-202.
14. Perutz, M.F., *Stereochemistry of cooperative effects in haemoglobin*. Nature, 1970. **228**(5273): p. 726-39.
15. Petrich, J.W., C. Poyart, and J.L. Martin, *Photophysics and reactivity of heme proteins: a femtosecond absorption study of hemoglobin, myoglobin, and protoheme*. Biochemistry, 1988. **27**(11): p. 4049-60.
16. Olson, J.S., R.J. Rohlfs, and Q.H. Gibson, *Ligand recombination to the alpha and beta subunits of human hemoglobin*. J Biol Chem, 1987. **262**(27): p. 12930-8.
17. Carver, T.E., et al., *Analysis of the kinetic barriers for ligand binding to sperm whale myoglobin using site-directed mutagenesis and laser photolysis techniques*. J Biol Chem, 1990. **265**(32): p. 20007-20.
18. Franzen, S., *Spin-dependent mechanism for diatomic ligand binding to heme*. Proc Natl Acad Sci U S A, 2002. **99**(26): p. 16754-9.
19. Ionascu, D., et al., *Temperature-dependent studies of NO recombination to heme and heme proteins*. J Am Chem Soc, 2005. **127**(48): p. 16921-34.
20. Olson, J.S., et al., *The role of the distal histidine in myoglobin and haemoglobin*. Nature, 1988. **336**(6196): p. 265-6.
21. Huang, X. and S.G. Boxer, *Discovery of new ligand binding pathways in myoglobin by random mutagenesis*. Nat Struct Biol, 1994. **1**(4): p. 226-9.
22. Scott, E.E., Q.H. Gibson, and J.S. Olson, *Mapping the pathways for O₂ entry into and exit from myoglobin*. J Biol Chem, 2001. **276**(7): p. 5177-88.
23. Case, D.A. and M. Karplus, *Dynamics of ligand binding to heme proteins*. J Mol Biol, 1979. **132**(3): p. 343-68.

24. Elber, R. and M. Karplus, *Enhanced sampling in molecular dynamics: use of the time dependent Hartree approximation for simulation of carbon monoxide diffusion through myoglobin*. J. Am. Chem. Soc., 1990. **112**(25): p. 9161-75.
25. Cohen, J., et al., *Imaging the migration pathways for O₂, CO, NO, and Xe inside myoglobin*. Biophys J, 2006. **91**(5): p. 1844-57.
26. Cohen, J. and K. Schulten, *O₂ migration pathways are not conserved across proteins of a similar fold*. Biophys J, 2007. **93**(10): p. 3591-600.
27. Cohen, J., K.W. Olsen, and K. Schulten, *Finding gas migration pathways in proteins using implicit ligand sampling*. Methods Enzymol, 2008. **437**: p. 439-57.
28. Elber, R., *Ligand diffusion in globins: simulations versus experiment*. Curr Opin Struct Biol, 2010. **20**(2): p. 162-7.
29. Ruscio, J.Z., et al., *Atomic level computational identification of ligand migration pathways between solvent and binding site in myoglobin*. Proc Natl Acad Sci U S A, 2008. **105**(27): p. 9204-9.
30. Schoenborn, B.P., H.C. Watson, and J.C. Kendrew, *Binding of xenon to sperm whale myoglobin*. Nature, 1965. **207**: p. 28-30.
31. Tilton, R.F., Jr., I.D. Kuntz, Jr., and G.A. Petsko, *Cavities in proteins: Structure of a metmyoglobin-xenon complex solved to 1.9 Å*. Biochemistry, 1984. **23**: p. 2849-2857.
32. Olson, J.S., J. Soman, and G.N. Phillips, Jr., *Ligand pathways in myoglobin: a review of Trp cavity mutations*. Iubmb Life, 2007. **59**(8-9): p. 552-62.
33. Tetreau, C., et al., *Competition with xenon elicits ligand migration and escape pathways in myoglobin*. Biophys J, 2004. **86**(1 Pt 1): p. 435-47.
34. Mouawad, L., J.D. Marechal, and D. Perahia, *Internal cavities and ligand passageways in human hemoglobin characterized by molecular dynamics simulations*. Biochim Biophys Acta, 2005. **1724**(3): p. 385-93.

35. Sottini, S., et al., *Geminate rebinding in R-state hemoglobin: kinetic and computational evidence for multiple hydrophobic pockets*. J Am Chem Soc, 2005. **127**(49): p. 17427-32.
36. Savino, C., et al., *Pattern of cavities in globins: the case of human hemoglobin*. Biopolymers, 2009. **91**(12): p. 1097-107.
37. Hofmann, F., *The biology of cyclic GMP-dependent protein kinases*. J Biol Chem, 2005. **280**(1): p. 1-4.
38. Olson, J.S., et al., *No scavenging and the hypertensive effect of hemoglobin-based blood substitutes*. Free Radic Biol Med, 2004. **36**(6): p. 685-97.
39. Herold, S., M. Exner, and T. Nauser, *Kinetic and mechanistic studies of the NO*-mediated oxidation of oxymyoglobin and oxyhemoglobin*. Biochemistry, 2001. **40**(11): p. 3385-95.
40. Yukl, E.T., S. de Vries, and P. Moenne-Loccoz, *The millisecond intermediate in the reaction of nitric oxide with oxymyoglobin is an iron(III)--nitrate complex, not a peroxynitrite*. J Am Chem Soc, 2009. **131**(21): p. 7234-5.
41. Brunori, M., *Nitric oxide, cytochrome-c oxidase and myoglobin*. Trends Biochem Sci, 2001. **26**(1): p. 21-3.
42. Brunori, M., *Nitric oxide moves myoglobin centre stage*. Trends Biochem Sci, 2001. **26**(4): p. 209-10.
43. Doherty, D.H., et al., *Rate of reaction with nitric oxide determines the hypertensive effect of cell-free hemoglobin*. Nat Biotechnol, 1998. **16**(7): p. 672-6.
44. Murray, J.A., et al., *The effects of recombinant human hemoglobin on esophageal motor functions in humans*. Gastroenterology, 1995. **109**(4): p. 1241-8.
45. Conklin, J.L., et al., *Effects of recombinant human hemoglobin on motor functions of the opossum esophagus*. J Pharmacol Exp Ther, 1995. **273**(2): p. 762-7.
46. Alayash, A.I. and R.E. Cashion, *Hemoglobin and free radicals: implications for the development of a safe blood substitute*. Mol Med Today, 1995. **1**(3): p. 122-7.

47. Rohlfis, R.J., et al., *Arterial blood pressure responses to cell-free hemoglobin solutions and the reaction with nitric oxide*. J Biol Chem, 1998. **273**(20): p. 12128-34.
48. Doyle, M.P., I. Apostol, and B.A. Kerwin, *Glutaraldehyde modification of recombinant human hemoglobin alters its hemodynamic properties*. J Biol Chem, 1999. **274**(4): p. 2583-91.
49. McCarthy, M.R., K.D. Vandegriff, and R.M. Winslow, *The role of facilitated diffusion in oxygen transport by cell-free hemoglobins: implications for the design of hemoglobin-based oxygen carriers*. Biophys Chem, 2001. **92**(1-2): p. 103-17.
50. Winslow, R.M., *Artificial blood: ancient dream, modern enigma*. Nat Biotechnol, 1998. **16**(7): p. 621-2.
51. Kim, H.W. and A.G. Greenburg, *Artificial oxygen carriers as red blood cell substitutes: a selected review and current status*. Artif Organs, 2004. **28**(9): p. 813-28.
52. Seghatchian, J. and G. de Sousa, *An overview of unresolved inherent problems associated with red cell transfusion and potential use of artificial oxygen carriers and ECO-RBC: current status/future trends*. Transfus Apher Sci, 2007. **37**(3): p. 251-9.
53. Schotte, F., et al., *Picosecond time-resolved X-ray crystallography: probing protein function in real time*. J Struct Biol, 2004. **147**(3): p. 235-46.
54. Hoffman, S.J., et al., *Expression of fully functional tetrameric human hemoglobin in Escherichia coli*. Proc Natl Acad Sci U S A, 1990. **87**(21): p. 8521-5.
55. Looker, D., et al., *Expression of recombinant human hemoglobin in Escherichia coli*. Methods Enzymol, 1994. **231**: p. 364-74.
56. Phillips, G.N., Jr., *Comparison of the dynamics of myoglobin in different crystal forms*. Biophys J, 1990. **57**(2): p. 381-3.
57. Phillips, G.N., Jr., et al., *Crystal structure of myoglobin from a synthetic gene*. Proteins, 1990. **7**(4): p. 358-65.

58. Maillett, D.H., *Engineering Hemoglobins and Myoglobins for Efficient O₂ Transport*, in *Biochemistry and Cell Biology*. 2003, Rice University: Houston.
59. Shen, T.J., et al., *Production of unmodified human adult hemoglobin in Escherichia coli*. Proc Natl Acad Sci U S A, 1993. **90**(17): p. 8108-12.
60. Shen, T.J., et al., *Production of human normal adult and fetal hemoglobins in Escherichia coli*. Protein Eng, 1997. **10**(9): p. 1085-97.
61. Parkhurst, K.M. and L.J. Parkhurst, *Rapid preparation of native alpha and beta chains of human hemoglobin*. Int J Biochem, 1992. **24**(6): p. 993-8.
62. Boyer, P.D., *Spectrophotometric Study of the Reaction of Protein Sulfhydryl Groups with Organic Mercurials*. J. Am. Chem. Soc., 1954. **76**(17): p. 4331-4337.
63. Monod, J., J. Wyman, and J.P. Changeux, *On the Nature of Allosteric Transitions: a Plausible Model*. J Mol Biol, 1965. **12**: p. 88-118.
64. Mathews, A.J. and J.S. Olson, *Assignment of rate constants for O₂ and CO binding to alpha and beta subunits within R- and T-state human hemoglobin*. Methods Enzymol, 1994. **232**: p. 363-86.
65. Olson, J.S., et al., *Measurement of rate constants for reactions of O₂, CO, and NO with hemoglobin*. Methods Mol Med, 2003. **82**: p. 65-91.
66. Gibson, Q.H., *The direct determination of the velocity constant of the reaction Hb₄(CO)₃ + CO-Hb₄(CO)₄*. J Physiol, 1956. **134**(1): p. 123-34.
67. Gibson, Q.H., *The photochemical formation of a quickly reacting form of haemoglobin*. Biochem J, 1959. **71**(2): p. 293-303.
68. Salter, M.D., et al., *The apolar channel in Cerebratulus lacteus hemoglobin is the route for O₂ entry and exit*. J Biol Chem, 2008. **283**(51): p. 35689-702.
69. Schweers, R., *Electrostatic regulation of O₂ and CO binding in the alpha and beta subunits of recombinant human hemoglobin*, in *Biochemistry and Cell Biology*. 2003, Rice University: Houston. p. 195.

70. Mathews, A.J., et al., *The assignment of carbon monoxide association rate constants to the alpha and beta subunits in native and mutant human deoxyhemoglobin tetramers*. J Biol Chem, 1991. **266**(32): p. 21631-9.
71. Unzai, S., et al., *Rate constants for O₂ and CO binding to the alpha and beta subunits within the R and T states of human hemoglobin*. J Biol Chem, 1998. **273**(36): p. 23150-9.
72. Jongeward, K.A., et al., *Picosecond and nanosecond geminate recombination of myoglobin with CO, O₂, NO, and isocyanides*. J Amer Chem Soc, 1988. **110**: p. 380-387.
73. Olson, J.S. and G.N. Phillips, Jr., *Kinetic pathways and barriers for ligand binding to myoglobin*. J Biol Chem, 1996. **271**(30): p. 17593-6.
74. Cassoly, R. and Q. Gibson, *Conformation, co-operativity and ligand binding in human hemoglobin*. J Mol Biol, 1975. **91**(3): p. 301-13.
75. Austin, R.H., et al., *Dynamics of ligand binding to myoglobin*. Biochemistry, 1975. **14**(24): p. 5355-73.
76. Blouin, G.C., R.L. Schweers, and J.S. Olson, *Alkyl Isocyanides Serve as Transition State Analogs for Ligand Entry and Exit in Myoglobin*. Biochemistry, 2010.
77. Elber, R. and Q.H. Gibson, *Toward quantitative simulations of carbon monoxide escape pathways in myoglobin*. J Phys Chem B, 2008. **112**(19): p. 6147-54.
78. Schmidt, M., et al., *Ligand migration pathway and protein dynamics in myoglobin: A time-resolved crystallographic study on L29W MbCO*. Proc Natl Acad Sci U S A, 2005. **102**(33): p. 11704-9.
79. Schoenborn, B.P. and C.L. Nobbs, *The binding of xenon of sperm whale deoxymyoglobin*. Mol Pharmacol, 1966. **2**(5): p. 495-8.
80. Scott, E.E. and Q.H. Gibson, *Ligand migration in sperm whale myoglobin*. Biochemistry, 1997. **36**(39): p. 11909-17.

81. Pesce, A., et al., *Ligand migration in the apolar tunnel of cerebratulus lacteus mini-hemoglobin*. J Biol Chem, 2010.
82. Franzen, S., *An Electrostatic Model for the Frequency Shifts in the Carbonmonoxy Stretching Band of Myoglobin: Correlation of Hydrogen Bonding and the Stark Tuning Rate*. Journal of the American Chemical Society, 2002. **124**(44): p. 13271-13281.
83. Li, T., et al., *Structural determinants of the stretching frequency of CO bound to myoglobin*. Biochemistry, 1994. **33**(6): p. 1433-46.
84. Morikis, D., et al., *Resonance raman investigations of site-directed mutants of myoglobin: effects of distal histidine replacement*. Biochemistry, 1989. **28**(11): p. 4791-800.
85. Phillips, G.N., et al., *Bound CO is a molecular probe of electrostatic potential in the distal pocket of myoglobin*. Journal of Physical Chemistry B, 1999. **103**(42): p. 8817-8829.
86. Tian, W.D., J.T. Sage, and P.M. Champion, *Investigations of ligand association and dissociation rates in the "open" and "closed" states of myoglobin*. J Mol Biol, 1993. **233**(1): p. 155-66.
87. Tian, W.D., et al., *Probing heme protein conformational equilibration rates with kinetic selection*. Biochemistry, 1996. **35**(11): p. 3487-502.
88. Perutz, M.F., *Preparation of haemoglobin crystals*. Journal of Crystal Growth, 1968. **2**: p. 54-56.
89. Quillin, M.L., et al., *High-resolution crystal structures of distal histidine mutants of sperm whale myoglobin*. J Mol Biol, 1993. **234**(1): p. 140-55.
90. Brucker, E.A., *Genetically crosslinked hemoglobin: a structural study*. Acta Crystallogr D Biol Crystallogr, 2000. **56**(Pt 7): p. 812-6.
91. Pflugrath, J.W., *The finer things in X-ray diffraction data collection*. Acta Crystallogr D Biol Crystallogr, 1999. **55**(Pt 10): p. 1718-25.

92. Brünger, A.T., et al., *Crystallography & NMR System: A New Software Suite for Macromolecular Structure Determination*. Acta Crystallographica, 1998. **D54**: p. 905-921.
93. Brucker, E.A., et al., *High resolution crystal structures of the deoxy, oxy, and aquomet forms of cobalt myoglobin*. J Biol Chem, 1996. **271**(41): p. 25419-22.
94. Adams, P.D., et al., *PHENIX: a comprehensive Python-based system for macromolecular structure solution*. Acta Crystallogr D Biol Crystallogr, 2010. **66**(Pt 2): p. 213-21.
95. Emsley, P. and K. Cowtan, *Coot: model-building tools for molecular graphics*. Acta Crystallogr D Biol Crystallogr, 2004. **60**(Pt 12 Pt 1): p. 2126-32.
96. Pauling, L., *The Nature of Iron-oxygen Bond in Oxyhaemoglobin*. Nature, 1964. **203**: p. 182-183.
97. Jameson, G.B., et al., *Models for the active site of oxygen-binding hemoproteins. Dioxygen binding properties and the structures of (2-methylimidazole)-meso-tetra($\alpha, \alpha, \alpha, \alpha$ -o-pivalamidophenyl)porphyrinatoiron(II)-ethanol and its dioxygen adduct*. J Amer Chem Soc, 1980. **102**: p. 3224–3237.
98. Slebodnick, C. and J.A. Ibers, *Myoglobin models and steric origins of the discrimination between O₂ and CO*. J Biol Inorg Chem, 1997. **2**(4): p. 521-525.
99. Traylor, T.G., et al., *Reactivity of ferrous heme proteins at low pH*. J Biol Chem, 1983. **258**(20): p. 12147-8.
100. Springer, B.A., et al., *Discrimination between oxygen and carbon monoxide and inhibition of autooxidation by myoglobin. Site-directed mutagenesis of the distal histidine*. J Biol Chem, 1989. **264**(6): p. 3057-60.
101. Springer, B.A., et al., *Mechanisms of ligand recognition in myoglobin*. Chem. Rev., 1994. **94**: p. 699-714.
102. Momenteau, M. and C.A. Reed, *Synthetic heme dioxygen complexes*. Chemical Reviews, 1994. **94**: p. 659–698.

103. Mathews, A.J., et al., *The effects of E7 and E11 mutations on the kinetics of ligand binding to R state human hemoglobin*. J Biol Chem, 1989. **264**(28): p. 16573-83.
104. Shaanan, B., *Structure of human oxyhaemoglobin at 2.1 Å resolution*. J Mol Biol, 1983. **171**(1): p. 31-59.
105. Spiro, T.G. and P.M. Kozlowski, *Is the CO Adduct of Myoglobin Bent, and Does It Matter?* Acc Chem Res, 2001. **34**(2): p. 137-144.
106. Park, E.S. and S.G. Boxer, *Origins of the Sensitivity of Molecular Vibrations to Electric Fields: Carbonyl and Nitrosyl Stretches in Model Compounds and Proteins*. J Phys Chem B, 2002. **106**(22): p. 5800-5806.
107. Yang, F. and G.N. Phillips, Jr., *Crystal structures of CO-, deoxy- and met-myoglobins at various pH values*. J Mol Biol, 1996. **256**(4): p. 762-74.
108. Lukin, J.A., et al., *NMR reveals hydrogen bonds between oxygen and distal histidines in oxyhemoglobin*. Proc Natl Acad Sci U S A, 2000. **97**(19): p. 10354-8.
109. Maillett, D.H., et al., *Interfacial and distal-heme pocket mutations exhibit additive effects on the structure and function of hemoglobin*. Biochemistry, 2008. **47**(40): p. 10551-63.
110. Smagghe, B.J., et al., *Correlations between oxygen affinity and sequence classifications of plant hemoglobins*. Biopolymers, 2009.
111. Trent, J.T., 3rd, R.A. Watts, and M.S. Hargrove, *Human neuroglobin, a hexacoordinate hemoglobin that reversibly binds oxygen*. J Biol Chem, 2001. **276**(32): p. 30106-10.
112. Trent, J.T., 3rd, A.N. Hvitved, and M.S. Hargrove, *A model for ligand binding to hexacoordinate hemoglobins*. Biochemistry, 2001. **40**(20): p. 6155-63.
113. Hvitved, A.N., et al., *Ligand binding and hexacoordination in synechocystis hemoglobin*. J Biol Chem, 2001. **276**(37): p. 34714-21.

114. Ikeda-Saito, M., et al., *Ligand diffusion in the distal heme pocket of myoglobin. A primary determinant of geminate rebinding.* J Biol Chem, 1993. **268**(10): p. 6855-7.
115. Gibson, Q.H., et al., *A kinetic description of ligand binding to sperm whale myoglobin.* J Biol Chem, 1986. **261**(22): p. 10228-39.
116. Zhang, Z., et al., *Measurements of heme relaxation and ligand recombination in strong magnetic fields.* J Phys Chem B, 2009. **113**(31): p. 10923-33.
117. Nienhaus, K., et al., *The origin of stark splitting in the initial photoproduct state of MbCO.* J Am Chem Soc, 2005. **127**(1): p. 40-1.
118. McKinnie, R.E. and J.S. Olson, *Effects of solvent composition and viscosity on the rates of CO binding to heme proteins.* J Biol Chem, 1981. **256**(17): p. 8928-32.
119. Olson, J.S., et al., *Mechanisms of ligand binding to pentacoordinate protoheme.* Journal of the American Chemical Society, 1983. **105**(6): p. 1522-7.
120. Hargrove, M.S., et al., *Characterization of recombinant soybean leghemoglobin a and apolar distal histidine mutants.* J Mol Biol, 1997. **266**(5): p. 1032-42.
121. Friedman, J.M., et al., *Localized control of ligand binding in hemoglobin: effect of tertiary structure on picosecond geminate recombination.* Science, 1985. **229**(4709): p. 187-90.
122. Ray, G.B., et al., *How far can proteins bend the FeCO unit? Distal polar and steric effects in heme proteins and models.* Journal of the American Chemical Society, 1994. **116**(1): p. 162-76.
123. Park, E.S., et al., *Vibrational Stark Spectroscopy in Proteins: A Probe and Calibration for Electrostatic Fields.* J Phys Chem B, 1999. **103**(45): p. 9813-9817.
124. Lin, S.H., et al., *Effect of the distal residues on the vibrational modes of the Fe-CO bond in hemoglobin studied by protein engineering.* Biochemistry, 1990. **29**(23): p. 5562-6.

125. Vojtechovsky, J., et al., *Crystal structures of myoglobin-ligand complexes at near-atomic resolution*. *Biophys J*, 1999. **77**(4): p. 2153-74.
126. Rohlf, R.J., et al., *The effects of amino acid substitution at position E7 (residue 64) on the kinetics of ligand binding to sperm whale myoglobin*. *J Biol Chem*, 1990. **265**(6): p. 3168-76.
127. Thorsteinsson, M.V., et al., *A cyanobacterial hemoglobin with unusual ligand binding kinetics and stability properties*. *Biochemistry*, 1999. **38**(7): p. 2117-26.
128. Srajer, V., et al., *Protein conformational relaxation and ligand migration in myoglobin: a nanosecond to millisecond molecular movie from time-resolved Laue X-ray diffraction*. *Biochemistry*, 2001. **40**(46): p. 13802-15.
129. Aranda, R.t., et al., *Time-dependent atomic coordinates for the dissociation of carbon monoxide from myoglobin*. *Acta Crystallogr D Biol Crystallogr*, 2006. **62**(Pt 7): p. 776-83.
130. Lai, H.H., et al., *Phe-46(CD4) orients the distal histidine for hydrogen bonding to bound ligands in sperm whale myoglobin*. *Proteins*, 1995. **22**(4): p. 322-39.
131. Goldbeck, R.A., et al., *Optical detection of disordered water within a protein cavity*. *J Am Chem Soc*, 2009. **131**(34): p. 12265-72.
132. Goldbeck, R.A., et al., *Water and ligand entry in myoglobin: assessing the speed and extent of heme pocket hydration after CO photodissociation*. *Proc Natl Acad Sci U S A*, 2006. **103**(5): p. 1254-9.
133. Bossa, C., et al., *Extended molecular dynamics simulation of the carbon monoxide migration in sperm whale myoglobin*. *Biophys J*, 2004. **86**(6): p. 3855-62.
134. Jenkins, J.D., et al., *Structure of relaxed-state human hemoglobin: insight into ligand uptake, transport and release*. *Acta Crystallogr D Biol Crystallogr*, 2009. **65**(Pt 1): p. 41-8.
135. Esquerra, R.M., et al., *Kinetic spectroscopy of heme hydration and ligand binding in myoglobin and isolated hemoglobin chains: an optical window into heme pocket water dynamics*. *Phys Chem Chem Phys*, 2010. **12**(35): p. 10270-8.

136. Halder, P., J.T. Trent, 3rd, and M.S. Hargrove, *Influence of the protein matrix on intramolecular histidine ligation in ferric and ferrous hexacoordinate hemoglobins*. *Proteins*, 2007. **66**(1): p. 172-82.
137. Hargrove, M.S., et al., *Quaternary structure regulates hemin dissociation from human hemoglobin*. *J Biol Chem*, 1997. **272**(28): p. 17385-9.
138. Arredondo-Peter, R., et al., *Rice hemoglobins. Gene cloning, analysis, and O₂-binding kinetics of a recombinant protein synthesized in Escherichia coli*. *Plant Physiol*, 1997. **115**(3): p. 1259-66.
139. Trevaskis, B., et al., *Two hemoglobin genes in Arabidopsis thaliana: the evolutionary origins of leghemoglobins*. *Proc Natl Acad Sci U S A*, 1997. **94**(22): p. 12230-4.
140. Hargrove, M.S., *A flash photolysis method to characterize hexacoordinate hemoglobin kinetics*. *Biophys J*, 2000. **79**(5): p. 2733-8.
141. Puranik, M., et al., *Dynamics of carbon monoxide binding to CooA*. *J Biol Chem*, 2004. **279**(20): p. 21096-108.
142. Mims, M.P., et al., *Ligand binding to heme proteins. An evaluation of distal effects*. *J Biol Chem*, 1983. **258**(23): p. 14219-32.
143. Quillin, M.L., et al., *Structural and functional effects of apolar mutations of the distal valine in myoglobin*. *J Mol Biol*, 1995. **245**(4): p. 416-36.
144. Richards, F.M., *Areas, volumes, packing and protein structure*. *Annu Rev Biophys Bioeng*, 1977. **6**: p. 151-76.
145. Matthews, B.W. and L. Liu, *A review about nothing: are apolar cavities in proteins really empty?* *Protein Sci*, 2009. **18**(3): p. 494-502.
146. Sugio, S., et al., *Crystal structure of human serum albumin at 2.5 Å resolution*. *Protein Eng*, 1999. **12**(6): p. 439-46.

147. Matsui, T., et al., *Dioxygen activation for the self-degradation of heme: reaction mechanism and regulation of heme oxygenase*. Inorg Chem, 2010. **49**(8): p. 3602-9.
148. Otting, G., et al., *NMR identification of hydrophobic cavities with low water occupancies in protein structures using small gas molecules*. Nat Struct Biol, 1997. **4**(5): p. 396-404.
149. Finzel, B.C., et al., *Crystal structure of recombinant human interleukin-1 beta at 2.0 Å resolution*. J Mol Biol, 1989. **209**(4): p. 779-91.
150. Knapp, J.E., et al., *Ligand migration and cavities within Scapharca Dimeric Hbl: studies by time-resolved crystallography, Xe binding, and computational analysis*. Structure, 2009. **17**(11): p. 1494-504.
151. de Sanctis, D., et al., *Mapping protein matrix cavities in human cytoglobin through Xe atom binding*. Biochem Biophys Res Commun, 2004. **316**(4): p. 1217-21.
152. Moschetti, T., et al., *The structure of neuroglobin at high Xe and Kr pressure reveals partial conservation of globin internal cavities*. Biophys J, 2009. **97**(6): p. 1700-8.
153. Hasegawa, J., et al., *Stabilization of Pseudomonas aeruginosa cytochrome c(551) by systematic amino acid substitutions based on the structure of thermophilic Hydrogenobacter thermophilus cytochrome c(552)*. J Biol Chem, 1999. **274**(53): p. 37533-7.
154. Anderson, D.E., et al., *Hydrophobic core repacking and aromatic-aromatic interaction in the thermostable mutant of T4 lysozyme Ser 117-->Phe*. Protein Sci, 1993. **2**(8): p. 1285-90.
155. Eriksson, A.E., et al., *A cavity-containing mutant of T4 lysozyme is stabilized by buried benzene*. Nature, 1992. **355**(6358): p. 371-3.
156. Eriksson, A.E., et al., *Response of a protein structure to cavity-creating mutations and its relation to the hydrophobic effect*. Science, 1992. **255**(5041): p. 178-83.

157. Lassalle, M.W., et al., *Filling a cavity dramatically increases pressure stability of the c-Myb R2 subdomain*. Proteins, 2001. **45**(1): p. 96-101.
158. Radding, W. and G.N. Phillips, Jr., *Kinetic proofreading by the cavity system of myoglobin: protection from poisoning*. Bioessays, 2004. **26**(4): p. 422-33.
159. Ostermann, A., et al., *Ligand binding and conformational motions in myoglobin*. Nature, 2000. **404**(6774): p. 205-8.
160. McNaughton, L., G. Hernandez, and D.M. LeMaster, *Equilibrium O₂ distribution in the Zn²⁺-protoporphyrin IX deoxymyoglobin mimic: application to oxygen migration pathway analysis*. J Am Chem Soc, 2003. **125**(13): p. 3813-20.
161. Liong, E.C., et al., *Waterproofing the heme pocket. Role of proximal amino acid side chains in preventing hemin loss from myoglobin*. J Biol Chem, 2001. **276**(12): p. 9093-100.
162. Tomita, A., et al., *'It's hollow': the function of pores within myoglobin*. J Exp Biol, 2010. **213**(Pt 16): p. 2748-54.
163. Nienhaus, K., et al., *Ligand migration and binding in the dimeric hemoglobin of Scapharca inaequalvis*. Biochemistry, 2007. **46**(49): p. 14018-31.
164. Boechi, L., et al., *Structural determinants of ligand migration in Mycobacterium tuberculosis truncated hemoglobin O*. Proteins, 2008. **73**(2): p. 372-9.
165. Adachi, S., et al., *Direct observation of photolysis-induced tertiary structural changes in hemoglobin*. Proc Natl Acad Sci U S A, 2003. **100**(12): p. 7039-44.
166. Sottini, S., et al., *Evidence for two geminate rebinding states following laser photolysis of R state hemoglobin encapsulated in wet silica gels*. J Phys Chem B, 2005. **109**(23): p. 11411-3.
167. Draghi, F., et al., *Controlling ligand binding in myoglobin by mutagenesis*. J Biol Chem, 2002. **277**(9): p. 7509-19.

168. Miele, A.E., et al., *Control of heme reactivity by diffusion: structural basis and functional characterization in hemoglobin mutants*. *Biochemistry*, 2001. **40**(48): p. 14449-58.
169. Wiltrout, M.E., et al., *A biophysical investigation of recombinant hemoglobins with aromatic B10 mutations in the distal heme pockets*. *Biochemistry*, 2005. **44**(19): p. 7207-17.
170. Looker, D., et al., *A human recombinant haemoglobin designed for use as a blood substitute*. *Nature*, 1992. **356**(6366): p. 258-60.
171. Chang, T.M., *Future generations of red blood cell substitutes*. *J Intern Med*, 2003. **253**(5): p. 527-35.
172. Gardner, P.R., et al., *Hemoglobins dioxygenate nitric oxide with high fidelity*. *J Inorg Biochem*, 2006. **100**(4): p. 542-50.
173. Weickert, M.J., et al., *A mutation that improves soluble recombinant hemoglobin accumulation in Escherichia coli in heme excess*. *Appl Environ Microbiol*, 1999. **65**(2): p. 640-7.
174. Graves, P.E., et al., *Enhancing stability and expression of recombinant human hemoglobin in E. coli: Progress in the development of a recombinant HBOC source*. *Biochim Biophys Acta*, 2008. **1784**(10): p. 1471-9.
175. Gibson, Q.H., L.J. Parkhurst, and G. Geraci, *The reaction of methemoglobin with some ligands*. *J Biol Chem*, 1969. **244**(17): p. 4668-76.
176. Olson, J.S. and Q.H. Gibson, *The reaction of n-butyl isocyanide with human hemoglobin. I. Determination of the kinetic parameters involved in the last step in ligand binding*. *J Biol Chem*, 1971. **246**(17): p. 5241-53.
177. Reisberg, P.I. and J.S. Olson, *Rates of isonitrile binding to the isolated alpha and beta subunits of human hemoglobin*. *J Biol Chem*, 1980. **255**(9): p. 4151-8.
178. Vandegriff, K.D., et al., *Determination of the rate and equilibrium constants for oxygen and carbon monoxide binding to R-state human hemoglobin cross-linked between the alpha subunits at lysine 99*. *J Biol Chem*, 1991. **266**(26): p. 17049-59.

179. Fronticelli, C., et al., *Recombinant human hemoglobin: modification of the polarity of the beta-heme pocket by a valine67(E11)-->threonine mutation*. *Biochemistry*, 1993. **32**(5): p. 1235-42.
180. Valdes, R., Jr. and G.K. Ackers, *Thermodynamic studies on subunit assembly in human hemoglobin. Self-association of oxygenated chains (alphaSH and betaSH): determination of stoichiometries and equilibrium constants as a function of temperature*. *J Biol Chem*, 1977. **252**(1): p. 74-81.
181. Brunori, M., et al., *The reactions of the isolated alpha and beta chains of human hemoglobin with oxygen and carbon monoxide*. *J Biol Chem*, 1966. **241**(22): p. 5238-43.

Appendix 1.

RELIABILITY OF RATE CONSTANT DETERMINATIONS

New results for both isolated subunits and wt/mutant hybrid tetramers (Tables 3.1-5, Chapter 3) demonstrate that His(E7) stabilizes bound O₂ in both subunits and acts as a gate to ligand entry. The cause of the discrepancy between the old and new results for the β GlyE7 and PheE7 hybrid tetramers remains unknown. In the older experiments, O₂ binding was measured after 10% laser photolysis of HbO₂ samples and O₂ release was measured by mixing equilibrium HbO₂ samples with CO. It is possible that most of the β Gly(E7) subunits were oxidized before the measurements were carried out or CO may not have been completely removed from the stored tetrameric samples. These problems are avoided in our current experimental approach of following ligand binding and displacement starting with HbCO samples in O₂/CO mixtures and using both hybrid tetramers and isolated mutant subunits to make unambiguous assignments.

In Table A1.1 I have summarized fitted values for wild-type, native, Gly(E7), and Leu(E7) HbA subunits that have been obtained in independent experiments over the past 20 years to assess the reliability of the determinations. There is more variability than anticipated, particularly for the α Leu(E7) mutant, but the overall conclusions are clear. The value of k_{O_2} for β Gly(E7) reported in 1989 is wrong and outside the expected error, which is roughly ± 20 -30%.

However, the previous conclusion that k'_{O_2} and k_{O_2} for wild-type α subunits are 2 to 3-fold less than those for β subunits is verified for R state tetramers. These differences are not observed for monomers, where the values are effectively the same considering the errors in the independent determinations, i.e. k'_{O_2} and k_{O_2} for both chains are $\sim 50 \pm 10 \mu M^{-1}$

$^1\text{s}^{-1}$ and $20\pm 4\text{ s}^{-1}$, respectively. This small effect of assembly into hetero-tetramers, primarily a lowering of the α subunit rate parameters, was first noted in the early 1970s [16, 175-177]. However, compared with the dramatic effects of His(E7) substitutions, these differences are small and subtle.

Table A1.1. Comparison of old and new measurements of O₂ binding to monomeric and tetramer HbA subunits. The superscripts M and T refer to isolated monomers or wild-type/mutant hybrid tetramers, respectively.

Subunit	k'_{RO_2} $\mu\text{M}^{-1}\text{s}^{-1}$	k_{RO_2} s^{-1}	K_{RO_2} μM^{-1}	Subunit	k'_{RO_2} $\mu\text{M}^{-1}\text{s}^{-1}$	k_{RO_2} s^{-1}	K_{RO_2} μM^{-1}
α WT ^T	29±11	14±8	2.5±1.2	β WT ^T	60±12	30±12	2.3±1.0
α Native ^{T,1}	28±9	12±3	2.3±0.9	β Native ^{T,1}	100±13	22±8	4.5±1.7
α Native ^{T,2}	28±1	9.0±0.2	3.1±0.3	β Native ^{T,2}	64±1	23±0.7	2.7±0.3
α Native ^{T,3}	34	13	2.6	β Native ^{T,3}	87	34	2.6
α Native ^{T,4}	36±3	16±7	2.3±1.2	β Native ^{T,4}	76±8	32±8	2.4±0.9
α_{ave}^T	31±4	13±3	2.6±0.3	β_{ave}^T	77±16	28±6	2.9±0.9
α Native ^M	40±2.4	22±5.5	1.9±0.5	β Native ^M	63±12	16±1.6	3.9±0.6
α Native ^{M,5}	50	28	1.8	β Native ^{M,5}	60	16	3.8
α WT ^{M,7}	40	16	2.5	β wild-type ^{M,7}	52	14	3.7
α_{ave}^M	43±6	22±6	2.1±0.4	β_{ave}^M	58±6	15±1	3.8±0.1
α GlyE7 ^T	190	500	0.38	β GlyE7 ^T	95	310	0.31
α GlyE7 ^M	250	540	0.45	β GlyE7 ^M	160	680	0.24
α GlyE7 ^{T,1}	220	620	0.40	β GlyE7 ^{T,1}	100	(37)	(2.7)
α Leu(E7) ^T	160	860	0.19	β Leu(E7) ^T	120	490	0.24
α Leu(E7) ^{T,6}	57	500	0.11	β Leu(E7) ^{T,6}	120	790	0.15
α Leu(E7) ^{T,7}	140	810	0.16	β Leu(E7) ^{T,7}	80	510	0.16
α 0.0 Leu(E7) ^T	48	550	0.09				
α Leu(E7) _{ave} ^T	100±60	680±180	0.14±0.05	β Leu(E7) _{ave} ^T	110±23	600±170	0.18±0.05
α Leu(E7) ^M	91	450	0.20	β Leu(E7) ^M	110	4600(40%) 630(60%)	0.17 0.02

Data sources: ¹Mathews et al. [103], ²Vandegriff et al.[178], ³Fronticelli et al. [179], ⁴Unzai et al. [71], ⁵Olson et al. [16], ⁶Erin Weber and Yi Dou, unpublished undergraduate research paper, and ⁷Rachel Schweers, PhD thesis [69]; other rate parameters were taken from Chapter 3. The dissociation rate and association equilibrium constants measured for β Gly(E7)^T in 1989 by Mathews *et al.* [103] and listed in parentheses are clearly too small and large, respectively, compared to the more recent results.

PROBLEMS ASSOCIATED WITH ISOLATED SUBUNIT AGGREGATION

In solution, isolated Hb chains exist in the equilibrium between monomeric and oligomeric forms. Isolated α chains form dimers: $2\alpha \rightarrow \alpha_2$, with $K_\alpha = 8.42 \times 10^3 \text{ M}^{-1}$, and purified β subunits form tetramers β_4 , also called hemoglobin H: $4\beta \rightarrow \beta_4$, with $K_\beta = 1.41 \times 10^{-16} \text{ M}^{-3}$ [180]. In the ligand binding experiments I used 50 μM Hb solutions. The fraction of monomers (Y_M) for α chains is given by:

$$Y_M = \frac{\sqrt{1 + 8[\alpha_{\text{total}}]K_\alpha} - 1}{4[\alpha_{\text{total}}]K_\alpha}$$

Equation A1.1

For $[\alpha_{\text{total}}] = 50 \mu\text{M}$, $Y_M = 0.65$. However, all time courses for ligand binding to isolated α wild-type and mutant subunits (except for Phe(E7) and Trp(E7) mutants) show homogeneous single exponential phases (see Fig 3.9). As has been observed by others, these results show that isolated monomeric and dimeric of α -subunits have identical, R-state like ligand binding parameters [3, 181]

In the case of β chains, at $[\beta_{\text{total}}] = 50 \mu\text{M}$ the fraction of monomers can be derived from the roots of:

$$4K_\beta[\beta_{\text{total}}]^3 Y_M^4 + Y_M - 1 = 0$$

Equation A1.2

and equals ~ 0.10 . Thus, at protein concentrations used in the laser photolysis experiments, described in Chapter 3, the isolated β subunits were mostly aggregated in

the form of β_4 tetramers. However, all previous work on ligand binding suggested or showed that isolated monomeric and tetrameric β subunits have similar R-state-like rate and equilibrium constants [3, 181]. Time courses for bimolecular CO and O₂ binding to most of the isolated β variants were monophasic, with the PheE7 and TrpE7 variants being the exceptions due to conformational heterogeneity of the aromatic rings. Similarly, most of the O₂ dissociation time courses were also monophasic.

However, O₂ displacement from isolated Leu(E7) β chains by CO exhibits biphasic time courses with 40% of the change occurring rapidly with $k_{O_2} = 4300 \text{ s}^{-1}$ and 60% slowly with $k_{O_2} = 630 \text{ s}^{-1}$. The amplitudes of the fast (~35%) and slow (~65%) phases do not correlate with a 10% β and 90% β_4 distribution, as predicted by the published equilibrium dissociation constant, $K_{4,1}$ [180]. These β LeuE7 mutants were expressed and isolated free of α subunits multiple times, and in each case biphasic O₂ time courses were observed. In order to prove that the biphasic nature of the replacement kinetic curves for β Leu(E7) is not caused by monomer-tetramer differences, I measured O₂ replacement by CO as function of β chain concentrations, from 5 to 100 μM in buffer containing 625 μM O₂ and 500 μM CO. Three time courses are shown in Fig. A1.1.

In each case, biphasic time courses were observed with similar rates and amplitudes, but there was no dependence on absolute $[\beta_{\text{total}}]$. Thus, the biphasic nature of O₂ dissociation from β Leu(E7) subunits is due to conformational heterogeneity intrinsic to the globin itself and not its quaternary state. Other factors such as the residual PMB (p-chlormercuribenzoate) attached to β Cys93 or the presence of partially unfolded subunits could also contribute to observed inhomogeneity of time courses, despite my best efforts to remove the mercurial with dithiothreitol and purify only holo-globin forms.

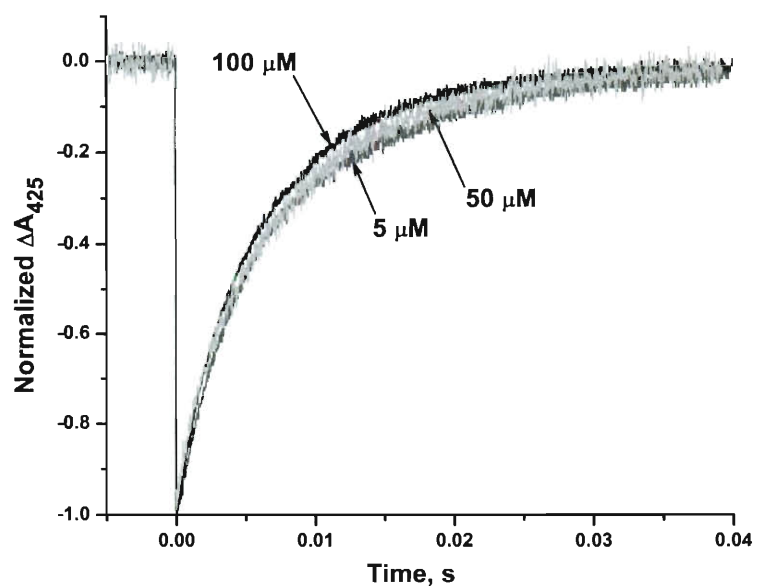
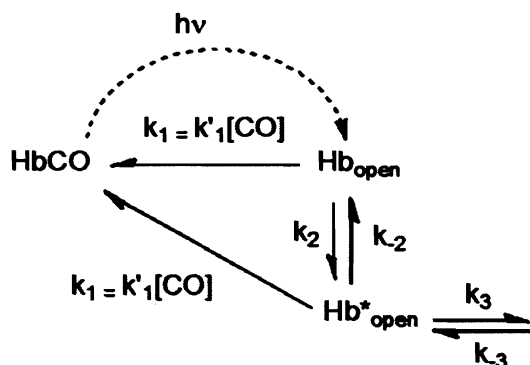


Figure A1.1. O_2 replacement by CO for isolated β Leu(E7) subunits. The reaction was carried out in the buffer containing 625 μM O_2 and 500 μM CO, conditions were the same as in Fig. 3.1. protein concentration was 5, 50 and 100 μM , as indicated.

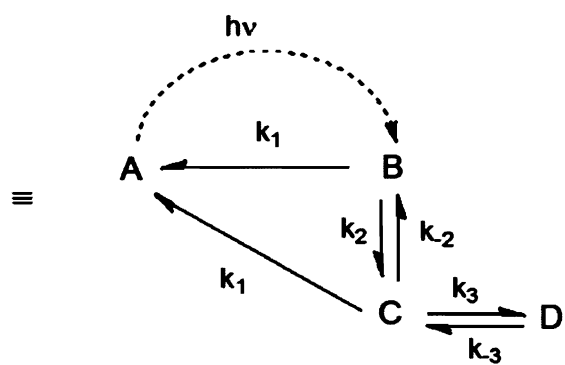
Appendix 2.

DERIVATIONS OF RATE EXPRESSIONS FROM KINETIC SCHEMES

A1. Derivations based on Scheme 4.2 (Chapter 4) for bimolecular CO rebinding to isolated Trp58(E7) α subunits after laser photolysis: expressions for f_{fast} and k_{fast} - In this scheme, ligands escape into solvent from an open conformation, Hb_{open} , and can rapidly re-enter and bind to the iron in this state, $k_1 = k'_1[CO]$. This bimolecular rebinding from solvent competes with a conformational transition, k_2 , to another open, more expanded state, Hb^*_{open} , which allows rapid inward movement of the large Trp(E7) side chain at rate of k_3 to close the E7 channel and restrict binding at the iron atom in the Hb_{closed} conformation.



Scheme 4.2 a



Scheme 4.2 b

In Scheme 4.2 b, $A = HbCO$, $B = Hb_{open}$, $C = Hb^*_{open}$, and $D = Hb_{closed}$; $k_1 = k'_1[CO]$. In order to derive an analytical expression for the rate and fraction of the fast phase for bimolecular CO rebinding, we made two simplifying assumptions. (a) The rate of the $Hb_{closed} \rightarrow Hb^*_{open}$ transition was assumed to be much slower than that for the formation of Hb_{closed} , i.e. $k_3 \gg k_{-3}$, and k_{-3} can be neglected in the analysis. (b) The Hb^*_{open} state was assumed to be short lived and in a steady state during the rebinding

reaction with $dC/dt \approx 0$. Under these conditions, the rate of re-formation of HbCO or A can be obtained from finding an analytical solution to the follow set differential equations.

$$\frac{dA}{dt} = k_1(B+C) \quad (S1)$$

$$\frac{dB}{dt} = -(k_1+k_2)B+k_{-2}C \quad (S2)$$

$$\frac{dC}{dt} = -(k_1+k_{-2}+k_3)C+k_2B=0, \Rightarrow C = \frac{k_2}{k_1+k_{-2}+k_3} B \quad (S3)$$

Substituting the steady state expression for C into equation S2 gives:

$$\frac{dB}{dt} = - (k_1+k_2)B+k_{-2}C = - (k_1+k_2)B + \frac{k_2k_{-2}}{k_1+k_{-2}+k_3} B = - \frac{k_1^2+k_1k_{-2}+k_1k_3+k_1k_2+k_3k_2}{k_1+k_{-2}+k_3} B$$

Integrating and applying the boundary conditions that at $t = 0$, $B = P_0$, gives B as function of time t:

$$B = P_0 \exp\left\{-\frac{k_1^2+k_1k_{-2}+k_1k_3+k_1k_2+k_3k_2}{k_1+k_{-2}+k_3} t\right\}, \quad (S4)$$

where P_0 is total protein. Substituting the expressions for C and B (Equations S3 and S4) into Equation S1 gives

$$\frac{dA}{dt} = k_1(B+C) = \left(k_1 + \frac{k_1k_2}{k_1+k_{-2}+k_3}\right) P_0 \exp\left\{-\frac{k_1^2+k_1k_{-2}+k_1k_3+k_1k_2+k_3k_2}{k_1+k_{-2}+k_3} t\right\} \quad (S5)$$

Integrating (S5) gives:

$$A = -\frac{k_1^2+k_1k_{-2}+k_1k_3+k_1k_2}{k_1^2+k_1k_{-2}+k_1k_3+k_1k_2+k_3k_2} P_0 \exp\left\{-\frac{k_1^2+k_1k_{-2}+k_1k_3+k_1k_2+k_3k_2}{k_1+k_{-2}+k_3} t\right\} + const \quad (S6)$$

Applying the boundary conditions immediately after complete laser photolysis that at $t = 0$, $A = 0$ gives:

$$const = \frac{k_1^2 + k_1 k_{-2} + k_1 k_3 + k_1 k_2}{k_1^2 + k_1 k_{-2} + k_1 k_3 + k_1 k_2 + k_3 k_2} P_0.$$

This integration constant then allows derivation of the final analytical expression for A as function of time:

$$A = \frac{k_1^2 + k_1 k_{-2} + k_1 k_3 + k_1 k_2}{k_1^2 + k_1 k_{-2} + k_1 k_3 + k_1 k_2 + k_3 k_2} P_0 \left\{ 1 - \exp \left[- \frac{k_1^2 + k_1 k_{-2} + k_1 k_3 + k_1 k_2 + k_3 k_2}{k_1 + k_{-2} + k_3} t \right] \right\} \quad (S7)$$

The amplitude and exponent in this equation provide expressions for the fraction and rate of the fast phase seen in the laser photolysis experiments.

$$f_{fast} = \frac{k_1^2 + k_1 k_{-2} + k_1 k_3 + k_1 k_2}{k_1^2 + k_1 k_{-2} + k_1 k_3 + k_1 k_2 + k_3 k_2} \quad (S8)$$

$$k_{fast} = \frac{k_1^2 + k_1 k_{-2} + k_1 k_3 + k_1 k_2 + k_3 k_2}{k_1 + k_{-2} + k_3} \quad (S9)$$

These complex expressions, with quadratic terms in [CO] (i.e. $k_1 = k'_1[\text{CO}]$), simplify greatly if $k_3 \gg (k_1, k_{-2}, \text{ and } k_2)$ so that only the terms containing k_3 are kept in the numerators and denominators. Under these conditions, the expressions reduce to:

$$f_{fast} \approx \frac{k_1}{k_1 + k_2} \text{ and } k_{fast} \approx k_1 + k_2 \quad (S10)$$

and are identical to those derived for the simple mechanism given in Scheme 4.1 and Equation 4.1-3 of the Chapter 4, where $k_1 = k'_1[\text{CO}]$ and k_2 is equivalent to k_{close} .

A2. Expression for k_{slow} after laser photolysis or for CO binding to the equilibrium form of Trp(E7) deoxy α subunits in rapid mixing experiments - To determine the expression for the dependence of the slow rate of bimolecular ligand rebinding to the closed form on [CO], all of the protein being examined in this phase is assumed to be initially in the Hb_{closed} state and then is completely converted into HbCO .

Because the overall process is slow but the individual rate parameters k_1 , k_{-2} , k_2 , and k_3 are large, steady state approximations can be assumed for B and C. In this case, the rate of conversion of Hb_{closed} to Hb^*_{open} defined by k_{-3} must be considered. Under these conditions, the formation of A from D is described by three differential equations two of which are set equal to zero based on steady state assumptions:

$$\frac{dA}{dt} = k_1(B + C) \quad (\text{S11})$$

$$\frac{dB}{dt} = -(k_1 + k_2)B + k_{-2}C = 0 \Rightarrow C = \frac{k_1 + k_2}{k_{-2}}B \quad (\text{S12})$$

$$\frac{dC}{dt} = -(k_1 + k_{-2} + k_3)C + k_2B + k_{-3}D = 0 \quad (\text{S13})$$

Combining Equations S11 and S12 gives:

$$\frac{dA}{dt} = \frac{k_1(k_1 + k_2 + k_{-2})}{k_{-2}}B \quad (\text{S14})$$

Inserting the expression for C from Equation S12 into Equation S13 and rearranging, gives:

$$D = \frac{(k_1 + k_{-2} + k_3)(k_1 + k_2) - k_2k_{-2}}{k_{-3}k_{-2}}B \quad (\text{S15})$$

The total protein in the reaction is given by

$$P_0 = A + B + C + D \Rightarrow (P_0 - A) = B + C + D \quad (\text{S16})$$

Inserting the expressions for C and D (Equations S12 and S15) into Equation S16 and solving for B gives:

$$B = \frac{k_{-3}k_{-2}}{(k_1 + k_{-3})(k_1 + k_2 + k_{-2}) + k_3(k_1 + k_2)}(P_0 - A) \quad (\text{S17})$$

Inserting the expression for B in Equation S17 into Equation S14, gives the following differential equation in A:

$$\frac{dA}{dt} + \frac{k_{-3}k_1(k_1+k_2+k_{-2})}{(k_1+k_{-3})(k_1+k_2+k_{-2})+k_3(k_1+k_2)} A = \frac{k_{-3}k_1(k_1+k_2+k_{-2})}{(k_1+k_{-3})(k_1+k_2+k_{-2})+k_3(k_1+k_2)} P_0 \quad (\text{S18})$$

The analytical solution for this linear first order differential equation gives the following expression for the observed slow rate of the formation of A:

$$k_{slow} = \frac{k_{-3}k_1(k_1+k_2+k_{-2})}{(k_1+k_{-3})(k_1+k_2+k_{-2})+k_3(k_1+k_2)} = \frac{k_{-3}k_1}{k_1+k_{-3} + \frac{k_3(k_1+k_2)}{(k_1+k_2+k_{-2})}} \quad (\text{S19})$$

At very high [CO], $k_1 \gg (k_2 \text{ and } k_{-2})$ and still assuming $k_3 > (k_{-3} \text{ and } k_1)$, the observed slow rate will be proportional to [CO] with an apparent bimolecular rate constant equal to k'_1/K_3 , where K_3 is the equilibrium constant for the $\text{Hb}^*_{\text{open}}$ to $\text{Hb}_{\text{closed}}$ conformational transition and is a very large number.

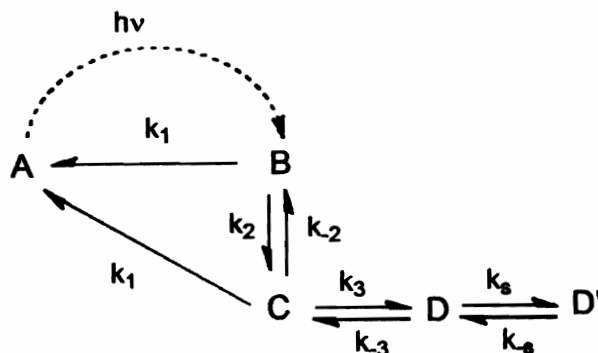
$$k_{slow} = \frac{k_{-3}k_1}{k_1+k_{-3} + \frac{k_3(k_1+k_2)}{(k_1+k_2+k_{-2})}} \approx \frac{k_{-3}k_1}{k_1+k_3} \approx \frac{k_{-3}k_1}{k_3} = \frac{1}{K_3} k_1 \quad (\text{S20})$$

Note that the equilibrium fraction of deoxy- α subunits that are present in intermediate C ($\text{Hb}^*_{\text{open}}$) state, resulting from opening of D ($\text{Hb}_{\text{closed}}$), φ_C , is given by:

$$\varphi_C = \frac{1}{1+K_3} \approx \frac{1}{K_3} \text{ because } K_3 \gg 1 \quad (\text{S21})$$

Thus, the rate of the slow phase is roughly proportional to the equilibrium fraction of $\text{Hb}^*_{\text{open}}$ states times the pseudo first order rate of ligand binding to the open state and, as a result, is linearly dependent on [CO]. At lower CO concentrations, k_{slow} shows a quadratic dependence on [CO], and the initial slope of the k_{slow} versus [CO] is greater than that observed at high ligand concentrations as is observed in Fig. 4.10 B of the Chapter 4.

A3. Derivation of expression for ultra slow phase seen in stopped flow rapid mixing experiments with isolated α subunits - To describe the ultra-slowly reacting species observed only in stopped flow experiments, we added an additional conformer (D') at the end of the Scheme 4.2 b.



Scheme 4.2 c

To determine the expression for the observed rate of ligand binding to D', we assume that B, C and D are in a steady state.

$$\frac{dB}{dt} = -(k_1 + k_2)B + k_{-2}C = 0 \Rightarrow C = \frac{k_1 + k_2}{k_{-2}} B \quad (\text{S22})$$

$$\frac{dC}{dt} = -(k_1 + k_{-2} + k_3)C + k_2B + k_{-3}D = 0 \quad (\text{S23})$$

$$\frac{dD}{dt} = -(k_{-3} + k_s)D + k_3C + k_{-s}D' = 0 \quad (\text{S24})$$

The rate of formation of HbCO is still given by:

$$\frac{dA}{dt} = k_1(B + C) = \frac{k_1(k_1 + k_2 + k_{-2})}{k_{-2}} B \quad (\text{S25})$$

The total protein, P_0 , in this case is defined by:

$$P_0 = A + B + C + D + D' \Rightarrow (P_0 - A) = B + C + D + D' \quad (\text{S26})$$

Again, the steady state approximations for B, C and D provide the expressions for C, D and D' in terms of B, which can be inserted into Equation S26 to derive an expression for B in terms of $(P_0 - A)$. This expression for B can be inserted into Equation S25 to generate a linear first order differential equation in A similar to Equation S18. The rate of the slow phase for the formation of A from D' derived from the solution of this differential equation is:

$$k_{obs} = \frac{k_1 k_{-3} \frac{k_{-S}}{k_S + k_{-S}}}{k_1 + k_{-3} \frac{k_1 + k_{-S}}{k_S + k_{-S}} + k_3 \frac{k_1 + k_2}{k_1 + k_2 + k_{-2}}} \quad (\text{S27})$$

If $k_3 \gg (k_1, k_{-3}, k_S, k_{-S})$ and $k_1 \gg (k_2 \text{ and } k_{-2})$ at very high [CO], Equation S27 reduces to

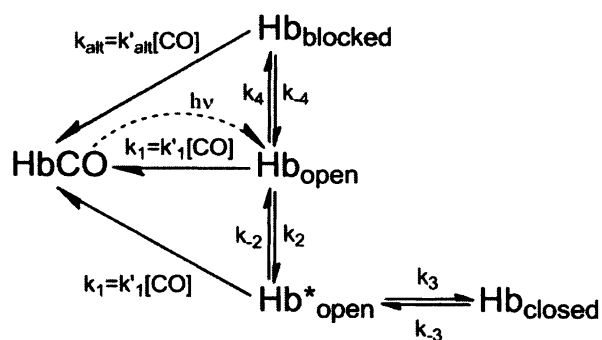
$$k_{obs} \approx k_1 \frac{k_{-3}}{k_3} \frac{k_{-S}}{k_S + k_{-S}} \approx k_1 \varphi_C \varphi_D, \quad (\text{S28})$$

where the fractions of C and D are given by:

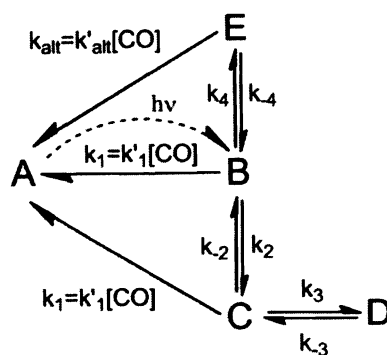
$$\varphi_C = \frac{1}{1 + K_3} \approx \frac{1}{K_3}, \text{ where } K_3 = \frac{k_3}{k_{-3}}, \text{ and } \varphi_D = \frac{1}{1 + K_S}, \text{ where } K_S = \frac{k_S}{k_{-S}}.$$

Thus, the rate of the ultra slow phase is roughly equal to that of the initial slow phases seen in both the laser and rapid mixing experiments times the fraction of deoxy- α subunits that are present in the D state at equilibrium. The dependence of the observed ultra-slow rate on [CO] was fit to this model, as shown in Figure 4.10 B of the Chapter 4, and the optimized parameters are $k_S = 610 \text{ s}^{-1}$, $k_{-S} = 200 \text{ s}^{-1}$.

B1. Derivation of expressions for the rates and fractions of the fast, moderate and slow phases observed for CO binding to Trp63(E7) β subunits – Scheme 4.3 describes bimolecular CO rebinding to isolated Trp(E7) β subunits after photodissociation. In this case, there are two slow phases which we have interpreted as *blocked* and *closed* states, in which Trp(E7) either blocks the entrance to the E7 channel as is observed in the crystal structure of Trp63(E7) β CO (Fig. 4.8 D, Chapter 4) or rotates into the distal pocket and completely closes the channel, as seen in the crystal structure of Trp58(E7) deoxy- α (Fig. 4.8 C, Chapter 4). The *blocked* state binds CO through alternative non-E7 pathways ($\text{Hb}_{\text{blocked}} \rightarrow \text{HbCO}$) as well as through the opening of the E7 gate ($\text{Hb}_{\text{blocked}} \rightarrow \text{Hb}_{\text{open}} \rightarrow \text{HbCO}$). In the *closed* conformer the access to Fe atom of the heme is severely hindered, and CO rebinding to $\text{Hb}_{\text{closed}}$ may occur only via the formation of the $\text{Hb}^*_{\text{open}}$ ($\text{Hb}_{\text{closed}} \rightarrow \text{Hb}^*_{\text{open}} \rightarrow \text{HbCO}$).



Scheme 4.3 a



Scheme 4.3 b

In Scheme 4.3 b, A represents HbCO, B represents Hb_{open}, C represents Hb*_{open}, E represents Hb_{blocked}, and D represent slowly reacting Hb_{closed}. The rate of the fast phase for bimolecular rebinding after laser photolysis describes the decay of the B and C states, all of which either rapidly bind CO or relax to the blocked and closed states after laser photolysis. The rate of formation of the HbCO state, A, is described by:

$$\frac{dA}{dt} = k_1(B + C) \quad (\text{S29})$$

Similar to the analysis for rapid CO binding to α subunits, we assume that the rates of ligand binding to the *blocked* and *closed* states are significantly slower than the other processes occurring during the fast phase. Expressions for B and C can be derived from the following differential equations.

$$\frac{dB}{dt} = -(k_1 + k_2 + k_4)B + k_{-2}C \quad (\text{S30})$$

Applying a steady state approximation to C gives:

$$\frac{dC}{dt} = -(k_1 + k_{-2} + k_3)C + k_2B = 0 \Rightarrow C = \frac{k_2}{k_1 + k_{-2} + k_3}B \quad (\text{S31})$$

Combining these equations gives,

$$\frac{dB}{dt} = - \left(k_1 + k_2 + k_4 - \frac{k_{-2}k_2}{k_1 + k_{-2} + k_3} \right) B \quad (\text{S32})$$

Integrating Equation S32 and using the boundary condition that at $t = 0$, $B = P_0$, the following expression is obtained for B:

$$B = P_0 \exp \left\{ - \left(k_1 + k_2 + k_4 - \frac{k_{-2}k_2}{k_1 + k_{-2} + k_3} \right) t \right\}, \quad (\text{S33})$$

where P_0 is total protein. The fraction of fast phase can be derived by obtaining a linear first order differential equation describing the change in A. Substituting the expressions for C and B from Equations S31 and S33 into Equation S29 gives

$$\frac{dA}{dt} = \left(k_1 + \frac{k_1k_2}{k_1 + k_{-2} + k_3} \right) P_0 \exp \left\{ - \left(k_1 + k_2 + k_4 - \frac{k_{-2}k_2}{k_1 + k_{-2} + k_3} \right) t \right\} \quad (\text{S34})$$

Integrating Equation S34 and using the boundary condition that at $t = 0$, $A=0$ gives:

$$A = \frac{k_1 + \frac{k_1k_2}{k_1 + k_{-2} + k_3}}{k_1 + k_2 + k_4 - \frac{k_{-2}k_2}{k_1 + k_{-2} + k_3}} P_0 \left(1 - \exp \left\{ - \left(k_1 + k_2 + k_4 - \frac{k_{-2}k_2}{k_1 + k_{-2} + k_3} \right) t \right\} \right)$$

where the rate of the fast phase, k_{fast} , and the fraction of A at the end of the fast phase, $f_{fast} = A_{t \rightarrow \infty} / P_0$, are given by:

$$k_{fast} = k_1 + k_2 + k_4 - \frac{k_{-2}k_2}{k_1 + k_{-2} + k_3} \quad (\text{S35})$$

$$f_{fast} = \frac{k_1 + \frac{k_1k_2}{k_1 + k_{-2} + k_3}}{k_1 + k_2 + k_4 - \frac{k_{-2}k_2}{k_1 + k_{-2} + k_3}} \quad (\text{S36})$$

If k_3 is much larger than all other rates in the scheme, then these complex expressions reduce to:

$$k_{fast} \approx k_1 + k_2 + k_4 \text{ and } f_{fast} \approx \frac{k_1}{k_1 + k_2 + k_4} \quad (\text{S37})$$

The fraction of $\text{Hb}_{\text{closed}}$, f_{closed} , is derived from the rate law for D and used to compute the slow phase rate:

$$\frac{dD}{dt} = k_3 C \quad (\text{S38})$$

Inserting the expressions for C and B from Equations S31 and S33 into Equation S38 gives:

$$\frac{dD}{dt} = \frac{k_2 k_3}{k_1 + k_{-2} + k_3} P_0 \exp\left\{-\left(k_1 + k_2 + k_4 - \frac{k_{-2} k_2}{k_1 + k_{-2} + k_3}\right)t\right\} \quad (\text{S39})$$

Integrating and applying the boundary condition that at $t = 0$, $D = 0$ gives an expression for D as function of time:

$$D = \frac{\frac{k_2 k_3}{k_1 + k_{-2} + k_3}}{k_1 + k_2 + k_4 - \frac{k_{-2} k_2}{k_1 + k_{-2} + k_3}} P_0 \left(1 - \exp\left\{-\left(k_1 + k_2 + k_4 - \frac{k_{-2} k_2}{k_1 + k_{-2} + k_3}\right)t\right\}\right),$$

where the term before parenthesis equals f_{slow} , which represents the fraction of the very slow phase in laser photolysis time courses for CO rebinding to Trp(E7) β subunits (Figs. 4.2 A and 4.11 A in the Chapter 4).

$$f_{\text{slow}} = \frac{\frac{k_2 k_3}{k_1 + k_{-2} + k_3}}{k_1 + k_2 + k_4 - \frac{k_{-2} k_2}{k_1 + k_{-2} + k_3}} \quad (\text{S40})$$

The fraction of moderately reacting $\text{Hb}_{\text{blocked}}$ states that is generated after laser photolysis can be derived from the rate law for E:

$$\frac{dE}{dt} = k_4 B \quad (\text{S41})$$

Using the expression for B from Equation S33 gives,

$$\frac{dE}{dt} = k_4 P_0 \exp\left\{-\left(k_1 + k_2 + k_4 - \frac{k_{-2}k_2}{k_1 + k_{-2} + k_3}\right)t\right\} \quad (\text{S42})$$

Integrating and applying the boundary condition that at $t = 0$, $E = 0$, gives:

$$E = \frac{k_4}{k_1 + k_2 + k_4 - \frac{k_{-2}k_2}{k_1 + k_{-2} + k_3}} P_0 \left(1 - \exp\left\{-\left(k_1 + k_2 + k_4 - \frac{k_{-2}k_2}{k_1 + k_{-2} + k_3}\right)t\right\}\right),$$

where the amplitude equals f_{middle} , which is defined experimentally as the middle or first slow phase seen in the laser photolysis data for Trp(E7) β subunits (Figs. 4.2 A and 4.11 A in the Chapter 4).

$$f_{middle} = \frac{k_4}{k_1 + k_2 + k_4 - \frac{k_{-2}k_2}{k_1 + k_{-2} + k_3}} \quad (\text{S43})$$

Again, if k_3 is much larger than all other rates in the scheme, the expressions for the fractions of closed and blocked species reduce to simple expressions that fit the [CO] dependence of the observed fast rate and fractions of closed (slow phase) and blocked (middle phase) species observed in our laser photolysis experiments (Fig. 4.11, Chapter 4).

$$f_{slow} \approx \frac{k_2}{k_1 + k_2 + k_4} \quad \text{and} \quad f_{middle} \approx \frac{k_4}{k_1 + k_2 + k_4} \quad (\text{S44})$$

These simplified expressions show that the values of k_{-2} and k_{-4} are effectively undefined by analysis of the fast phase rate and fractions of the fast, middle and slow phases.

B2. Derivation of expressions for the dependence of the rates of the middle and slow phases observed for CO binding to Trp63(E7) β subunits on ligand concentration – In the analysis of the middle phase we assume that the fast phase is

already over and $t = 0$ corresponds to the beginning of the middle phase, while the slow phase hasn't started yet, *i.e.* k_3 is ignored (Scheme 4.3). The rate of decay of the *blocked* conformer is described by the following differential equation:

$$\frac{dE}{dt} = -(k_{alt} + k_{-4})E + k_4B \quad (S45)$$

The steady state assumptions are invoked for the rate of change of B and C:

$$\frac{dC}{dt} = 0 = -(k_1 + k_{-2} + k_3)C + k_2B \Rightarrow C = \frac{k_2}{k_1 + k_{-2} + k_3}B \quad (S46)$$

$$\frac{dB}{dt} = 0 = -(k_1 + k_2 + k_4)B + k_{-4}E + k_{-2}C \Rightarrow B = \frac{k_{-4}}{k_1 + k_2 + k_4 - \frac{k_{-2}k_2}{k_1 + k_{-2} + k_3}}E \quad (S47)$$

Inserting S47 into S45, integrating and applying boundary conditions that at $t = 0$, $E = E_0$ we obtain the following expression for E:

$$E = E_0 \exp \left\{ - \left[k_{alt} + k_{-4} \left(1 - \frac{k_4}{k_1 + k_2 + k_4 - \frac{k_{-2}k_2}{k_1 + k_{-2} + k_3}} \right) \right] t \right\} \quad (S48)$$

where E_0 is the total amount of the middle phase immediately after the fast phase and equals $f_{middle}P_0$. The expression for the rate of the middle phase is

$$k_{middle} = k_{alt} + k_{-4} \left(1 - \frac{k_4}{k_1 + k_2 + k_4 - \frac{k_{-2}k_2}{k_1 + k_{-2} + k_3}} \right) \quad (S49)$$

If k_3 is much larger than all other rates in the mechanism, the expression for the k_{middle} can be reduced to the following expression,

$$k_{middle} = k_{alt} + k_{-4} \left(1 - \frac{k_4}{k_1 + k_2 + k_4 - \frac{k_{-2}k_2}{k_1 + k_{-2} + k_3}} \right) = k_{alt} + k_{-4} (1 - f_{middle}) \quad (S50)$$

Here, f_{middle} is the fraction of middle phase defined in Equation S43 and $\approx k_4/(k_1+k_2+k_4)$. Thus, the decay of $\text{Hb}_{\text{blocked}}$ involves either direct CO binding to the *blocked* conformer, isomerization to the Hb_{open} conformation with subsequent CO binding, or eventual transitioning to $\text{Hb}_{\text{closed}}$.

The slow phase for CO binding to β Trp(E7) represents CO rebinding to the *closed* conformer ($\text{Hb}_{\text{closed}}$ or D), and is measured as reappearance of A from D after the fast and middle phases have already occurred (i.e. the reaction starts with all the protein being in the form of D, Scheme 4.3). The expression for the slow rate dependence on $[\text{CO}]$ is derived from the following set of differential equations,

$$\frac{dA}{dt} = k_1(B+C) + k_{\text{alt}}E \quad (\text{S51})$$

$$\frac{dE}{dt} = -(k_{\text{alt}} + k_{-4})E + k_4B = 0 \Rightarrow E = \frac{k_4}{k_{\text{alt}} + k_{-4}}B \quad (\text{S52})$$

$$\begin{aligned} \frac{dB}{dt} &= -(k_1 + k_2 + k_4)B + k_{-2}C + k_{-4}E = 0 \Rightarrow C = \frac{(k_1 + k_2 + k_4)B - k_{-4}E}{k_{-2}} = \\ &= \frac{(k_1 + k_2 + k_4)B - \frac{k_{-4}k_4}{k_{\text{alt}} + k_{-4}}B}{k_{-2}} = \frac{k_1 + k_2 + \frac{k_{\text{alt}}k_4}{k_{\text{alt}} + k_{-4}}}{k_{-2}}B \end{aligned} \quad (\text{S53})$$

$$\begin{aligned} \frac{dC}{dt} &= -(k_1 + k_{-2} + k_3)C + k_2B + k_{-3}D = 0 \Rightarrow D = \frac{(k_1 + k_{-2} + k_3)C - k_2B}{k_{-3}} = \\ &= \frac{(k_1 + k_{-2} + k_3) \left(k_1 + k_2 + \frac{k_{\text{alt}}k_4}{k_{\text{alt}} + k_{-4}} \right) - k_2k_{-2}}{k_{-2}k_{-3}}B = \frac{k_2(k_3 + k_1) + \left(k_1 + \frac{k_{\text{alt}}k_4}{k_{\text{alt}} + k_{-4}} \right) (k_1 + k_{-2} + k_3)}{k_{-2}k_{-3}}B \end{aligned}$$

(S54)

The total protein is expressed as,

$$\begin{aligned}
 P_0 &= A + B + C + D + E \Rightarrow P_0 - A = B + C + D + E = \\
 &= B \left[1 + \frac{k_1 + k_2 + \frac{k_{alt}k_4}{k_{alt} + k_{-4}}}{k_{-2}} + \frac{k_2(k_3 + k_1) + \left(k_1 + \frac{k_{alt}k_4}{k_{alt} + k_{-4}}\right)(k_1 + k_{-2} + k_3)}{k_{-2}k_{-3}} + \frac{k_4}{k_{alt} + k_{-4}} \right] = \\
 &= B \frac{k_{-2}k_{-3} \left(1 + \frac{k_4}{k_{alt} + k_{-4}} \right) + k_2(k_1 + k_3 + k_{-3}) + \left(k_1 + \frac{k_{alt}k_4}{k_{alt} + k_{-4}}\right)(k_1 + k_{-2} + k_3 + k_{-3})}{k_{-2}k_{-3}} \Rightarrow \\
 \Rightarrow B &= \frac{k_{-2}k_{-3}}{k_{-2}k_{-3} \left(1 + \frac{k_4}{k_{alt} + k_{-4}} \right) + k_2(k_1 + k_3 + k_{-3}) + \left(k_1 + \frac{k_{alt}k_4}{k_{alt} + k_{-4}}\right)(k_1 + k_{-2} + k_3 + k_{-3})} (P_0 - A)
 \end{aligned} \tag{S55}$$

Inserting expressions for B (S55), C (S53) and E (S52) into Equation S51 and rearranging gives linear first order differential equation for A,

$$\frac{dA}{dt} = \frac{k_{-3} \left((k_1 + k_{-2}) \left(k_1 + \frac{k_{alt}k_4}{k_{alt} + k_{-4}} \right) + k_1k_2 \right)}{k_{-2}k_{-3} \left(1 + \frac{k_4}{k_{alt} + k_{-4}} \right) + k_2(k_1 + k_3 + k_{-3}) + \left(k_1 + \frac{k_{alt}k_4}{k_{alt} + k_{-4}}\right)(k_1 + k_{-2} + k_3 + k_{-3})} (P_0 - A) \tag{S56}$$

Solving this equation provides the expression for k_{slow} ,

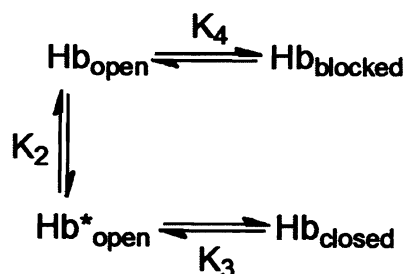
$$k_{slow} = \frac{k_{-3} \left((k_1 + k_{-2}) \left(k_1 + \frac{k_{alt}k_4}{k_{alt} + k_{-4}} \right) + k_1k_2 \right)}{k_{-2}k_{-3} \left(1 + \frac{k_4}{k_{alt} + k_{-4}} \right) + k_2(k_1 + k_3 + k_{-3}) + \left(k_1 + \frac{k_{alt}k_4}{k_{alt} + k_{-4}}\right)(k_1 + k_{-2} + k_3 + k_{-3})} \tag{S57}$$

Again, if we assume that k_3 is larger than all other rates in the mechanism and remove the terms in the Equation S57 that do not contain k_3 , then the expression for k_{slow} will reduce to

$$k_{slow} \approx \frac{1}{1+K_3} \left(k_1 + k_{-2} \frac{k_1 + \frac{k_{alt}k_4}{k_{alt} + k_{-4}}}{k_1 + k_2 + \frac{k_{alt}k_4}{k_{alt} + k_{-4}}} \right) \quad (S58)$$

where K_3 is equilibrium constant for the formation of Hb^*_{open} from Hb_{closed} and equals k_3/k_{-3} . The $1/(1+K_3)$ term here represents roughly the fraction of Hb^*_{open} formed from Hb_{closed} (φ_C). Note that $\varphi_C = 1/(1+K_3) \approx 1/K_3$, since $K_3 \gg 1$.

B3. Derivation of equilibrium fraction of closed versus blocked Trp(E7) deoxy β conformers – At equilibrium, all the Trp(E7) β subunits react slowly with CO at a rate equal to that when starting with the closed conformer. The fraction of closed conformer can be computed from Scheme 4.4.



Scheme 4.4

In this scheme, the fraction of Hb_{closed} conformer is given by:

$$F_{closed} = \frac{[Hb_{closed}]}{[Hb_{open}] + [Hb^*_{open}] + [Hb_{blocked}] + [Hb_{closed}]} \quad (S59)$$

The equilibrium relationships are:

$$K_2 = \frac{[Hb^*_{open}]}{[Hb_{open}]}; K_3 = \frac{[Hb_{closed}]}{[Hb^*_{open}]}; K_4 = \frac{[Hb_{blocked}]}{[Hb_{open}]} \quad (S60)$$

Then the relative probabilities or concentrations of the conformers are given by:

$$[Hb_{open}] = 1; [Hb^*_{open}] = K_2; [Hb_{closed}] = K_2 K_3; [Hb_{blocked}] = K_4 \quad (S61)$$

and the fraction of Hb_{closed} conformers at equilibrium will be:

$$F_{closed} = \frac{K_2 K_3}{1 + K_2 + K_4 + K_2 K_3} \quad (S62)$$

From the kinetic experiments $K_2 = k_2/k_{-2} \approx 3.64$, $K_3 = k_3/k_{-3} \approx 1660$, $K_4 = k_4/k_{-4} \approx 1250$. Thus, $F_{closed} \approx 0.83$ for the isolated β Trp(E7) subunits.